

**PREFERENTIAL FLOW AND TRANSPORT THROUGH  
DEFORMATION BAND FAULTS IN THE SEMI-ARID VADOSE  
ZONE OF THE RIO GRANDE RIFT, NEW MEXICO, USA**

by

**JOHN MICHAEL SIGDA**

Submitted in partial fulfillment  
of the requirements for the degree of  
Doctor of Philosophy (Hydrology)

New Mexico Institute of Mining and Technology  
Department of Earth and Environmental Science  
Socorro, New Mexico

May, 2004

© COPYRIGHT 2004, John M. Sigda  
All rights reserved.

This work is dedicated to my parents, Helen and Walter Sigda, and most especially to Becky, Zachariah, and Hannah, who are my joy and my support. Sina maneno yenye utamu na unguvu ya kutosha kwa kuwashukuru. To you, all my love and gratitude.

## ABSTRACT

Discerning preferential flow and solute transport through the arid and semi-arid sedimentary basins of the American Southwest is critical to preserving and protecting vital ground water resources. Commonly found throughout these basins, deformation band faults are tabular dipping structures with severe reductions in grain and pore sizes relative to their parent sands. These faults act as barriers to saturated flow and, potentially, as preferential flow paths through the vadose zone. This study presents the first measurements of unsaturated hydraulic properties for these faults and modeling of fault-induced preferential flow and transport through poorly lithified vadose-zone sands.

The hydraulic properties of intact samples from five faults, with different displacements, and their associated parent sand (protolith) were measured using standard laboratory methods and the Unsaturated Flow Apparatus (UFA). The UFA is a centrifuge system equipped to measure the moisture content – matric potential,  $\theta(\psi)$ , and hydraulic conductivity – moisture content,  $K(\theta)$ , relationships. Measured hydraulic relations were used in simple, one-dimensional, steady flow models to assess the potential for preferential flow and transport through faulted sands under semi-arid and arid conditions. X-ray diffraction revealed the samples have two different mineral assemblages in their clay size fraction (CSF): samples from one study area contain pure and possibly authigenic smectite, whereas samples from the other area contain a mixture

of smectite and other minerals. At saturation, hydraulic conductivity ( $K$ ) for sand protolith from the area with pure smectite CSF is at least two orders of magnitude less than the  $K$  for sand protolith from the other area with mixed clay minerals in the CSF.

Deformation band faults possess strikingly different saturated and unsaturated hydraulic properties than their parent sands. Saturated  $K$  is one to three orders of magnitude lower in faults than protolith. As conditions become drier, unsaturated  $K$  decreases more abruptly in protolith than faults, so that protolith and fault unsaturated  $K$  reach equivalence (crossover point), and, for still drier conditions, fault unsaturated  $K$  exceeds protolith unsaturated  $K$  by several orders of magnitude. Crossover points and fault unsaturated  $K$  functions differ with CSF mineral composition. Fault unsaturated  $K$  functions do not vary significantly for the range of vertical displacements studied (0.2 to  $\geq 3$  m).

Simple one-dimensional models of water movement, solute transport, and diagenesis reveal that deformation band faults can act as conduits through moderately dry vadose-zone sands. Capillary wicking through finer-grained deformation bands significantly accelerates water and solute transport, driven downward by gravity or upward by evaporation, for a range of moderately dry vadose-zone conditions like those observed in the Rio Grande rift of central New Mexico. Observed fault spatial densities are sufficient for capillary wicking to locally enhance recharge or evaporative discharge. Faults can also accelerate contaminant migration because capillary wicking shortens solute residence times by several orders of magnitude under moderately dry conditions. Diagenesis is much more likely to occur in faults than protolith because faults are

predicted to transmit up to  $10^4$  pore volumes in the time needed to transmit a single pore volume through the protolith, given the same moderately dry conditions. Under conditions slightly drier than the crossover point, vapor-phase transport dominates in the protolith while liquid-phase transport dominates in the fault. Far drier conditions are required for vapor-phase transport to also dominate in the fault. CSF composition and the density of deformation bands within the fault significantly affect flow and transport, but the range of fault displacements studied appears to have little effect.

Two-dimensional numerical simulations reveal that non-vertically dipping faults can act as catchments under relatively wet climates. Like a surface-water catchment, such faults intercept and channel infiltrating water, creating a zone of enhanced water content perched atop the fault. This zone of enhanced water content accelerates infiltration and reduces solute residence time. Catchment behavior could also occur along large-displacement faults, clastic dikes, and other non-vertically dipping geologic structures.

Deformation band faults can hasten infiltration, exfiltration, contaminant migration, and diagenesis through vadose-zone sands. By acting as conduits in moderately dry climatic conditions or as catchments in wet climates, deformation band faults create preferential flow and transport pathways through poorly lithified sands.

## ACKNOWLEDGMENTS

The National Science Foundation's Hydrologic Sciences Program funded this study, grant number EAR-9614385. A Horton grant from the American Geophysical Union's Hydrology Section also helped fund this work.

First and foremost, I gratefully acknowledge the care, support, patience, and never-ceasing flow of wonderful ideas and advice from my advisor, John L. Wilson, Department of Earth and Environmental Science at New Mexico Tech. Thank you so very much, John! I am also indebted to my committee members for their generosity in time, ideas, and patience: Laurel Goodwin and Peter Mozley in the Department of Earth and Environmental Science at New Mexico Tech, Bob Glass at Sandia National Laboratories, and Jill Buckley at NM Tech's Petroleum Resource Recovery Center.

I thank the staff of the Bosque del Apache National Wildlife Refuge and the Burlington Northern Santa Fe Railroad for access to the study site; fellow members of New Mexico Tech's Faults and Fluid Flow group, especially Bill Haneberg (now at Haneberg Geoscience), Matt Herrin, and Geoff Rawling for helpful discussions; James Conca (now at Los Alamos National Laboratories), Judith Wright, and Paula Heller of UFA Ventures for access to multiple UFA systems and assistance in conducting the UFA experiments; Sandia National Laboratories for use of their Flow and Transport Laboratory; John Hawley, emeritus New Mexico Bureau of Geology and Mineral

Resources, together with Dave Love, for help with site locations and the geologic framework; and Bob Holt of the University of Mississippi for many, many fruitful discussions. In memory of the late Professor Allan Gutjahr, I offer heartfelt gratitude for his inspiring example as teacher, researcher, and *mensch*: Mwenyeze Mungu akubariki kwa milele na milele.

## TABLE OF CONTENTS

	<u>PAGE</u>
ACKNOWLEDGMENTS	ii
List of Tables	vii
List of Figures	viii
List of Symbols	x
CHAPTER 1: INTRODUCTION	1-1
CHAPTER 2: ARE FAULTS PREFERENTIAL FLOW PATHS THROUGH SEMI-ARID AND ARID VADOSE ZONES?	
2.0 Abstract	2-1
2.1 Introduction	2-2
2.2 Geologic Setting	2-6
2.3 Methods	2-10
2.4 Results	2-17
2.5 Discussion	2-26
2.6 Conclusions	2-34
2.7 Appendix 2.A	2-36
2.8 Appendix 2.B	2-39
2.9 References	2-40
CHAPTER 3: PREDICTING VADOSE-ZONE PREFERENTIAL FLOW AND TRANSPORT BY CAPILLARY WICKING THROUGH DEFORMATION BAND FAULTS	
3.0 Abstract	3-1
3.1 Introduction	3-2
3.2 Conceptual Model	3-8

3.3	Methods	3-13
3.4	Results	3-25
3.5	Discussion	3-36
3.6	Conclusions	3-51
3.7	References	3-54

#### CHAPTER 4: HOW VARIABLE IS VADOSE-ZONE PREFERENTIAL FLOW AND DIAGENESIS IN DEFORMATION BAND FAULTS?

4.0	Abstract	4-1
4.1	Introduction	4-3
4.2	Methods	4-6
4.3	Geologic Setting	4-12
4.4	Protolith and Fault Properties	4-20
4.5	Flow and Transport Modeling	4-32
4.6	Conclusions	4-47
4.7	Appendix 4.A Flow and transport models	4-50
4.8	Appendix 4.B Sample MvG model fits	4-57
4.9	References	4-60

#### CHAPTER 5: FROM CATCHMENTS TO CONDUITS: VADOSE-ZONE FAULTS AND CLIMATE

5.0	Abstract	5-1
5.1	Introduction	5-2
5.2	Methods	5-7
5.3	Results	5-12
5.4	Discussion	5-31
5.5	Conclusions	5-37

5.6	References	5-38
CHAPTER 6: CONCLUSIONS AND RECOMMENDATIONS FOR FUTURE WORK		
6.0	Conclusions	6-1
6.1	Recommendations for Future Work	6-5
CHAPTER 7: REFERENCES		7-1
CHAPTER 8: APPENDICES		
APPENDIX 8.A: CENTRIFUGE METHODS		
8.A.1:	Forces in a Centrifugal Field	8-1
8.A.2:	Measuring Moisture Retention Curves	8-5
8.A.3:	Measuring $K$ – Moisture Content Curves	8-15
APPENDIX 8.B: BROOKS AND COREY MODEL FITS		8-25
APPENDIX 8.C: USING PIECEWISE CONTINUOUS GARDNER $K(\psi)$ MODELS		
8.C.1:	Introduction	8-28
8.C.2:	Approach	8-29
8.C.3:	References	8-35
8.C.4:	Mathematica Code	8-36
APPENDIX 8.D: CENTRIFUGE EXPERIMENT DATA TABLES		
8.D.1:	Table of Samples	8-42
8.D.2:	Moisture Retention Data	8-45
8.D.3:	$K(\theta)$ Data	8-51

## LIST OF TABLES

TABLE	PAGE
Table 2.1: Unsaturated Flow Apparatus (UFA) experimental conditions	2-13
Table 2.2: Measured properties	2-19
Table 2.3: Fitted parameter values for Mualem-van Genuchten model	2-23
Table 3.1: Metrics to test hydrologic significance of deformation band faults	3-11
Table 3.2: Fitted parameter values for Mualem-van Genuchten model	3-14
Table 4.1: Metrics to test hydrologic significance of deformation band faults	4-11
Table 4.2: Point count data for Elmendorf and Canyon Trail sands	4-15
Table 4.3: X-ray diffraction of clay size fraction	4-21
Table 4.4: Sample characteristics	4-23
Table 4.5: Fitted parameter values for Mualem-van Genuchten model	4-26
Table 4.6: Fault-protolith pairs for modeling	4-33
Table 5.1: Parameter values for Mualem-van Genuchten model	5-10
Table 5.2: Minima and maxima matric potential $\psi$ (cm) for 2D numerical models	5-13
Table 5.3: Flux density comparison for 1D analytical and 2D numerical models	5-14
Table 8.A.1: Measured flow rates for selected AVI pumps	8-20

## LIST OF FIGURES

FIGURE	PAGE
Figure 2.1: Site location and fault architecture	2-7
Figure 2.2: UFA measurements of unsaturated hydraulic relations	2-21
Figure 2.3: $K$ - $\psi$ relationships for Canyon Trail E10	2-24
Figure 2.4: Solute residence time for E10 samples	2-27
Figure 2.A.1: UFA measurements and Mualem-van Genuchten model fits for individual samples	2-37
Figure 3.1: Deformation band faults in the Rio Grande rift	3-4
Figure 3.2: Idealized columns for determining fault spatial density impact	3-15
Figure 3.3: $K$ - $\psi$ relationships for fault E10 from fitted Mualem-van Genuchten parameters	3-27
Figure 3-4: Solute residence times for gravity-driven scenario	3-29
Figure 3-5: Gravity-driven scenario	3-31
Figure 3-6: Composite liquid-phase flux density, $q_c$ , for gravity scenario	3-32
Figure 3-7: Evaporation-driven flow from a shallow water table	3-34
Figure 3-8: Residence time for evaporation-driven solute transport	3-35
Figure 3-9: Fault density and evaporation-driven flow	3-37
Figure 3-10: Number of fault pore volumes per sand pore volume	3-42
Figure 4.1: Location of study areas and Elmendorf study area	4-13
Figure 4.2: Canyon Trail study area	4-16
Figure 4.3: Fitted $K(\psi)$ relationships	4-28
Figure 4.4: Gravity-driven flow	4-35
Figure 4.5: Transport in gravity-driven flow	4-38


Figure 4-6: Evaporation-driven flow	4-41
Figure 4-7: Evaporation-driven transport	4-43
Figure 4.A.1: Idealized columns for determining impact of fault spatial density	4-52
Figure 4.B.1: Mualem-van Genuchten model fits	4-58
Figure 5.1: $K$ - $\psi$ relationships and gravity-driven flux density for Canyon Trail site E10 showing crossover points	5-4
Figure 5.2: Domain meshes for vertical plane model	5-9
Figure 5.3: Matric potential distributions for domains with a fault dipping $65^\circ$	5-16
Figure 5.4: Volumetric moisture content ( $\theta$ ) distributions for domains with a fault dipping $65^\circ$	5-18
Figure 5.5: Differences between unfaulted and faulted flux density distributions for $65^\circ$ dip domain	5-19
Figure 5.6: Close-up of differences in flux density between faulted and unfaulted domains with $65^\circ$ dip	5-23
Figure 5.7: Differences between unfaulted and faulted seepage velocity distributions for $65^\circ$ dip domain	5-26
Figure 5.8: Matric potential distributions for partially faulted domains with a $65^\circ$ dip fault	5-29
Figure 8.A.1: Inertial and rotating reference frames	8-2
Figure 8.B.1: Brooks and Corey fits to UFA experimental results	8-25
Figure 8.C.1: Piecewise continuous Gardner models of MvG $K(\psi)$	8-34

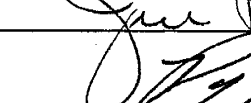
## LIST OF SYMBOLS

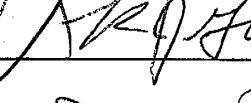
SYMBOL	DEFINITION
$C$	Concentration (-)
$C_0$	Source concentration (-)
$D$	Diffusion coefficient ( $L^2T^{-1}$ )
$D(\theta)$	Effective diffusion coefficient for porous media ( $L^2T^{-1}$ )
$D_{atm}$	Molecular diffusivity of water vapor in air ( $L^2T^{-1}$ )
$D_v$	Effective vapor diffusivity ( $L^2T^{-1}$ )
$E$	Enhancement factor (-)
$H$	Depth to water table (L)
$K$	Hydraulic conductivity ( $LT^{-1}$ )
$K_s$	Saturated hydraulic conductivity ( $LT^{-1}$ )
$L$	Length of vertical column or distance from constant source boundary (L)
$T$	Temperature (degrees K)
$W_f$	Width of fault in sand column (L)
$W_s$	Width of sand column (L)
$d_f$	Normalized fault spatial density (-)
$m$	van Genuchten parameter (-)
$n$	van Genuchten parameter (-)
$q$	Darcian flux density ( $LT^{-1}$ )
$q_c$	Composite liquid-phase Darcian flux density ( $LT^{-1}$ )

$q_c^{faulted}$	Composite liquid-phase flux density for a faulted sand column ( $LT^{-1}$ )
$q_c^{unfaulted}$	Composite liquid-phase flux density for an unfaulted sand column ( $LT^{-1}$ )
$q_f$	Liquid-phase Darcian flux density through fault ( $LT^{-1}$ )
$q_l$	Liquid-phase Darcian flux density ( $LT^{-1}$ )
$q_s$	Liquid-phase Darcian flux density through sand ( $LT^{-1}$ )
$q_v$	Thermal vapor-phase flux density ( $LT^{-1}$ )
$r$	Radial distance (L)
$t$	Time (T)
$t_a$	Solute residence time for advection only (T)
$t_d$	Solute residence time for diffusion only (T)
$t_r$	Solute residence time (T)
$v_s$	Seepage velocity ( $LT^{-1}$ )
$z$	Elevation (L)
$z_B$	Elevation of bottom boundary (L)
$z_T$	Elevation of top boundary (L)
$v_s$	Seepage velocity ( $LT^{-1}$ )
$\alpha$	van Genuchten parameter, inverse of air entry matric potential ( $L^{-1}$ )
$\beta$	Mualem-van Genuchten parameter (-)
$\gamma$	Geothermal gradient ( $^{\circ}K L^{-1}$ )
$\xi(\theta, \theta_s)$	Philip and DeVries [1957] factor to account for the difference in temperature gradient between the vapor phase and the bulk soil (-)
$\nu$	Philip and DeVries [1957] mass flow constant (-)
$\theta$	Volumetric moisture content ( $L^3 L^{-3}$ )

$\theta_r$	Residual volumetric moisture content ( $L^3L^{-3}$ )
$\theta_s$	Saturated volumetric moisture content ( $L^3L^{-3}$ )
$\tau$	Tortuosity factor (-)
$\omega$	Angular velocity ( $T^{-1}$ )
$\psi$	Matric potential (L)
$\psi_B$	Matric potential at bottom boundary (L)
$\psi_T$	Matric potential at top boundary (L)


  
Advisor





5 May 2004  
Date

I release this document to the New Mexico Institute of Mining and Technology.

  
Student's Signature

4 May 2004  
Date

## **CHAPTER 1: INTRODUCTION**

Faulting of sand or high porosity sandstone can produce an intriguing variety of structures, including deformation bands. By definition, deformation bands encompass cataclastic or shear bands [Aydin, 1978], compaction bands, and dilatant bands [Antonellini et al., 1994; Mollema and Pollard, 1995]. Each type of deformation band is the result of one or more processes acting on the grains, and, therefore, potentially rearranging the networks of pores through which water, air, and other fluids can flow. Cataclastic or shear deformation bands are the focus of this study, in part because, relative to the other types of deformation bands, they appear to be more common in the Rio Grande rift and also because shearing grains and pores is more likely to dramatically change hydraulic properties than either compaction or dilation.

In continental extensional environments, tectonic extension, uplift, erosion, and deposition combine to produce thick, basin-fill deposits of variably lithified sediments crosscut by an abundance of faults and deformation bands. These faulted sediments are common in areas of the American Southwest, such as the Basin and Range province and the Rio Grande rift [Hawley, 1978; Hawley et al., 1995, 2001; Connell et al., 1999; Hawley and Kernodle, 2000]. Our understanding of the impacts of faulting on fluid flow through the vital but increasingly stressed aquifers and associated zones of vadose water in this region is only nascent.

Faulting-induced compaction and cataclasis of poorly lithified sands or porous, well-lithified sandstone can create cataclastic deformation bands- narrow, tabular zones of reduced pore and grain sizes - which possess markedly different hydraulic properties than the parent material [Aydin, 1978; Pittman, 1981; Edwards et al., 1993; Antonellini and Aydin, 1994; Fowles and Burley, 1994; Sigda et al., 1999; Heynekamp et al., 1999; Rawling et al., 2001]. Hereafter, the term “deformation band” refers only to a cataclastic or shear deformation band, unless otherwise indicated. Substantial decreases in porosity and reductions of several orders of magnitude in saturated hydraulic conductivity have been long established for deformation bands in porous well-lithified sandstones [Aydin, 1978; Pittman, 1981; Edwards et al., 1993; Antonellini and Aydin, 1994; Fowles and Burley, 1994]. Similar reductions have been measured in deformation bands and zones of bands formed within poorly lithified sands [Sigda et al., 1999; Hong, 1999; Rawling et al., 2001; Herrin, 2001; Sigda and Wilson, 2003].

Deformation band faults comprise individual deformation bands as well as zones of deformation bands [Mollema and Antonellini, 1996; Aydin and Myers, 1997]. Architecturally and hydraulically distinct from faults in crystalline rocks [Smith et al., 1989; Caine et al., 1996; Fischer et al., 1998; Heynekamp et al., 1999; Rawling et al., 2001], deformation band faults can be difficult to identify or map because many are created by displacements much less than the minimum decameter displacement typically represented on most geological maps or detectable by present-day geophysical techniques. Formed by displacements of a centimeter or less, individual deformation bands are typically a few millimeters thick and meters or tens of meters in length, whereas a zone of deformation bands ranges between a centimeter and decimeters in

thickness, between hundreds and thousands of meters in length, and can be created by displacements on the order of a decimeter [Aydin, 1978; Antonellini and Aydin, 1994]. Displacements larger than a decameter can create numerous and complex arrays of individual deformation bands and zones of deformation bands in sands and sandstone. Although large-displacement fault zones are vertically continuous in the Santa Fe Group of the Rio Grande rift and similarly heterolithic deposits, deformation band faults within those fault zones are likely to be vertically discontinuous because the character of the fault can change with lithology [cf. Wilson et al., 2003]. The distinction between individual deformation bands and zones of bands is important, but scale-dependent, because deformation bands can be closely or widely spaced within a zone, introducing the possibility for zones with dense distributions of deformation bands to demonstrate significantly different hydraulic behavior than zones with diffuse distributions. This study focuses only on zones of deformation bands because they typically have much greater lengths than individual deformation bands and so are more likely to influence water and solute transport at larger scales than the individual deformation bands. It is also far easier to isolate and measure the hydraulic properties of a 1 cm wide zone of deformation bands than a single 2 mm wide deformation band [cf. Chapters 2 and 4 with Hong, 1999]. We do not consider deformation band faults in sandstones because our study areas only contain faults in poorly lithified sand. For simplicity and unless indicated otherwise, I refer to zones of deformation bands formed in poorly lithified sands as deformation band faults or just faults throughout the dissertation.

The large differences in porosity and saturated hydraulic conductivity values for protolith and deformation band faults are caused by the faulting-related changes in pore-

size characteristics, which suggests that faults and protolith could also differ significantly in their unsaturated hydraulic properties [Sigda et al., 1999]. In particular, the dramatic reduction in pore sizes suggests that these faults retain a high water saturation, relative to protolith, even under dry conditions, potentially enabling faults to act as “fast paths” through vadose-zone beds in arid and semi-arid areas. Previously published investigations of unsaturated hydraulic properties for fault and protolith only examined deformation band faults in well-lithified porous sandstone and focused solely on the pressure–saturation relationship [Antonellini and Aydin, 1994; Ogilvie et al., 2001], which is only one of several relationships necessary to predict flow and transport under unsaturated conditions.

Two sets of independent observations attest to the likelihood that deformation band faults act as fast paths for fluid flow and solute transport through the Rio Grande rift vadose zone. We have observed that some deformation band faults appear much wetter than their adjacent sands several days after a rainstorm. Also, many deformation band faults in the Rio Grande rift are well cemented, in contrast to the adjacent uncemented protolith (for an example, see Figure 3.1a). The stark difference in cementation suggests unsaturated flow and solute transport were focused in the faults, because the cementation rate depends in part on the number of pore volumes of water passed through a material in a given amount of time (see discussion of Santa Fe Group cementation and fluid flow in Hall et al., 2004).

If deformation band faults significantly accelerate water and solute movement through poorly lithified vadose-zone sands, they might prove important exceptions to the

commonly held idea that, under arid and semi-arid conditions, downward unsaturated flow and transport are negligible or extremely slow [Winograd, 1981; Scanlon et al., 1997]. Little is known about the numbers or spatial distribution of smaller displacement faults in the Rio Grande rift, but locally high fault densities have been reported, including an average density of one deformation band fault every 4 m in our study area in the Bosque del Apache National Wildlife Refuge in central New Mexico [Herrin 2001]. Sufficiently large numbers of deformation band faults could locally increase infiltration, enhancing aquifer recharge, violating capillary barriers [e.g., Ross, 1990; Selker et al., 1999], and threatening vadose-zone nuclear waste repositories such as the Yucca Mountain Project. Contaminant solutes could be transported quickly enough and in sufficient quantity to adversely affect aquifer water quality within an engineering or managerially important time frame. For example, faults underlying landfills, USTs, livestock waste lagoons, industrial sites, and other potential contaminant sources could induce unwanted solutes to traverse arid and semi-arid vadose-zone sands more rapidly than would be expected for unfaulted sands. Over longer time scales, accelerated transport of naturally occurring solutes could induce preferential cementation of the faults, creating an even lower permeability barrier to cross-fault saturated flow. The faults could then compartmentalize aquifers, much as they compartmentalize petroleum reservoirs [Smith, 1966], should the preferentially cemented fault segments subsequently be moved into the saturated zone by tectonic activity or by a rising water table.

This study addresses three research questions:

Do deformation band faults have significantly different unsaturated hydraulic properties than their parent sands?

Are these differences hydrologically significant under the relatively dry conditions of semi-arid and arid vadose zones? In particular, do these differences create opportunities for preferential flow and transport by accelerating the movement of liquid-phase water, contaminants, or diagenetically important solutes through the vadose zone?

What conditions specific to protolith, faults, or arid and semi-arid vadose zones influence the potential for fault-induced preferential flow and transport in vadose-zone sands?

The initial answers to these questions are presented in the following chapters. My collaborators and I tested for differences in unsaturated hydraulic properties between faults and protolith by experimentally measuring key unsaturated relationships. Then we assessed the hydrologic significance of fault-protolith differences using analytical and numerical models of flow and transport behavior under arid and semi-arid vadose-zone conditions. Using numerous experimentally tested field samples, an intensive study of the unsaturated hydraulic properties for a single fault and its hanging wall and footwall protolith is described in Chapter 2. This chapter is presented in the format for *Water Resources Research*, in which it was published [Sigda and Wilson, 2003]. The other three chapters of results are also presented in the same paper format in anticipation of submission for publication. In Chapter 3, we tested the hydrologic significance of preferential flow and transport resulting from the differences in hydraulic properties for the same fault and protolith described in Chapter 2. Our test employed simple flow scenarios and one-dimensional, steady-state, analytical models to examine liquid-phase flow processes (infiltration and exfiltration) and solute transport processes (advection, diffusion, and diagenesis) [Chapter 3]. We sought to corroborate these results at four other fault sites and also investigated the influence of fault displacement, density of

deformation bands, and mineralogy of the clay size fraction [Chapter 4]. Last, we used two-dimensional numerical models to confirm predictions from the one-dimensional models and to examine the influence of fault dip on preferential flow under both wet and dry climates [Chapter 5]. Conclusions and recommendations [Chapter 6], references [Chapter 7], and appendices [Chapter 8] complete the dissertation.

## CHAPTER 2: ARE FAULTS PREFERENTIAL FLOW PATHS THROUGH SEMI-ARID AND ARID VADOSE ZONES?

### 2.0 Abstract.

Numerous faults crosscut the poorly lithified, basin-fill sands found in New Mexico's Rio Grande rift and in similar extensional regimes. The deformational processes that created these faults sharply reduced both fault porosity and fault saturated hydraulic conductivity by reducing grains and pore size, particularly in structures referred to as deformation bands. The resulting changes in pore distribution create barriers to saturated flow, but enhance fault unsaturated flow relative to parent sand under the relatively dry conditions of the semi-arid southwest. We report the first measurements of unsaturated hydraulic properties for intact samples from a small-displacement normal fault and parent sand (protolith) in the Bosque del Apache Wildlife Refuge, central New Mexico. Fault samples were taken from a narrow zone of deformation bands. The Unsaturated Flow Apparatus (UFA) centrifuge system was used to measure both relative permeability and moisture retention curves. We compared these relations and fitted hydraulic conductivity ( $K$ ) – matric potential models to test whether the fault has significantly different unsaturated hydraulic properties than its parent sand. Saturated  $K$  is three orders of magnitude less in the fault than the protolith. As matric potential decreases from 0 to -

200 cm, unsaturated  $K$  decreases roughly one order of magnitude in the fault, but five to six orders of magnitude in protolith. Fault  $K$  is greater by 2-6 orders of magnitude at matric potentials between -200 and -1000 cm, which are typical potentials for semi-arid and arid vadose zones. The fault has a much higher air-entry matric potential than protolith and remains near saturation at conditions where the protolith approaches residual moisture content. Under steady state, 1D, gravity-driven flow, advection of water and solutes is  $10^2$  to  $10^6$  times larger in the fault than protolith. Deformation band faults are sufficiently conductive to hasten the downward movement of water and solutes through vadose-zone sands under semi-arid and arid conditions like those in the Rio Grande rift, potentially enhancing recharge, contaminant migration, and diagenesis.

## 2.1 Introduction

Faults are common features in the poorly-lithified clastic sediments of many extensional environments, such as the Rio Grande rift and the Basin and Range physiographic province. As in porous sandstones and crystalline rock, faults in poorly lithified clastic sediments can extend for tens of kilometers in length and meters in width. Faults in such poorly lithified sediments can display core, damage, and mixed zones, which completely lack macroscopic fractures [Heynekamp et al., 1999; Rawling et al., 2001]. This architecture differs substantially from the gouge-filled core zone and fracture-dominated damage zone architecture common to faults in crystalline rock [Smith et al., 1989; Caine et al., 1996] and from the core zone and deformation band-rich damage zone

described for faults in well-lithified porous sandstones [Aydin, 1978; Antonellini and Aydin, 1994; Caine et al., 1996]. Deformation bands are narrow, quasi-tabular zones of localized deformation [e.g., Aydin, 1978; Pittman, 1981; Edwards et al., 1993; Cashman and Cashman, 2000]. Deformation bands and zones of deformation bands are common elements within the damage and mixed zones of larger displacement faults in poorly lithified sediments [Heynekamp et al., 1999; Rawling et al., 2001] and may be the only visible element in smaller displacement faults [Sigda et al., 1999; Herrin, 2001]. Small-displacement faults comprising only zones of deformation bands (hereafter called deformation band faults) can be locally numerous and both laterally and vertically extensive. Deformation band faults in the variably lithified sands of the Rio Grande rift are poorly exposed and are not typically mapped at conventional geological scales (1:24,000 or smaller).

Shear deformation bands are formed by cataclasis (grinding and breaking of grains) and compaction, even from displacements as small as a few millimeters [Aydin, 1978; Sigda et al., 1999; Cashman and Cashman, 2000; Taylor and Pollard, 2000; Herrin, 2001]. We do not consider non-cataclastic deformation bands (i.e., compaction and dilation bands [Antonellini et al., 1994]) because we have not observed them in the Rio Grande rift or found reports of their occurrence there in the literature. Cataclasis and shear-induced compaction drastically reduce mean pore size, increase clay-size fraction, and decrease sorting, thereby reducing porosity and saturated hydraulic conductivity relative to parent sandstone [Pittman, 1981; Antonellini and Aydin, 1994; Ogilvie et al., 2001] or sand

[Hong, 1999; Sigda et al., 1999]. The extent of reduction in porosity and saturated conductivity differs with degree of protolith (parent material) lithification. The porosity of deformation bands in sandstones is almost completely eliminated and saturated conductivity is reduced one to seven orders of magnitude (relative to the protolith) [Aydin, 1978; Fowles and Burley, 1994; Antonellini and Aydin, 1994; Ogilvie et al., 2001]. Deformation bands in poorly lithified sands demonstrate saturated conductivity decreases of only two to four orders of magnitude, and significant macro and micro-porosity remain [Sigda et al; 1999; Hong, 1999; Herrin, 2001]. Irrespective of the degree of protolith lithification, deformation processes create sizeable structures with very different saturated hydraulic properties than the surrounding matrix.

The striking changes in pore-size characteristics suggest that deformation band faults should differ significantly from their protolith in hydraulic properties beyond porosity and saturated hydraulic conductivity [Sigda et al., 1999]. In particular, the dramatic reduction of pore size suggests that these faults retain relatively high water saturation even under dry conditions. Consequently, we raise two sets of questions:

Do deformation band faults have significantly different unsaturated hydraulic properties than their protolith?

Are these differences hydrologically significant under the relatively dry conditions of semi-arid and arid vadose zones? In particular, do these differences accelerate the movement of moisture, contaminants, or diagenetically important solutes through the vadose zone?

Only the first of these questions has received any attention in the past, but solely for deformation band faults in well-lithified porous sandstone, and even then the focus was limited to only the pressure-saturation relationship in the context of capillary barrier petroleum traps [Antonellini and Aydin, 1994; Ogilvie et al., 2001].

To address these questions for poorly lithified sediments we studied a small-displacement deformation band fault in the poorly lithified sand of central New Mexico's Rio Grande rift. Studying a small displacement fault allowed us to minimize the confounding effect of juxtaposition between different lithologies and so more clearly contrast the hydraulic behavior of the fault with that of its parent sand. We measured moisture content  $\theta$  as a function of matric potential (or moisture potential, tension head, suction, etc.)  $\psi$ , and unsaturated hydraulic conductivity  $K$  as a function of moisture content  $\theta$ , for intact samples of both the deformation band fault and the undeformed parent sand. Hydraulic property measurements were made with specially equipped centrifuges and then fitted to theoretical  $\theta(\psi)$  and  $K(\theta)$  models. We compared model fits and the resulting  $K(\psi)$  relationships for both faulted and parent sand to investigate the potential for significant impacts of faults on water and solute movement through the vadose zone. We've already noted that when potential  $\psi = 0$  (saturation), undeformed sand has roughly two to four orders of magnitude greater saturated hydraulic conductivity than the fault [Sigda et al., 1999; Hong 1999]. The work presented here demonstrates that at some lower matric potential value (termed the crossover  $\psi$  value), the two

materials have the same unsaturated conductivity because sand  $K(\psi)$  decreases more steeply than fault  $K(\psi)$  with decreasing  $\psi$ . As matric potential decreases further, the fault becomes more conductive than the sand. We use the fitted  $K(\psi)$  relationships and a steady, gravity-driven flow model to show that faults should be preferred flow paths for both water and solutes under these dry conditions.

## 2.2 Geologic setting

Located near the southern end of the Rio Grande rift's Socorro basin in central New Mexico, our Canyon Trail field site includes two 135 m long outcrops separated by a railroad cut within the Bosque del Apache Wildlife Refuge, approximately 160 km south of Albuquerque, NM (Figure 2.1a). The outcrops expose many faults crosscutting a poorly lithified, well-sorted, very fine to medium-grained sand overlain by a well-lithified, very poorly sorted, matrix-supported conglomerate containing large cobbles and boulders (Figure 2.1b). The conglomeratic unit is interpreted as a piedmont facies, while the sand unit comprises a lower bed of fine-grained sand, interpreted as an eolian facies, and an upper bed of medium-grained sand with a likely fluvial origin [Hong, 1999; Herrin, 2001]. Varying in thickness from 1 to 10 m where exposed, the two sand beds are easily friable to the touch except for local cementation, usually localized along bedding planes. Both conglomerate and sand units are interpreted as part of the Miocene-age Popotosa Formation (correlative with the Albuquerque Basin's lower Santa Fe Group), which

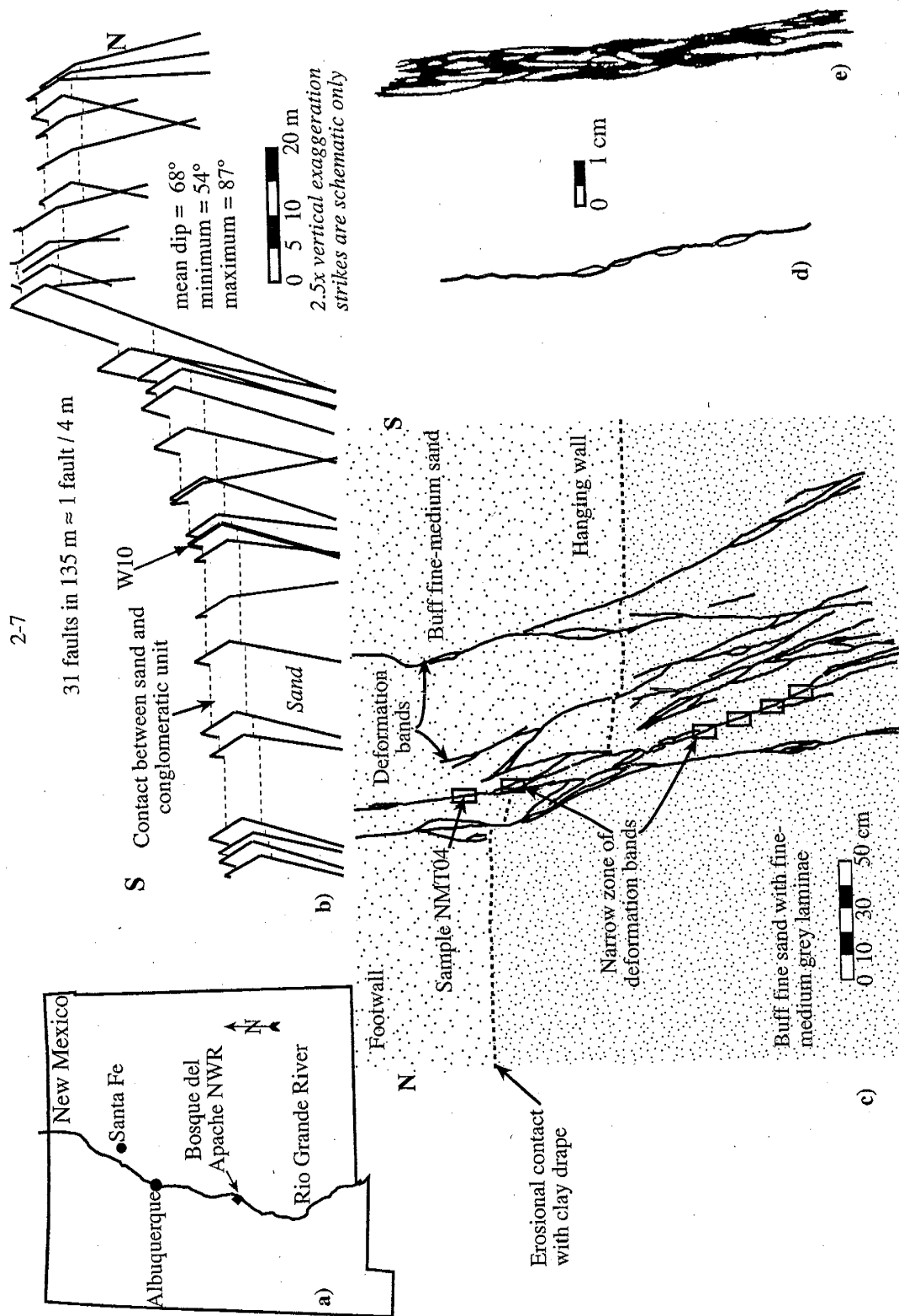


**Figure 2.1:** Site location and fault architecture. **a)** Bosque del Apache National Wildlife Refuge, NM. **b)** Fault distribution and geology along west face of Canyon Trail field site. Each plane represents a mapped fault (true strikes not shown). **c)** Site E10 (20 m east of fault W10 shown above in b) showing assemblage of individual deformation bands and the narrow zone of deformation bands. Boxes show the locations of fault samples. Sand samples (not shown) were collected 3 to 3.5 m north of fault E10 (footwall) and 1.1 to 1.9 m south of fault E10 (hanging wall). **d)** Sketch of an individual deformation band. **e)** Sketch of a narrow zone of deformation bands. Sketches **b**, **d**, and **e** adapted from Herrin [2001].

forms the vadose and aquifer units in this area and in other parts of the Socorro and La Jencia basins [Hawley, 1978]. Poorly lithified, well sorted, eolian and fluvial sands such as these are common throughout the Rio Grande rift in the Santa Fe Group basin fill [Hawley and Kernodle, 2000], which forms the major aquifer and vadose zone units in the Albuquerque, Las Cruces, and El Paso-Ciudad Juárez metropolitan areas [Connell et al., 1999; Hawley et al., 1995, 2001].

Both east and west sand outcrops at our study site are cut by numerous deformation band faults and associated individual deformation bands (Figure 2.1b). Most clearly visible in the sand unit, individual deformation bands ( $\leq 1$  cm vertical displacement) closely resemble those described in other poorly lithified Rio Grande rift sands [Heynekamp et al., 1999; Sigda et al., 1999]. Fault-zone architecture varies from small displacement ( $\leq 1$  m vertical displacement), mostly sub-parallel, narrow or diffuse zones of deformation bands at the southern end, such as those described by Sigda et al [1999], to larger displacement faults ( $1 \text{ m} < \text{vertical displacement} < 15 \text{ m}$ ) in the northern end with complex packages of deformation bands, zones of deformation bands, and pods of little-deformed sand that exhibit both sub-parallel and antithetical orientations [Herrin, 2001]. Roughly 30 faults have been identified in the sand unit and although we did not count them all, we estimate there are hundreds to several thousand individual deformation bands located within and between fault zones. This yields an average fault density of one fault every 4 m. Fault dip varies between  $54^\circ$  and  $87^\circ$ , and displacement is predominantly normal with evidence of minor strike slip [Herrin, 2001]. Fault-zone width varies

considerably along dip and along strike, as do the number and orientation of splays [Herrin, 2001]. Only one of the faults at the site was cemented.

We emphasize there are no open, macroscopic fractures within any fault in the sand units, although fractures commonly cut through cobbles near faults in the conglomerate. Faults crosscutting both sand and conglomerate have a different appearance in the two units [Herrin, 2001]. Instead of the splaying, anastomosing zones of deformation bands with highly variable widths and orientations observed in the sand, faults appear macroscopically as relatively planar tabular zones with reduced grain size and fairly consistent width and orientation in the conglomerate [Herrin, 2001].

The eastern outcrop exposure of fault 10 (E10) was selected for intensive study because it possesses a small-displacement fault with a well-defined, vertically continuous, narrow zone of deformation bands within the sand unit (Figure 2.1c). Individual deformation bands were judged unsuitable for this study because they are too fragile and possess too little volume for effective measurements using the centrifuge method. Fault E10 crosscuts ~3 m of conglomerate and nearly 5 m of sand, which itself is divided by an erosional contact (clay drape) into an upper bed of fine to medium grained sand roughly 3.5 m thick and a 1.5 m thick unit of fine grained sand with interbeds of slightly coarser gray sand (Figure 2.1c). The fault zone comprises a narrow zone of anastomosing deformation bands, which is a planar tabular structure 0.5 - 1.5 cm wide and dipping 60 degrees, and an accompanying network of splaying deformation bands (Figure 2.1c-e).

The traces of these structural elements appear as white lineations on the outcrop surface. The zones of bands are better indurated than the poorly lithified parent sand and together have accommodated 55 cm of vertical displacement (Figure 2.1c).

## 2.3 Methods

**Sample collection.** Undisturbed samples of undeformed and faulted fine grained sand were collected from fault E10 and its footwall and hanging wall (Figure 2.1c) during two field seasons. The dimensions of the centrifuge rotors dictated sample sizes. Parent sand samples were cylindrical in shape with mean length and volume 5.3 cm and 68 cm<sup>3</sup> for large samples and 4.1 cm and 28 cm<sup>3</sup> for small samples. All five fault samples were hexahedral with mean length and volume 5.9 cm and 37 cm<sup>3</sup> for large samples and 4.9 cm and 16 cm<sup>3</sup> for small samples. Multiple sand samples were taken from the same (lower) bed on both E10's hanging wall and footwall. All but one of the fault samples were collected along the fault's down-dip length into which only materials from the same lower bed were entrained. The remaining fault sample, NMT04, was taken from the portion of the fault into which only the coarser upper sands were entrained (Figure 2.1c).

**Sample preparation.** Samples were carefully cut, then measured for bulk density using the clod method and oven-dry weight. Selected samples were jacketed with Devcon 2-Ton epoxy and then epoxied into Delrin sleeves to prevent short-circuiting of flow along the sample perimeter. One fault sample, DL02, was epoxied using the much denser

Devcon F2 aluminum epoxy. Hexahedral fault samples were oriented so that flow through the sample was parallel to dip, reproducing down-fault flow. Flow was directed parallel to bedding (denoted hereafter as bedding<sub>||</sub>) for nearly all sand samples because of difficulties in extracting intact samples with the longitudinal axis oriented normal to bedding (denoted as bedding<sub>⊥</sub>). One pair of sand samples was successfully extracted from the footwall with longitudinal axes bedding<sub>||</sub> (DS22) and bedding<sub>⊥</sub> (DS23). Different combinations (bottom assemblies) of plastic/stainless steel grids and filter paper/stainless steel filter mesh were joined to the sleeve bottoms to prevent sample slump or loss. Following transport to a lab in Richland, WA, samples were saturated using a vacuum chamber with deaired Hanford vadose zone water [Wright et al., 1994].

***K-θ relationships.*** Centrifuge *K-θ* curves were measured using Unsaturated Flow Apparatus (UFA) centrifuge systems (Beckman L8, J6, and J2 models) and the method described by Conca and others [Conca and Wright, 1990 and 1992; Khaleel et al., 1995; Conca et al., 1999]. In this method, each of a pair of initially liquid-saturated samples is inserted into a sample bucket with an effluent collection chamber at the bottom, and then affixed to the UFA rotor. The samples are subjected to a stepwise-increasing series of angular velocities while applying a constant liquid flux to the inlet face of the sample via a proprietary liquid dispersion cap. Effluent liquid stored in the collection chamber after passing through the sample is periodically weighed and emptied by stopping the centrifuge. Sample bucket design ensures that collection chamber effluent will not create any backpressure as long as the centrifuge run time is carefully monitored. The liquid flux

rate and angular velocity are held constant until the sample reaches steady state, and then the final average liquid content is gravimetrically determined. Steady state implies that the sample weight ceases to change and that volumetric moisture content is essentially uniform throughout the sample [Nimmo et al., 1987; Appendix 8.A]. The procedure is repeated after increasing the angular velocity,  $\omega$ , to the next level and either maintaining or reducing the liquid flux rate (Table 2.1). In our experiments, the UFA was periodically stopped and samples were removed and weighed without sample buckets (to ensure greater accuracy) to determine whether sample weight had ceased changing. The distance from the axis of rotation to the outflow face was 10.73 cm for the large sample rotor and 11.73 cm for the small sample rotor. Sample weight was judged to be at steady state if the weight had changed by  $\leq 0.05$  gm, which represented 0.6 - 2.0% of saturation (saturation = 100%) for the smaller fault samples and 0.4 - 0.8% of saturation for the larger sand samples. Data recorded included centrifugation run times (to the nearest minute - average values for sand shown in Table 2.1), flux rate, sample weight, and weight of expelled water (all weights were measured to the laboratory scale's maximum accuracy of  $\pm 0.01$  gm).

Saturated hydraulic conductivity was measured at the start of each sample's  $K-\theta$  experiment using the UFA centrifuge system as a constant head permeameter. A fully water saturated sample was spun at the minimum speed ( $\geq 300$  rpm which is equivalent to a 50 cm head difference for a small sample 5.3 cm long) required to establish steady flow.

**Table 2.1:** Unsaturated Flow Apparatus (UFA) experimental conditions

$K$ - $\theta$ experimental conditions		
Rotor speed (rpm)	Microinfusion pump rate (ml/hr)	Average run time (hr)
300	50	4
600	50	4
1000	50	4
1500	50	4
2000	40	4
2000	15	8
2000	5	8
2000	1	8
2000	0.5	8
2300	0.2	12
2500	0.1	12
3000	0.01	12

$\psi$ - $\theta$ experimental conditions	
Rotor speed (rpm)	Minimum run time (hr)
300, 600, 800	24
1200, 1500, 2100, 3000, 4000, 5000, 7000, 9000	12

Volumetric flux rate was determined by measuring bubble travel times through the supply tubing. Weight measurements showed sample moisture content did not change appreciably indicating that the measured hydraulic conductivity value was associated with a moisture content very close to saturation.

**$\theta$ - $\psi$  relationships.** Centrifuge drainage curves were measured following Hassler and Brunner's [1945] centrifuge method, adapted for the UFA. In this method, which has

been a mainstay of petroleum core analysis laboratories since its introduction, an initially liquid-saturated sample is subjected to a stepwise-increasing series of angular velocities while carefully monitoring the change in liquid content. Air is allowed to freely enter the sample and leave the effluent collection chamber. Angular velocity is held constant until the capillary and centrifugal forces equilibrate, forcing liquid flux to zero, and then a final average liquid content is noted. The procedure is repeated after increasing the angular velocity to the next level (Table 2.1). In our experiments, sample weights were checked periodically by stopping the centrifuge to remove and weigh the samples without sample buckets. A sample weight was judged to have reached equilibrium conditions if the weight had changed by  $\leq 0.05$  gm after at least several hours of centrifugation. We recorded centrifugation run times (to the nearest minute), sample weight, and weight of expelled water. The average moisture content – rpm data produced by an experiment were inverted to  $\theta$ – $\psi$  values using the method of Forbes [1994] as adapted for vadose zone hydrology conditions [Appendix 8.a].

**Fitting models.** Theoretical models of unsaturated hydraulic properties were simultaneously fit to each sample's  $K(\theta)$  and  $\theta(\psi)$  data using a trial and error approach. Goodness-of-fit was subjectively determined by visual comparison of the fitted curves and data as parameter values were varied. We also applied the automatic curve fitting program RETC [van Genuchten et al., 1991], but rejected its use as it typically yielded poor fits. The commonly used Mualem-van Genuchten (MvG) theoretical model was fit to the UFA data for each sample [Mualem, 1976; van Genuchten, 1980]:

$$\theta(\psi) = \theta_r + (\theta_s - \theta_r) \left(1 + |\alpha\psi|^n\right)^{-m} \quad \text{where } m = (n-1)/n \quad (2.1)$$

$$K(\theta) = K_s \left( \frac{\theta - \theta_r}{\theta_s - \theta_r} \right)^\beta \left\{ 1 - \left[ 1 - \left( \frac{\theta - \theta_r}{\theta_s - \theta_r} \right)^{1/m} \right]^m \right\}^2 \quad (2.2)$$

where  $K_s$  is the saturated hydraulic conductivity ( $\text{LT}^{-1}$ ),  $\alpha$  is the inverse of the air entry matric potential ( $\text{L}^{-1}$ ),  $\theta_s$  is saturated volumetric moisture content ( $\text{L}^3\text{L}^{-3}$ ) and equals the connected porosity for vacuum saturation,  $\theta_r$  is the residual volumetric moisture content ( $\text{L}^3\text{L}^{-3}$ ), and  $n$  and  $\beta$  are dimensionless fitting parameters. The  $n$  parameter is an index of the pore size variability (commonly taken as the inverse of the pore size standard deviation) for the MvG model, whereas  $\beta$  represents the tortuosity and the partial correlation in pore radius between two adjacent pores at a given saturation [Mualem, 1976]. During parameter fitting we constrained the measured parameters,  $K_s$ ,  $\alpha$ ,  $\theta_s$ , and  $\theta_r$ , much more than the  $n$  and  $\beta$  fitting parameters. Once the data were fitted to these two equations the  $K(\psi)$  relationship was easily calculated. The Brooks and Corey [1964] model was also fit to the experimental data and yielded very similar results (Appendix 8.B).

We subsequently calculated a set of parameter values that correspond to a “mean” undeformed sand and to a “mean” fault by averaging estimated values for each parameter across all samples for each material. Thus, the mean fault  $\alpha$  is the arithmetic average of

the set of  $\alpha$  values estimated for all fault samples. Mean values for the  $\theta_s$ ,  $\theta_r$ ,  $n$ , and  $\beta$  parameters were calculated in the same fashion. Mean saturated hydraulic conductivity,  $K_s$ , was calculated by geometric averaging of the estimated  $K_s$  values.

**Potential hydrologic relevance.** Our preliminary assessment of the potential hydrologic significance of deformation band faults used a simple, one dimensional, analytical model of steady flow. We chose an analytical modeling approach because it addresses the essential features of the second research question without introducing conceptual complexity. We calculated and compared downward moisture and solute movement in the fault and in the parent sand. A numerical model should be used to examine other factors influencing the hydrologic importance of faults, such as transient flow, fault architecture, spatial density, dip, and other spatially varying characteristics, but it will introduce approximation issues. In particular, numerical approximations must resolve the effects of large hydraulic property changes over the sub-centimeter scale while modeling flow in domains that extend for tens of meters (see Figure 2.1).

The unsaturated hydraulic conductivity is numerically equal to the liquid-phase flux density (specific discharge) when faults are vertical, there is no exchange of moisture between fault and sand, and the hydraulic behavior is sufficiently constant over long time periods to be considered steady state. Such conditions are most likely to be found in the middle portion of a thick, arid or semi-arid vadose zone, well below the root zone and well above the capillary fringe, where gravity, as the sole driving force, induces a unit

gradient. Steady downward liquid-phase advection of water and solute is thus determined by the ambient matric potential, which is assumed to be constant, and the material's  $K(\psi)$  relation. Under these assumptions, the liquid-phase flux density,  $q_l$ , is given by

$$q_l(\psi) = -K(\psi) = -K_s \left(1 + |\alpha\psi|^n\right)^{-m\beta} \left\{1 - \left[1 - \left(1 + |\alpha\psi|^n\right)^{-1}\right]^m\right\}^2 \quad (2.3)$$

Advective transport of non-reactive, non-volatile solutes is calculated using the seepage velocity, defined as the flux density (2.3) divided by the effective moisture content:  $q_l/\theta_{eff}$ . As a simplification, we approximate the effective moisture content by the total volumetric moisture content for the governing matric potential:  $\theta_{eff} = \theta(\psi)$ . Rather than examine velocity we studied solute advective residence time,  $t_r$  (years). For a vertical column of length  $L$  (cm) this is given by

$$t_r(\psi) = L/v_s(\psi) = L\theta(\psi)/q_l(\psi) \quad (2.4)$$

where  $v_s$  is the seepage velocity (cm/year) and  $\theta$  is the volumetric moisture content ( $\text{cm}^3\text{cm}^{-3}$ ). The advective residence time depends on the ambient matric potential.

## 2.4 Results

Nearly two dozen samples were collected from the fault E10 site. Six samples were collected from the fault, seven from the footwall sand, and ten from the hanging wall sand.

Measurements for all properties were successfully completed on slightly over half of these samples (Table 2.2).

Undeformed hanging wall and footwall sand samples appear quite similar in bulk density, porosity, and saturated hydraulic conductivity,  $K_s$ , with a slight difference in bulk density between the upper and lower sand beds (Table 2.2). The UFA  $K_s$  results for hanging wall and footwall sands are quite close to Hong's [1999] water permeameter measurements and our unpublished air mini-permeameter measurements made on the same units near fault E10.

The fault samples also have very similar porosity and bulk density values, but the sample from the coarser-grained upper sand bed, NMT04, has a larger  $K_s$  than that observed in the lower bed samples (Table 2.2). Fault samples have greater bulk density and lower porosity than their parent sands. Comparison of  $K_s$  measurements between fault and parent sand demonstrates that parent sand  $K_s$  is two to approximately three orders of magnitude larger than fault  $K_s$ . This pattern corroborates previous observations made at Canyon Trail's fault E10 site [Hong, 1999] as well as other deformation band fault sites in the Rio Grande rift, such as the Santa Ana site in the Albuquerque Basin of New Mexico [Sigda et al., 1999]. Our UFA centrifuge  $K_s$  measurements also compare very well with Hong's [1999] flexible-wall water permeameter measurements for materials from the fault E10 site.

Table 2.2: Measured properties

Sample ID	Description <sup>a</sup>	Sample volume (cm <sup>3</sup> )	Bulk density (g/cm <sup>3</sup> )	Porosity (cm <sup>3</sup> cm <sup>-3</sup> )	Saturated hydraulic conductivity (cm/s)
<i>Footwall</i>					
DL06	buff	73.8	1.68	0.31	$1.2 \times 10^{-3}$
DS08	gray	34.9	1.67	0.30	$2.2 \times 10^{-3}$
DS22	buff and gray    to bedding	24.7	1.70	0.30	$2.3 \times 10^{-3}$
DS23	buff and gray $\perp$ to bedding	25.6	1.66	0.29	$2.1 \times 10^{-3}$
	All lower bed samples		$1.68 \pm 0.02$ (5) <sup>b</sup>	$0.30 \pm 0.01$ (4)	$1.9 \times 10^{-3} \pm 0.13$ (4)
	All upper bed samples		$1.81 \pm 0.02$ (2)	$0.30 \pm 0.01$ (2)	NM <sup>c</sup>
<i>Hanging wall</i>					
DL07	buff and gray	62.0	1.63	0.33	$1.1 \times 10^{-3}$
DS07	buff and gray	29.2	1.61	0.31	$2.0 \times 10^{-3}$
NMT15	buff	23.7	1.63	0.31	NM
	All lower bed samples		$1.66 \pm 0.05$ (7)	$0.32 \pm 0.02$ (3)	$1.5 \times 10^{-3} \pm 0.18$ (2)
	All upper bed samples		$1.75 \pm 0.03$ (3)	$0.31 \pm 0.02$ (2)	NM
<i>Fault</i>					
DL02	lower fault	38.1	1.94	0.21	$9.5 \times 10^{-6}$
DL20	lower fault	36.2	1.91	0.20	$3.5 \times 10^{-6}$
NMT11	lower fault	12.9	1.89	0.20	$3.7 \times 10^{-6}$
NMT18	lower fault	20.0	2.04	0.20	$8.3 \times 10^{-6}$
	All lower bed ZDB <sup>d</sup> samples		$1.95 \pm 0.07$ (4)	$0.20 \pm 0.01$ (4)	$5.7 \times 10^{-6} \pm 0.23$ (4)
NMT04	above erosional contact	15.0	1.95	0.22	$2.0 \times 10^{-5}$
	All upper bed ZDB samples		$1.95 \pm 0.01$ (2)	$0.24 \pm \text{NA}$ (1)	$1.96 \times 10^{-5} \pm \text{NA}$ (1)

<sup>a</sup>Buff sand is very fine to fine grained; gray sand is fine to medium grained.

<sup>b</sup>Mean  $\pm$  standard deviation and (number of samples).  $K_s$  statistics are calculated for the base 10 logarithms of the measured values. The (geometric) mean  $K_s$  value shown is the back-transformed mean log value, but the standard deviation shown is the standard deviation of the logarithms. (The sixth fault sample has only a bulk density measurement due to time constraints.) Aggregate statistics for sand beds and faults are based on all samples for which any measurements were made, not just those samples for which UFA analyses were completed. <sup>c</sup>NM, not measured; NA, not applicable. <sup>d</sup>ZDB = zone of deformation bands.

Eleven intact samples were used in both  $K$ - $\theta$  and  $\theta$ - $\psi$  experiments (Table 2.2). Only  $\theta$ - $\psi$  data were measured for hanging wall sample NMT15.  $\theta$ - $\psi$  experiments for two samples, DS22 and DS23, were not executed according to protocol and may not have fully achieved equilibrium conditions.  $\theta$ - $\psi$  data for DS22 were discarded because the sample dried out prematurely, making it impossible to fit model parameters. We retained

DS22's  $K$ - $\theta$  data for comparison.  $K$ - $\theta$  experiments for 11 samples yielded ranges of  $0.07 \leq \theta \leq 0.33$  and  $10^{-9} \leq K \leq 10^{-3}$  cm/s for undeformed sand, and  $0.13 \leq \theta \leq 0.24$  and  $10^{-9} < K < 10^{-5}$  cm/s for faults (Figure 2.2). The UFA method has been reported able to measure hydraulic conductivity as low as  $\sim 10^{-10}$  cm/s [Conca and Wright, 1998], but all our measurements less than  $10^{-9}$  cm/s were rejected because of a procedural error. (Sample collection chambers with holes were used, instead of those without holes, for the lowest flow rate, possibly leading to non-steady flow conditions from evaporation.)  $\theta$ - $\psi$  experiments for 11 samples yielded ranges of  $0.06 \leq \theta \leq 0.24$  for faults,  $0.04 \leq \theta \leq 0.34$  for undeformed sand, and  $-5.0 \times 10^5 < \psi < 0$  cm for all samples (Figure 2.2). Replicate  $\theta$ - $\psi$  experiments for fault sample DL02 show good agreement (Appendix 2.A.g).

Each of the samples with complete analyses was parameterized for the Mualem-van Genuchten (MvG) models for  $K$ - $\theta$  and  $\theta$ - $\psi$  by simultaneously fitting (2.1) and (2.2). The results are reported in Table 2.3; plots of individual fits are shown in Appendix 2.A. Fitted and measured  $K_s$  values were not constrained to match exactly, and estimates of the  $\theta_s$  and  $\theta_r$  parameters were selected to give the best overall fit to both  $K$ - $\theta$  and  $\theta$ - $\psi$  curves. If fitted independently, estimates of residual moisture content ( $\theta_r$ ) were typically higher for the  $K$ - $\theta$  than the  $\theta$ - $\psi$  curves, particularly for the last several centrifuge speed steps (Appendix 2.A). Variability in water storage volume and drainage behavior of the sample holder's bottom assembly, particularly those that used filter papers, had a significant influence on saturated moisture content ( $\theta_s$ ) for smaller samples. We used data from

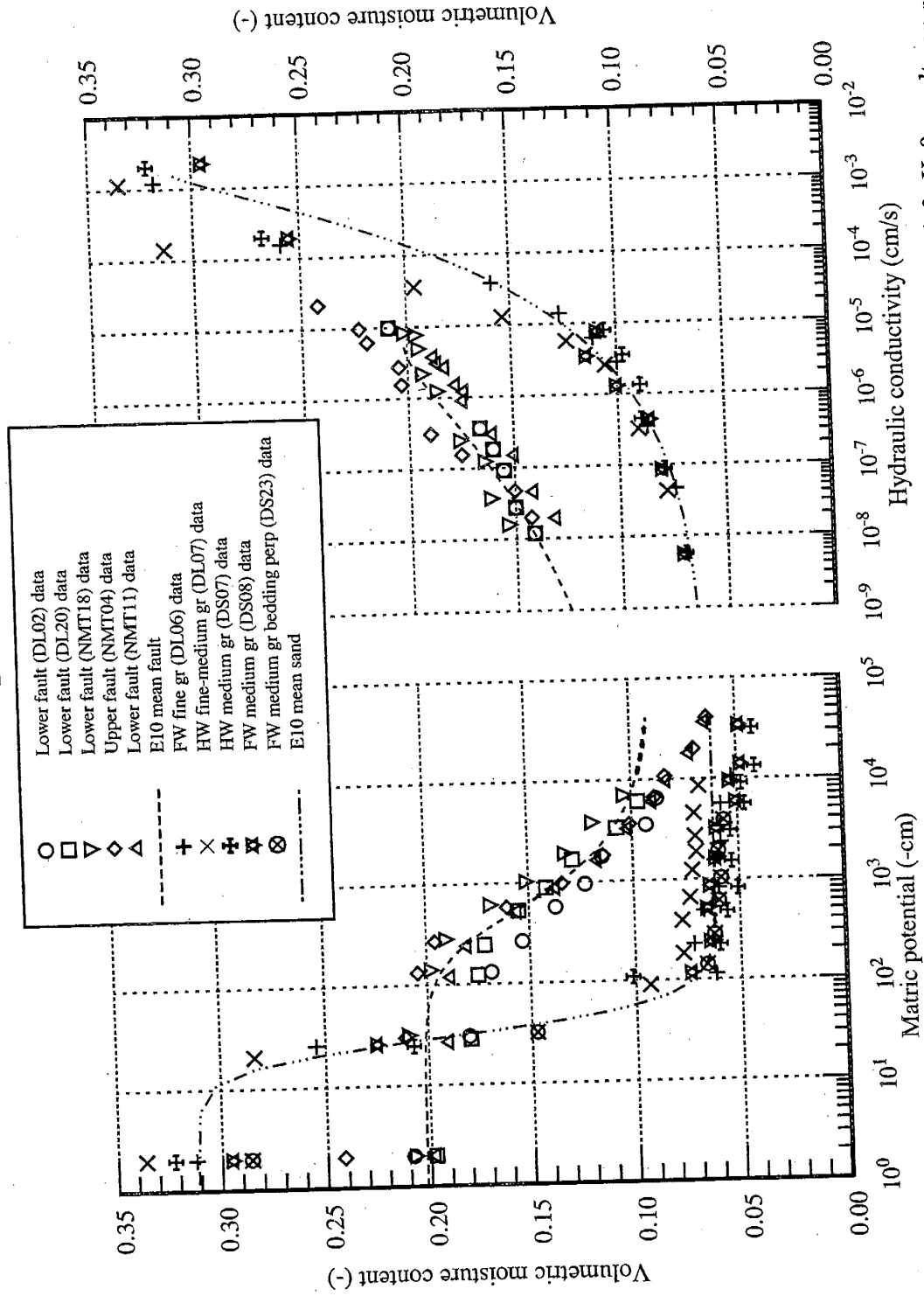


Figure 2.2: UFA measurements of unsaturated hydraulic relations.  $\theta$ - $\psi$  results shown on the left, K- $\theta$  results on right. Dashed lines show the fitted curves for the E10 mean sand and mean fault set of parameters.

control experiments on empty sample holders to minimize the confounding influence of bottom assembly drainage on sample data, but disparities as small as 0.01 units of volumetric moisture content in  $\theta_s$  significantly enlarge the feasibility space for  $n$  and  $\beta$  parameter estimates. It was not possible to fit the MvG (or Brooks and Corey) model to closely match the  $K$ - $\theta$  data just below saturation and still maintain a reasonably good fit at mid and lower saturation for the sand samples; however, this was seldom a problem for fault samples (Appendix 2.A).

Fault air entry matric potential values ( $\alpha^{-1}$ ) range between -250 and -450 cm of matric potential and are ten to 20 times greater than the -20 to -30 cm values estimated for undeformed sand samples (Figure 2.2 and Table 2.3). Estimates of the MvG scaling variables  $n$  and  $\beta$  show consistent differences between fault and sands. Sands have  $n$  values close to three, whereas fault values fall between one and two (Table 2.3). In contrast, sand  $\beta$  values are always less than fault  $\beta$  values and are reasonably close to the 0.5 estimated by Mualem [1976] for 45 different soils (Table 2.3). Fault  $\beta$  values appear more variable than those for sands and are consistently larger than the commonly assumed value of 0.5.

$K$ - $\psi$  curves calculated from fitted MvG parameters show significantly different unsaturated behaviors for parent sand and deformation band faults (Figure 2.3). Sand  $K$  rapidly decreases two orders of magnitude once matric potentials drop below the sand air entry potential, reaching a crossover  $\psi$  (between -35 and -80 cm) where sand  $K$  equals

**Table 2.3:** Fitted parameter values for Mualem-van Genuchten model.

Sample ID	$\theta_s$	$\theta_r$	$\alpha$ (1/cm)	$n$	$\beta$	$K_s$ (cm/s)*
<i>Footwall sand</i>						
DL06	0.315	0.058	0.03	3.4	0.2	$1.20 \times 10^{-3}$
DS08	0.300	0.062	0.035	3.2	0.7	$2.40 \times 10^{-3}$
DS23	0.287	0.060	0.046	2.9	0.8	$2.20 \times 10^{-3}$
<i>Hanging wall sand</i>						
DL07	0.335	0.07	0.034	3.5	0.1	$1.20 \times 10^{-3}$
DS07	0.320	0.058	0.045	3.7	0.3	$2.00 \times 10^{-3}$
<b>mean</b>	<b>0.318</b>	<b>0.062</b>	<b>0.038</b>	<b>3.34</b>	<b>0.42</b>	<b><math>1.72 \times 10^{-3}</math></b>
<b>std</b>	<b>0.014</b>	<b>0.005</b>	<b>0.01</b>	<b>0.30</b>	<b>0.31</b>	<b><math>1.46 \times 10^{-1}</math></b>
<i>Fault</i>						
DL02	0.196	0.105	0.0032	1.80	0.9	$9.9 \times 10^{-6}$
DL20	0.198	0.105	0.0040	1.80	1.2	$3.5 \times 10^{-6}$
NMT11	0.190	0.075	0.0022	1.80	1.1	$3.8 \times 10^{-6}$
NMT18	0.200	0.085	0.0028	1.55	2.7	$8.3 \times 10^{-6}$
NMT04	0.227	0.075	0.0035	1.75	1.9	$2.0 \times 10^{-5}$
<b>mean</b>	<b>0.202</b>	<b>0.089</b>	<b>0.003</b>	<b>1.74</b>	<b>1.56</b>	<b><math>7.36 \times 10^{-6}</math></b>
<b>std</b>	<b>0.014</b>	<b>0.015</b>	<b>0.001</b>	<b>0.11</b>	<b>0.74</b>	<b><math>3.15 \times 10^{-1}</math></b>

\* Mean and standard deviation for  $K_s$  are calculated for the base 10 logarithms of the estimated values. The (geometric) mean value shown is the back-transformed mean log value, but the standard deviation shown is the standard deviation of the logarithms.

the fault  $K$  (Figure 2.3). Below this crossover  $\psi$  the sand  $K$  is much more sensitive to matric potential than the fault, so that sand  $K$  is at least four orders of magnitude less than fault  $K$  at  $\psi = -500$  cm.  $K$ - $\psi$  plots for the mean fault and the mean sand fall near the middle of the appropriate set of material curves and so adequately describe “average” sand and fault behaviors (Figure 2.3). Fault sample NMT04, which had the largest parent sand grain size, maintains an appreciably larger hydraulic conductivity across much of the  $\psi$  range. We observed little systematic difference between large volume (DL) and small

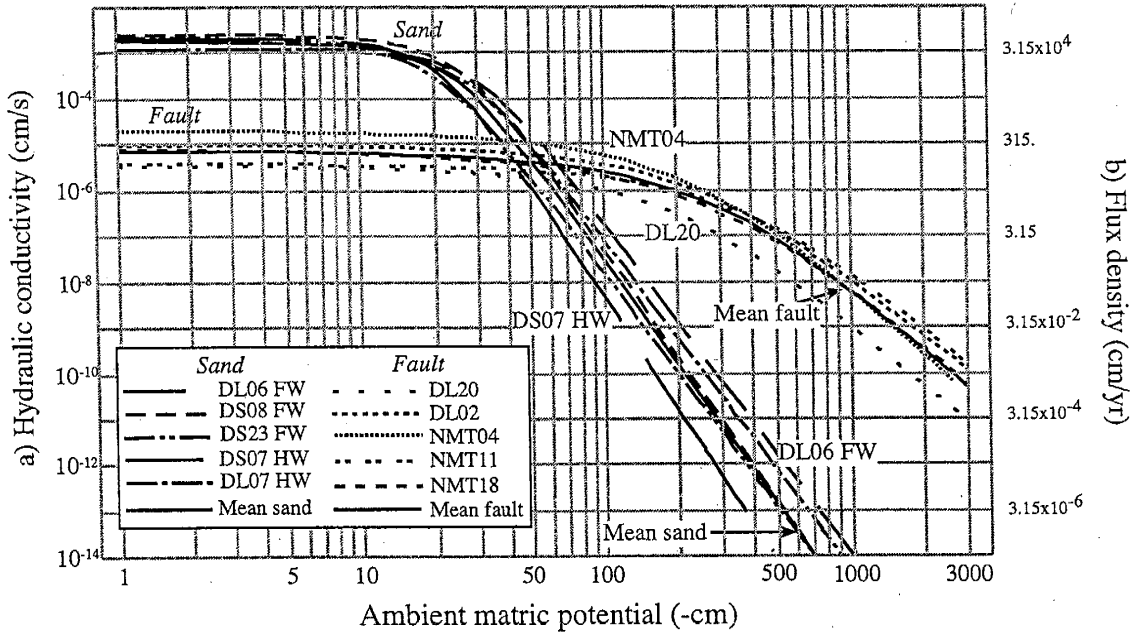


**Figure 2.3:** a)  $K$ - $\psi$  relationships for Canyon Trail E10 from fitted Mualem-van Genuchten parameters. FW = footwall; HW = hanging wall. b) The liquid-phase downward flux density for gravity-driven flow  $q_L(\psi) = K(\psi)$ .

volume (DS and NMT) samples.

Sand saturated conductivity  $K_s$  is lower for the bedding<sub>⊥</sub> DS23 sample than the bedding<sub>∥</sub> DS22 sample, and though the margin of difference is somewhat smaller than that determined by Hong [1999], it is still larger than the observed variability in experimental flow rates (coefficients of variation = 3% for both DS22 and DS23). Our sand  $K_s$  anisotropy estimate of 0.92 is smaller than Hong's estimate of 0.66, which was based on more measurements. We found that for moisture contents less than saturation, bedding<sub>⊥</sub>  $K(\theta)$  (DS23) is larger than bedding<sub>∥</sub>  $K(\theta)$  (DS22) (Appendix 2.A). This difference may be real, if unexpected, but the close agreement in  $\psi$ - $\theta$  and  $K$ - $\theta$  data between the bedding<sub>⊥</sub> DS23 sample and two other bedding<sub>∥</sub> footwall samples, DL06 and DS08, suggests that the DS22 data may have been compromised by unknown error. Although we have no measurements of anisotropy in the fault, Hong [1999] measured  $K_s$  anisotropy in a narrow zone of deformation bands and found fault anisotropy is much larger than sand anisotropy; normal-to-dip fault  $K_s$  is only 10% of parallel-to-dip fault  $K_s$ .

The  $K$ - $\psi$  plot (Figure 2.3) also describes how the sand and fault gravity-driven, liquid-phase flux densities vary with matric potential. Below the  $\psi$  crossover of -35 to -80 cm, fault liquid-phase flux density exceeds sand liquid-phase flux density by orders of magnitude so that gravity-driven steady infiltration through the fault far exceeds infiltration through the adjacent sand. Thus, gravity-driven, steady infiltration is 10 to 1000 times faster through the deformation band fault than the parent sand whenever  $\psi = -$

100 cm, and at -500 cm, the flux density disparity increases to between  $10^4$  and  $10^6$ . Advective solute residence times,  $t_r$ , increase much more rapidly for sand, as matric potential decreases, than for faults (Figure 2.4). At high matric potentials, sand residence time is two orders of magnitude shorter, but sand and fault residence times  $t_r$  are equivalent for slightly dryer conditions,  $-40 \leq \psi \leq -90$  cm. At  $\psi = -200$  cm fault  $t_r$  increases by less than an order of magnitude from its value at  $\psi = 0$ , yet sand  $t_r$  increases by five to seven orders of magnitude over the same interval.

## 2.5 Discussion

The measured values of porosity and saturated hydraulic conductivity confirm previous findings that deformation band faults have much lower porosity and saturated conductivity,  $K_s$ , values than their parent sands. In our fault E10 samples,  $K_s$  is shown to be  $\sim 10^{-3}$  cm/s for flow through poorly lithified sands oriented bedding<sub>||</sub> and  $\sim 10^{-6}$  to  $\sim 10^{-5}$  cm/s for narrow zones of deformation bands with flow oriented parallel to dip (Table 2.2). In comparison, Hong [1999] measured  $K_s$  values for bedding<sub>||</sub> flow of  $2.3 - 9.1 \times 10^{-3}$  cm/s in fault E10 footwall and hanging wall finer-grained sands, and values of  $2.5 - 3.7 \times 10^{-7}$  cm/s for flow oriented normal to fault E10 deformation bands.

In answer to our first research question, the centrifuge data and model fitting support the hypothesis that deformation band faults have significantly different unsaturated hydraulic properties than their parent sands. Deformation band faults possess smaller

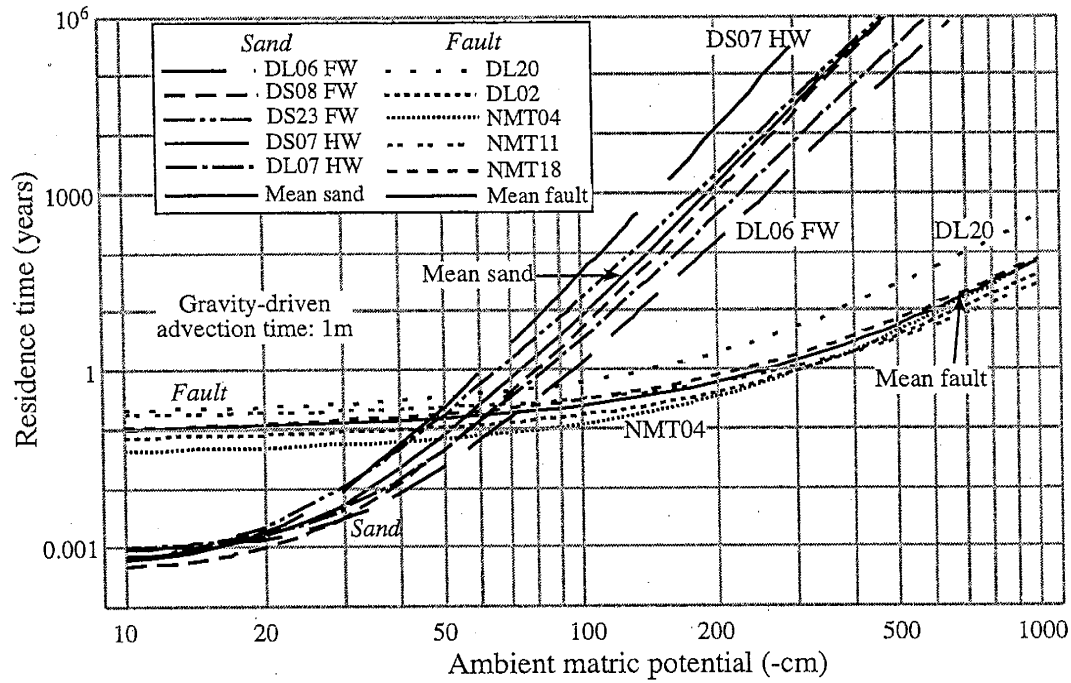


**Figure 2.4:** Solute residence time as a function of the matric potential for E10 samples. FW = footwall; HW = hanging wall. Gravity-driven advection time,  $t_r$  (years), for a conservative solute to travel 1 m with no dispersion.

pores and greater variability in pore sizes, leading to higher residual moisture contents and higher air entry matric potential values than their poorly lithified parent sands. The van Genuchten  $n$  parameter, which is proportional to the inverse of the pore size distribution's standard deviation, is much lower for fault than sand. This difference in fitted  $n$  values is supported by previous thin section observations that grain and pore sizes are much more variable in deformed than undeformed sediments [Sigda et al., 1999; Herrin, 2001]. The large difference in air entry values indicates that faults remain near saturation or have higher moisture contents when adjacent sands have almost entirely drained. Higher  $\theta_r$  values for faults suggest that faults contain a vertically and horizontally continuous network of wholly or nearly saturated pores within the individual deformation bands even under dry vadose-zone conditions.

Sand unsaturated hydraulic conductivity drops six orders of magnitude as matric potential decreases from 0 to -200 cm, whereas fault conductivity decreases only one order of magnitude over the same  $\psi$  range and remains close to saturation. At a matric potential of -500 cm, fault conductivity exceeds sand conductivity by at least four orders of magnitude. Whereas sand samples begin draining at  $\psi = -30$  cm and reach residual moisture content near  $\psi = -200$  cm, fault samples do not drain appreciably until  $\psi$  reaches -200 cm, and do not approach residual moisture content until  $\psi$  is less than -10,000 cm (Appendix 2.A). The  $\psi$ - $\theta$ ,  $K$ - $\theta$ , and  $K$ - $\psi$  relationships are consistent for all sand samples, indicating no appreciable differences between hanging wall and footwall samples (Figure 2.2 and Appendix 2.A). Even though NMT04 is not directly comparable to the other

four fault samples because it was formed from the coarser upper sand, the five fault samples display consistent  $K$ - $\psi$  relations. Choice of theoretical model, Mualem-van Genuchten or Brooks and Corey, has no impact on the relative differences in sand and fault behavior [Appendix 8.A].

Our observations may hold for similar structures in poorly lithified sand. Although our measurements were restricted to centimeter-wide zones containing numerous deformation bands, it is reasonable to speculate that individual deformation bands (~1-2 mm in width), which are often very numerous, demonstrate similar hydraulic behavior because they are also created by compaction and cataclasis. We also speculate that deformation band faults in medium and coarse sands will show larger relative differences in unsaturated properties than those we have reported here for fine sands. This assumes that deformed grain size is independent of parent grain size for the bulk of the protolith, which may not be a valid assumption [Rawling et al., 2001]. The larger mean pore sizes for coarse or medium grained sand are likely to have much larger van Genuchten  $n$  values and lower air entry potentials which would cause the  $K$ - $\psi$  crossover to occur at larger matric potentials (nearer to zero) and lead to greater differences between fault and sand.

Although this paper is the first work investigating the unsaturated flow properties of faults in poorly lithified sands, there is previously published work on the petroleum reservoir capillary sealing properties of cataclastic deformation band faults in well-lithified porous sandstones. Antonellini and Aydin [1994] used image analysis to

estimate pore sizes for interconnected pores in both deformation bands and protolith. They estimated air entry matric potential for these faults as one to two orders of magnitude larger than that for the protolith. Ogilvie et al [2001] used mercury porosimetry to measure the drainage capillary pressure-saturation relationships (analogous to the  $\psi$ - $\theta$  relationship) of protolith and a narrow zone of deformation bands. Their results yielded a 9% fault porosity, 20% sandstone porosity, and a fault air entry matric potential on the order of 40 m versus a value no larger than 4 m for the sandstone protolith, again about an order of magnitude difference. The air entry values in these studies are much larger than those estimated for the poorly lithified sand ( $\sim 30$  cm) and faults ( $\sim 300$  cm) in this study because of the great differences in lithology, diagenesis, and pore networks. Yet the relative differences in air entry value between protolith and fault are similar, that is about an order of magnitude or more. The Ogilvie et al [2001] capillary pressure – saturation curves (their Figure 2.2b) for a well-lithified sandstone and fault are quite similar in shape to the  $\psi$ - $\theta$  curves (Figure 2.2; Appendix 2.A) that we report in this paper for poorly lithified sand and fault. Neither sandstone study investigated the relationship between hydraulic conductivity and moisture content (relative permeability curve), and their results cannot be used to address our second research question (see below), i.e., “Do these faults significantly affect variably saturated fluid flow?”, without making additional assumptions about the  $K$ - $\theta$  relationship.

Measuring both  $\psi$ - $\theta$  and  $K$ - $\theta$  relationships with the UFA centrifuge is relatively new (e.g., Flint et al [1999] and this study), so we note several procedural issues that we

encountered in the hopes of improving the methodology. Porosity and drainage characteristics of the sample holder's bottom assembly must be determined and, if possible, the volume stored at any time be minimized, especially for small sample volumes. Proper choice of bottom assembly materials will help ensure that  $\theta_s$  estimates from separate  $\psi$ - $\theta$  and  $K$ - $\theta$  experiments will match closely, thus simplifying estimation of the  $K$ - $\psi$  model's scaling parameters, e.g., the  $n$  and  $\beta$  parameters in the Mualem- van Genuchten model. The moisture retention data and fits demonstrate that the centrifuge schedule of angular velocities (Table 2.1) captured most of the drainage behavior for the fault samples, but missed much of the sand's mid-saturation behavior (Figure 2.2 and Appendix 2.A). Increasing the number of experimental steps at low centrifuge speeds should improve resolution of the moisture retention curves for sands and reduce data loss during data inversion using the method of Forbes [1994] (or other similar methods). Our data also suggest that high centrifuge speeds ( $> 5000$  rpm) may induce moisture loss through evaporation, losing the expected balance between matric forces and the centrifugal body force. Another problem is our inability to fit the MvG model to the sand 300 and 600 rpm experimental steps for  $K$ - $\theta$ . This was not a problem for most fault samples, which required centrifuge speeds  $\geq 1000$  rpm to induce flow. Perhaps a hydraulic steady state had not been achieved in the sand even though sample weight changed by  $\leq 0.05$  gm, or the Mualem-van Genuchten model does not fit these materials very well near saturation. It is also likely that the experiment's principal assumption that the centrifugal

body force gradient is far greater than the matric potential gradient [Nimmo et al., 1987; Conca and Wright, 1990 and 1992] has been violated.

Although we can only begin to answer our second question, the observed differences in hydraulic properties already suggest that faults have a significant hydrologic impact under relatively dry climatic conditions. Under those conditions and using the hydraulic properties described here, the simple, gravity-driven, steady flow model predicts downward, liquid-phase flux densities that are  $10^2$  to  $10^5$  times larger in faults than in their parent sands (Figure 2.3), and reduce non-reactive solute travel times by similar orders of magnitude (Figure 2.4). Such an enormous disparity between sand and fault behavior increases the likelihood that deformation band faults act as preferential flow paths through vadose zones with steady matric potentials in the range of  $-100$  to  $-2000$  cm. Determining the extent of faults' hydrologic importance requires further investigation to consider, among others, ambient matric potential conditions, moisture and solute exchange between fault and sand, the role of competing processes, as well as fault architecture, dip, and spatial density.

Ambient matric potential data for the Rio Grande rift indicate that preferential liquid-phase flow through faults can occur, but is likely to be spatially variable. Most measurements of shallow ambient matric potentials for this area are in the tensiometer range:  $0 \leq \psi < \sim 600$  cm [Stephens and Knowlton, 1986; Mattson, 1989; McCord et al., 1991; Brainard et al., 2002], a wetter subset of the range considered in this paper. In

combination with the  $\psi(\theta)$  relations estimated in this study, our own measurements of *in situ* moisture content demonstrate that the near surface matric potential is between  $-180$  and  $-380$  cm (Appendix 2.B). In contrast, data from a recent Albuquerque Basin infiltration experiment revealed drier conditions with matric potential values well below the tensiometer range in the top eight meters [Brainard, 1997], likely indicating liquid-phase infiltration through sand is negligible at that location. Vapor-phase flux eventually becomes more important than liquid-phase flux as sand becomes sufficiently dry. Thermal vapor-phase flux density values have been estimated to fall between  $1.0 - 3.0 \times 10^{-3}$  cm/year (compare to right hand axis of Figure 2.3) for other arid vadose zones in the American Southwest [Ross, 1984; Scanlon et al., 1997]. For a certain range of drier conditions, it is likely that water transport through the sand is dominated by vapor-phase processes, whereas the faults could still be dominated by liquid-phase transport. The dominant mechanism for solute movement through the sand should also switch, from advection to diffusion, as matric potential drops. Solute transport through the fault could still be dominated by advection, until much lower matric potentials are reached.

Although deformation band faults appear to provide a liquid-phase “fast path” for water and solutes through the sandy parts of the Rio Grande rift vadose zone, it is still not clear whether such “fast paths” are significant. The minimum fault density required to affect groundwater recharge may only occur in a small portion of the Rio Grande rift. There are clearly areas with no faults, but we and others (e.g., Carter and Winter [1995] and Grauch [2001]) have found many locations in the Rio Grande rift with moderate to

high densities of faults, such as the Canyon Trail site of this paper. With at least one fault every four meters, and assuming fault conditions are similar at depth, infiltration through the sand beds at the Canyon Trail site could be locally enhanced several fold. Fault density is less critical when considering contaminant transport. One or more faults beneath a contaminated surface site could redistribute contaminants downward so that underlying aquifers are adversely affected. Fault "fast paths" are also more likely to experience more rapid diagenesis than the parent sand. As an example, a simple diagenesis model relates the amount of diagenetic change observed in a given volume of sediments to the number of pore volumes of aqueous solution that pass through those sediments. At an ambient matric potential of -200 cm a fault will advect more than a hundred pore volumes under gravity-driven flow in the time taken to advect a single pore volume through the sand (Figure 2.4). Although our results indicate a propensity for faults to enhance recharge, shorten contaminant residence times, and accelerate diagenesis, more study is needed to test for hydrologic significance.

## **2.6 Conclusions**

Deformation band faults resulting from relatively small displacements possess strikingly different saturated and unsaturated hydraulic properties than their poorly lithified parent sands. Saturated hydraulic conductivity values for fault E10 at the Canyon Trail site are three orders of magnitude smaller than those for the parent sand, in good agreement with previously published values for this fault and other faults. For

unsaturated conditions, fault E10 conductivity equals sand conductivity in the (crossover) matric potential range of -35 to -80 cm, a condition that is relatively high (wet) for much of the Rio Grande rift. As matric potential  $\psi$  decreases into the drier range, fault conductivity,  $K$ , declines much less rapidly than does sand  $K$ . For matric potentials less than -100 cm, typical for semi-arid and arid zones, fault conductivity exceeds sand  $K$  by two to six orders of magnitude. The observed  $K(\psi)$  behavior shows relatively little variability between hanging wall and footwall sand samples and between various fault samples. Under conditions of steady gravity-driven flow, faults permit downward, liquid-phase flux densities  $10^2$  to  $10^6$  times larger than those in their parent sands, and reduce non-reactive solute travel times by similar orders of magnitude. If our measured hydraulic properties describe faults and sands in other poorly lithified vadose zones, and we believe they do, deformation band faults can significantly enhance gravity-driven downward moisture and solute transport through vadose zones where the matric potential is much less than -100 cm. If present in sufficient density, faults encountered in semi-arid and arid climates should enhance recharge, hasten contaminant migration, and accelerate diagenesis.

**Acknowledgements.** The National Science Foundation's Hydrologic Sciences Program funded this study, grant number EAR-9614385. We thank the staff of the Bosque del Apache National Wildlife Refuge and the Burlington Northern Santa Fe Railroad for access to the study site; our fellow members of New Mexico Tech's Faults and Fluid Flow group, especially Laurel Goodwin, Peter Mozley, Bill Haneberg, Matt

Herrin, and Geoff Rawling for many hours of helpful discussion; James Conca, Judith Wright, and Paula Heller of UFA Ventures for access to multiple UFA systems and assistance in conducting the UFA experiments; Bob Glass of Sandia National Laboratories for use of his Flow and Transport Laboratory; John Hawley, emeritus New Mexico Bureau of Geology and Mineral Resources for help with the geologic framework; and Bob Holt of the University of Mississippi for many fruitful discussions. We are grateful to the three anonymous reviewers for their generous efforts to improve this paper.

## **Appendix 2.A: Sample Mualem-van Genuchten model fits**

Plots of  $K-\theta$  and  $\theta-\psi$  experimental results and final simultaneous fits to (2.1) and (2.2) are shown in Figure 2.A-1 for samples with complete UFA analyses.

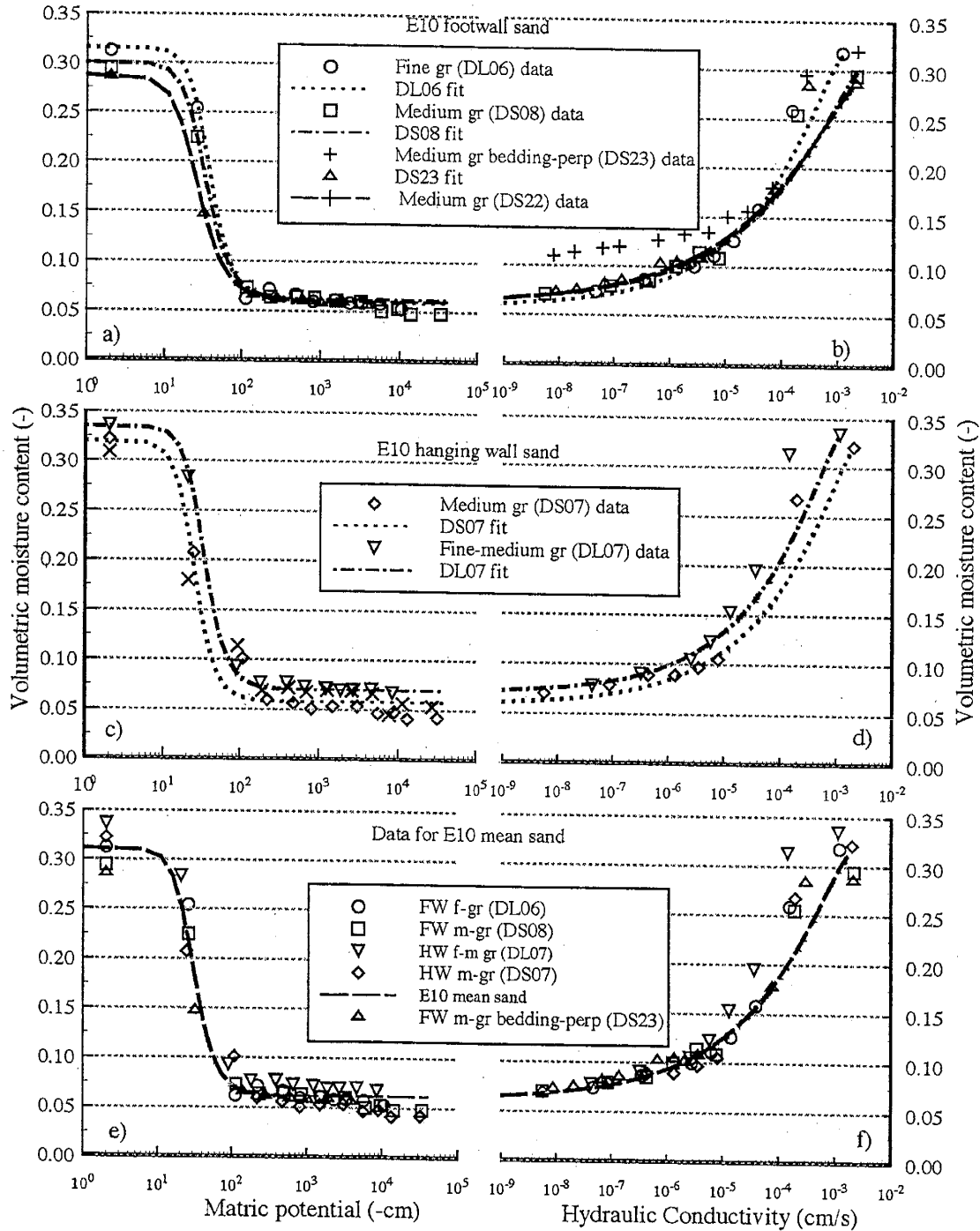


Figure 2.A.1.a-l: UFA measurements and Mualem-van Genuchten model fits for individual samples. The left-hand plots show  $\theta$ - $\psi$  results and the right hand plots show  $K$ - $\theta$  results. Lines depict the theoretical curves for the fitted Mualem-van Genuchten models using parameters shown in Table 2.3.

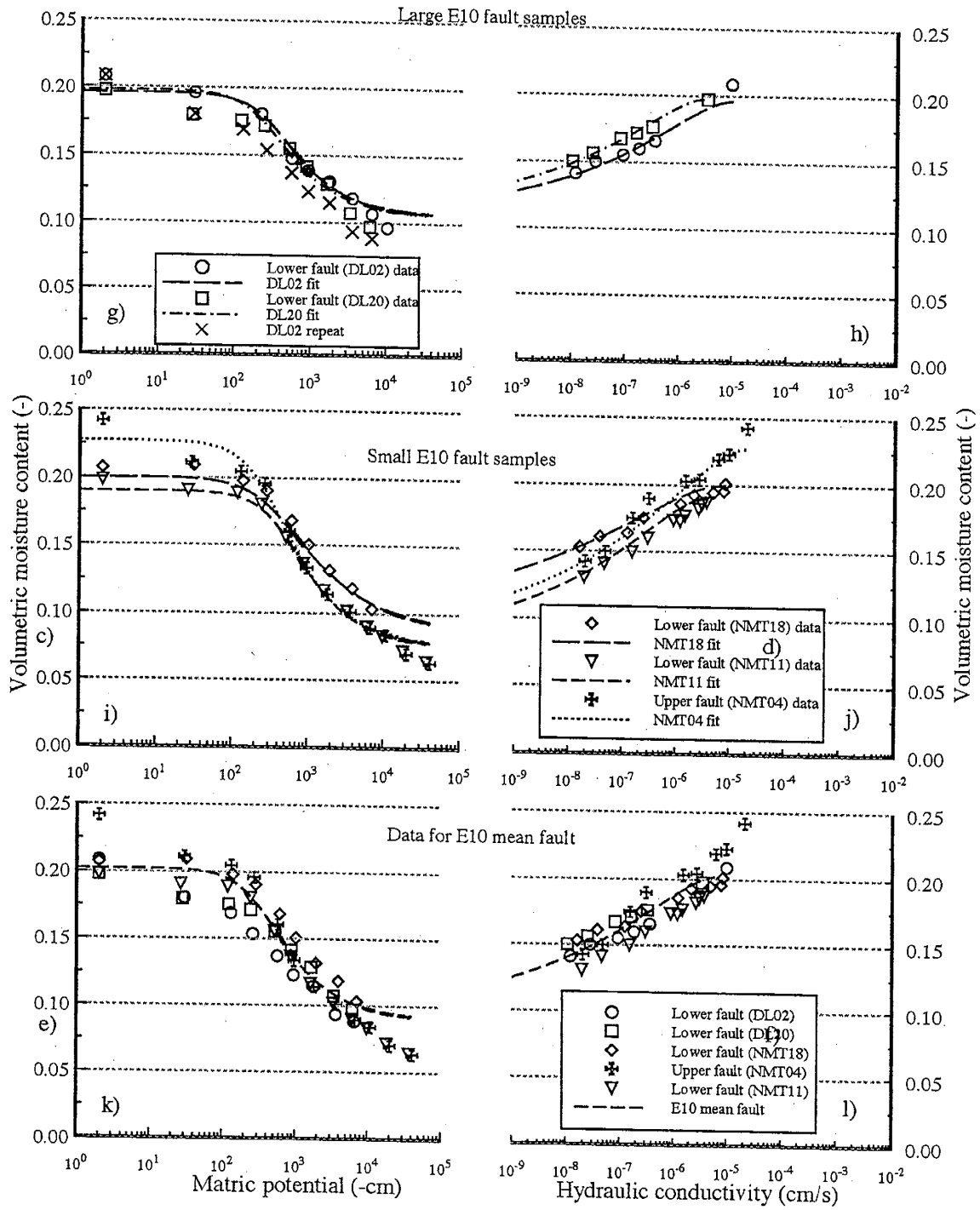


Figure 2.A.1.a-l: UFA measurements and Mualem-van Genuchten model fits for individual samples. The left-hand plots show  $\theta$ - $\psi$  results and the right hand plots show  $K$ - $\theta$  results. Lines depict the theoretical curves for the fitted Mualem-van Genuchten models using parameters shown in Table 2.3.

## Appendix 2.B: Local E10 matric potential estimates

The larger air entry matric potentials and relatively gradual decline in the  $\theta$ - $\psi$  relations for deformation band faults (Figure 2.2 and Appendix 2.A) suggest such faults may provide a very efficient means of quickly estimating the ambient matric potential at a vadose zone outcrop exposure using simple gravimetric methods and fitted  $\theta$ - $\psi$  curves. One determines *in situ*  $\theta$  from a fault sample's volume (or bulk density) and its moisture weight, then reads off the corresponding matric potential  $\psi$  from the fault  $\theta$ - $\psi$  curve.

We applied this approach at fault E10, gravimetrically measuring moisture content for four fault samples. Mean volumetric moisture content ( $\pm$  one standard deviation) for the fault samples was 18% ( $\pm$  1%). We used (1) inverted to solve for  $\psi$  as a function of  $\theta$ , the four fault *in situ* moisture contents, and mean fault parameters (Table 2.3) to estimate the ambient matric potential near fault E10. The matric potentials of the four samples were estimated to be -187, -243, -335, and -379 cm. Using the mean moisture content of these four samples, the estimated matric potential is -283 cm. These estimates apply to a zone roughly 30 cm behind the outcrop face, thus the ambient matric potential deeper within the outcrop is likely to be higher (closer to zero).

If this approach is valid, matric potential in the adjacent sand should be similar. We can use these estimated potentials and the sand  $\theta$ - $\psi$  relationships to estimate sand moisture contents, and check these with field samples. For this range of matric potentials the sand  $\theta$ - $\psi$  curves in Figure 2.2 suggest that the sand should be at or near residual

moisture content. Four representative samples were collected from the lower sand unit, three from the footwall and one from the hanging wall. of the. The mean  $\theta$  was 4.7% ( $\pm$  1.6%), near to, as expected, but less than any of the estimated sand residual moisture content values (Table 2.3).

## 2.7 References

- Antonellini, M. and A. Aydin, Effect of faulting on fluid flow in porous sandstones: petrophysical properties, *AAPG Bull.*, 78, 355-377, 1994.
- Antonellini, M., A. Aydin, and D. Pollard, Microstructure of deformation bands in porous sandstones at Arches National Park, Utah, *J. Struct. Geol.*, 16, 941-959, 1994.
- Aydin, A., Small faults formed as deformation bands in sandstone, *Pure Applied Geophys.*, 116, 913-930, 1978.
- Brainard, J. R., Glass, R. J., Alumbaugh D. L., Paprocki, L., Labrecque, D. J., Yang, X., Yeh, T.-C. J., Baker, K. E., and Rautman, C. A., The Sandia-Tech Vadose Zone Facility experimental design and data report of a constant flux infiltration experiment, Sandia Rep. SAND02-2168, Sandia Natl. Laboratories, Albuquerque, N. M., 2002.
- Brainard, J. R., Vadose zone flow processes in heterogeneous alluvial fan deposits: experimental design, data evaluation, and error analysis, M.S. (Geology), University of New Mexico, Albuquerque, New Mexico, 1997.
- Brooks, R. H. and A. T. Corey, Hydraulic properties of porous media, *Hydrology Paper No. 3*, Colorado State University, Fort Collins, CO, 1964.

- Caine, J.S., J.P. Evans, and C.B. Forster, Fault zone architecture and permeability structure, *Geology*, 24, 1025-1028, 1996.
- Carter K.E. and C.L. Winter, Fractal nature and scaling of normal faults in the Espanola Basin, Rio Grande rift, New Mexico: Implications for fault growth and brittle strain, *J. Struct. Geol.*, 17, 863-873, 1995.
- Cashman, S. and K. Cashman, Cataclasis and deformation-band formation in unconsolidated marine terrace sand, Humboldt County, California, *Geology*, 28, 111-114, 2000.
- Conca, J. L. and J. V. Wright, Diffusion coefficients in gravel under unsaturated conditions, *Water Resour. Res.*, 26, 1055-1066, 1990.
- Conca, J. L. and J. V. Wright, Flow and diffusion in unsaturated gravel, soil and whole rock, *Applied Hydrogeology*, 1, 5-24, 1992.
- Conca, J. L. and J. V. Wright, The UFA method for rapid, direct measurements of unsaturated transport properties in soil, sediment, and rock, *Australian J. Soil Res.*, 36, 291-315, 1998.
- Conca, J., D. Levitt, P. Heller, T. Mockler, and M. Sully, Direct UFA measurements of unsaturated hydraulic conductivity, comparisons to van Genuchten/Mualem estimations, and applications to recharge mapping in arid regions, in *Characterization and Measurement of the Hydraulic Properties of Unsaturated Porous Media*, M. Th. van Genuchten, F. J. Leij, and L. Wu (eds.), Univ. Calif., Riverside, CA, 2, 1173-1197, 1999.

- Connell, S.D., Koning, D.J., and Cather, S.M., Revisions to the stratigraphic nomenclature of the Santa Fe Group, northwestern Albuquerque Basin, New Mexico: New Mexico Geological Society Guidebook, 50<sup>th</sup> Field Conference, p. 337-353, 1999.
- Edwards, H. E., A.D. Becker, and J.A. Howell, Compartmentalization of an eolian sandstone by structural heterogeneities: Permo-Triassic Hopeman Sandstone, Moray Firth, Scotland, in *Characterization of Fluvial and Aeolian Reservoirs*, edited by C. P. North and D. J. Prosser, Geologic Society (UK), London, 339-365, 1993.
- Flint, L.E., D. B. Hudson, and A.L. Flint, Unsaturated hydraulic parameters determined from direct and indirect methods, in *Characterization and Measurement of the Hydraulic Properties of Unsaturated Porous Media*, M. Th. van Genuchten, F. J. Leij and L. Wu (eds.), Univ. Calif., Riverside, CA, 293-302, 1999.
- Fowles, J. and S. Burley, Textural and permeability characteristics of faulted, high porosity sandstones, *Mar. Petrol. Geol.*, 11, 608-623, 1994.
- Forbes, P. L., Simple and accurate methods for converting centrifuge data into drainage and imbibition capillary pressure curves, *Log Analyst*, 35, 31-53, 1994.
- Grauch, V. J., High-resolution aeromagnetic data, a new tool for mapping intrabasinal faults: Example from the Albuquerque basin, New Mexico, *Geology*, 29, 367-370, 2001.
- Hassler, G. L., and E. Brunner, Measurement of capillary pressures in small core samples, *Transactions, AIME*, 160, 114-123, 1945.
- Hawley, J. W., compiler, *Guidebook to Rio Grande Rift in New Mexico and Colorado*, New Mexico Bureau of Mines and Mineral Resources, Socorro, New Mexico, 1978.

Hawley, J.W. and Kernodle, J.M., Overview of the hydrogeology and geohydrology of the northern Rio Grande basin—Colorado, New Mexico, and Texas, *in* Ortega-Klett, C.T., ed., Proceedings of the 44<sup>th</sup> Annual New Mexico Water Conference: New Mexico Water Resources Research Institute Report 312, 79-102, 2000.

<http://wrri.nmsu.edu/publish/watcon/proc/proc44/contents.html>

Hawley, J. W., Haase, C. S., and Lozinsky, R. P., An underground view of the Albuquerque Basin, New Mexico, *in* Ortega-Klett, C. T., ed., Proceedings of the 39th Annual New Mexico Water Conference, New Mexico Water Resource Research Institute Report 290, 37-55, 1995.

Hawley, J.W., Kennedy, J.F., Creel, B.J., The Mesilla Basin aquifer system of New Mexico, West Texas and Chihuahua—an overview of its hydrogeologic framework and related aspects of groundwater flow and chemistry, *in* Angle, E.S., and Mace, R.E., Aquifers of West Texas: Texas Water Development Board Special Conference Proceedings Volume, 76-99, 2001.

<http://www.twdb.state.tx.us/publications/reports/GroundWaterReports/GWReports/Individual%20Report%20htm%20files/Report%20356.htm>

Herrin, J. M., Characteristics of deformation bands in poorly lithified sand: Rio Grande rift, New Mexico, M.S. (Geology), New Mexico Institute of Mining and Technology, Socorro, New Mexico, 2001.

Heynekamp, M. R., L.B. Goodwin, P.S. Mozley, and W.C. Haneberg, Controls on fault-zone architecture in poorly lithified sediments, Rio Grande Rift, New Mexico;

- implications for fault-zone permeability and fluid flow, in *Faults and Subsurface Fluid Flow in the Shallow Crust*, W. C. Haneberg, P.S. Mozley, J.C. Moore, and L.B. Goodwin, eds., *American Geophysical Union Monograph* 113, Washington, DC, US, 27-49, 1999.
- Hong, S., Anisotropic hydraulic conductivity of faulted poorly consolidated eolian sands: Bosque, New Mexico, M.S. (Geology), New Mexico Institute of Mining and Technology, Socorro, New Mexico, 1999.
- Khaleel, R., J. F. Relyea, and J. L. Conca, Estimation of van Genuchten-Mualem relationships to estimate unsaturated hydraulic conductivity at low water contents, *Water Resour. Res.*, 31, 2659-2668, 1995.
- Mattson, E.D., Field simulation of waste impoundment seepage in the vadose zone: Experiment design in two dimensional modeling, M.S. (Hydrology) thesis, New Mexico Institute of Mining and Technology, Socorro, New Mexico, , 1989.
- McCord, J. T., D. B. Stephens, and J. L. Wilson, Hysteresis and state-dependent anisotropy in modeling unsaturated hillslope hydrologic processes. *Water Resour. Res.* 27:1501-1518, 1991.
- Mualem, Y, A new model for predicting the hydraulic conductivity of unsaturated porous media, *Water Resour. Res.*, 12, 513-522, 1976.
- Nimmo, J. R., J. Rubin, and D. P. Hammermeister, Unsaturated flow in a centrifugal field: measurement of hydraulic conductivity and testing of Darcy's law, *Water Resour. Res.*, 23, 124-134, 1987.

Ogilvie, S. R., J.M. Orribo, and P.W. Glover, The influence of deformation bands upon fluid flow using profile permeametry and positron emission tomography, *Geophys. Res. Lett.*, 28, 61-64, 2001.

Pittman, E.D., Effect of fault-related granulation on porosity and permeability of quartz sandstones, Simpson Group (Ordovician), Oklahoma, *AAPG Bull.*, 65, 2381-2387, 1981.

Rawling, G. C., Goodwin, L. B., Wilson, J. L, Internal architecture, permeability structure, and hydrologic significance of contrasting fault-zone types, *Geology*, 29, 43-46, 2001.

Ross, B., A conceptual model of deep unsaturated zones with negligible recharge, *Water Resour. Res.*, 28, 1627-1629, 1984.

Scanlon, B. R., S.W. Tyler, and P.J. Wierenga, Hydrologic issues in arid, unsaturated systems and implications for contaminant transport, *Reviews of Geophysics*, 35, 461-490, 1997.

Sigda, J. M., L. B. Goodwin, P. S. Mozley, and J. L. Wilson, Permeability alteration in small-displacement faults in poorly lithified sediments; Rio Grande Rift, central New Mexico, in *Faults and Subsurface Fluid Flow in the Shallow Crust*, W. C. Haneberg, P.S. Mozley, J.C. Moore, and L.B. Goodwin, eds. *American Geophysical Union Monograph* 113, Washington, DC, US, 51-68, 1999.

Smith, L., Forster, C., and Evans, J., Interaction of fault zones, fluid flow, and heat transfer at the basin scale, in Neuman, S.P. and Neretnieks, I., eds., *Hydrogeology of*

*Low Permeability Environments*, Verlag Heinz Heise, Hannover, Germany, 41-67, 1989.

Stephens, D. B. and R. Knowlton Jr., Soil water movement and recharge through sand at a semiarid site in New Mexico, *Water Resour. Res.*, 22, 881-889, 1986.

Taylor, W.L. and D.D. Pollard., Estimation of in situ permeability of deformation bands in porous sandstone, Valley of Fire, Nevada, *Water Resour. Res.*, 36, 2595-2606, 2000.

van Genuchten, M. T., A closed-form equation for predicting the hydraulic conductivity of unsaturated soils, *Soil Sci. Soc. Am. J.*, 44, 892-898, 1980.

van Genuchten, M. T., F. J. Leij, and S.R. Yates, The RETC code for quantifying the hydraulic functions of unsaturated soils, EPA/600/2-91/065, U. S. Environ. Protection Agency, Cent. Environ. Res. Inf., Cincinnati, OH, United States, 1991.

Wright, J. V., J. L. Conca, and X. Chen.. Hydrostratigraphy and recharge distributions from direct measurements of hydraulic conductivity using the UFA™ method, Technical Report PNL-9424, Pacific Northwest Laboratory, Richland, Washington, 1994.

# **CHAPTER 3: PREDICTING VADOSE-ZONE PREFERENTIAL FLOW AND TRANSPORT BY CAPILLARY WICKING THROUGH DEFORMATION BAND FAULTS**

## **3.0 Abstract**

Recent hydraulic property measurements of deformation band faults and their parent sands reveal striking differences related to the relatively smaller pores of the deformation bands. The differences are large enough to allow vertical preferential flow and transport by capillary wicking through the sandy beds of relatively dry arid and semi-arid vadose zones. Although deformation band faults have been observed in poorly lithified sands from California to the Rio Grande rift, the hydrologic significance of fault-related preferential flow is not yet clear. We investigated the hydrologic significance of these faults in the mid and shallow parts of arid and semi-arid vadose zones, like those of the Rio Grande rift, by comparing water movement, solute transport, and diagenesis using metrics determined from measured hydraulic properties and simple, 1D, steady-state flow models. Hydrologic significance hinges on how competing flow and transport processes differ for a fault versus sand. Capillary wicking within faults can significantly accelerate local water and solute transport, driven downward by gravity (infiltration) or upward by

evaporation (exfiltration), for fault spatial densities, water table depths, and matric potential ranges observed in the Rio Grande rift. If their spatial density is sufficient, faults can locally enhance recharge or discharge. Faults are sites for rapid diagenesis and fast paths for solute transport through sand beds, shortening solute residence times by two or more orders of magnitude. Our modeling results indicate that deformation band faults are hydrologically significant within parts of the Rio Grande rift vadose zone and, perhaps, in other semi-arid and arid areas.

### 3.1. Introduction

Where faulting cuts sandy sediments, shearing may create narrow, tabular zones of reduced pore and grain sizes, called deformation bands, which possess markedly different hydraulic properties than the porous parent sands or sandstones [e.g., Aydin, 1978; Pittman, 1981; Edwards et al., 1993; Antonellini and Aydin, 1994; Fowles and Burley, 1994; Sigda et al., 1999; Heynekamp et al., 1999; Rawling et al., 2001; Sigda and Wilson, 2003]. We consider only cataclastic or shear deformation bands in this paper. Near elimination of porosity and reduction in saturated hydraulic conductivity,  $K_s$ , by many orders of magnitude have been long established for deformation bands in porous, well-lithified sandstones [Aydin, 1978; Pittman, 1981; Edwards et al., 1993; Antonellini and Aydin, 1994; Fowles and Burley, 1994]. Analogous changes also occur in deformation bands and zones of deformation bands, called deformation band faults, formed in poorly lithified sands, such as those found in the basin-fill sediments of the Rio Grande rift

[Sigda et al., 1999; Hong, 1999; Rawling et al., 2001; Herrin, 2001; Sigda and Wilson, 2003]. Faulting can also create large differences in unsaturated hydraulic properties, as demonstrated by our recent measurements of a small-displacement deformation band fault and its poorly lithified parent sand [Sigda and Wilson, 2003]. Fault and protolith hydraulic properties differ sufficiently to permit this and similar faults to act as paths for preferential flow and solute transport under the relatively dry conditions of arid and semi-arid vadose zones. The hydrologic significance of these potential “fast paths”, broached in our earlier paper, remains an open research question with possibly important management and engineering applications.

A variety of geologic processes combine to produce thick, basin-fill deposits of variably lithified sediments crosscut by an abundance of faults. These faulted sediments form vital saturated and vadose zones in areas like the Basin and Range province of the American Southwest and our area of interest, the Rio Grande rift. Within the basins of the Rio Grande rift, the estimated number of faults continues to increase as mapping coverage expands and geophysical techniques improve [Carter and Winter, 1995, Grauch, 2001]. Little is known about the numbers or spatial distribution of smaller displacement faults, but high fault densities have been observed, including an average density of one deformation band fault every 4 m at our field site in the Bosque del Apache National Wildlife Refuge in central New Mexico [Herrin 2001; Sigda and Wilson 2003]. We have observed a still higher deformation band fault density, roughly one fault every 2 m, in an area located several kilometers further south (Figure 3.1a).

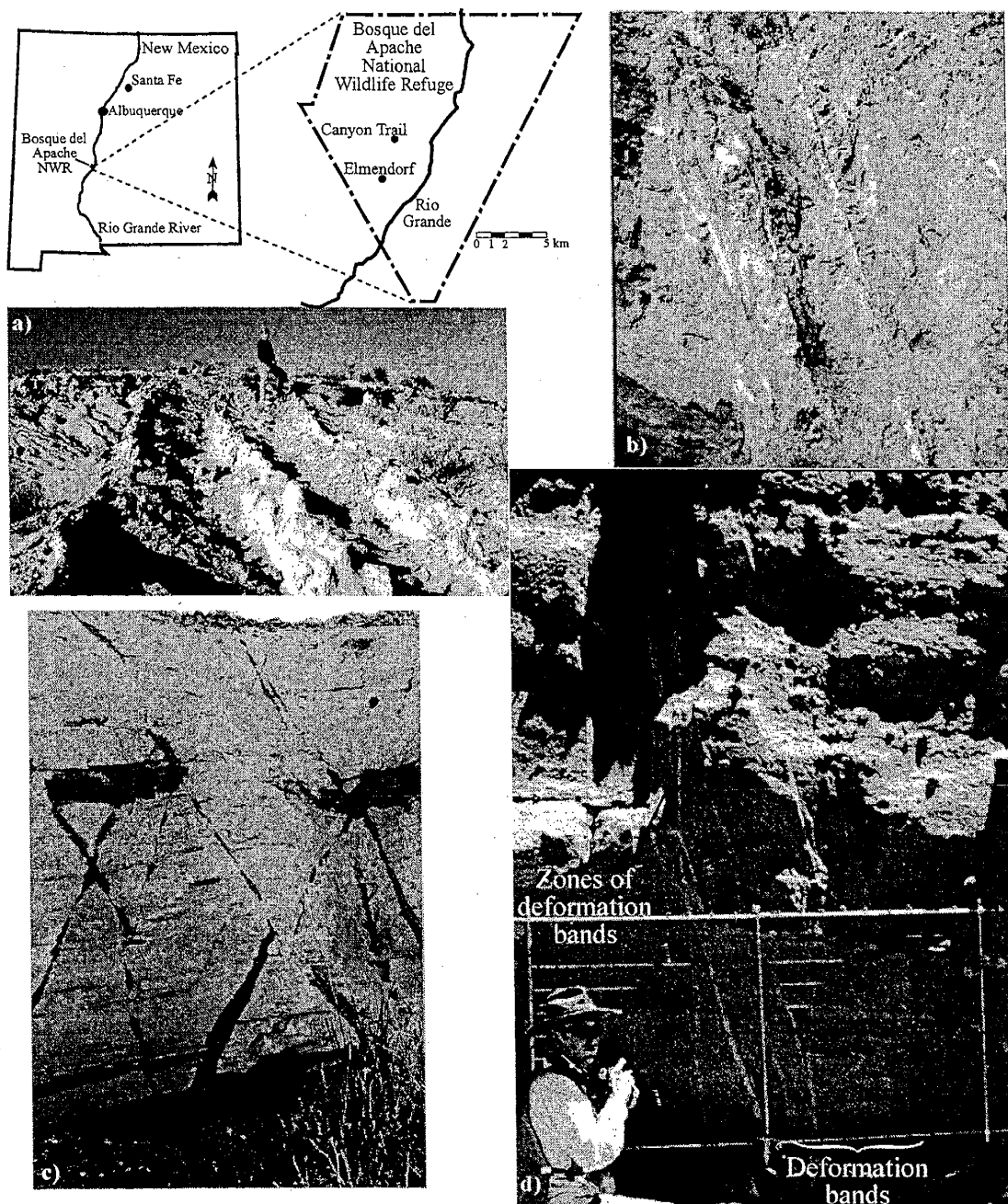


**Figure 3.1:** Deformation band faults in the Rio Grande rift. **a)** Elmendorf fault zone located in Bosque del Apache National Wildlife Refuge, NM, within the Socorro Basin of the Rio Grande rift. Well-cemented faults form regularly spaced inclined planes with 1.5 - 2.0 m between each fault. The parent sand is uncemented and friable. This pattern extends for nearly 100 m. **b)** Wide zone of deformation bands in the large displacement (~600 m) Sand Hill fault zone, just west of Albuquerque. Note the footwall bedding at the left. Flagging indicates 50 cm intervals. Adapted from Rawling et al [2001]. **c)** Wetted narrow zones of deformation bands (sub-vertical) and cemented lamina (sub-horizontal) several days after a rain storm at the Canyon Trail site, Bosque del Apache National Wildlife Refuge, NM. Total outcrop height is 5 m. Adapted from Herrin [2001]. **d)** Canyon Trail fault E10 showing individual deformation bands and the narrow zone of deformation bands investigated by Sigda and Wilson [2003]. Grid is 1 m high.

The term “deformation band fault”, a deformation band or zone of bands, warrants amplification because it is not in general use in the hydrology community. Deformation band faults are architecturally and hydraulically distinct from faults in crystalline rocks, which comprise gouge and fracture zones [Smith et al., 1989; Caine et al., 1996; Fischer et al., 1998; Heynekamp et al., 1999; Rawling et al., 2001]. Cataclastic deformation band faults can only be created by shearing sand-rich beds, so a fault zone which crosscuts beds of various lithologies (clay, sand, silt, etc.) will not create deformation band faults in sand-poor beds. However, a fault zone crosscutting sand-rich beds may comprise one or more zones of deformation bands, especially in larger-displacement fault zones (Figure 3.1b). This study focuses only on zones of deformation bands because they typically have much greater lengths than individual deformation bands and so are more likely to influence water and solute transport at larger scales than individual bands.

Several independent observations attest to the likelihood that deformation band faults act as fast paths for fluid flow and solute transport through the vadose zone of the Rio Grande rift. Some deformation band faults appear to remain much wetter than their adjacent sands several days after a rainstorm (Figure 3.1c). Centrifuge measurements [Sigda and Wilson, 2003] of volumetric moisture content  $\theta$  as a function of matric potential  $\psi$ , and unsaturated hydraulic conductivity  $K$  as a function of moisture content  $\theta$ , for a deformation band fault and its undeformed parent sand (Figure 3.1d) revealed that the sand and fault  $K(\psi)$  functions crossover as  $\psi$  decreases from 0 cm. Under wetter conditions ( $\psi$  near 0 cm) sand  $K \gg$  fault  $K$ , but under drier conditions sand  $K \ll$  fault  $K$ ,

and between these two end cases there is a  $\psi$  value ( $-35 \geq \psi \geq -80$  cm), called the crossover point, at which fault  $K =$  sand  $K$ . Fault  $K$  is two to four orders of magnitude less than sand  $K$  if the matric potential is greater than the crossover  $\psi$ , but becomes orders of magnitude larger than sand  $K$  for  $\psi$  less than the crossover  $\psi$ . Sigda and Wilson [2003] used a simple, gravity-driven, steady flow model to predict that, under dry conditions, downward, liquid-phase flux densities are  $10^2$  to  $10^5$  times larger in the fault than in its parent sands and that non-reactive solute residence times from advection through the fault are reduced by similar orders of magnitude. In the Rio Grande rift, we have also observed well cemented deformation band faults, whereas their parent or adjacent sands have little or no cement (Figure 3.1a). This suggests unsaturated flow and solute transport were focused almost entirely within the faults because the cementation rate depends, in part, on the number of water pore volumes passed through a material in a given amount of time.

If deformation band faults significantly accelerate water and solute movement through poorly lithified vadose zone sands, they might prove important exceptions to the commonly held idea that, under arid and semi-arid conditions, downward unsaturated flow and transport are negligible or extremely slow [Winograd, 1981; Scanlon et al., 1997]. Large numbers of deformation band faults in a given area could locally increase infiltration, enhancing aquifer recharge, violating capillary barriers [e.g., Ross, 1990; Selker et al., 1999], and threatening vadose-zone nuclear waste repositories such as the Yucca Mountain Project (deformation band faults have also been observed in non-welded ignimbrites [Wilson et al., 2003]). Contaminants could be transported quickly enough and

in sufficient quantity to adversely affect aquifer water quality within an engineering or managerially significant amount of time. For example, faults underlying landfills, underground storage tanks, livestock waste lagoons, industrial sites, and other potential contaminant sources could transport unwanted solutes through arid and semi-arid vadose-zone sands more rapidly than would be expected for unfaulted sands. Over longer time scales, accelerated transport of naturally occurring solutes could cause preferential cementation of the faults, further reducing fault saturated conductivity and creating better barriers to cross-fault saturated flow. Aquifers could then be compartmentalized by faults, much as petroleum reservoirs are compartmentalized [Smith, 1966], should the preferentially cemented fault segments subsequently be moved into the saturated zone by tectonic activity or by a rising water table.

Are the observed differences in fault and protolith hydraulic properties hydrologically important in semi-arid and arid vadose zones? Under which conditions do these differences significantly accelerate the movement of water, contaminants, or diagenetically important solutes through the vadose zone? We examine how liquid-phase transport processes (infiltration and exfiltration), advective solute transport, and diagenesis differ in sands and faults for simple flow scenarios. Each advective liquid-phase process is contrasted against a competing vadose zone process. Infiltration and exfiltration are compared to thermally driven vapor-phase water flux in the sand. Liquid-phase advective transport of solutes is compared with transport by diffusion. We assess all processes for each flow scenario using simple, one-dimensional, steady-state models that also

accommodate varying fault spatial density. For the present we ignore transient flow, variations in fault dip and architecture, spatially varying lithology of the parent sediments, and cross-flow between the fault and surrounding sand.

### **3.2. Conceptual model**

A dauntingly wide array of forces drives water and solute movement through semi-arid and arid vadose zones. The relative importance of osmotic, gravitational, thermal, density, and matric potential gradients can each vary greatly, both spatially and temporally, as can the resulting liquid-phase, vapor-phase, and net water flux directions and magnitudes. For example, liquid-phase flux can be overshadowed by vapor transport given the geothermal gradients and low moisture contents reported for areas of the western US [Ross, 1984; Scanlon et al., 1997]. Solute flux may be controlled by liquid-phase advection only, diffusion only, or some combination of the two. Appropriate time scales can vary from the near surface's diurnal periodicity to the multi-millennial variability governing deep arid vadose zones. Vadose-zone thickness ranges between meters and a kilometer, and hydrogeologic characteristics encompass a tremendous range of grain sizes, sorting, depositional environments, and lithification and other diagenetic changes.

Our hydrogeologic conceptual model was constructed from a subset of this complex array of processes and scales. It is based on known or inferred characteristics of the middle Rio Grande vadose zone. Average annual precipitation of ~22 cm/year, reports of

downward liquid-phase fluxes [Stephens and Knowlton, 1986; Phillips et al., 1988; McCord et al., 1991], and measurements of shallow ambient matric potentials in the tensiometer range (0 to  $\sim$ 600 cm matric potential) [Stephens and Knowlton, 1986; Mattson, 1989; McCord et al., 1991; Brainard et al., 2001; Sigda and Wilson, 2003] indicate recharge is important in some areas of the middle Rio Grande rift. In contrast, data from an Albuquerque Basin infiltration experiment revealed matric potentials within the top eight meters that were well below the tensiometer range [Brainard, 1997], indicating infiltration through sand is likely negligible at that site. In response, our conceptual model considers a wide range of possible matric potentials from zero (near saturation) to values below tensiometer range. Significant geothermal gradients within the rift's vadose zone [Reiter, 1999] raise the possibility that upward water movement via vapor-phase transport can dominate liquid-phase movement in areas with low liquid-phase fluxes [Walvoord et al., 2002]. Accordingly, the model employs estimates of upward vapor-phase water fluxes to provide a lower bound on the significance of liquid-phase processes. We investigated both local downward (infiltration) and, for discharge areas with a shallow water table, local upward (exfiltration) liquid-phase flow. Diffusion-driven solute transport in the liquid phase was also considered, as it can equal or exceed advective liquid-phase transport if the moisture content becomes sufficiently small. The model is an idealized representation of the Canyon Trail site E10 in the Bosque del Apache National Wildlife Refuge, central New Mexico, for which  $K$ - $\theta$  and  $\theta$ - $\psi$  data are recently available [Sigda and Wilson, 2003]. E10 is a relatively uniform, steeply dipping,

narrow zone of deformation bands, which cuts a bed of relatively uniform, well-sorted, poorly lithified sand (Figure 3.1d). It appears very similar to most of the deformation band faults observed at other Canyon Trail faults (e.g., Figure 3.1c), at the nearby Elmendorf fault zone (Figure 3.1a) [see also Sigda et al., 1999], and as elements of many larger displacement faults (Figure 3.1b) [Heynekamp et al., 1999; Rawling et al., 2001].

The gravity-driven (infiltration) model's vertical length scale was set as 10 m because sand-only bed thickness is typically  $\leq 10$  m in the middle Rio Grande rift [Davis et al., 1993; Mozley et al., 1995]. Even though fault zones can extend continuously across the vadose zone from their origin, which may be kilometers below ground surface, deformation band faults within those fault zones are likely to be vertically discontinuous because the character of the fault can change with lithology [cf. Wilson et al., 2003]. The deformation band fault unsaturated hydraulic properties measured by Sigda and Wilson [2003] may not accurately describe another portion of the same fault if, for example, it cuts a lithologic unit with relatively little sand, such as a well-lithified debris-flow bed or a clay-rich bed.

We tested whether deformation band faults are hydrologically significant in the mid and shallow parts of a moderately dry vadose zone like the Rio Grande rift by comparing the metrics for water flow, contaminant transport, and diagenesis shown in Table 3.1. These metrics were determined from previously measured hydraulic properties and our simple, 1D, steady-state conceptual model. The infiltration scenario examined gravity-

driven flow through the middle portion (below the root zone and above the capillary fringe) of a thick vadose zone where there is relatively little vertical change in moisture content and matric potential. The exfiltration scenario examined flow through a shallow vadose zone where surface evaporation (or an active, near-surface root zone) draws liquid-phase water upward from the water table (e.g., Gardner [1958]). We considered only one-dimensional, steady-state, liquid-phase flow, which is controlled by the ambient matric potential under the gravity-driven scenario and by the depth to the water table under the evaporation-driven scenario. We also compared diffusive and advective solute transport for each flow scenario. Diagenesis was investigated using the number of pore volumes passing through a given column length of material as a proxy for diagenesis. Under our conceptual model's assumptions, the solute residence time for a given column length equals the time required to push a pore volume through the same column length. We assume an unlimited supply of reactants, instantaneous equilibrium chemistry, and that diagenesis does not substantially change fault or protolith hydraulic properties.

**Table 3.1:** Metrics to test hydrologic significance of deformation band faults

Process	Gravity-driven, liquid-phase flow	Evaporation- driven, liquid- phase flow	Comparator
Water flow	downward flux density	upward flux density	vapor-phase flux density
Solute transport	advective residence time		diffusion residence time
Diagenetic change	time to push one pore volume		-

One diagenetic change commonly encountered in arid and semi-arid vadose zones, including the Rio Grande rift, is calcite cementation of poorly lithified sediments. The sedimentary rock fragments and carbonate-rich soils prevalent throughout the middle Rio Grande basins [Hawley and Haase, 1992; Mozley et al., 1995] and the typically high vadose-zone CO<sub>2</sub> partial pressures [e.g., Wood et al., 1993; Affek et al., 1998] provide abundant carbonate and calcium ions. Seepage velocities under relatively dry conditions are sufficiently slow that calcite equilibrium is a reasonable assumption [Selker et al., 1999, p. 179]. By narrowing pores, calcite cementation may actually increase, rather than decrease, unsaturated hydraulic conductivity over some unknown time scale in arid or semi-arid vadose zones, and therefore casts our assumptions of steady flow and negligible changes in protolith hydraulic properties as potentially conservative assumptions.

Our conceptual model should be applicable to other semi-arid and arid vadose zones with deformation band faults. Net water fluxes and matric potentials vary widely for the few sites investigated. The middle Rio Grande rift studies cited above suggest that matric potentials range from -10 to <-600 cm in the top 10 m of the vadose zone, whereas observations at several locations in Texas and Nevada [Scanlon, 1992, 1994; Scanlon et al., 1997; Walvoord et al., 2002] show matric potentials are on the order of megapascals (1 MPa  $\approx$  10,000 cm). Our model is unlikely to be valid for such extremely dry regions, which lie beyond the limiting conditions we calculate, but it may be applicable to areas within these dry regions where liquid-phase flow is locally important, such as recharge areas. Moreover, the model can be used to investigate situations in which different

processes dominate in each material, such as liquid-phase advection in the fault and vapor-phase transport or liquid-phase solute diffusion in the surrounding protolith.

### 3.3. Methods

#### 3.3.1 Theoretical hydraulic relations

Experimental  $K$ - $\theta$  and  $\theta$ - $\psi$  data were fit to the commonly used Mualem-van Genuchten (MvG) theoretical model [Mualem, 1976; van Genuchten, 1980]. The data were obtained from UFA centrifuge experiments on intact samples from the Canyon Trail E10 site. The resulting data were simultaneously fit to Equations (3.1) and (3.2) using a trial and error approach, yielding a final  $K(\psi)$  relation [Sigda and Wilson, 2003].

$$\theta(\psi) = \theta_r + (\theta_s - \theta_r) \left(1 + |\alpha\psi|^n\right)^{-m} \quad \text{where } m = (n-1)/n \quad (3.1)$$

$$K(\theta) = K_s \left(\frac{\theta - \theta_r}{\theta_s - \theta_r}\right)^\beta \left\{1 - \left[1 - \left(\frac{\theta - \theta_r}{\theta_s - \theta_r}\right)^{1/m}\right]^m\right\}^2 \quad (3.2)$$

In this paper we limit our analyses to two pairs of the fault and protolith MvG parameter sets (Table 3.2) from the group of five fault and seven sand samples measured by Sigda and Wilson [2003]. The first pair, DL06 sand and DL20 fault, show the smallest difference in their  $K(\psi)$  relations and so provide an indication of the minimum difference to be expected in flow and transport through fault and protolith. The second

pair is the set of mean parameters for all E10 sands (“mean sand”) and the set of mean parameters for all fault samples (“mean fault”).

**Table 3.2:** Fitted parameter values for Mualem-van Genuchten model

Sample ID	$\theta_s$ ( $\text{cm}^3 \text{ cm}^{-3}$ )	$\theta_r$ ( $\text{cm}^3 \text{ cm}^{-3}$ )	$\alpha$ ( $\text{cm}^{-1}$ )	$n$ (-)	$\beta$ (-)	$K_s$ ( $\text{cm/s}$ )*
Footwall sand						
DL06	0.315	0.058	0.03	3.4	0.2	$1.20 \times 10^{-3}$
Mean sand	0.318	0.062	0.038	3.34	0.42	$1.72 \times 10^{-3}$
Fault DL20	0.198	0.105	0.004	1.80	1.2	$3.5 \times 10^{-6}$
Mean fault	0.202	0.089	0.003	1.74	1.56	$7.36 \times 10^{-6}$

\*Mean  $K_s$  values are the geometric means of the measured saturated hydraulic conductivity values. All other means are arithmetic averages of estimated parameter values. Values taken from Sigda and Wilson [2003].

### 3.3.2 Testing hydrologic significance

The hydrologic significance of faults was investigated for three processes: water movement, solute transport, and diagenesis, operating in two different vadose-zone scenarios under semi-arid or arid conditions. We used a simple, one-dimensional model with steady-state flow to compare the relative differences between deformed and undeformed sand (Figure 3.2). To identify transitions from one dominant process to another (e.g., from liquid-phase to vapor-phase flow), the matric potential for the gravity-driven scenario was varied from zero to several thousand cm (several bar), and depth to water table was varied over a relatively large range, 10 to 1000 cm, for the evaporation-driven scenario. Upscaling from a single fault to a zone of faults, we also examined how the relative differences in liquid-phase water movement change with fault spatial density.

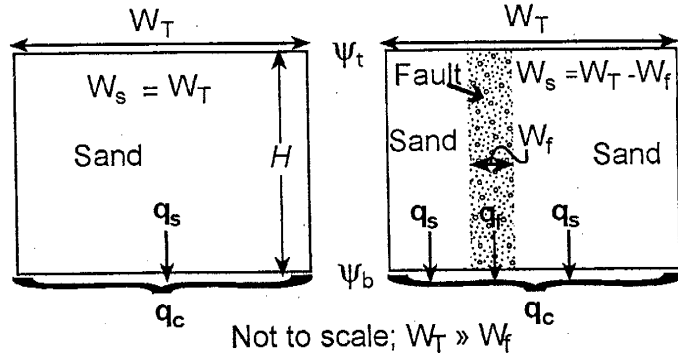


**Figure 3.2:** Idealized columns for determining impact of fault spatial density. Fault width ( $W_f=1$  cm) is much smaller than total column width ( $W_T=100, 10$ , or  $2$  m). Composite flux density for column is  $q_c$ . Sand and fault flux densities,  $q_s$  and  $q_f$ , are shown for the gravity-driven scenario in which the matric potential is uniform throughout column ( $\psi_t = \psi_b$ ). For the evaporation-driven scenario,  $H$  is the water table depth, the bottom boundary is at the water table ( $\psi_b = 0$  cm) and the top boundary at ground level ( $\psi_t = -10,000$  cm).

Our conceptual model assumes that faults are vertical (90° dip), exchange of water or solute is negligible between fault and sand, hysteresis and osmotic gradients are negligible, and hydraulic behavior is sufficiently constant over long time periods to be considered steady flow. Furthermore, the flow and transport analyses assume effective volumetric moisture content equals total volumetric moisture content ( $\theta_{eff} = \theta$ ); i.e., advection and diffusion of water and solutes continue to occur even when  $\theta$  is close to residual, ( $\theta \approx \theta_r$ ), because the MvG model approaches  $\theta_r$  asymptotically. Advective solute transport assumes negligible dispersion and a non-reactive solute.

**3.3.2.1 Gravity-driven scenario: advection.** The first scenario, which focuses on the middle portion of a thick vadose zone well below the root zone and well above the capillary fringe, continues the preliminary analysis of gravity-driven advection presented by Sigda and Wilson [2003]. Driven by the gravity-induced unit gradient, steady downward liquid-phase advection of water and solutes (assuming no dispersion) is wholly a function of the ambient matric potential and the material's unsaturated hydraulic properties, which are both assumed to remain constant within the 10 m domain length. Under these assumptions, the liquid-phase flux density,  $q_l$ , is given by

$$q_l(\psi) = -K(\psi) = -K_s \left(1 + |\alpha\psi|^n\right)^{-m\beta} \left\{1 - \left[1 - \left(1 + |\alpha\psi|^n\right)^{-1}\right]^m\right\}^2, \quad (3.3)$$

where the z-axis is positive upwards. We examined how the sand and fault flux densities changed as matric potential was decreased from 0 cm, passing through some crossover

matric potential,  $\psi_x$ , down to a minimum of  $-3000$  cm (roughly  $-3$  bar), an arbitrarily chosen limit below which liquid-phase flow and transport are presumed to be no longer significant. The advective solute residence time,  $t_r$  (years), for a conservative solute moving with no dispersion through a uniform, vertical column of length  $L$  (cm) under the gravity-driven scenario is given by

$$t_r(\psi) = L / v_s(\psi) = L\theta(\psi) / q_l(\psi), \quad (3.4)$$

where  $v_s$  is the seepage velocity (cm/year) and  $\theta$  is the volumetric moisture content ( $\text{cm}^3 \text{cm}^{-3}$ ). The advective residence time depends on the ambient matric potential.

**3.3.2.2 Gravity-driven scenario: diffusion.** Diffusion-only transport is used to establish a lower bound for advective transport, which rapidly decreases as moisture content decreases. We applied Fick's second law using a volumetric moisture content-dependent diffusion coefficient, a semi-infinite domain bounded by a constant concentration ( $C_0$ ) boundary at  $L = 0$ , and a zero initial concentration throughout the medium. The solution for a conservative solute and this set of initial and boundary conditions is [Crank, 1975, pp. 20-21]

$$C(L,t)/C_0 = 1 - \text{erf}(L/2\sqrt{Dt}), \quad (3.5)$$

where  $L$  (L) is the distance from the constant source boundary,  $\text{erf}$  is the error function, and  $D$  is the diffusion coefficient ( $\text{L}^2/\text{T}$ ). The time needed for the solute concentration at a distance  $L$  (cm) from the boundary to reach the arbitrary value  $0.5C_0$  can be calculated

by simplifying (3.5) and recalling that the error function value essentially equals its argument value if the latter is near 0.5, or

$$t_d(\psi) \equiv L^2 / D(\theta(\psi)). \quad (3.6)$$

Here  $t_d$  is the diffusion residence time (years) and  $D(\theta)$  is the effective diffusion coefficient ( $\text{cm}^2/\text{year}$ ) for a porous medium with volumetric moisture content  $\theta$ . Substituting  $D(\theta)$  for  $D$  in (3.5) is valid for the gravity-driven scenario, as moisture content is constant throughout the domain length. As it continues to be an area of research (e.g., Olesen et al. [2001]), we consider two different models for  $D(\theta)$ . The first is the commonly used Millington and Quirk [1961] (MQ) model in which the effective diffusion coefficient is the product of the free water diffusion coefficient,  $D_0$ , (with a maximum, say, near  $2 \times 10^{-5} \text{ cm}^2/\text{s}$ ) and a tortuosity factor,  $\tau$ , that depends on  $\theta$  and  $\theta_s$ :

$$\text{MQ: } D(\theta) = D_0 \tau(\theta) = D_0 \theta^{\frac{10}{3}} \theta_s^{-2} \quad (3.7).$$

The second model (CW) is a linear regression fit to a logarithmic transform of experimental measurements of effective diffusion coefficients for soils and sands from Conca and Wright [1992].

$$\text{CW: } D(\theta) = 10^{-4.32 - 0.432 \log_{10}(\theta)} \quad (3.8)$$

The effective diffusion coefficients (3.7 and 3.8) and diffusion residence time (3.6) can all be restated as functions of the ambient matric potential using the fitted  $\theta$ - $\psi$  curves.

We selected this set of conditions because a constant source concentration is appropriate for the relatively short travel distances considered and a semi-infinite domain is reasonable given the vadose zone length and time scales considered. There are other permissible choices of initial, boundary, and breakthrough conditions, but they do not change the relative differences observed in fault and sand behavior. By comparing sand and fault residence times, as well as the matric potential values where  $t_r = t_d$  for sand and fault, we identified which process will drive breakthrough by a solute under gravity-driven flow and how the switch in dominant process varies with governing matric potential.

**3.3.2.3 Geothermal-driven vapor-phase flow.** In the presence of a geothermal gradient and sufficiently low moisture contents, upward vapor-phase flux may be as large or larger than downward liquid-phase flow. Thus the matric potential value at which liquid-phase flux density equals vapor-phase flux density represents a lower bound on the significance of liquid-phase flow in either the sand or fault. In the absence of thermal property measurements for faults, we made a conservative assumption that there is no significant difference between vapor-phase flow in sand and in a fault. Assuming that both mass flow of gas (advective vapor movement) and isothermal vapor-phase flow (i.e., diffusive vapor transport driven by matric potential gradients) are negligible, we calculated the thermal vapor-phase flux density in poorly lithified sand using the approach described by Ross [1984] and Philip and DeVries [1957],

$$q_v(T, \gamma) = -D_v(T) \gamma \frac{d\rho_v}{dT}, \quad (3.9)$$

in which  $q_v$  is the vapor-phase flux density (L/T),  $T$  is temperature (°K),  $\gamma$  is the geothermal gradient,  $D_v$  is the effective vapor diffusivity (L<sup>2</sup>/T), and the last term is the derivative of saturated vapor density with regard to temperature. The effective vapor diffusivity term is calculated according to Philip and DeVries [1957],

$$D_v(T) = \theta_s D_{atm}(T) \nu \xi(\theta, \theta_s), \quad (3.10)$$

where  $D_{atm}$  is the molecular diffusivity of water vapor in air (L<sup>2</sup>T<sup>-1</sup>),  $\nu$  is a "mass flow" constant roughly equal to 1 (-), and  $\xi(\theta, \theta_s)$  accounts for the difference in temperature gradient between the vapor phase and the bulk soil (-). Taken from a table in Philip and DeVries [1957], the latter term is a function of the ambient moisture content, assumed here to range between 0.05 and 0.10, as well as the sand's mineral composition and porosity. The molecular diffusivity and saturated vapor density's temperature derivative are functions of temperature, which, based on vadose-zone temperature measurements collected within the Rio Grande rift's Albuquerque Basin by Reiter [1999], ranges between 15 and 30° C. Minimum and maximum values of 20 and 40° C/km for the geothermal gradient,  $\gamma$ , were calculated from Reiter's [1999] data.

**3.3.2.4 Diagenesis.** Given assumptions of instantaneous kinetics relative to seepage velocity and an ample supply of reactants relative to kinetics, we argue that the number of pore volumes which flow through a column provides a proxy for diagenesis. The unit time required to pass one pore volume through a column of length  $L$  is then the inverse of

the solute residence time,  $1 / t_r$ . Solute residence time, however, will depend on advection for certain governing conditions and on diffusion for other conditions. A process-independent solute residence time,  $t_r^*$ , can be estimated by taking the smaller of the diffusion and advection solute residence times:

$$t_r^* = \begin{cases} t_a & \text{if } t_a < t_d \\ t_d & \end{cases} \quad (3.11)$$

where  $t_a$  and  $t_d$  are the advection and diffusion residence times, respectively. The exact residence time can be calculated by finding appropriate time solutions to the 1D advection-diffusion equation for steady flow:

$$\theta(z) \frac{\partial C}{\partial t} = \frac{\partial}{\partial z} \left[ \theta(z) D(\theta) \frac{\partial C}{\partial z} \right] - \theta(z) v(z) \frac{\partial C}{\partial z} \quad (3.12)$$

where  $C$  is the solute concentration ( $\text{ML}^{-3}$ ), the seepage velocity ( $\text{LT}^{-1}$ ) and volumetric moisture content are functions of elevation, and the effective diffusion coefficient  $D$  is a function of moisture content. A relative unit time per pore volume,  $T_{pv}$ , can then be computed from the process-independent solute residence times:

$$T_{pv} = (\text{fault } t_r^*)^{-1} / (\text{sand } t_r^*)^{-1} = \text{sand } t_r^* / \text{fault } t_r^* \quad (3.13).$$

**3.3.2.5 Evaporation-driven scenario: advection.** Estimating advective flow upwards from a shallow water table to the ground surface allows comparison of fault and sand behavior with matric potential and moisture content varying within the domain. Driven upwards by a matric potential gradient, liquid-phase flux density is a function of the domain length, material properties, and the upper boundary matric potential ( $\psi = 0$

cm at the water table bottom boundary). Under conditions of one dimensional, steady flow, the solution can be written in integral form as [Irmay, 1968]

$$z_T - z_B = - \int_{\psi_B=0}^{\psi_T} \left[ \frac{q_l}{K(\psi)} + 1 \right]^{-1} d\psi, \quad (3.14)$$

where  $z$  is the vertical axis (positive upwards),  $z_T$  and  $z_B$  are the elevations (L) of the top and bottom boundaries,  $\psi_T$  and  $\psi_B$  are the matric potential values (L) at those boundaries,  $q_l$  is the flux density ( $LT^{-1}$ ) through the column (positive for upward flow), and  $K(\psi)$  is the hydraulic conductivity ( $LT^{-1}$ ). We take  $z_T = 0$  and  $z_B = -H$ , where  $H$  (L) is the depth to the water table. By assuming  $K(\psi)$  is an exponential function of the form

$$K(\psi) = K_s \exp(-\alpha|\psi|), \quad (3.15)$$

Gardner [1958] solved (3.14) analytically and then determined the maximum evaporative flux density,  $q_b$ , by setting  $\psi_T = -\infty$ . As (3.15) provided a poor match to the MvG  $K(\psi)$  functions used in this study, we fit a series of piecewise continuous Gardner exponential functions (3.15) to the estimated sand and fault MvG  $K(\psi)$  functions. This allowed us to rewrite the analytical solution to (3.14) as a system of nonlinear equations for each depth to the water table,  $H$ , which was varied from 10 to 1000 cm, and the system of equations was solved for  $q_l$  for each value of  $H$  (Appendix 8.C). The upper boundary potential,  $\psi_T$ , was set to  $-10,000$  cm ( $-1$  MPa), a value we judged representative of long-term surface matric potential for many semi-arid and arid vadose zones. This value is larger (wetter) than the  $-4$  to  $-8$  MPa (the lower limit for field thermocouple psychrometers)

measured by Scanlon [1994] at 30 cm below ground level in west Texas. It is much less than the -40 to -90 cm measured at the same depth by Stephens and Knowlton [1986] in the middle Rio Grande rift, but their data do not agree with those of McCord et al. [1991], who observed that the surface matric potential was less than the lower limit for tensiometer measurements (i.e., < -600 cm) at the same general location. The flux density  $q_l(H)$  is, however, insensitive to the top boundary potential once the latter drops below a certain value (e.g., -1000 cm) [Gardner, 1958; Selker et al., 1999, p. 127]. Calculation of the evaporation-driven solute residence time for a solute moving from the water table upwards to the ground surface requires the seepage velocity distribution along the column length. Solving the system of nonlinear equations for a given water table depth also yields discrete information about the matric potential distribution along column length, from which we calculated the volumetric moisture content using (1). The advective solute residence time was then calculated from

$$t_r(H) = q_l(H)^{-1} \int_{z=H}^{z=0} \theta(z) dz \quad . \quad (3.16)$$

The right-hand side integral, which is analogous to the product  $L\theta(\psi)$  in (3.4), accommodates the spatially varying moisture content and was evaluated numerically.

The evaporation-driven residence time,  $t_r$  (3.16), differs conceptually from the gravity-driven  $t_r$ , (3.4), because the former is for a variable length,  $H$ , while the latter is for a fixed length,  $L$ . Neither residence time nor number of pore volumes are directly comparable between the gravity- and evaporation-driven scenarios.

**3.3.2.6 Evaporation-driven scenario: diffusion.** We estimated diffusion residence time for each value of  $H$  in a manner similar to that for the gravity driven scenario,

$$t_d(H) \equiv H \int_{z=H}^{z=0} [D(\theta(z))]^{-1} dz. \quad (3.17)$$

$D(\theta(z))$  is the spatially varying effective diffusion coefficient estimated from either the MQ or CW model (3.7 or 3.8). We evaluated the integral numerically.

**3.3.2.7 Fault spatial density.** We gauged the effect of the number of deformation band faults per unit area on liquid water movement by calculating the relative increase in exfiltration or infiltration through an idealized vadose zone column as a function of fault spatial density (Figure 3.2). The composite flux density for a given column was determined by weighting the flow through fault and through sand according to their relative contributions to the column's total width ( $W_T$ ). Sand and fault properties were each considered uniform. Faults were assumed to have a constant width of 1 cm (like fault E10), 90° dip, and spatial densities ranging between one fault /10 m and one fault/1000 m (denoted as  $1:10^3$  cm and  $1:10^5$  cm). As fault width was always much less than the column width occupied by sand (thus  $W_T \equiv W_s$ ), the expression for liquid-phase composite flux density could be simplified:

$$q_c = \frac{q_s W_s + q_f W_f}{W_s + W_f} \equiv \frac{q_s W_s + q_f W_f}{W_s} = q_s + \frac{W_f}{W_s} q_f \equiv q_s + d_f q_f, \quad (3.15)$$

where  $q_c$  is the composite liquid-phase flux density for the entire column (L/T);  $W_s$ ,  $W_f$ ,  $q_s$ , and  $q_f$  are the widths (L) and flux densities (L/T) for the sand and fault components,

respectively; and  $d_f$  is the fault spatial density (-). Dividing the composite flux density for the faulted domain (3.15) by the composite flux density for the unfaulted domain yields a dimensionless liquid-phase infiltration/exfiltration enhancement factor,  $E$ , which describes how much more liquid-phase water flows through the column because of the presence of the fault:

$$E = \frac{q_c^{faulted}}{q_c^{unfaulted}} = 1 + d_f \frac{q_f}{q_s} \quad (3.16)$$

An enhancement factor value of 1 indicates the fault has no impact whereas a value of 2 indicates the flux through the composite column is twice that through a sand-only column. The composite flux density and enhancement factors were calculated as functions of fault spatial density and either matric potential or depth to water table.

### 3.4 Results

The terms “fault” and “sand” used below refer to faults and sands which have similarly contrasting hydraulic properties as the E10 fault and its parent sand. Poorly lithified, well sorted, eolian and fluvial sands such as those found in the Canyon Trail area are common throughout the Santa Fe Group, which constitutes the major aquifer and vadose zone units for the Albuquerque, Santa Fe, Las Cruces, and El Paso - Juarez metropolitan areas [Hawley, 1978; Connell et al., 1999; Hawley et al., 1995, 2001; Hawley and Kernodle, 2000]. These sands can be expected to have hydraulic properties similar to those measured for the E10 sands if the grain and pore size distributions are

reasonably similar. We believe that other deformation band faults will behave like the E10 fault because most of the faults we have observed macroscopically resemble fault E10.

**3.4.1. Gravity-driven scenario.** The  $K$ - $\psi$  plot in Figure 3.3 shows how the sand and fault hydraulic conductivity and gravity-driven, liquid-phase flux density ( $q_l$ ) vary with matric potential. Below the crossover matric potential,  $\psi_x = -50$  to  $-80$  cm, fault liquid-phase flux density exceeds sand liquid-phase flux density by orders of magnitude [Sigda and Wilson, 2003]. However, as the sand becomes drier, the vapor-phase flux density  $q_v$  becomes increasingly important. Our calculations reveal that the thermal vapor-phase flux density ranges between  $9.0 \times 10^{-4}$  and  $3.0 \times 10^{-3}$  cm/year, depending on the geothermal gradient and ambient moisture content. (We assume that the geothermal-driven upward  $q_v$  is equal in both sand and fault.) Represented by the hatched area in Figure 3.3, this flux density range agrees with the  $1.0 - 3.0 \times 10^{-3}$  cm/year estimated for vapor-phase flux density in other arid vadose zones [Ross, 1984; Scanlon et al., 1997]. Liquid-phase flux density values for the parent sands (DL06 and the mean) intercept the maximum vapor-phase flux density in the range  $-200 \geq \psi \geq -300$  cm and become negligible, relative to vapor-phase movement, if the matric potential drops below  $-400$  cm. Fault  $q_l$  doesn't cross over the vapor-phase flux density  $q_v$  until the matric potential is much lower,  $-1700 \geq \psi \geq -2600$  cm (Figure 3.3), suggesting that water movement in deformation band faults will be dominated by downward liquid-phase movement, even where the surrounding sand is dominated by upward vapor-phase movement.

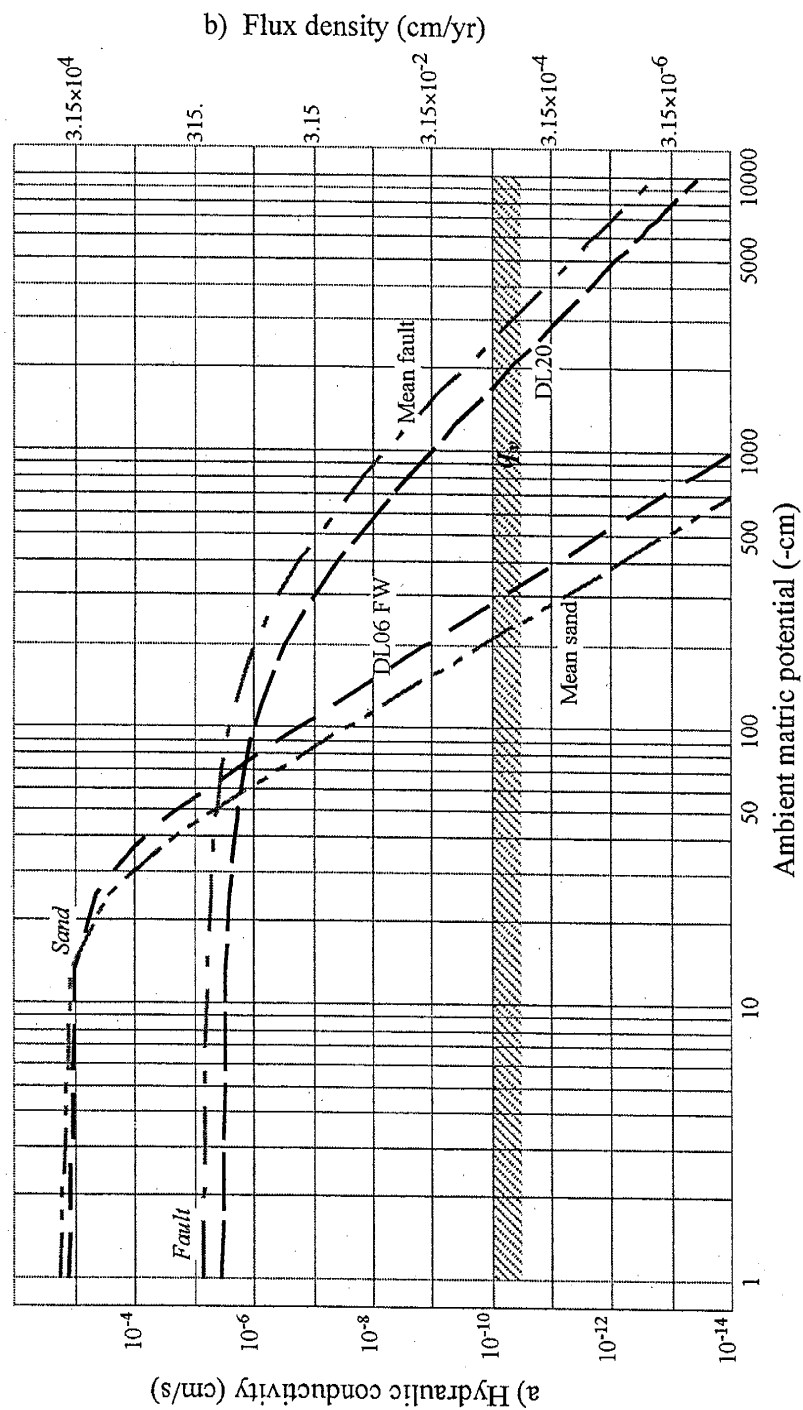


**Figure 3.3:** a)  $K$ - $\psi$  relationships for fault E10 from fitted Mualem-van Genuchten parameters. b) For gravity-driven flow the liquid-phase downward flux density  $q_L(\psi) = K(\psi)$ . The hatched area denotes the ranges of upward thermal vapor flux density,  $q_v$ , estimated for moisture contents and geothermal gradients applicable to Rio Grande rift vadose zones.  $K$ - $\psi$  curves are adapted from Sigda and Wilson [2003].

Advective solute residence times,  $t_a$ , for an  $L = 100$  cm column of sand increase much more rapidly than fault residence times as matric potential decreases (Figure 3.4). At high (wet) matric potentials, sand residence time is much shorter than fault  $t_a$ . Sand and fault residence times are equivalent at the crossover matric potential:  $-50 \geq \psi_x \geq -80$  cm. At  $\psi = -200$  cm, fault  $t_a$  is less than an order of magnitude larger than its value at  $\psi = 0$ , yet sand  $t_a$  becomes five to six orders of magnitude larger over the same interval. Fault diffusion residence time  $t_d$  for a 100 cm column length varies little over the full  $\psi$  range, is relatively insensitive to the choice of MQ or CW model for the effective diffusion coefficient, and is at least an order of magnitude less than diffusion  $t_d$  in sand. In contrast, sand diffusion  $t_d$  changes by roughly two orders of magnitude as  $\psi$  decreases; moreover, the predicted MQ residence time is significantly larger than that predicted by the CW model (Figure 3.4). The dominant mechanism for solute movement through the sand switches from advection to diffusion if the matric potential is less than  $-200$  to  $-400$  cm, depending on the choice of sample and  $D(\theta)$  model, whereas solute advection through the fault is much faster than diffusion until  $\psi$  is between  $-1050$  and  $-1800$  cm (Figure 3.4). Differences between advective and diffusive residence times may actually be somewhat greater as Olesen et al. [1996] have demonstrated that the MQ model overestimates the effective diffusion coefficient by 200 to nearly 400% for several sandy soils and loams with moisture contents between 0.10 and 0.20. Irrespective of the  $D(\theta)$  model chosen for the sand, deformation band faults can provide a significant liquid-phase “fast path” for non-reactive chemicals through the sandy parts of a moderately dry vadose zone, whether

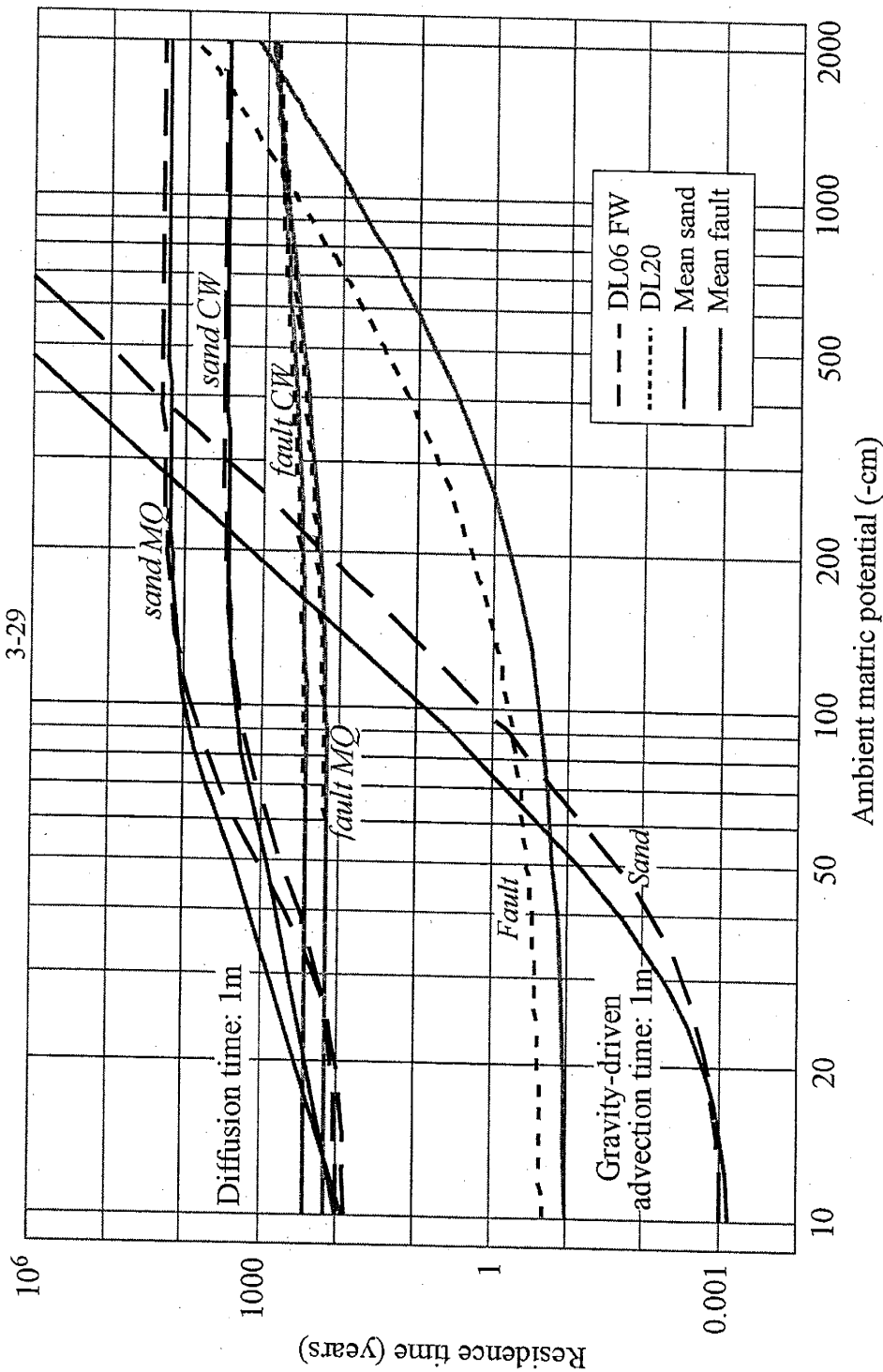


Figure 3.4: Solute residence times for gravity-driven scenario. Advection time curves show residence time,  $t_r$  (years), for a conservative solute to travel 1 m with no dispersion (after Sigda and Wilson [2003]). Diffusion curves give the time,  $t_d$  (years), for the solute concentration located 1 m from a constant source boundary to reach 50% of the source concentration. Two sets of  $t_d$  curves are shown: one set calculated with the Millington-Quirk [1961] approach (MQ) and the other calculated from data from Conca and Wright [1992] (CW). Our proxy for diagenesis, the number of pore volumes passing through a column in a given amount of time, is inversely proportional to the residence time. Thus, number of pore volumes is greater towards the bottom of the graph.

by advection or by diffusion. Our results also indicate fault “fast paths” are more likely to experience more rapid diagenetic change than the sand. When  $\psi = -200$  cm, the fault will advect more than a hundred pore volumes under gravity-driven flow in the time taken to advect a single pore volume through the sand (Figure 3.4).

A faulted sand column can infiltrate significantly more water than an unfaulted sand column under steady gravity-driven conditions even if fault spatial density is smaller than those observed at our study site (Figure 3.5). In unfaulted columns ( $d_f = 0$ ), downward liquid-phase composite flux density  $q_c$  (3.15) abruptly decreases with decreasing  $\psi$ , so that net water flux is downward for  $\psi > -200$  cm and upward for  $\psi < -300$  cm (i.e., upward geothermal-driven  $q_v$  dominates). Faults contribute so little additional downward flux at a spatial density of one 1 cm wide fault in 1 km (1:1km) that net water flux is still upward (Figure 3.5). For this case, the infiltration enhancement factor,  $E$ , (3.16) has a value very close to one (Figure 3.5). Increasing fault spatial density above 1:1 km increases  $q_c$  and  $E$  until net water flux switches from upward to downward. At a fault density of 1:10 m,  $q_c$  exceeds the greater of unfaulted  $q_c$  or upward  $q_v$  by as much as two orders of magnitude for  $-100 > \psi > -500$  cm (Figure 3.5). The sharp increase in  $E$  at this spatial density is caused by the abrupt decrease in sand liquid-phase  $q_b$  relative to fault  $q_b$  as  $\psi$  decreases (Figure 3.3). The 1:4 m fault density reported for the Canyon Trail field site [Herrin, 2001; Sigda and Wilson, 2003] more than doubles the downward liquid-phase  $q_c$  predicted for a 1:10 m fault density, thereby extending net downward water flux across an even wider span of matric potentials (Figure 3.6).

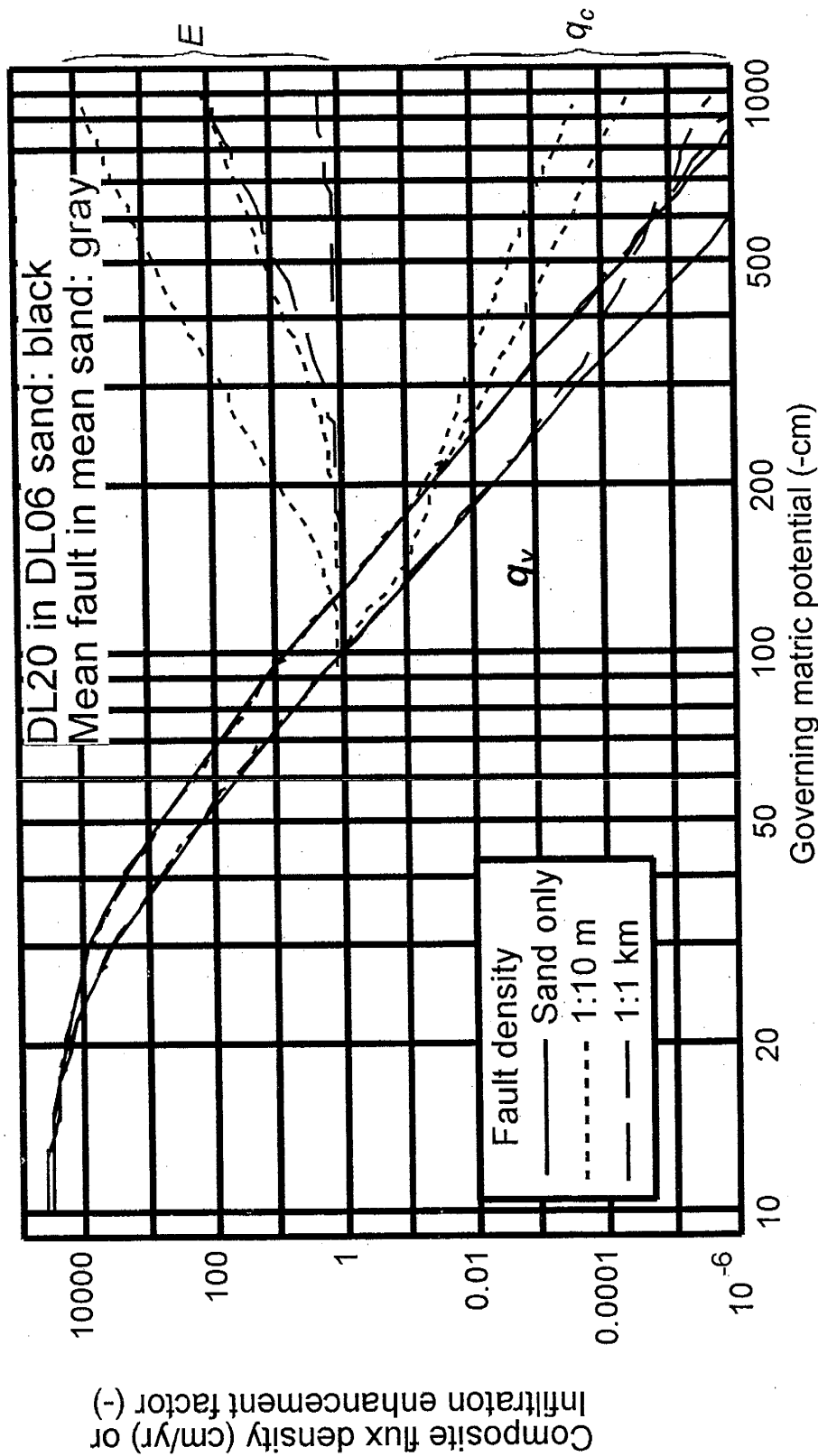
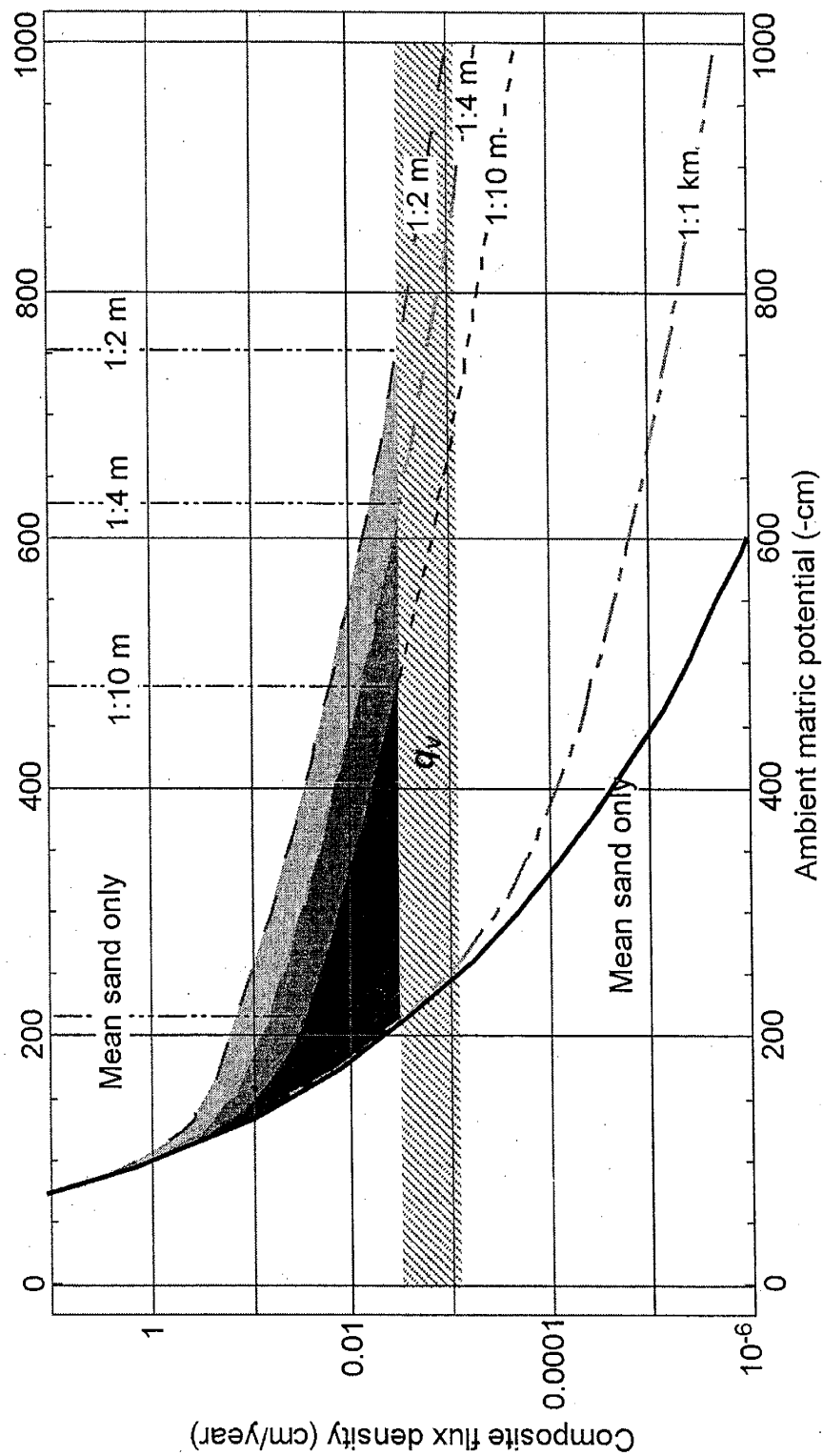


Figure 3.5: Gravity-driven scenario. Downward liquid-phase composite flux density,  $q_c$  (cm/yr), and enhancement factor,  $E$  (-), for 1D model outcrops. Fault density of 1:1 km equals an average of one 1 cm wide fault per 1 km of sand. Sand only curves show  $q_c$  for unfaulted outcrops. Hatched area depicts maximum nonisothermal vapor-phase flux density,  $q_v$ , estimated for Rio Grande rift vadose-zone conditions. The  $q_c$  curves show three different liquid-phase behaviors. For fault density = 1:10 m, 1) flow through the sand dominates the idealized column for  $\psi > -100$  cm, 2) fault flow begins to contribute to the system's total flow for  $-100 > \psi > -200$  cm, and 3) flow through the fault dominates the system for  $-200 > \psi > -500$  cm. Should the vapor-phase flux density  $q_v$  be less than the values estimated in this study, the hatched area would shift downward, significantly increasing fault-enhanced infiltration.



**Figure 3.6:** Composite liquid-phase flux density  $q_c$  for gravity scenario. Gray-shaded areas depict areas of increased infiltration through faulted beds for the mean sand - mean fault case. Mean sand only curves show  $q_c$  for unfaulted outcrops. Hatched area depicts nonisothermal vapor flux density,  $q_v$ . As fault density increases, increased infiltration extends further and further into lower matric potentials. Areas of increased infiltration are arbitrarily truncated at the maximum  $q_v$  value of 0.003 cm/year.

**3.4.2. Evaporation-driven scenario.** Differences between sand and fault liquid-phase flux density,  $q_l$ , are at least as large for evaporation-driven upward flow as for the downward gravity driven case (Figure 3.7). Upward sand and fault flux densities are equivalent at crossover water table depths of  $40 < H_x < 70$  cm, above which fault  $q_l$  decreases much more gradually than sand  $q_l$ . At  $H = 100$  cm, fault  $q_l$  is roughly one to two orders of magnitude greater than sand  $q_l$ , and the disparity widens to two to four orders of magnitude at  $H = 200$  cm (Figure 3.7). Although we have no steady-state estimator for a lower bound (the geothermal-driven vapor flux model is inappropriate for a shallow vadose zone), modeling results by Scanlon and Milly [1994] (their Figure 12) for a site near the Rio Grande river in west Texas yielded a maximum downwards thermal (driven by surface temperature) vapor-phase flux density of  $1.0 \times 10^{-3}$  cm/year and a maximum upwards thermal vapor-phase flux density of  $5.0 \times 10^{-4}$  cm/year, both at a depth of  $\sim 2$  m. Choosing the value of  $10^{-3}$  cm/year as a first cut approximation for downwards thermal vapor-phase  $q_v$  in the shallow vadose zone, we see that the upwards fault  $q_l$  exceeds downwards thermal  $q_v$  by at least two orders of magnitude throughout the entire  $H$  range, whereas sand flux density falls well below thermal  $q_v$  once  $H$  exceeds 200 to 400 cm (Figure 3.7).

First advection, then diffusion, dominates solute transport through sand as water table depth increases, whereas only advection dominates transport through the fault (Figure 3.8). Sand advective solute residence times drop to the order of diffusion residence times for water table depths between 200 and 400 cm (Figure 3.8). Fault advection residence

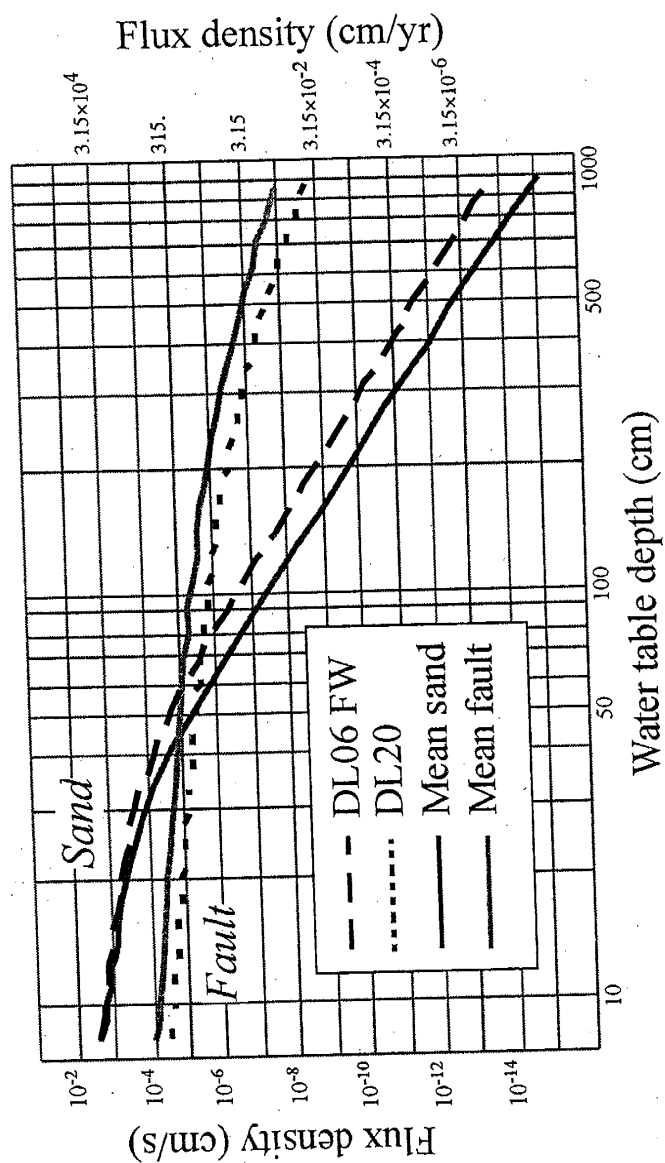


Figure 3.7: Evaporation-driven flow from a shallow water table. Upward liquid-phase flux density,  $q_p$ , is plotted as a function of water table depth for fault and sand.

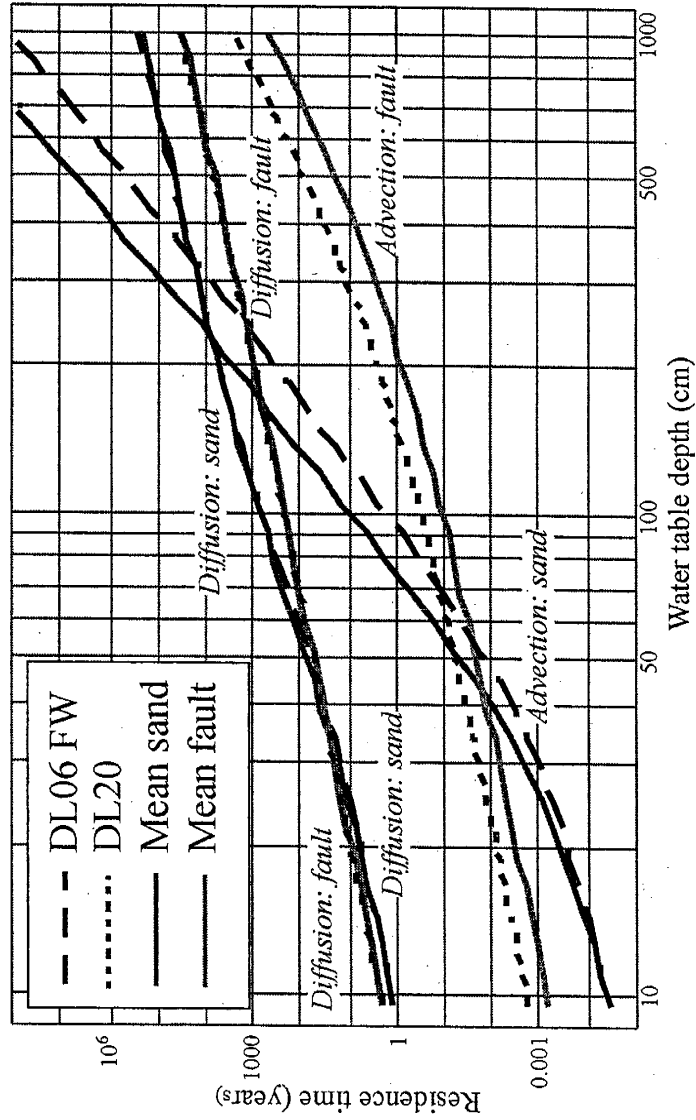


Figure 3.8: Residence time for evaporation-driven solute transport. Advection-only (upward),  $t_r$ , and diffusion-only residence time,  $t_d$ , for fault and sand is shown as a function of water table depth below ground surface. There is little difference between the Millington-Quirk [1961] (MQ) and Conca and Wright [1992] (CW) diffusion-only curves for each material.

times are much shorter than sand advective residence times for water table depths greater than 60-80 cm (Figure 3.8). Thus, a unit cross-sectional area of fault will advect roughly a thousand pore volumes upwards through a 300 cm column in the ten thousand years required to diffusively transport a single pore volume through a sand column of the same dimensions, given a steady water table position.

Faulted sand beds can significantly increase net exfiltration of water upward from the water table, relative to an unfaulted sand bed, if fault spatial density  $> 1:1$  km and  $H > 100$  cm (Figure 3.9). As with the gravity scenario, estimates of the liquid-phase exfiltration enhancement factor,  $E$ , increase very rapidly with water table depth because sand flux density diminishes at a far faster rate than fault flux density (Figure 3.9).

### 3.5. Discussion

As climate conditions change from wet to dry, flow and transport shifts from sand (distributed fluxes) to the fault (focused fluxes). Enhanced fault fluxes are persistent for conditions that aren't so wet that flow and transport processes in sand dominate, or so dry that competing vapor-phase processes dominate both fault and sand. In answer to our first research question this demonstrates that faults can be hydrologically significant within arid and semi-arid vadose zones. By predicting how the dominant processes change in each material as governing conditions vary, our conceptual model provides a useful first cut answer to our second research question about the conditions necessary for accelerating flow and transport through vadose-zone faults.

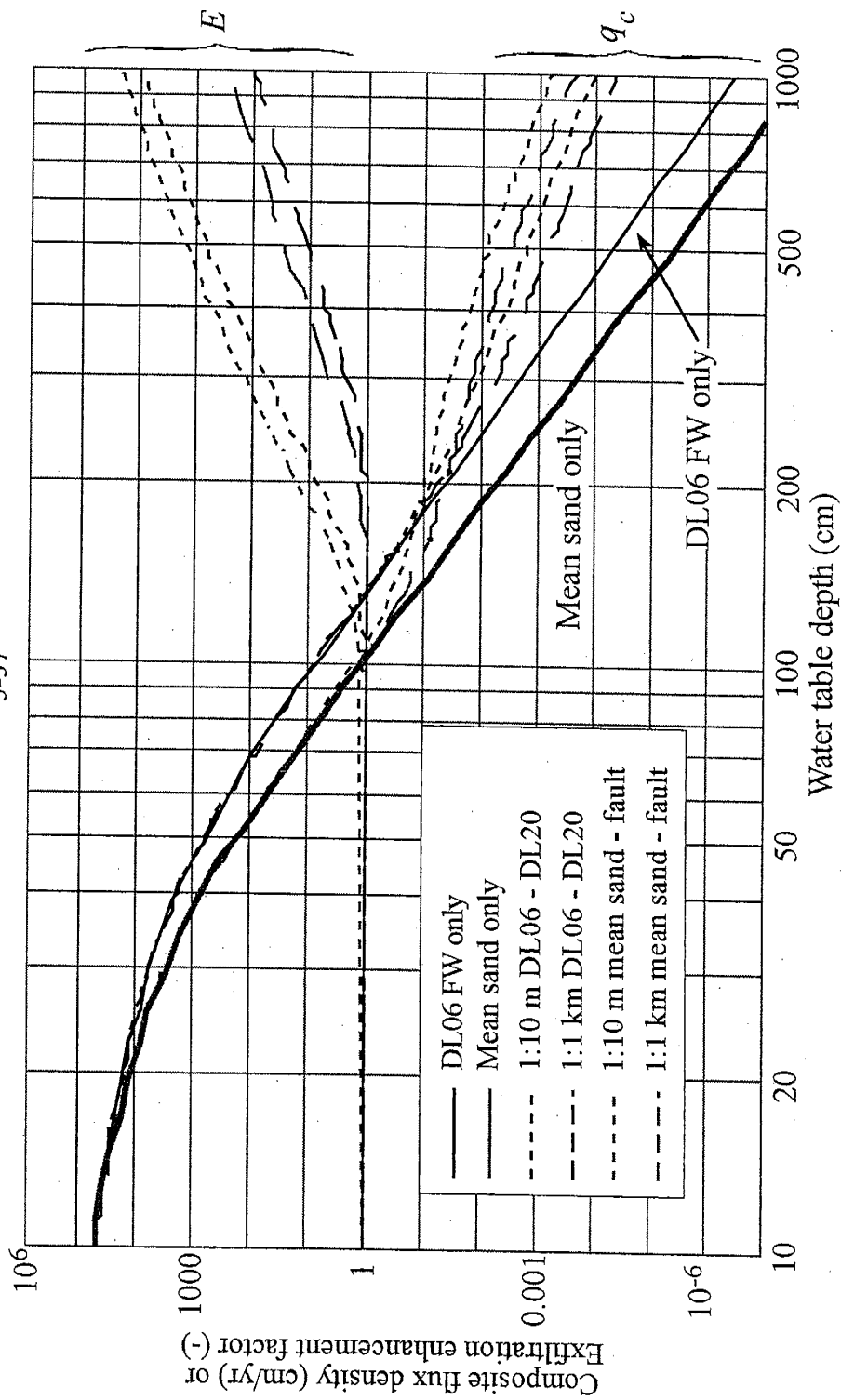


Figure 3.9: Fault density and evaporation-driven flow. Liquid-phase composite density,  $q_c$ , for 1D model outcrops is shown as a function of water table depth and fault spatial density. DL06 and mean sand curves show  $q_c$  for unfaulted outcrops. Liquid-phase exfiltration enhancement factor ( $E$ ) curves describe the proportional increase in liquid-phase  $q_c$  for faulted outcrops relative to unfaulted outcrops:  $E = 1$  shows no increase and  $E = 10$  shows a 10-fold increase.

Our results reveal two significant transitions that are critical to understanding and comparing sand and fault hydraulic behavior. The first transition is the crossover point, which is the value of the governing variable ( $\psi_x$  for matric potential and  $H_x$  for water table depth) at which the two materials have equivalent liquid-phase flow or transport fluxes. The second transition occurs where a new set of flow or transport processes overtakes in magnitude or significance the previously dominant set of processes. This “dominance threshold” has a value appropriate to each material and pair of processes. For example, downward advective liquid-phase water flow dominates all other flow processes in sand under relatively wet gravity-driven flow conditions, but at some lower matric potential value the sand’s liquid-phase flux is so small that it equals the estimated maximum geothermal-driven, upward vapor-phase flux. The dominance threshold for vapor-phase flow in the sand is thus this matric potential value because vapor-phase flow dominates liquid-phase flow for sand beds under drier conditions (lower  $\psi$ ). Similarly, dominance by advective solute transport in the same sand will give way to dominance by diffusive solute transport if the sand is sufficiently dry. The relative positions of sand and fault transition points, both crossover points and dominance thresholds, determine preferential flow and transport through a faulted sand bed.

Results for poorly lithified sands show that the shift in dominant flow and transport processes occurs at relatively wet conditions. Under the gravity-driven scenario, advective processes dominate flow and transport in sand for high matric potential values ( $\psi$  near 0 cm). Dominance by steady, downward, advective liquid-phase water flux ( $q_l$ )

gives way to dominance by upward, vapor-phase water movement ( $q_v$ ), and advective solute transport gives way to diffusion, when the governing matric potential is less than -200 to -300 cm. This, then, is the dominance threshold for both geothermal-driven vapor-phase flow and diffusive transport for sand under the gravity-driven flow scenario. A similar pattern is observed for the evaporation-driven flow scenario: liquid-phase advection through the sand upwards from a shallow water table dominates in relatively wet conditions ( $H$  small). The decrease in upwards advection with increasing  $H$  shifts the dominant water flow process from liquid-phase advection to thermal vapor-phase flow between water table depths of 200 and 400 cm, using Scanlon and Milly's [1994]  $q_v$  estimate. The dominance threshold for diffusive solute transport occurs around the same water table depth. Thus, when vadose-zone sand beds are stressed by a thermal gradient and are so dry that diffusion controls solute transport, water movement in the vapor-phase also dominates that in the liquid-phase. Our sand model predictions agree with previous studies that have shown liquid-phase flow and transport through sandy beds is very small under relatively dry vadose zone conditions [Winograd, 1981; Scanlon et al., 1997; Walvoord et al., 2002].

The dominant flow and transport processes in faults, on the other hand, shift at much drier conditions than those in sand. Faults in a gravity-driven flow scenario are predicted to have a dominance threshold of  $-1700 > \psi > -2600$  cm for geothermal-driven vapor-phase flow and  $-1050 > \psi > -1800$  cm for solute transport by diffusion. Under the evaporation-driven scenario, advective liquid-phase processes remain dominant over

thermal vapor-phase flow and diffusion-driven solute transport processes across the entire range of water table depths considered. (Again, we have assumed that thermal fluxes through faults and sands are not significantly different.) The dominance thresholds for these competing processes within the fault evaporation-driven scenario occur at conditions far drier than those examined in this study.

Directly comparing fault and sand behavior reveals conditions for preferential flow and transport through a deformation band fault, beginning at the crossover point and ending at the point where some other competing process dominates at lower matric potentials. We first consider solute transport. Whether by advection or diffusion, solute transport is always more rapid within faults than in sands if the governing variable has a drier value than its crossover points for both gravity- and evaporation-driven flow scenarios. For either flow or solute transport, these crossover points fall within  $-50 > \psi > -70$  cm for the gravity-driven flow scenario and within  $40 > H > 80$  cm for the evaporation-driven scenario. The diffusion dominance thresholds for faults,  $-1050 > \psi > -1800$  cm for the gravity-driven scenario and approximately  $2000 < H < 3000$  cm for the evaporation-driven scenario, are found in far drier conditions than the same thresholds for sand, increasing the likelihood that much more solute will be transported through faults than sands. Diffusive solute flux through the fault remains roughly an order of magnitude more rapid than sand solute flux for the governing variable ranges considered (Figures 3.4 and 3.8). Whether by advection or diffusion, contaminants could short-circuit sand beds which have been usually regarded as effective obstacles to solute transport through arid

and semi-arid vadose zones. For example, at  $\psi = -200$  cm under steady gravity-driven flow, a solute could advectively break through a 1 m thick sand bed containing one or more faults in roughly 7 months to 2 years, compared with the 150 to 1400 years needed to advectively break through an unfaulted sand bed. The disparity persists for lower matric potentials: at  $\psi = -1000$  cm, fault solute advective breakthrough requires 70 - 400 years, rather than the 17,000 - 21,000 years needed to diffusively break through the unfaulted sand bed.

Such large differences in solute residence times create large disparities in the rate and amount of diagenesis in vadose zone sands and faults. The number of pore volumes passed through a sand diminishes sharply, as conditions change from wetter to drier, compared to a much more gradual decline in faults. In the gravity-driven flow scenario the ratio of the number of fault pore volumes, per sand pore volume, ranges from several hundred to several thousand, depending on the  $D(\theta)$  model (Figure 3.10). The ratio is even greater for the evaporation-driven scenario: from several thousand to several tens of thousands (Figure 3.10). The maximum ratios occur at matric potentials between  $-300 < \psi < -500$  cm and at water table depths between  $200 < H < 300$  cm. Even under the driest conditions considered, between  $\sim 10$  to several thousand pore volumes pass through a fault in the time needed to pass a single pore volume through the same amount of sand. These processes may be responsible for the cementation of faults observed in the Rio Grande rift (Figure 3.1a), leading to the formation of the “fault-fin” landscapes [Davis, 1998] such as those in Figure 3.1a.

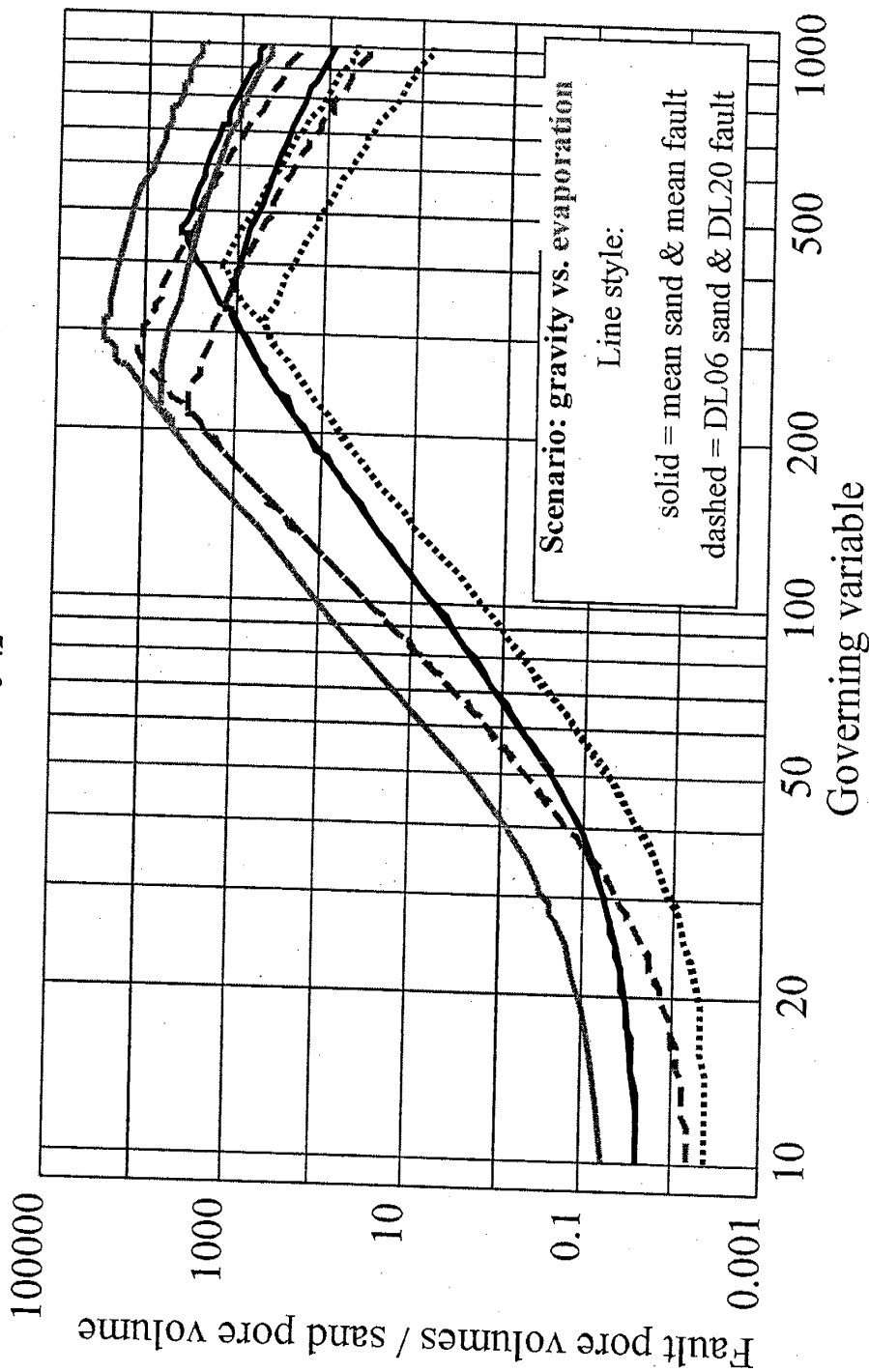


Figure 3.10: Number of fault pore volumes per sand pore volume. Gravity-driven scenario curves (black) are plotted versus governing matrix potential (-cm). Evaporation-driven curves (gray) are plotted versus governing depth to water table (cm).

However, this cementation of vadose-zone faults should not be confused with the saturated-zone cementation of faults also observed in the Rio Grande rift [Mozley and Goodwin, 1995; Heynekamp et al., 1999].

Several field tests of the preferential flow and transport behavior predicted for faults are possible. Assuming samples can be recovered from depth, stable isotope tracers collected from deformation band faults and poorly lithified sands should differ significantly under steady gravity-driven flow, if the tracers are specific to liquid-phase water movement. Calcite cementation textures and distributions within and adjacent to faults could also potentially reflect the expected disparities in saturation.

Fault “fast path” flow behavior requires fault liquid-phase flow  $q_l$  to substantially exceed both sand  $q_s$  and the competing vapor-phase flow  $q_v$ . In a direct comparison of sand and fault fluxes, preferential flow occurs in the fault at governing variable values between the crossover point and the dominance threshold, estimated for thermal vapor-phase flow in the fault, under both gravity- and evaporation-driven flow scenarios (Figures 3.3-4 and 3.7-8). Taking the gravity-driven flow scenario as an example, preferential flow occurs at matric potentials within the range  $-50 > \psi > -2600$  cm, where -50 cm is the  $\psi_x$  upper limit and -2600 cm is the dominance threshold lower limit for upward vapor-phase flow in the fault. Liquid-phase flow through the fault dominates in this range because it exceeds sand or competing fault fluxes by one to four orders of magnitude (Figure 3.3).

Upscaling to incorporate fault spatial density into our flow model demonstrates that fault preferential flow remains important for observed fault densities and vadose conditions. Volumetrically, faults constitute much less of the vadose zone than the dominance threshold shifts to wetter conditions whereas the crossover point (area-weighted average of sand and fault flux densities) effectively shifts to drier conditions, narrowing the range of conditions for which fault liquid-phase flow is important to, say, recharge or discharge. Although we did not plot them, the positions of the effective crossover points for the composite columns can be inferred from the composite flux density plots by looking for the governing variable value at which the faulted sand bed first deviates from the  $q_c$  curve for a sand-only column (Figure 3.9). Alternatively, we define net flux ( $N$ ) as the difference between composite flux density ( $q_c$ ) for the faulted domain and the larger of unfaulted  $q_c$  and vapor-phase

$$N = |q_c^{\text{faulted}}| - \max(|q_c^{\text{unfaulted}}|, |q_v|) \quad .$$

For gravity-driven flow through a faulted sand bed, positive net flux can be represented as the filled areas in Figure 3.6, which increase in size (width and height) with increasing fault spatial density. The maximum net flux, regardless of fault spatial density, occurs at the dominance threshold for geothermal-driven vapor-phase flow in unfaulted sand,  $\psi = -212.3$  cm for a system with mean sand – mean fault properties (Figure 3.6). For a given fault density, the dominance threshold for vapor-phase flow in the faulted domain, marking the onset of positive net flux, occurs at progressively drier  $\psi$  values as fault density increases.

crossover point for faulted and unfaulted  $q_c$  moves further into wetter conditions with increasing fault density. Thus, for a system with mean sand and mean fault properties, the matric potential range for positive net flux is  $-102 < \psi < -487$  cm at 1:10 m,  $-89 < \psi < -630$  cm at 1:4 m, and  $-80 < \psi < -755$  cm at 1:2 m (Figure 3.6). Whereas maximum net flux scales roughly linearly with fault density (3.15), the matric potential span within which net flux is possible does not. Note that positive net flux and its associated matric potential span are still significant for a DL06 sand - DL20 fault system that has the least difference in measured hydraulic properties, but with smaller magnitudes than a mean sand – mean fault system (Figure 3.5). Deformation band faults can shift net water flux from upward to downward in arid-like vadose zone sands under gravity-driven flow conditions given fault densities observed in the middle Rio Grande rift, and can therefore promote greater liquid-phase infiltration under far drier conditions than can be expected from unfaulted sand beds.

Evaporation-driven exfiltration from a faulted sand bed requires a lower fault spatial density to significantly enhance water flux than does gravity-driven infiltration. The minimum fault density for significantly enhanced exfiltration is less than 1:1 km, whereas positive net flux for infiltration does not begin until the fault density is  $\sim 1:10$  m (Figures 3.5 and 3.9). At a fault density of 1:10 m, maximum upward  $q_c$  through a faulted domain is 60-70 times larger than either thermal  $q_v$  or liquid-phase  $q_c$  for an unfaulted domain, compared to only 10 times for similar comparisons with the gravity-driven flow scenario (Figures 3.6 and 3.9). Exfiltration through deformation band faults is thus likely to be

hydrologically significant where the water table is between 1 and 9 m from the surface at fault densities of 1:1 km and greater, densities which we personally have observed in the middle Rio Grande rift.

The transition points (dominance thresholds) to transport dominated by diffusion from that dominated by advection depend on the conceptual model's definition of breakthrough. In our model, advective breakthrough is velocity-based, not concentration dependent, whereas diffusive breakthrough is signified by our arbitrary choice of  $0.5 * C_0$  for the breakthrough concentration. No single value of diffusive breakthrough concentration is appropriate for all needs, thus, the position of a diffusion dominance threshold within the range of governing variable considered will vary with the selected value. For example, choosing  $0.9 * C_0$  (i.e., concentration at the point of interest is 90% of the source concentration) as the breakthrough concentration shifts all diffusion residence time curves upwards by a factor of roughly 25 (or a little over one log cycle on Figures 3.4 and 3.8). This causes each diffusion dominance threshold to shift into drier conditions, yet widens the disparity between fault and sand residence times by over an order of magnitude. Choosing a proportion less than  $C_0 / 2$  instead shifts the diffusion dominance thresholds into wetter conditions, but still maintains a significant difference between fault and sand residence times. In all cases, faults act as fast paths for solute transport across some significant span of governing variable values.

The predicted differences in solute residence time could also be affected by transport processes not included in our conceptual model, particularly differences in retardation and dispersivity between fault and parent sand. The clay size fraction, which may contain clay minerals in addition to clay-sized feldspar, quartz, and lithic fragments, occupies 5% of the sand volume and 30% of fault volume at the Canyon Trail field site [Herrin, 2001] and at other fault sites in the Rio Grande rift [Sigda et al., 1999]. A fault's relatively greater clay-size fraction could retard progress of a reactive chemical (e.g., through sorption), depending on the chemistry of solute and matrix, thereby increasing the effective solute residence time. Dispersivity for transport through partially saturated media is primarily controlled by moisture content, pore size distribution, and the tortuosity of interconnected water filled pores, films, and pendular rings. Sand dispersivity can be expected to abruptly decrease for matric potential values  $< -50$  cm until reaching residual moisture content, leaving water distributed in poorly interconnected films and pendular rings. In contrast, fault dispersivity should change much less over the same matric potential range because fault moisture content changes less abruptly with matric potential than sand  $\theta$ . Both the realignment of elongate grains from parallel-to-bedding to parallel-to-dip during formation of deformation band faults, and the sub-vertical continuity of the fault clay-size fraction (gouge or cataclasite) within the elongate pores, [Goodwin and Tikoff, 2002; Sigda et al., 1999; Herrin, 2001] suggest that fault dispersivity is likely to be highly anisotropic.

Despite its simplistic fault arrangement, our conceptual model can be extended to other faults dips and widths, albeit with some caveats. By limiting fault dip to  $90^\circ$ , the conceptual model overestimates liquid-phase flux density and underestimates solute residence time for less steeply dipping faults. Nearly all of the deformation band faults we have observed in the Rio Grande rift have dips between  $55^\circ$  and  $90^\circ$ . Model estimates can be easily corrected for less steeply dipping faults by multiplying (dividing) by the sine of the dip for flux density (residence time). Corrected flux density values for the observed dip range would then equal 82 to 91% of the model's estimated value. Fault width can vary along both dip and strike for a given fault as the zone of deformation bands widens, narrows, or splays [Herrin, 2001]. Zones of deformation bands reach widths of 10 to 20 cm in other Canyon Trail faults [Herrin, 2001] and 50 cm in some large displacement faults (Figure 3.1b). Accommodating different fault widths requires redefining fault density to equal the ratio of total fault width to total column width, so a 50 cm wide fault every kilometer gives a fault density of  $5 \times 10^{-4}$ . This correction assumes that zones with more diffusely distributed deformation bands have hydraulic properties similar to those used in this study, i.e., those for a narrow zone of deformation bands. "Diffuse" zones of deformation bands as well as individual deformation bands likely possess similar hydraulic properties because they were formed by the same processes of cataclasis and shear-induced compaction, but this hypothesis must be tested. A more complete analysis of the effects of fault dip and architecture on unsaturated hydraulic behavior requires two-dimensional numerical modeling, which could also be

used to test whether deformation band faults can enable preferential infiltration and solute transport through sand beds which are wetter ( $\psi$  nearer to zero) than the crossover  $\psi$  value. With a lower  $K$  than the surrounding sand, a fault could form an extensive dipping catchment that intercepts and concentrates infiltrating liquid-phase water along its hanging wall contact. Though similar to the “funnel-flow” observed by Kung [1990a,b] along the top of an inclined coarse sand bed, fault catchment flow behavior would depend only on a sharp contrast in hydraulic conductivity, not water entry pressure (i.e., capillary barrier behavior).

Observations of preferential flow and transport through the vadose zone have previously been limited to macropores, gravity fingers [Hillel, 1998; Selker et al., 1999], and funnel flow [Kung, 1990ab, 1993]. Neither macropore nor fingering flow appropriately describe the preferential flow and transport predicted here for deformation band faults. Like preferential flow through a macropore network, preferential infiltration through a fault is driven by gravity and abetted by the large difference between the hydraulic conductivities of the structure and its surrounding matrix. Deformation band faults, however, are far richer in micropores and much poorer in macropores than the surrounding protolith. Furthermore, macropore flow through arid and semi-arid vadose zones is a transient phenomenon limited to rapid saturation or positive water pressures at the upper boundary, unlike the steady preferential flow - upward or downward - through faults described in this paper. Preferential flow through gravity fingers appears to be able to persist for years or decades [Selker et al., 1999], but the agents (hydrophobicity, air

pressure gradients, wetting – drying history, etc.) thought to cause fingering do not cause the fault fluxes described here. Because it also depends on contrasts in capillarity and thus hydraulic conductivity, the funnel flow observed by Kung [1990ab, 1993] along the contact between an inclined coarse-grained sand lens and a finer-grained matrix bears some resemblance to the preferential flow and transport predicted here for faults. Funnel flow, however, would not occur for a vertically oriented coarse lens, is solely limited to downward movement, and can be self-limiting as continued interception of liquid-phase water along the contact will eventually reach a matric potential sufficiently large to allow breakthrough into the coarse lens. Preferential flow and transport through deformation band faults can be either upward or downward (depending on the boundary conditions), can occur in vertical and sub-vertical faults, and is not self-limiting. We believe the key is that both phenomena are created by a crosscutting feature or structure which possesses a markedly different  $K(\psi)$  function than the surrounding matrix. Although the definition of “funnel flow” could be expanded to include enhanced fluxes through faults in poorly lithified sands, another term which more clearly identifies causation for a more general class of phenomena may be more appropriate.

We propose to call the category of preferential flow and transport phenomena driven by heterogeneities in capillarity, “capillary wicking”. This emphasizes the causal role of differences in fault and protolith capillarity. Although small-scale (centimeter to meter) sedimentary features such as flame, pillow, and ball structures (see pages 163-166 in Boggs [1987]) may behave similarly to fault capillary wicks, it is likely that the larger-

scale structures such as deformation band faults, clastic dikes, or slump structures from syn-sedimentary folding and faulting will prove to be more hydrologically important.

### 3.6. Conclusions

Substantial vadose-zone preferential flow and solute transport occurs within deformation band faults, thin tabular extensive zones of reduced grain and pore sizes, under the relatively dry conditions of arid and semi-arid areas. As conditions become drier, unsaturated hydraulic conductivity, flux density and seepage velocity switch from being far greater in the poorly lithified parent sand to being far greater in the fault. This pattern was observed for a scenario with steady, one-dimensional, gravity-driven downwards flow in which matric potential  $\psi$  is the governing variable, as well as an evaporation-driven scenario in which water table depth  $H$  governs the steady flux upwards from a shallow water table to the ground surface. Flux density and seepage velocity are at least two orders of magnitude larger in sand than in a fault for governing variable values nearest to saturation ( $\psi$  or  $H$  near 0); however, flux rates drop far faster in sand than in the fault as the governing variables become drier ( $\psi$  decreasing or  $H$  increasing), so that fault and sand fluxes are equivalent at some point (crossover point:  $\psi = \psi_x$  or  $H = H_x$ ), and under still drier conditions fault fluxes exceed sand fluxes by two to five orders of magnitude ( $\psi < \psi_x$  or  $H > H_x$ ).

Preferential flow and transport through faulted sand beds depends on the specific flow and transport processes active in the system, fault and sand hydraulic properties, and the relative proportions of sand and fault. Two transitions are important indicators of which materials and which processes dominate water or solute fluxes. Between these transitions flow and transport is dominated by liquid-phase water flow and solute advection in the fault. At the wet end is the crossover point, where fluxes through fault and sand are equal. For conditions wetter than the crossover point, the sand is more important. At the dry end is a dominance threshold, where a competing flow or transport process begins to take over, e.g., vapor-phase water flux or diffusive solute transport. In between the crossover point and the vapor-phase flux threshold, flow through faults exceeds that through sand by two or more orders of magnitude. Upscaling to a zone of faults, the faults begin to quantitatively effect infiltration through a deep vadose zone at fault spatial densities of one 1 cm wide fault per 10 m, and begin to affect exfiltration from a shallow water table at only one fault per 1000 m.

Even where water movement in the parent sand is dominated by vapor-phase transport, faults can have a significant liquid-phase movement in the other direction. Observed fault densities and matric potentials in the basins of the Rio Grande rift are sufficient to switch upward vapor movement to locally downward liquid-phase infiltration. In areas with shallow water tables up to 10 m below ground level, rift fault densities are more than sufficient to significantly enhance local liquid-phase exfiltration. Faults also act as fast paths for contaminants and other solutes under both gravity-driven

and evaporation-driven scenarios. Residence times for a non-reactive solute are many orders of magnitude shorter in faults than sand, potentially causing much earlier breakthrough in a sand bed than would be otherwise expected. The dominance threshold for diffusive transport (diffusive transport begins to dominate advective transport) lies in much wetter conditions for sands than faults, enabling advective transport to persist in a fault for a much larger range of governing conditions than the sand. Fault diffusive residence times are roughly one to two orders of magnitude less than those for sand. Faults are expected to be loci for much more rapid diagenesis than sands by transmitting as many as  $10^4$  pore volumes in the time required to transmit a single pore volume through an equivalent length of parent sand.

We propose the term “capillary wicking” as a new category of preferential flow and transport to describe the behavior we predict for cross-cutting deformation band faults in poorly lithified sands. Our predictions of preferential flow and transport by capillary wicking through deformation band faults demonstrates that deformation band faults can have significant impacts on vadose zone hydrology in the Rio Grande rift and other semi-arid and arid areas.

**Acknowledgements.** The National Science Foundation’s Hydrologic Sciences Program funded this study, grant number EAR-9614385. Support from the American Geophysical Union’s Horton Grant is also gratefully acknowledged. We thank our fellow members of New Mexico Tech’s Faults and Fluid Flow group, Laurel Goodwin, Peter

Mozley, Bill Haneberg, Matt Herrin, and Geoff Rawling; Bob Glass of Sandia National Laboratories; and Bob Holt of the University of Mississippi for planting the seed of the exfiltration modeling method.

### 3.7 References

- Affek, H. P., D. Ronen, and D. Yakir, Production of CO<sub>2</sub> in the capillary fringe of a deep phreatic aquifer, *Water Resour. Res.*, 34, 989-996, 1998.
- Antonellini, M. and A. Aydin, Effect of faulting on fluid flow in porous sandstones: petrophysical properties, *AAPG Bulletin*, 78, 355-377, 1994.
- Aydin, A., Small faults formed as deformation bands in sandstone, *Pure and Applied Geophysics*, 116, 913-930, 1978.
- Boggs, S., *Principles of Sedimentology and Stratigraphy*, Macmillan Publishing Co., New York, NY, 784 pages, 1987.
- Brainard, J. R., Glass, R. J., Alumbaugh D. L., Paprocki, L., Labrecque, D. J., Yang, X., Yeh, T.-C. J., Baker, K. E., and Rautman, C. A., The Sandia-Tech Vadose Zone Facility experimental design and data report of a constant flux infiltration experiment, publication in progress, Sandia National Laboratories, Albuquerque, New Mexico, 2002.
- Brainard, J. R., Vadose zone flow processes in heterogeneous alluvial fan deposits: experimental design, data evaluation, and error analysis, M.S. (Geology), University of New Mexico, Albuquerque, New Mexico, 1997.

- Caine, J.S., J.P. Evans, and C.B. Forster, Fault zone architecture and permeability structure, *Geology*, 24, 1025-1028, 1996.
- Carter K.E. and C.L. Winter, Fractal nature and scaling of normal faults in the Espanola Basin, Rio Grande rift, New Mexico: Implications for fault growth and brittle strain, *J. Struct. Geol.*, 17, 863-873, 1995.
- Cashman, S. and K. Cashman, Cataclasis and deformation-band formation in unconsolidated marine terrace sand, Humboldt County, California, *Geology*, 28, 111-114, 2000.
- Conca, J. L. and J. V. Wright, Flow and diffusion in unsaturated gravel, soil and whole rock, *Applied Hydrogeology*, 1, 5-24, 1992.
- Connell, S.D., Koning, D.J., and Cather, S.M., Revisions to the stratigraphic nomenclature of the Santa Fe Group, northwestern Albuquerque Basin, New Mexico: New Mexico Geological Society Guidebook, 50<sup>th</sup> Field Conference, p. 337-353, 1999.
- Crank, J., *The Mathematics of Diffusion*, 2nd edition, Oxford University Press, Oxford, UK, 414 pages, 1975.
- Davis, G. H., Fault-fin landscape, *Geological Magazine*, 135, 283-286, 1998.
- Davis, J. M., R. C. Lohmann, F.M. Phillips, J.L. Wilson, and D. W. Love, Architecture of the Sierra Ladrones Formation, central New Mexico: depositional controls on the permeability correlation structure, *Geological Society of America Bulletin*, 105, 998-1007, 1993.

- Edwards, H. E., A.D. Becker, and J.A. Howell, Compartmentalization of an eolian sandstone by structural heterogeneities: Permo-Triassic Hopeman Sandstone, Moray Firth, Scotland, in *Characterization of Fluvial and Aeolian Reservoirs*, edited by C. P. North and D. J. Prosser, Geologic Society (UK), London, pages 339-365, 1993.
- Fischer, U., B. Kulli, and H. Fuhler, Constitutive relationships and pore structure of undisturbed fracture zone samples with cohesionless fault gouge layers, *Water Resour. Res.*, 34, 1695-1702, 1998.
- Fowles, J. and S. Burley, Textural and permeability characteristics of faulted, high porosity sandstones, *Mar. Petrol. Geol.*, 11, 608-623, 1994.
- Gardner, W. R., Some steady state solutions of the unsaturated moisture flow equation with application to evaporation from a water table, *Soil Science*, 85, 228-232, 1958.
- Goodwin, L.B. and B. Tikoff, Competency contrast, kinematics, and the development of foliations and lineations in the crust, *J. Struct. Geol.*, 24, 1065-1085, 2002.
- Grauch, V. J., High-resolution aeromagnetic data, a new tool for mapping intrabasinal faults: Example from the Albuquerque basin, New Mexico, *Geology*, 29, 367-370, 2001.
- Hawley, J. W., compiler, *Guidebook to Rio Grande Rift in New Mexico and Colorado*, New Mexico Bureau of Mines and Mineral Resources, Socorro, New Mexico, 1978.
- Hawley, J.W. and Kernodle, J.M., Overview of the hydrogeology and geohydrology of the northern Rio Grande basin—Colorado, New Mexico, and Texas, in Ortega-Klett, C.T., ed., *Proceedings of the 44<sup>th</sup> Annual New Mexico Water Conference*: New

Mexico Water Resources Research Institute Report 312, 79-102, 2000.

<http://wrri.nmsu.edu/publish/watcon/proc/proc44/contents.html>

Hawley, J. W., Haase, C. S., and Lozinsky, R. P., An underground view of the Albuquerque Basin, New Mexico, *in* Ortega-Klett, C. T., ed., Proceedings Annual New Mexico Water Conference, New Mexico Water Resource Research Institute Report 290, 37-55, 1995.

Hawley, J.W., Kennedy, J.F., Creel, B.J., The Mesilla Basin aquifer system in Mexico, West Texas and Chihuahua—an overview of its hydrogeologic framework and related aspects of groundwater flow and chemistry, *in* Angle, E.S., and Moore, J.C., eds., Mesilla Basin Aquifers of West Texas: Texas Water Development Board Special Conference Proceedings Volume, 76-99, 2001.

<http://www.twdb.state.tx.us/publications/reports/GroundWaterReports/individual%20Report%20htm%20files/Report%20356.htm>

Herrin, J. M., Characteristics of deformation bands in poorly lithified sand: Rio Grande rift, New Mexico, M.S. (Geology), New Mexico Institute of Mining and Technology, Socorro, New Mexico, 2001.

Heynekamp, M. R., L.B. Goodwin, P.S. Mozley, and W.C. Haneberg, Correlation of fault-zone architecture in poorly lithified sediments, Rio Grande Rift, New Mexico: implications for fault-zone permeability and fluid flow, *in* *Faults and fluid flow in the shallow crust*, W. C. Haneberg, P.S. Mozley, J.C. Moore, and

- Goodwin, eds., *American Geophysical Union Monograph* 113, Washington, DC, US, pages 27-49, 1999.
- Hillel, D., *Environmental Soil Physics*, Academic Press, San Diego, CA, 771 p., 1998.
- Hong, Sung-ho, Anisotropic hydraulic conductivity of faulted poorly consolidated eolian sands: Bosque, New Mexico, M.S. (Geology), New Mexico Institute of Mining and Technology, Socorro, New Mexico, 1999.
- Irmay, S., Solutions of the non-linear diffusion equation with a gravity term in hydrology, H. W. Rijtema and P. E. Wassink, editors, In Symposium on Water in the Unsaturated Zone, International Association of Scientific Hydrology-UNESCO, 1966, Wageningen, Netherlands, 1968.
- Kelley, V.C., Geology of Albuquerque Basin, New Mexico, Memoir 33, New Mexico Bureau of Mines and Mineral Resources, Socorro, NM, 60 pages, 1977.
- Kung, K-J.S., Preferential flow in a sandy vadose zone. 1. Field observation, *Geoderma*, 46, 51-58, 1990.
- Kung, K-J.S., Preferential flow in a sandy vadose zone. 2. Mechanism and implications, *Geoderma*, 46, 59-71, 1990.
- Kung, K-J.S., Laboratory observation of funnel flow mechanism and its influence on solute transport, *J. Environmental Quality*, 22, 91-102, 1993.
- Mattson, E.D. Field simulation of waste impoundment seepage in the vadose zone: Experiment design in two dimensional modeling, M.S. (Hydrology) thesis, New Mexico Institute of Mining and Technology, Socorro, New Mexico, 213 pages, 1989.

- McCord, J. T., D. B. Stephens, and John L. Wilson. 1991. Hysteresis and state-dependent anisotropy in modeling unsaturated hillslope hydrologic processes. *Water Resour. Res.* 27:1501-1518.
- McCord, J. T. and D. B. Stephens, Lateral moisture flow beneath a sandy hillslope without an apparent impeding layer, *Hydrological Processes*, 1, 225-238, 1987.
- Millington, R.J. and J.P. Quirk, Permeability of porous solids, *Trans. Faraday Soc.*, 57, 1200-1207, 1961.
- Mozley, P. S., and L. B. Goodwin, Patterns of cementation along a Cenozoic normal fault: A record of paleoflow orientations, *Geology*, 23, 539-542, 1995.
- Mozley, P., J. Beckner, and T. M. Whitworth, Spatial distribution of calcite cement in the Santa Fe Group, Albuquerque Basin, NM; implications for ground-water resources, *New Mexico Geology*, 17, 88-93, 1995.
- Mualem, Y, A new model for predicting the hydraulic conductivity of unsaturated porous media, *Water Resour. Res.*, 12, 513-522, 1976.
- Ogilvie, S. R., J.M. Orribo, and P.W. Glover, The influence of deformation bands upon fluid flow using profile permeametry and positron emission tomography, *Geophysical Research Letters*, 28, 61-64, 2001.
- Olesen, T., P. Moldrup, K. Henriksen, and L. W. Petersen, Modeling diffusion and reaction in soils: IV. New models for predicting ion diffusivity, *Soil Science*, 161, 633-645, 1996.

- Philip, J.R. and D.A. DeVries, Moisture movement in porous materials under temperature gradients, *Trans. Am. Geophysical Union*, 38, 222-228, 1957.
- Phillips, F. M., J.L. Mattick, and T.A. Duval, Chlorine 36 and tritium from nuclear weapons fallout as tracers for long-term liquid and vapor movement in desert soils, *Water Resour. Res.*, 24, 1877-1891, 1988.
- Pittman, E.D., Effect of fault-related granulation on porosity and permeability of quartz sandstones, Simpson Group (Ordovician), Oklahoma, *AAPG Bull.*, 65, 2381-2387, 1981.
- Rawling, G. C., Goodwin, Laurel B., Wilson, John L, Internal architecture, permeability structure, and hydrologic significance of contrasting fault-zone types, *Geology*, 29, 43-46, 2001.
- Reiter, M., Hydrothermal studies on the southern part of Sandia National Laboratories/Kirtland Air Force Base; data regarding ground-water flow across the boundary of an intermontane basin, in *Faults and subsurface fluid flow in the shallow crust*, W. C. Haneberg, P.S. Mozley, J.C. Moore, and L.B. Goodwin, eds., *American Geophysical Union Monograph* 113, Washington, DC, US, pages 207-222, 1999.
- Ross, B., A conceptual model of deep unsaturated zones with negligible recharge, *Water Resour. Res.*, 28, 1627-1629, 1984.
- Ross, B., The diversion capacity of capillary barriers, *Water Resour. Res.*, 26, 2625-2629, 1990.

- Scanlon, B. R., Evaluation of liquid and vapor water flow in desert soils based on chlorine 36 and tritium tracers and nonisothermal flow simulations, *Water Resour. Res.*, 28, 285-297, 1992.
- Scanlon, B. R., Water and heat fluxes in desert soils, 1, Field studies, *Water Resour. Res.*, 30, 709-720, 1994.
- Scanlon, B. R., S.W. Tyler, and P.J. Wierenga, Hydrologic issues in arid, unsaturated systems and implications for contaminant transport, *Reviews of Geophysics*, 35, 461-490, 1997.
- Scanlon, B. R. and P. C. Milly, Water and heat fluxes in desert soils, 2, Numerical simulations, *Water Resour. Res.*, 30, 721-734, 1994.
- Selker, J. S., C. K. Keller, and J. T. McCord, *Vadose Zone Processes*, CRC Press LLC, Boca Raton, Florida, 339 pages, 1999.
- Sigda, J., Effects of small-displacement faults on the permeability distribution of poorly consolidated Santa Fe Group sands, Rio Grande rift, New Mexico, MS. (Hydrology) thesis, New Mexico Institute of Mining and Technology, Socorro, New Mexico, 1997.
- Sigda, J.M. and J.L. Wilson. Are faults preferential flow paths through semi-arid and arid vadose zones?, *Water Resour. Res.*, 39, 1225, doi:10.1029/2002WR001406, 2003.
- Sigda, J. M., L. B. Goodwin, P. S. Mozley, and J. L. Wilson, Permeability alteration in small-displacement faults in poorly lithified sediments; Rio Grande Rift, central New Mexico, in *Faults and subsurface fluid flow in the shallow crust*, W. C. Haneberg, P.S.

- Mozley, J.C. Moore, and L.B. Goodwin, eds., *American Geophysical Union Monograph* 113, Washington, DC, US, pages 51-68, 1999.
- Smith, L., Forster, C., and Evans, J., Interaction of fault zones, fluid flow, and heat transfer at the basin scale, in Neuman, S.P. and Neretnieks, I., eds., *Hydrogeology of Low Permeability Environments*, Verlag Heinz Heise, 41-67, 1989.
- Stephens, D. B. and R. Knowlton Jr., Soil water movement and recharge through sand at a semiarid site in New Mexico, *Water Resour. Res.*, 22, 881-889, 1986.
- van Genuchten, M. T., A closed-form equation for predicting the hydraulic conductivity of unsaturated soils, *Soil Science Society of America Journal*, 44, 892-898, 1980.
- Walvoord M., M.A. Plummer, F.M. Phillips F. M., and A.V. Wolfsberg, Deep arid system hydrodynamics, Part 1: Equilibrium states and response times in thick desert vadose zones, *Water Resour. Res.*, 38 (12), 1308, doi:10.1029/2001WR000824, 2002.
- Wilson, J.E., Goodwin, L.B., Lewis, C.J., 2003, Deformation bands in nonwelded ignimbrites: Petrophysical controls on fault-zone deformation and evidence of preferential fluid flow, *Geology*, 31, 837-840, 2003.
- Wood, B. D., C. K. Keller, and D. L. Johnstone, In situ measurement of microbial activity and controls on microbial CO<sub>2</sub> production in the unsaturated zone, *Water Resour. Res.*, 29, 647-660, 1993.

## **CHAPTER 4: HOW VARIABLE IS VADOSE-ZONE PREFERENTIAL FLOW AND DIAGENESIS IN DEFORMATION BAND FAULTS?**

### **4.0 Abstract.**

Recently published measurements and modeling of a single deformation band fault and its poorly lithified parent sand suggest that such faults can significantly accelerate unsaturated liquid-phase flow and transport in arid and semi-arid vadose zones. We report confirmatory measurements and modeling for four other small-displacement normal faults and adjacent sands in the Bosque del Apache Wildlife Refuge, central New Mexico, USA. Two of these faults are at the Canyon Trail study area, the location of the original study, and the other two are at the Elmendorf area, three km further south. Poorly lithified sand, protolith, is macroscopically similar for all sites. The new faults in this study accommodated a range of displacements. Unsaturated hydraulic relations were measured with the Unsaturated Flow Apparatus (UFA) centrifuge system. Measured properties were used in simple, one-dimensional, steady flow models to assess the potential for preferential flow and solute transport through faulted sands under semi-arid and arid conditions. X-ray diffraction revealed the clay size fraction (CSF) from Elmendorf samples contains pure and possibly authigenic smectite, whereas Canyon Trail samples contain a mixture of smectite and other minerals. Saturated hydraulic

conductivity,  $K_s$ , for protolith with pure smectite CSF is at least two orders of magnitude less than the  $K_s$  for protolith with mixed clay minerals in the CSF. The difference between fault and protolith  $K_s$  is several orders of magnitude for samples with mixed clay minerals but only an order of magnitude for pure smectite CSF samples. Unsaturated property measurements show that as conditions become drier,  $K$  decreases more abruptly in protolith than faults, so that protolith and fault  $K$  reach equivalence (crossover point), and, for still drier conditions, fault  $K$  exceeds protolith  $K$  by several orders of magnitude. Fault  $K$  functions and fault – sand crossover points differ significantly between the pure smectite and mixed clay mineral samples, whereas they do not vary significantly for the vertical displacements studied. Given appropriate conditions and depending on CSF composition, more water can infiltrate and exfiltrate through faulted sands than unfaulted sands by orders of magnitude. Faults are also conduits for solute transport because solute residence time is far longer in protolith than faults for dry climate conditions. Diagenesis is much more likely to occur in faults than protolith because faults are predicted to transmit up to  $10^4$  pore volumes in the time needed to transmit a single pore volume through the protolith. Composition of the CSF and the density of deformation bands within the fault can significantly affect flow and transport. The range of fault displacements studied does not affect properties or behavior. Our results demonstrate that deformation band faults can significantly accelerate liquid-phase infiltration, exfiltration, solute transport, and diagenesis in arid and semi-arid vadose zones.

## 4.1 Introduction\*

Recent studies of a single small-displacement fault from the Rio Grande rift suggest that the unsaturated hydraulic properties of a poorly lithified sand and its crosscutting deformation band fault differ so substantially that, in the rift's relatively dry climate, the fault acts as a path for preferential flow and solute transport through the vadose zone [Sigda and Wilson, 2003; Chapter 3]. Fault unsaturated hydraulic conductivity,  $K$ , decreases with decreasing matric potential,  $\psi$ , at a slower rate than does protolith  $K$ , so that below matric potentials of  $-40$  to  $-80$  cm, fault  $K$  exceeds protolith  $K$  by as much as four to six orders of magnitude [Sigda and Wilson, 2003]. Preferential flow and solute transport through the sand beds of a moderately dry vadose zone would focus within this fault, enhancing infiltration (downward flow) for steady gravity-driven flow, enhancing exfiltration (upward flow) for steady evaporation-driven flow from a shallow water table, and accelerating diagenesis under both scenarios [Sigda and Wilson, 2003; Chapter 3]. If other deformation band faults in the Rio Grande rift and hydrogeologically comparable basin-fill vadose zones (e.g., Basin and Range Province) behave similarly, there could be important consequences for burgeoning cities, for hazardous and nuclear waste sites, and for weapons testing sites in those regions. We report new measurements of unsaturated properties and new predictions of unsaturated preferential flow and diagenesis for four other nearby deformation band faults and their poorly lithified parent sands, and we contrast these new results with those for the previously studied site.

---

\* As this chapter was prepared for submission to a journal for publication, it by necessity revisits some of the introductory material previously presented in Chapters 2 and 3. Readers eager to avoid any repetition are urged to skip page 4-5 and begin with the research questions.

A variety of processes created numerous, extensive, and thick packages of variably lithified, heterolithic sediments, which in turn form zones of saturation and zones of vadose water in the American Southwest. Examples include the Rio Grande rift and the Basin and Range Province. Flow and solute transport through the vadose zones in these areas is generally expected to be extremely slow given semi-arid or arid conditions and the limited ability of sandy beds to transmit, via the liquid phase, significant amounts of water or solutes under such dry conditions [Winograd, 1981; Ross, 1994; Scanlon et al., 1997]. The relative insignificance of recharge underpins arguments for long-term isolation of radioactive waste and other contaminants in these vadose-zone environments [Winograd, 1981]. Such arguments could be undercut by the presence of “fast paths” for preferential flow and solute transport through these relatively dry vadose zones, such as macropore networks, gravity fingering, or, perhaps, deformation band faults.

Where numerous syn- and post-depositional faults crosscut sandy sediments, creating quasi-tabular zones called deformation bands, compaction and cataclasis can greatly reduce pore and grain sizes. Despite the small displacements (on the order of centimeters), deformation bands possess markedly different hydraulic properties than their parent materials, whether in well lithified porous sandstones [Aydin, 1978; Antonellini and Aydin, 1994; Taylor and Pollard, 2000; Ogilvie et al., 2001] or poorly lithified sands [Sigda et al., 1999; Hong, 1999; Cashman and Cashman, 2000; Herrin, 2001; Sigda and Wilson, 2003]. Deformation processes drastically reduce mean pore size, increase clay size fraction, and decrease sorting within individual deformation bands and zones of bands, thereby substantially decreasing porosity and saturated hydraulic conductivity,  $K_s$ , by several orders of magnitude relative to parent sand or sandstone  $K_s$ .

Faulting can also produce non-cataclastic structures such as compaction and shear bands [Antonellini et al., 1994; Mollema and Pollard, 1995], which are expected to have very different pore networks because of their different formative processes. This study focuses solely on shear deformation bands, within which cataclasis has accompanied faulting. We use the term “deformation band faults” [Mollema and Antonellini, 1994; Aydin and Myers, 1997; Sigda and Wilson, 2003] to describe groups or zones of deformation bands because they form abrupt discontinuities in hydraulic properties that persist, both vertically and laterally, across decameters to kilometers [Aydin, 1994; Antonellini and Aydin, 1994; Herrin, 2001].

Starting from the original study, which investigated a single fault site, we ask the following research questions.

Do other deformation band faults and their parent sands show similarly large differences in unsaturated hydraulic properties?

How do the differences vary with characteristics of the fault (e.g., displacement, dip) and parent sand protolith (e.g., grain size distribution, mineral composition, etc.)?

Are observed differences in sand and fault properties hydrologically significant? Do differences between protolith and fault characteristics cause significant preferential solute transport through faulted vadose-zone sand beds?

We began by measuring the unsaturated hydraulic properties of four other faults, assessing their behavior under semi-arid and arid vadose-zone conditions, and comparing the results to those for the previously studied fault. The chosen sites within central New Mexico’s Rio Grande rift, allow us to investigate the effects of fault characteristics, fault displacement, density of deformation bands within a fault, mineral composition of the clay size fraction (CSF), on differences in sand and hydraulic properties as well as differences in flow and transport behavior. Cl

fractions from faults and protolith were analyzed by X-ray diffraction to evaluate whether CSF composition influences hydraulic behavior. The fault and sand site (Canyon Trail E10) studied by Sigda and Wilson [2003 and Chapter 3] is contrasted with this study's four new sites. Two of this study's four faults are located at the same outcrop as the previously studied fault, but have different displacements, one larger and one smaller than the original fault. The remaining two faults, which are located 3 km further south in another outcrop of poorly lithified sand, have displacements less than and nearly equivalent to that for the original fault [Sigda et al., 1999]. We collected samples from each fault and nearby protolith, then tested for differences in unsaturated hydraulic properties by measuring moisture content as a function of matric potential,  $\theta(\psi)$ , and unsaturated hydraulic conductivity as a function of moisture content,  $K(\theta)$ , for each sample. Measurements were made with specially equipped centrifuges and the resulting data were fitted to theoretical  $\theta(\psi)$  and  $K(\theta)$  models as described by Sigda and Wilson [2003]. These parameter fits were used in simple one-dimensional steady state models, in the manner of Chapter 3, to investigate the potential for significant impacts on gravity-driven (infiltration) and evaporation-driven (exfiltration) flow and diagenesis.

## 4.2 Methods

### 4.2.1 Geologic characterization

Grain size and bedding orientation were noted for all protolith samples. A set of samples, independent of the samples for hydraulic properties (Section 4.3.2), were collected from both fault and protolith at two Canyon Trail sites, E10 and E14, and at the

fault A site in the Elmendorf study area. The clay size fraction ( $< 2 \mu\text{m}$  in size) of each sample was separated and analyzed using X-ray diffraction (XRD) by George Austin at the New Mexico Bureau of Geology and Mineral Resources. The relative proportions of the constituents in the clay size fraction were characterized using a semi-quantitative scale (parts out of ten) based on the intensity of the XRD reflection peaks.

#### 4.2.2 Measuring hydraulic properties

Hydraulic properties measured include porosity, bulk density, saturated hydraulic conductivity, air entry matric potential, residual moisture content, the drainage moisture content – matric potential relation,  $\theta(\psi)$  (also known as the moisture retention relation), and the drainage hydraulic conductivity –moisture content  $K(\theta)$  relation. More detailed descriptions of our methods are given in Sigda and Wilson [2003] and Sigda [2004].

**4.2.2.1 Sample collection.** Intact samples of fault and protolith were collected from each site using hand tools or a gas-powered coring device. Sample sizes were dictated by the dimensions of the centrifuge rotors and successful extraction of intact pieces from the outcrops. All protolith samples were cylindrical in shape, as were five fault samples, because they were collected with the coring device: two samples from fault E13's 15 cm wide zone of densely distributed deformation bands, one from E14's diffuse zone of deformation bands, and one each from Elmendorf faults A and B. Cylindrical samples had a mean volume of  $68 \text{ cm}^3$  for large samples and  $28 \text{ cm}^3$  for small samples. The remaining fault samples from E14's splay D and the Elmendorf fault A were hexahedral with mean volume of  $37 \text{ cm}^3$  for large samples and  $16 \text{ cm}^3$  for small samples.

**4.2.2.2 Sample preparation.** Samples were cut and shaped by hand, then measured for bulk density and oven-dry weight. Selected samples were jacketed with Devcon 2-ton epoxy and then epoxied into Delrin sleeves. Fault samples NMT19, DS01, and DS02 were epoxied into sleeves using the much denser Devcon F2 aluminum epoxy. Hexahedral fault samples were oriented so that flow through the sample was parallel to dip - reproducing down-fault flow. Cylindrical fault cores were oriented so that flow was parallel to fault strike, i.e., emulating horizontal flow through the fault. Flow was directed parallel to bedding (denoted hereafter as  $\text{bedding}_{\parallel}$ ) for nearly all sand samples because of difficulties in extracting intact samples with longitudinal axes oriented normal to bedding (denoted as  $\text{bedding}_{\perp}$ ). We extracted one pair of matching  $\text{bedding}_{\parallel}$  and  $\text{bedding}_{\perp}$  sand samples: DS24 and DS25 from site E14's hanging wall. Sand samples from the E14 hanging wall (DS03 and NMT07) are also have  $\text{bedding}_{\perp}$ .

**4.2.2.3 Centrifuge measurements.**  $K$ - $\theta$  curves were measured using Unsaturated Flow Apparatus (UFA<sup>TM</sup>) centrifuges and the method described by Conca and others [Conca and Wright, 1992; Khaleel et al., 1995; Conca et al., 1999]. Centrifuge drainage curves were measured following Hassler and Brunner's [1945] centrifuge method, adapted for the UFA. The set of average moisture content – rpm pairs produced by each experiment were inverted to  $\theta$ - $\psi$  values using the method of Forbes [1994], as adapted for vadose zone hydrology.

**4.2.2.4 Fitting models.** Theoretical models of unsaturated hydraulic properties were simultaneously fit to each sample's  $K$ -  $\theta$  and  $\theta$ - $\psi$  data using a trial and error approach.

The commonly used Mualem-van Genuchten (MvG) theoretical model [Mualem, 1976; van Genuchten, 1980] was fit to the experimental data for each sample:

$$\theta(\psi) = \theta_r + (\theta_s - \theta_r) \left(1 + |\alpha\psi|^n\right)^{-m} \quad \text{where } m = (n-1)/n \quad (4.1)$$

$$K(\theta) = K_s \left( \frac{\theta - \theta_r}{\theta_s - \theta_r} \right)^\beta \left\{ 1 - \left[ 1 - \left( \frac{\theta - \theta_r}{\theta_s - \theta_r} \right)^{1/m} \right]^m \right\}^2 \quad (4.2)$$

Fitted model parameters include both measured and empirical quantities. Measured parameters were  $K_s$  (saturated hydraulic conductivity),  $\alpha$  (taken as one over the air entry matric potential),  $\theta_s$  (saturated volumetric moisture content, which equals the porosity for vacuum saturation), and  $\theta_r$  (residual volumetric moisture content). The empirical parameters were  $n$  and  $\beta$ : the former is an index of the pore size variability for the MvG model, whereas the latter represents the tortuosity and the partial correlation in pore radius between two adjacent pores at a given saturation [Mualem, 1976].

#### 4.2.3 Assessing preferential flow and transport

We tested whether the faults are likely to induce preferential flow and solute transport with respect to surrounding sands, by comparing calculated metrics for liquid-phase flow, solute transport, and diagenesis. The metrics were determined from the measured properties and a simple, 1D, steady state conceptual model. Appendix 4.A summarizes the modeling methods used in this study, but Chapter 3 gives a more detailed description. We briefly summarize the conceptual model below.

A simple, steady state, one-dimensional, hydrogeologic conceptual model is used to represent liquid-phase flow through sand beds with and without a fault. Whether in liquid or vapor-phase, water is transported through the vadose zone by a number of driving forces in semi-arid and arid areas, including body force (gravity), matric potential (capillarity), and thermal gradients. All three gradients are known or inferred to be active within the Rio Grande vadose zone [Chapter 3]. Two liquid-phase flow scenarios: water driven downward by gravity and water driven upward from a shallow water table by surface evaporation (or plant transpiration) are examined and contrasted with vapor-phase water movement driven by thermal gradients. The gravity-driven scenario applies to the middle portion (below the root zone and above the capillary fringe) of a thick vadose zone where there is relatively little vertical change in matric potential so that only gravity causes advective infiltration. The evaporation-driven scenario applies to areas with shallow water tables and dry surface conditions, so that liquid-phase water is drawn up through the vadose zone by the matric potential gradient.

The conceptual model is used to estimate and compare liquid-phase and vapor-phase fluxes, as well as advective and diffusive solute fluxes, through both faults and sands (Table 4.1). The metric for the gravity-driven steady flow (infiltration) scenario is the downward, liquid-phase flux density. This metric is contrasted against a vapor-phase flux density,  $q_v$ , driven upward through the vadose zone by the geothermal gradient. The vapor-phase flux density has been estimated to fall between  $0.9$  and  $3.0 \times 10^{-3}$  cm/year in the Albuquerque Basin vadose zone [Chapter 3]. Our metric for the evaporation-driven steady flow (exfiltration) scenario is the upward liquid-phase flux density, which is associated with its own vapor-phase comparator (Table 4.1). This downward vapor-

phase flux density is driven by near surface temperature gradients and has been estimated to reach  $1 \times 10^{-3}$  cm/year for a site in the Rio Grande valley near El Paso, Texas [Scanlon and Milly, 1994]. Our model is also used to explore the importance of the spatial distribution of faults by calculating infiltration and exfiltration fluxes through faulted sand beds as a function of fault spatial density. Advective residence time is the solute transport metric for both scenarios and is contrasted against the diffusive residence time (Table 4.1 and Appendix 4.A). The unit time required to pass one pore volume, by either advection or diffusion, through a given column length is our proxy measure for rate of diagenesis and is inversely proportional to residence time [Chapter 3 and Appendix 4.A].

**Table 4.1:** Metrics to test hydrologic significance of deformation band faults

Process	Gravity-driven scenario 1 m column length		Evaporation-driven scenario variable column length	
	Metric	Comparator	Metric	Comparator
Water flow	downward $q_l$	upward $q_v$	upward $q_l$	downward $q_v$
Solute transport	advective $t_r$	diffusion $t_r$	advective $t_r$	diffusion $t_r$
Diagenesis	Unit time per pore volume	None	Unit time per pore volume	None

$q_l$  = liquid-phase flux density;  $q_v$  = vapor-phase flux density;  $t_r$  = solute residence time.

We briefly note the assumptions for the flow and transport models. Only steady flow is considered. Faults have a uniform thickness and a uniform vertical dip. Fault and protolith have uniform properties with negligible exchange of water or solutes between them. Hysteretic effects are negligible. Supply of reactants is unlimited, chemical kinetics occur instantaneously relative to seepage velocity (typically very small in arid and semi-arid environments), and diagenesis does not substantially change the hydraulic

properties of the sand or fault. Vertical length is 10 m because sand bed thickness in the middle Rio Grande rift is rarely thicker [Davis et al., 1993; Mozley et al., 1995].

### 4.3 Geologic Setting

Deformation band faults exhibit a wide variability in their internal distribution of deformed and relatively undeformed material. Deformation bands can occur singly or in zones, within which the distribution of bands ranges from widely spaced (diffuse) to closely spaced (dense) [Aydin, 1978; Sigda et al., 1999; Herrin, 2001]. In this study, we investigated only zones of deformation bands for two reasons. First, individual deformation bands are too thin and friable to allow centrifuge measurement of hydraulic properties. Second, zones of deformation bands are more likely to persist in both continuity and orientation across the entire bed thickness because they are longer and wider than individual deformation bands [Aydin, 1978; Antonellini and Aydin, 1994; Sigda et al., 1999; Herrin, 2001]. Note that mappable (i.e., at 1:24,000 and larger scales) fault zones with moderate to large displacement in poorly lithified sediments can contain numerous deformation band faults in their mixed and damage zones [Heynekamp et al., 1999; Rawling et al., 2001]. For the remainder of this paper, the terms “fault” and “deformation band fault” are used to refer to the dense and diffuse zones of deformation bands in poorly lithified sands that we have studied.

Located in the Bosque del Apache Wildlife Refuge roughly 200 km south of Albuquerque, New Mexico (Figure 4.1a), the two study areas contain outcrops of predominantly fine grained, well sorted, poorly lithified sand cross cut by multiple

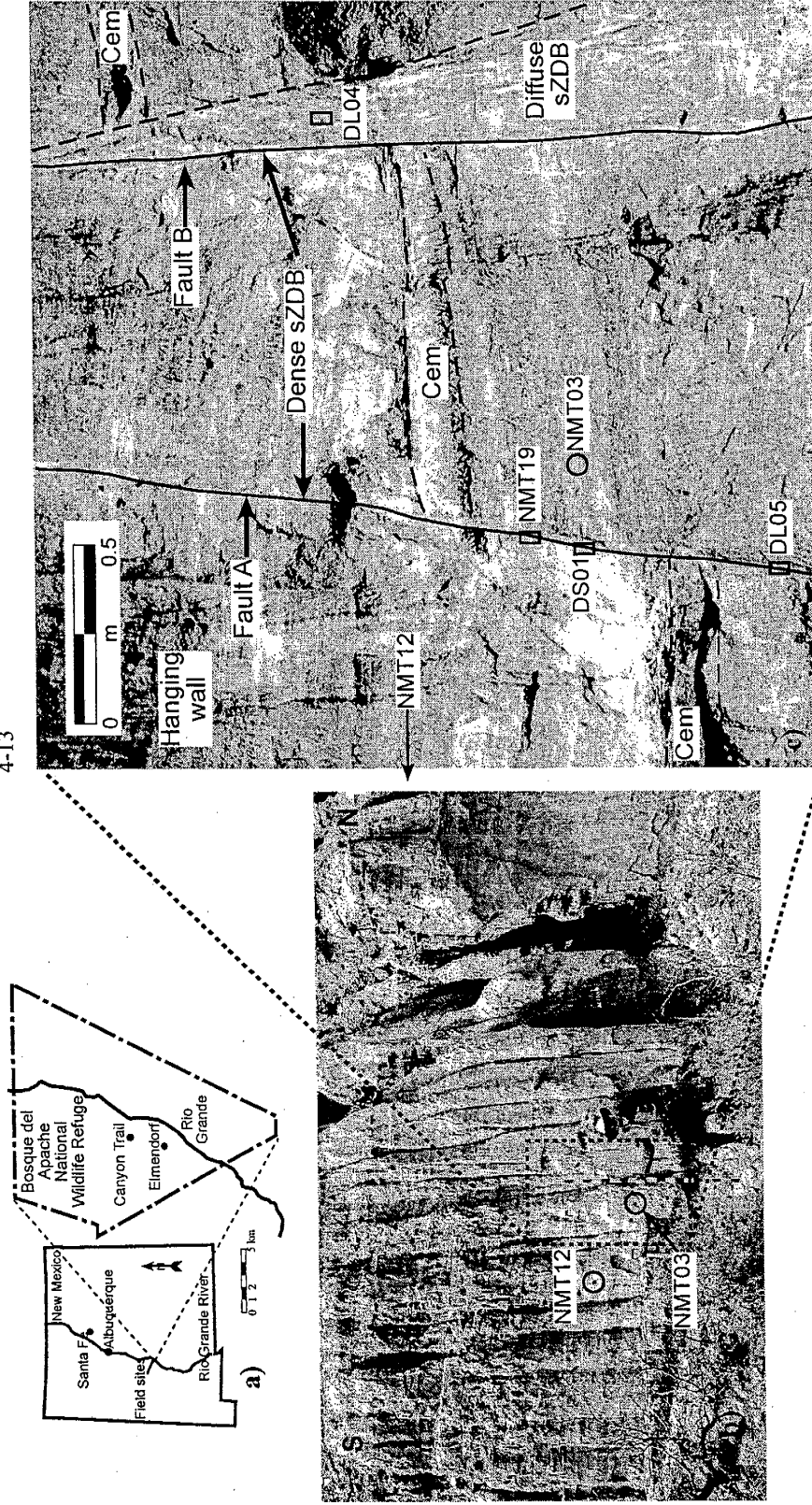


**Figure 4.1:** Location of study site and Elmendorf study area. a) Bosque del Apache National Wildlife Refuge, NM. b) Elmendorf study area. c) Close-up of field site. Sample locations are shown by circles (protolith) and boxes (faults). sZDB = small-displacement zone of deformation bands; Cem = cemented bed, used to determine displacement.

deformation band faults. The Elmendorf study area is located roughly 6 km south of the Refuge Visitor Center, near the southern end of the Socorro Basin of the Rio Grande rift. The other study area, called Canyon Trail, lies 3 km south of the Refuge Visitor Center and 3 km north of the Elmendorf study area. It is also the location for the E10 fault and protolith previously studied by Sigda and Wilson [2003]. We refer to the previously studied fault site as the baseline site to distinguish it from the four new study sites.

Detailed geologic descriptions of the Elmendorf study area can be found in Sigda [1997] and Sigda et al. [1999], whereas the Canyon Trail study area is described by Hong [1999], Herrin [2001], and Sigda and Wilson [2003]. The two study areas are interpreted to be part of the Miocene-age Popatosa Formation (correlative with the Albuquerque Basin's lower Santa Fe Group), which forms vadose and aquifer units in this area and throughout the Socorro and La Jencia basins [Hawley, 1978]. Poorly lithified, well sorted sands similar to those found in our study areas are common throughout the Rio Grande rift region [Hawley and Kernodle, 2000] in the Santa Fe Group basin fill, which forms the major aquifer and vadose zone units for the Albuquerque, Las Cruces, and El Paso-Ciudad Juárez metropolitan areas [Connell et al. 1999; Hawley et al., 1995, 2001].

#### **4.3.1 Protolith**

The protolith at the Elmendorf study area is a fine-grained, well-sorted, poorly lithified sand roughly 5 to 8 m thick with both cross and horizontal planar bedding present [Sigda et al., 1999] (Figure 4.1b). Interpreted to be primarily eolian in origin, the sand is an arkosic litharenite with a significant proportion of volcanic lithic fragments, a

relatively small clay size fraction, and moderate porosity (Table 4.2) [Sigda, 1997; Sigda et al., 1999]. Mean grain size is between 0.125 and 0.354 mm [Sigda, 1997].

**Table 4.2:** Point count results (%) for Elmendorf and Canyon Trail faults and protolith

<i>Constituent</i>	Elmendorf		Canyon Trail E10	
	HW protolith	Fault A: dense ZDB	HW protolith (SH-1)	Dense ZDB (SH-2)
Detrital quartz	14	15	18	31
Total feldspars	28	23	10	16
Total rock fragments	27	21	27	19
Other	0	0	4	2
Clay size fraction	6	23	4	30
Porosity				
Macroporosity	20	7	33	0
Microporosity	5	10	4	3

% sample volume occupied by each constituent is calculated by dividing the total count for each zone, protolith or fault, into the count for each constituent in that zone.

Dense ZDB = zone of deformation bands with closely spaced bands. HW = hanging wall.

Elmendorf data, from Sigda et al.[1999], are based on two thin sections, each with three replicate counts of 300 points. One thin section was collected from protolith nearly 2 m from the fault. Canyon Trail data from Herrin [2001] are based on two thin sections each with counts of 300 points for protolith and counts of 150 points for fault. Sample SH-1 contained both deformation bands and protolith but only protolith data are presented.

At the Canyon Trail study area, two 135 m long outcrops, separated by a railroad cut, expose a poorly lithified, well-sorted, fine to medium-grained eolian and fluvial sand (Figure 4.2). There is nearly 5 m of poorly lithified sand, with an upper bed of fine to medium-grained sand and a lower 1.5 m thick bed of fine-grained sand, all beneath a conglomeratic unit (Figure 4.2). The sand is an arkosic litharenite with a large proportion of volcanic lithic fragments (Table 4.2 and Herrin [2001]). Cross bedding is more common than planar bedding [Herrin, 2001]. Elmendorf and Canyon Trail sands appear similar in grain size, sorting, and mineral composition (Table 4.2).

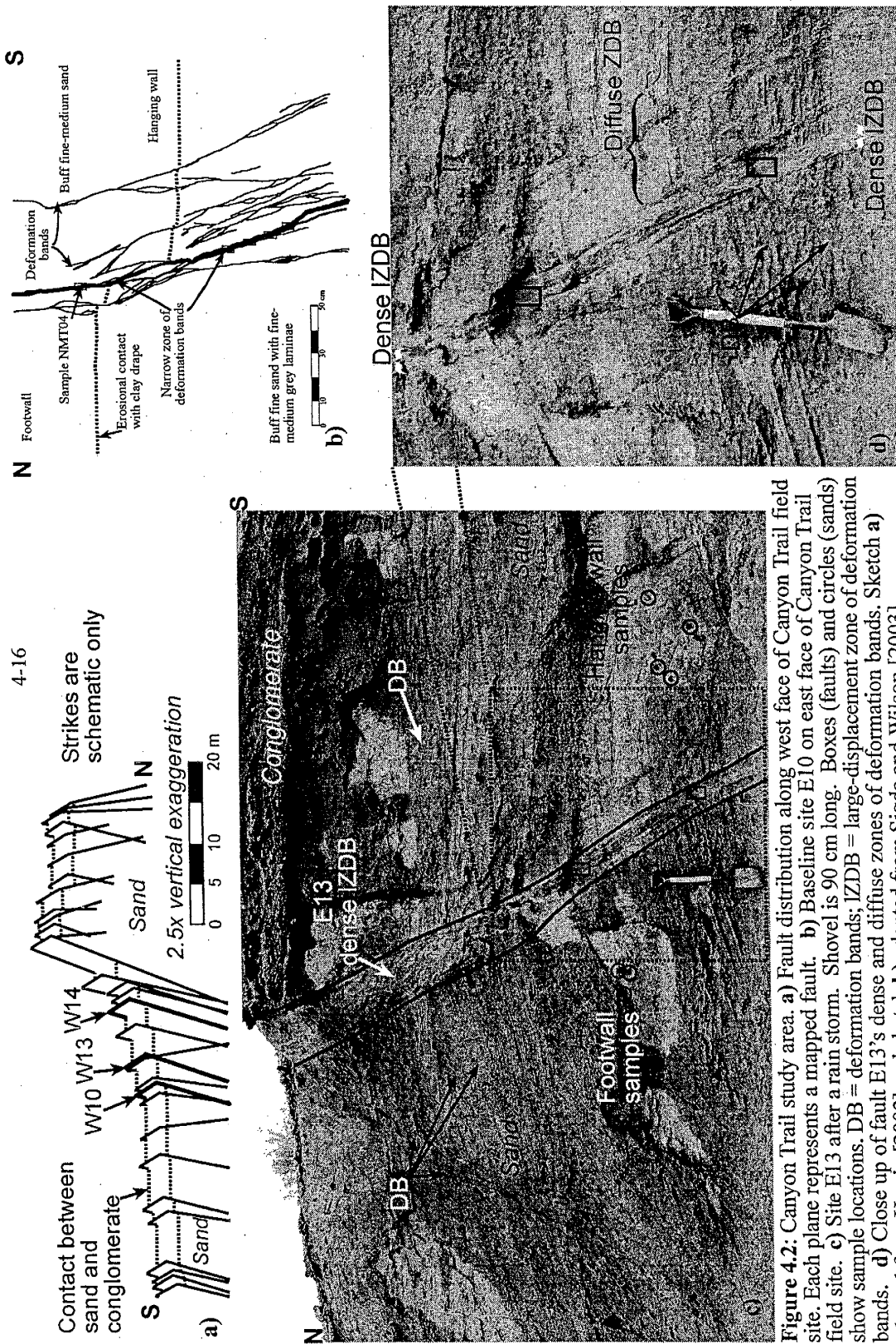
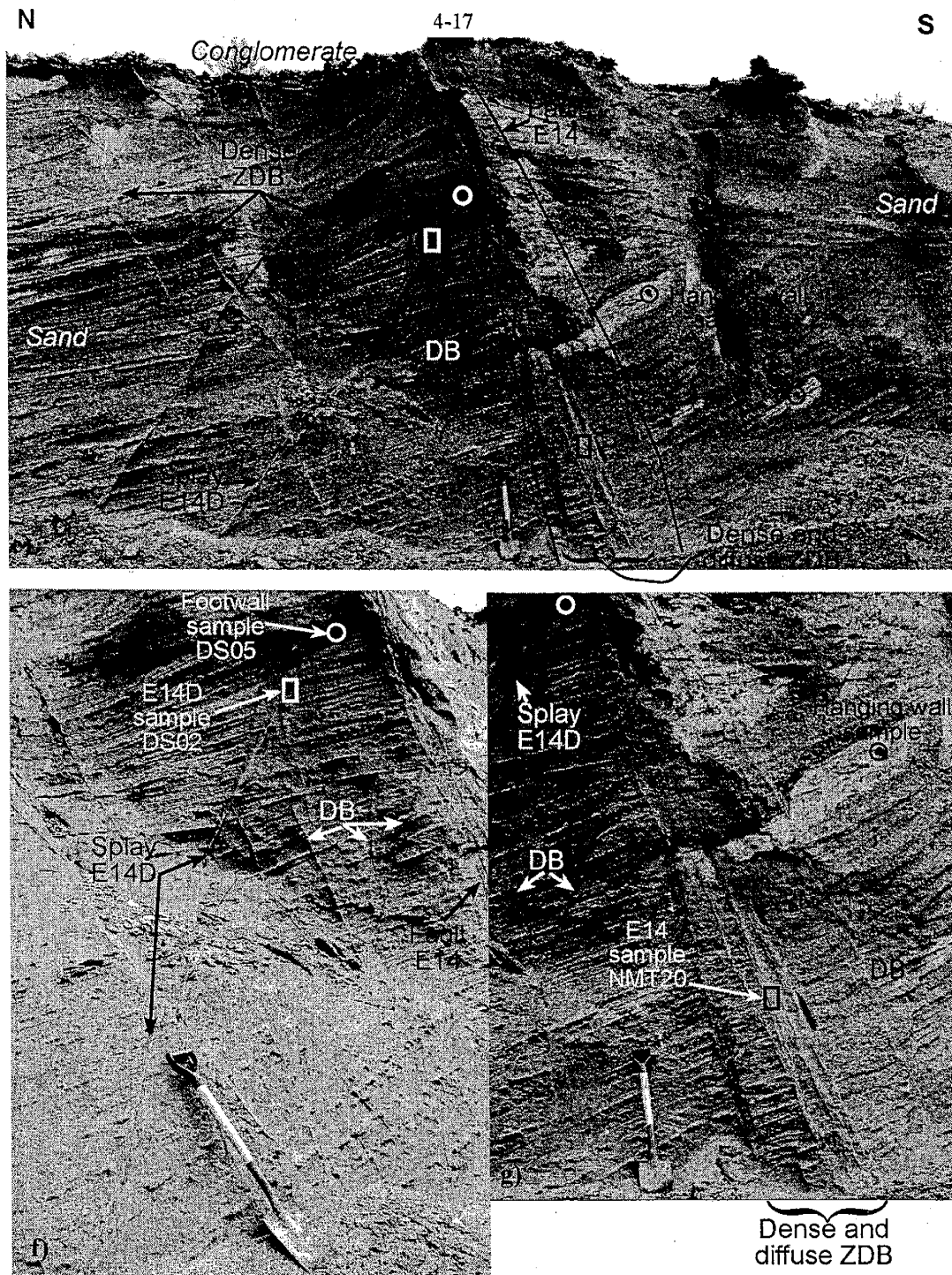


Figure 4.2: Canyon Trail study area. a) Fault distribution along west face of Canyon Trail field site. Each plane represents a mapped fault. b) Baseline site E10 on east face of Canyon Trail field site. c) Site E13 after a rain storm. Shovel is 90 cm long. Boxes (faults) and circles (sands) show sample locations. DB = deformation bands; IZDB = large-displacement zone of deformation bands. d) Close up of fault E13's dense and diffuse zones of deformation bands. Sketch a) adapted from Herrin [2003] and sketch b) adapted from Sigda and Wilson [2003].



**Figure 4.2:** Canyon Trail study area, continued. **e)** Site E14 after a rain storm. Shovel is 90 cm long. Boxes (faults) and circles (sands) show sample locations. DB = deformation bands; ZDB = zone of deformation bands. **f)** Close up (along strike) of E14D, which is a dense, narrow ZDB crosscut by other dense ZDB as well as individual bands. **g)** Close up of E14 fault zone comprising dense and diffuse ZDBs and individual deformation bands.

### 4.3.1 Elmendorf faults

Faults in the northern part of the Elmendorf study site are numerous, spaced every 150 to 200 cm, less friable, and appear to have been preferentially cemented (Figure 3.1a). Faults in the southern part are not cemented and look very similar to the Canyon Trail faults (compare Figure 4.1c with Figure 4.2b-g). We studied two of these normal faults in the southern part, labeled A and B in Figure 4.1c. These faults are narrow zones of deformation bands which have dips between 65 and 75°, widths between 5 and 15 mm, and reduced grain size as well as increased induration relative to the protolith (Figure 4.1c). Fault A accommodated 54 cm of vertical displacement, whereas Fault B accommodated 35 – 40 cm of vertical displacement in its narrow, dense zone of bands and 20 – 25 cm in an adjacent, wider zone of diffusely distributed bands (Figure 4.1c). There are no mesoscopic, open fractures in any of the faults studied.

### 4.3.2 Canyon Trail faults

Roughly 30 faults have been identified in the Canyon Trail sands. Average fault density is 1 fault per 4 m along a north-south transect (Figure 4.2a) [Herrin, 2001]. Faults vary from small displacement ( $\leq 1$  m vertical displacement), mostly sub-parallel, dense to diffuse zones of anastomosing deformation bands in the south, such as those described by Sigda et al. [1999], to much larger displacement faults (1 – 15 m vertical displacement) in the north that include complex arrangements of deformation bands, zones of deformation bands, and pods of little-deformed sand (see Figure 4.2b-g and Herrin [2001]). Fault dip varies between 54 and 87°, and displacement is predominantly normal with local minor

strike slip [Herrin, 2001]. Fault zone width varies considerably along dip and along strike, as do the number and orientation of splays (Figure 4.2b-g). Only one of the faults in the sand is cemented. There are no open, mesoscopic fractures within any of the deformation band faults studied.

The baseline fault E10, studied by Sigda and Wilson [2003], has a well-defined, vertically continuous, narrow, dense zone of deformation bands (Figure 4.2b). Adjacent to the fault is a zone of splaying, diffusely distributed deformation bands (Figure 4.2b). The dense, narrow zone of bands varies between 0.5 and 1.5 cm in width and dips roughly 60°. The bands and zones of bands appear as white traces on the outcrop surface, are better indurated than the protolith, and collectively have accommodated 55 cm of vertical displacement, although nearly all the displacement was accommodated within the narrow, dense zone of bands. Point-count analysis of the fault shows that large increases in clay size fraction and microporosity were balanced by decreases in macroporosity and in feldspar and volcanic lithic content, compared to the protolith (Table 4.2).

The two Canyon Trail fault zones investigated in this study, E13 and E14, have larger displacements and more complex arrangements of deformation bands than the baseline fault. E13 has a relatively wide (6 to 15 cm) zone of densely distributed deformation bands, a zone of diffusely distributed bands, and individual deformation bands, which collectively have accommodated a minimum vertical displacement of 3 m (Figure 4.1c-d). The dense zone of deformation bands dips 58° to the south and appears to have accommodated most of the vertical displacement compared to that accommodated by the adjacent individual bands and zone of diffuse bands. Fault E14 displays a much more

complex spatial distribution of deformed material than either fault E10 or E13 in its assemblages of individual deformation bands and numerous zones of bands (Figure 4.1e-g). We studied both the main fault zone and a nearby smaller-displacement fault. The narrow, dense zone of deformation bands, E14D, dips 70° to the north and accommodated only 20 cm of vertical displacement (Figure 4.2f). The main fault zone, E14, comprises both diffuse and dense zones of bands (Figure 4.2g) and dips 60° to the south with an estimated minimum vertical displacement of 5 m.

#### **4.4 Protolith and fault properties**

In the following sections, “fault” refers to the deformation structure itself, “site” refers to a fault and its protolith, and adjacent sites constitute an “area”, e.g., the Canyon Trail study “area”.

##### **4.4.1 Geologic characterization**

The XRD results for clay size fractions from fault and protolith samples revealed unanticipated differences in mineral composition between the Canyon Trail and Elmendorf sites (Table 4.3). Although it represents only 4-6% of protolith composition at both study areas (Table 4.2), the clay size fraction (CSF) from Elmendorf protolith is wholly composed of smectite clay minerals whereas the CSF from Canyon Trail protolith contains a wide variety of clays and other minerals (Table 4.3). Smectite purity (i.e., other clay minerals are minor or absent) and distribution as grain coatings or rims [Figure 18 in Sigda, 1997] in the Elmendorf protolith indicate that the smectite is

**Table 4.3:** X-ray diffraction analyses of clay size fraction

Sample Location/Description	Kaolinite	Illite	Smectite	Illite/ Smectite	Other
<b>Canyon Trail</b>					
<b>E10</b>					
<i>Sand</i>					
FW buff f gr		4	6		<b>Cli</b> , Ort, Q
FW gray m gr	1	3	6		<b>Cli</b> , Fel, <i>Cal?</i>
HW gray m gr		5	5	<i>tr</i>	<b>Cli</b> , Fel, <i>Q?</i>
<i>Fault</i>					
Narrow, dense ZDB		3	7	<i>tr</i>	Q, <b>Cli</b> , Ort, Pla, Cal
Narrow, dense ZDB		2	8		<b>Cli</b> , Q, Pla, Ort, Cal
<b>E14</b>					
<i>Sand</i>					
Gray-buff f-m gr	2	3	4	1	<b>Cli</b> , Ort, Pla
Buff f gr	2	5	3		<b>Cli</b> , Ort, Q, Pla
<i>Fault</i>					
Wide, diffuse ZDB		2	6		Q, <b>Cli</b> , Pla, Ort, <i>Cal?</i>
Narrow, dense ZDB		2	6		<b>Cli</b> , Q, Ort, Pla, <i>Cal?</i>
E14D dense ZDB	1	3	4	1	<b>Cli</b> , Ort, Pla, Q
<b>Elmendorf</b>					
<i>HW sand</i>					
Buff f gr			10		
Buff m gr			10	<i>tr</i>	
<i>Fault</i>					
Fault A dense ZDB			9	1	Fel

Semi-quantitative ranking of clay mineral abundance in parts of 10. m gr = medium grained; f gr = fine grained; *tr* = trace; ZDB = zone of deformation bands. Other constituents include clinoptilolite (Cli), orthoclase (Ort), plagioclase (Pla), other feldspars (Fel), quartz (Q), and calcite (Cal). Quantity of "Other" is indicated by boldface (major) and italics (minor).

authigenic [Wilson and Pittman, 1977; Wilson and Stanton, 1994]. Differences in CSF composition between the two study areas persists in the fault samples studied (Table 4.3).

We frame our comparison of the four new fault sites and the previously studied, baseline site (E10) according to three geologic characteristics. Protolith is characterized as having either pure smectite CSF (Elmendorf) or mixed clay minerals CSF (Canyon Trail). Faults are characterized according to deformation band density and vertical displacement. Zones of bands with closely spaced bands are called dense, whereas those with  $> 1$  cm between bands are called diffuse. Displacements between 20 and 60 cm are called small and abbreviated as sZDB for small-displacement zone of deformation bands, whereas greater displacements are called large and are abbreviated as lZDB. Where possible, we compare each fault with its protolith from both foot and hanging walls.

#### 4.4.1 Hydrologic characterization

Differences in the CSF mineralogy for protolith samples can yield large differences in hydraulic properties. Protolith with mixed clay mineral CSF, all from the Canyon Train area, have similar porosity, bulk density, and  $K_s$  values (Table 4.4). The small variability in  $K_s$  values is larger than the expected margin of error for UFA  $K$  measurements [Appendix 8.A]. Protolith samples from the Elmendorf area, all with pure smectite CSF, have substantially lower saturated hydraulic conductivity ( $K_s$ ), yet the bulk density and porosity values are similar to the Canyon Trail values (Table 4.4). The UFA  $K_s$  values for Elmendorf protolith with pure smectite are also three to four orders of magnitude lower than previous  $K_s$  measurements at nearby locations on the same outcrop made with an air mini-permeameter [Sigda et al., 1999]. UFA  $K_s$  measurements of Canyon Trail baseline (E10) protolith agreed with previous air mini-permeameter and flexible-wall water permeameter measurements [Sigda and Wilson, 2003].

Table 4.4: Sample characteristics

Area	Site	Sample ID	Description	$\psi$ - $\theta$	K- $\theta$	Sample volume (cm <sup>3</sup> )	Porosity (cm <sup>3</sup> cm <sup>-3</sup> )	Bulk density (g/cm <sup>3</sup> )	K <sub>s</sub> (cm/s)
E10 baseline		Multiple samples	Mean FW sand	See Sigda		37.3 ± 20.8 (5)	0.30 ± 0.01 (4)	1.68 ± 0.02 (5)	1.9 × 10 <sup>-3</sup> ± 0.1 (4)
			Mean HW sand	and Wilson		32.3 ± 13.4 (7)	0.32 ± 0.02 (3)	1.66 ± 0.05 (7)	1.5 × 10 <sup>-3</sup> ± 0.2 (2)
			Mean for dense sZDB	[2003]		23.9 ± 10.7 (6)	0.21 ± 0.02 (5)	1.95 ± 0.05 (6)	7.3 × 10 <sup>-6</sup> ± 0.3 (5)
E13 Canyon Trail (mixed clay mineral CSF)	E13	NMT01	FW buff	Y	Y	20.7	0.30	1.77	3.0 × 10 <sup>-3</sup>
			Mean FW sand				0.33 ± 0.04 (2)	1.73 ± 0.06 (2)	3.0 × 10 <sup>-3</sup> ± NA (1)
			Mean HW sand				NM	1.68 ± 0.0 (2)	NM
	DL08		Core A of dense lZDB	Y	Y	70.1	0.25	1.97	1.4 × 10 <sup>-5</sup>
		NMT05	Core B of dense lZDB	N	N	24.7	0.22	1.90	1.1 × 10 <sup>-5</sup>
			Mean dense lZDB (core)				0.24 ± 0.03 (2)	1.93 ± 0.03 (3)	1.2 × 10 <sup>-5</sup> ± 0.09 (2)
	E14	DS05	FW buff bedding	Y	Y	27.9	0.31	1.70	2.6 × 10 <sup>-3</sup>
		DS03	HW buff bedding ⊥	Y	Y	28.0	0.30	1.65	3.1 × 10 <sup>-3</sup>
		NMT07	HW buff bedding ⊥	N	Y	29.2	0.31	1.70	1.1 × 10 <sup>-3</sup>
		DS24	HW buff bedding	Y	Y	27.6	0.31	1.70	1.7 × 10 <sup>-3</sup>
		DS25	HW buff bedding ⊥	Y	Y	28.9	0.30	1.65	2.0 × 10 <sup>-3</sup>
Fault A (pure smectite CSF)	NMT20		Core of E14 diffuse lZDB	N	N	20.8	0.23	1.94	2.8 × 10 <sup>-6</sup>
		DS02	E14D dense sZDB	Y	Y	21.5	0.22	1.72	1.5 × 10 <sup>-5</sup>
	NMT03		FW buff	Y	Y	25.3	0.30	1.70	2.6 × 10 <sup>-5</sup>
		NMT12	HW buff	Y	Y	30.4	0.29	1.61	3.4 × 10 <sup>-6</sup>
		DS01	Upper dense sZDB	Y	Y	13.9	0.21	1.72	5.6 × 10 <sup>-7</sup>
	NMT19		Upper dense sZDB	Y	Y	13.7	0.18	1.88	2.9 × 10 <sup>-6</sup>
		DL05	Core of lower dense sZDB	Y	N	47.3	0.27	1.87	NM
	Fault B	DL04	Core of diffuse sZDB	Y	Y	64.0	0.28	1.88	4.6 × 10 <sup>-6</sup>

FW = footwall; HW = hanging wall; CSF = clay size fraction. UFA analyses: Y = yes, N = no. ZDB = zone of deformation bands; sZDB = small-displacement ZDB; lZDB = large-displacement ZDB. NM = not measured; NA = not applicable.

Fault samples have significantly different porosity, bulk density, and  $K_s$  values relative to their associated protolith samples (Table 4.4). In all cases, faults have much higher bulk density and much lower porosity than their respective parent sands. In all but one case, fault  $K_s$  values are significantly lower than protolith values, by two to three orders of magnitude. The sole exception is Elmendorf fault sample NMT19, which has a  $K_s$  value that is only marginally lower than its hanging wall protolith (NMT12)  $K_s$  value, but is roughly an order of magnitude lower than its footwall protolith  $K_s$  value. These new  $K_s$  measurements corroborate previous reports that faults are much less conductive under saturated conditions than their poorly lithified parent sands [Sigda et al., 1999; Hong, 1999; Sigda and Wilson, 2003]. The significant differences in bulk density, porosity, and  $K_s$  between faults and protolith persist regardless of protolith CSF mineralogy, fault displacement, or deformation band density (Table 4.4).

Twelve of the nearly two dozen samples collected from the four sites were successfully analyzed for both  $K$ - $\theta$  and  $\theta$ - $\psi$  experiments and fits made to the Mualem-van Genuchten (MvG) model. Only one of the two centrifuge experiments was successfully completed for two other samples (Table 4.4). A partial  $\theta$ - $\psi$  data set was collected for the sole E14 foot wall protolith sample (DS05), but the data were sufficient to fit both relations. Complete centrifuge results were obtained for matching pairs of fault and protolith for all sites with the exception of E14, from which only protolith samples were analyzed. Complete data sets were obtained for fault E14D (DS02), which cross cuts the E14 footwall (represented by sample DS05), but is separated from the E14

hanging wall protolith samples DS03, DS24, DS25, and NMT07 by the relatively large-displacement fault E14 (see Figure 4.2e-g).

The UFA  $K$ - $\theta$  and  $\theta$ - $\psi$  experiments (Appendix 4.B) and the fitted MvG parameter values (Table 4.5) reveal that protolith and faults have strikingly different unsaturated properties and that protolith unsaturated properties vary significantly with CSF mineralogy. Protolith samples with mixed clay CSF show steep declines in volumetric moisture content ( $\theta$ ) with decreasing matric potential (drainage  $\theta(\psi)$  relation), whereas protolith samples with pure smectite CSF show declines that are less steep, and fault samples show declines that are even more gradual (Appendix 4.B). This is corroborated by the fitted values for the  $\alpha$  parameter (inverse of the air entry matric potential) and the  $n$  parameter: values are smallest for faults, intermediate for pure smectite protolith, and greatest for mixed clay protolith (Table 4.5). The smaller the  $\alpha$  value, the larger (i.e., closer to  $\psi = 0$ ) the matric potential at which the material begins to dewater. Similarly, the larger the  $n$  value, the steeper the decline in the drainage  $\theta(\psi)$  relation. The difference between protolith and fault  $n$  values is much larger for sites with mixed clay CSF than sites with pure smectite CSF (Table 4.5). Residual moisture content,  $\theta_r$ , was lower for protolith than faults for only two sites (Appendix 4.B). The  $K(\theta)$  experimental data show that  $K$  decreases in a relatively gradual, log-linear fashion with decreasing moisture content for faults, but decreases much more steeply for protolith, and most steeply for protolith with mixed clay mineral CSF (Appendix 4.B). Fitted  $\beta$  values vary widely with no consistent trend within or between fault and protolith samples. However, many of the protolith samples with mixed clay mineral CSF have  $\beta$  values close to the

**Table 4.5:** Fitted parameter values for Mualem-van Genuchten model

Sample ID	$\theta_s$ (cm <sup>3</sup> cm <sup>-3</sup> )	$\theta_r$ (cm <sup>3</sup> cm <sup>-3</sup> )	$\alpha$ (cm <sup>-1</sup> )	$n$ (-)	$\beta$ (-)	$K_s$ (cm/s)
<b>Canyon Trail (mixed clay mineral CSF)</b>						
<b>E10 Baseline</b>						
Mean for FW & HW	0.318	0.062	0.038	3.3	0.4	$1.7 \times 10^{-3}$
std	0.014	0.005	0.01	0.30	0.3	0.15
Mean for dense sZDB	0.202	0.089	0.003	1.7	1.6	$7.4 \times 10^{-6}$
std	0.014	0.015	0.001	0.11	0.7	0.32
<b>E13</b>						
FW (NMT01)	0.300	0.053	0.04	3.1	2.1	$3.0 \times 10^{-3}$
Dense lZDB (DL08)	0.255	0.100	0.009	1.4	-1.3	$1.5 \times 10^{-5}$
<b>E14</b>						
HW (DS03) bedding <sub>⊥</sub>	0.300	0.070	0.04	2.6	0.6	$3.1 \times 10^{-3}$
HW (DS24)	0.320	0.095	0.03	2.7	0.8	$1.6 \times 10^{-3}$
HW (DS25) bedding <sub>⊥</sub>	0.295	0.085	0.025	2.8	0.5	$2.0 \times 10^{-3}$
FW (DS05)	0.307	0.053	0.045	3.5	0.4	$2.6 \times 10^{-3}$
E14D dense sZDB (DS02)	0.220	0.076	0.0075	1.9	-1.2	$2.0 \times 10^{-5}$
<b>Elmendorf (pure smectite CSF)</b>						
FW (NMT03)	0.301	0.100	0.018	2.1	1.0	$2.6 \times 10^{-5}$
HW (NMT12)	0.295	0.122	0.0095	1.7	1.4	$3.2 \times 10^{-6}$
Fault A dense sZDB (DS01)	0.185	0.105	0.0025	1.5	0.2	$3.8 \times 10^{-7}$
Fault A dense sZDB (NMT19)	0.157	0.110	0.003	1.4	2.9	$2.9 \times 10^{-6}$
Fault B diffuse sZDB (DL04)	0.285	0.095	0.009	1.5	1.0	$5.0 \times 10^{-6}$

FW = footwall protolith; HW = hanging wall protolith; CSF = clay size fraction; sZDB = small-displacement zone of deformation bands; lZDB = large-displacement ZDB. Sand samples are bedding<sub>||</sub> unless otherwise indicated.  $K_s$ , MvG values differ slightly from measured values to improve fits for a few samples (see Table 4.4). E10 data taken from Sigda and Wilson [2003].

0.5 estimated by Mualem [1976] for 45 different soils (Table 4.5). There is little difference between the matched bedding<sub>⊥</sub> and bedding<sub>||</sub> samples from the E14 site hanging wall, although  $K_s$  is marginally greater for the bedding<sub>⊥</sub> sample (Appendix 4.B). The fault sample with diffusely distributed deformation bands (Elmendorf fault B) is

more conductive than samples from the fault with densely distributed bands (fault A) under wetter conditions ( $\psi$  near 0), but is much less conductive at drier conditions,  $\psi < -200$  cm (Figure 4.3c).  $K(\theta)$  curves for the two dense ZDB samples from fault A are based on fewer data than those for dense ZDB samples with mixed clays because the angular velocity range for the centrifuge could induce only relatively small departures in  $\theta$  from saturation for the samples with pure smectite CSF (Appendix 4.B).

$K(\psi)$  curves plotted from the fitted MvG parameters reveal that fault  $K$  exceeds protolith  $K$  by orders of magnitude for a large  $\psi$  range (Figure 4.3). As depicted, each  $K(\psi)$  curve has two limbs. In the first limb, which is nearly horizontal,  $K$  decreases very gradually as  $\psi$  decreases from zero (saturation) to  $\psi$  slightly greater than the air entry matric potential. In the second limb,  $K$  decreases much more steeply as  $\psi$  decreases below the air entry matric potential. The first limb spans a relatively narrow  $\psi$  range for mixed clay protolith, a wider range for pure smectite protolith, and the widest range of all for faults, regardless of fault CSF mineralogy. The second limb decreases most steeply for mixed clay protolith, less steeply for pure smectite protolith, and most gradually for faults, again, regardless of fault CSF mineralogy (Figure 4.3). Each pair of  $K(\psi)$  curves for fault and protolith from the same site reveals a crossover point [Sigda and Wilson, 2003; Chapter 3],  $\psi_x$ , where the fault and protolith  $K$  values are equivalent. Protolith  $K$  is greater than fault  $K$  for  $\psi$  values greater than the crossover point, whereas fault  $K$  exceeds protolith  $K$  for  $\psi$  values less than the crossover point (Figure 4.3). Crossover points occur at larger  $\psi$  values for mixed clay mineral CSF sites relative to the crossover points for pure smectite CSF sites. For Canyon Trail sample pairs,  $\psi_x = -44$  cm at fault E13 in

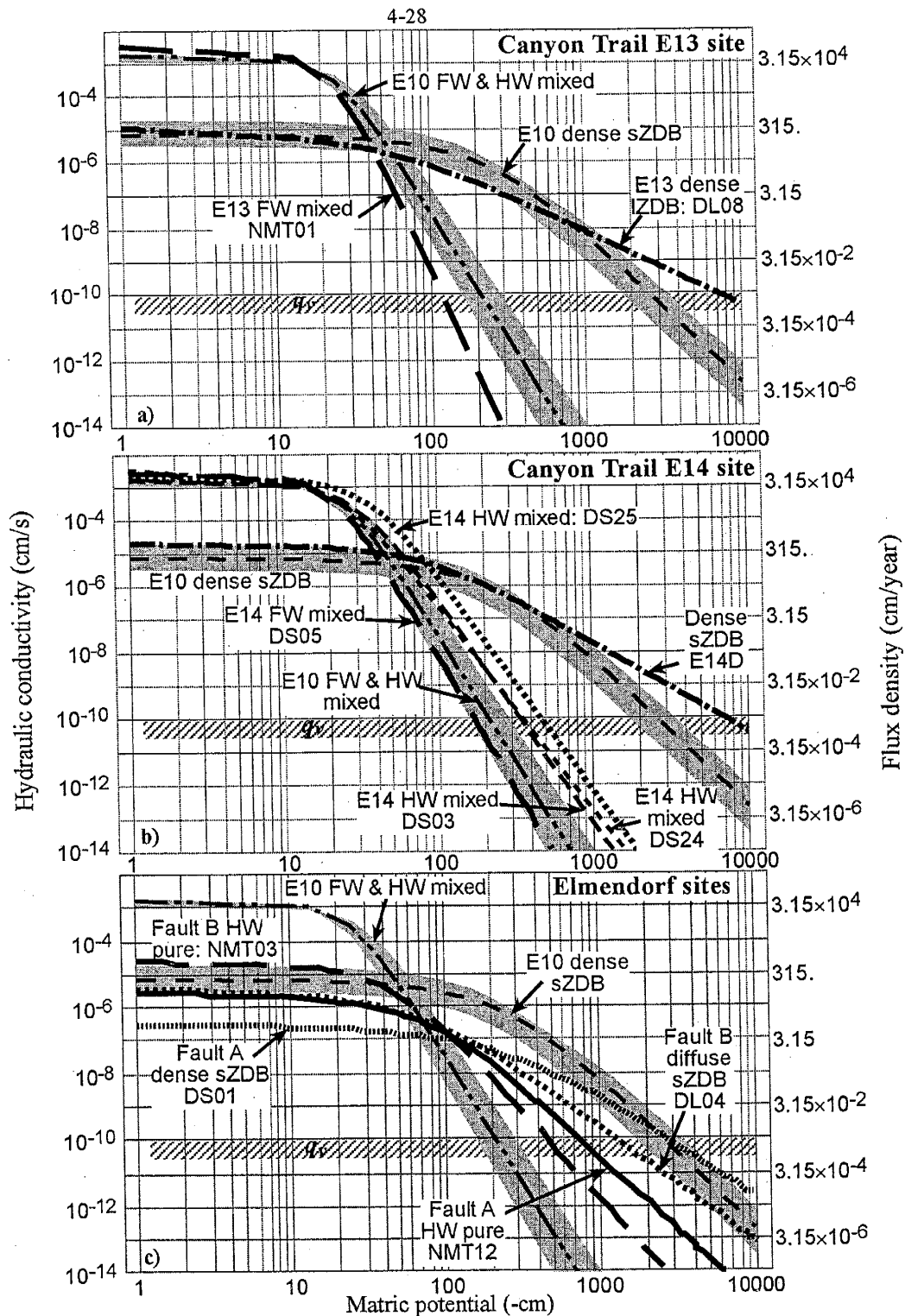


**Figure 4.3:** Fitted  $K(\psi)$  relationships. Shading depicts range of  $K(\psi)$  relations for all samples around the mean sand and fault curves for the E10 (baseline) site. Hatching shows the maximum geothermal vapor-phase flux density,  $q_v$ . FW = footwall; HW = hanging wall; mixed = mixed clay mineral CSF; pure = pure smectite CSF; sZDB = small-displacement zone of deformation bands; LZDB = large-displacement ZDB.

its footwall, -40 cm at fault E14D in its footwall, -51 cm for the baseline mean fault in the mean sand. For Elmendorf sample pairs, the crossover point is -119 cm at fault A in its footwall and -125 cm in its hanging wall, and -95 cm for fault B in its hanging wall. Differences between  $K(\psi)$  curves for related fault and protolith samples are greatest for sites with mixed clay CSF and smallest for sites with pure smectite CSF.

#### 4.4.2 Discussion of property measurements

The centrifuge experiments and fits to the Mualem-van Genuchten model demonstrate that saturated and unsaturated hydraulic properties for protolith and faults differ significantly at the four new sites. The stark contrasts in hydraulic properties observed for the paired protolith and fault samples confirm previous findings [Sigda and Wilson, 2003] that cataclasis and compaction create fault structures which have greater moisture retention and hydraulic conductivity than their poorly lithified parent sands under moderately dry vadose-zone conditions. These measurements also provide a partial answer to the question, “How do the differences vary with characteristics of the fault (e.g., displacement, dip, etc.) and protolith (e.g., grain size distribution, mineral composition, etc.)?”.

Compared to protolith samples, the variation in fault unsaturated hydraulic properties is small and depends more on deformation band density and CSF mineralogy than on fault displacement. The  $K(\psi)$  curves (Figure 4.3) for the three Canyon Trail faults, all of which have dense distributions of deformation bands and mixed clay mineral CSF, are very similar despite vertical displacements of 20 cm for E14D, 55 cm for E10, and a

minimum of 3 m for E13. Note that the variability in  $K(\psi)$  curves for the E10 baseline fault, based on five samples, encompasses the  $K(\psi)$  curves for Canyon Trail faults E13 and E14D for nearly all of the matric potential range greater than  $-1000$  cm (Figure 4.3). In contrast, comparing the  $K(\psi)$  curves for the two dense ZDB with nearly equivalent displacements but different CSF compositions, Canyon Trail E10 (55 cm) and Elmendorf A (54 cm), demonstrates that CSF mineralogy has a greater impact on fault properties than displacement. This is confirmed by comparing the  $K(\psi)$  curves for the two faults with the smallest displacements, Canyon Trail E14D's dense ZDB (20 cm of displacement) and Elmendorf fault B's diffuse ZDB (20-25 cm displacement). The largest differences in fault properties appear to be associated with CSF mineralogy rather than density of deformation bands. The  $K(\psi)$  curves for the two Elmendorf faults A and B, which have pure smectite CSF, differ substantially from one another, perhaps because of deformation band density (fault A is a dense ZDB whereas fault B is a diffuse ZDB), or because of differences in displacement (54 cm for fault A versus 20-25 cm for fault B). The similarity in hydraulic properties for all dense zones of deformation bands suggests that cataclasis and compaction produce fairly consistent changes in pore networks, regardless of displacement magnitude or CSF composition, for the ranges studied here.

Protolith hydraulic properties show greater variability than fault properties, but this is only partially explained by differences in the mineralogy of the clay size fraction. Compared to Canyon Trail protolith and its mixed clay CSF, the Elmendorf protolith, with its pure smectite CSF, has much lower  $K_s$  values and crossover points which occur at much lower (drier) matric potential values (Figure 4.3). The pure smectite CSF makes

Elmendorf sands more conductive than the nearly all of the Canyon Trail sands under dry (low matric potentials) conditions (Figure 4.3). With the exception of a single sample (DS05 from E14 foot wall), the E13 and E14 protolith  $K(\psi)$  curves fall almost wholly outside the range observed for E10 protolith (Figure 4.3), despite their similarities in grain size, composition, and mixed clay CSF, which suggests moisture content and hydraulic conductivity will vary substantially across the sand beds given a single governing matric potential.  $K(\psi)$  curves for protolith with pure smectite CSF are even farther separated from those observed for E10 protolith samples with mixed clay CSF.

The contrast in hydraulic properties between related samples of fault and protolith appears to depend more on the protolith's CSF mineralogy and the fault's density of deformation bands than on fault displacement. The contrast between protolith and fault hydraulic properties is consistently much larger for sites with mixed clay CSF than sites with pure smectite CSF. The protolith – fault disparity is limited to a narrower  $\psi$  range for faults with widely spaced deformation bands than faults with more closely spaced deformation bands.

We attribute the large and unexpected difference between air and water  $K_s$  values for Elmendorf sands and faults to the pure, and likely authigenic, smectite CSF. SEM micrographs show some sand grains from the Elmendorf site are rimmed with plates of smectite, oriented normal to grain surfaces as either low-relief ridges or interwoven pillars that bridge intergranular pores [Sigda, 1997]. These bridge and ridge textures observed in the Elmendorf protolith are associated with authigenic smectite, which has been shown to severely reduce  $K_s$  in petroleum reservoir sandstones [Wilson and Pittman,

1977; Wilson and Stanton, 1994]. This raises a question about the role of the sizeable amounts of smectite detected in the Canyon Trail samples that did not show any significant difference between water-based and gas-based  $K_s$  measurements, whereas the pure smectite CSF in the Elmendorf samples reduced water-based  $K_s$  measurements by at least three orders of magnitude relative to gas-based  $K_s$  measurements. These results suggest that air permeability analyses be supplemented by analyses of CSF mineralogy in areas where pure smectite CSF might be present.

#### **4.5 Flow and transport modeling**

The four new fault sites demonstrate large differences in unsaturated hydraulic properties. Are these differences geologically or hydrologically significant? The following analyses and discussion focus on the flow and transport behavior predicted for two scenarios, gravity-driven and evaporation-driven flow, in the context of competing processes. Each site is represented by at least one protolith – fault pair (Table 4.6) to investigate crossover behavior and the impacts of fault spatial density. Fault spatial densities of one 1 cm wide fault per every 100, 10, and 2 m of sand along an arbitrary horizontal axis are denoted as dimensionless ratios  $1:10^4$ ,  $1:10^3$ , and  $1:200$ , respectively.

**Table 4.6: Fault-protolith pairs for modeling**

Site/sample pairs	Pair name	Crossover $\psi$ (cm)
<b>Canyon Trail (mixed clay mineral CSF)</b>		
<b>E10 baseline</b>		
Mean dense sZDB in mean sand	E10	-51
<b>E13</b>		
Dense lZDB (DL08) in FW sand (NMT01)	E13	-44
<b>E14D</b>		
Dense sZDB (DS02) in FW sand (DS05)	E14D-1	-40
Dense sZDB (DS02) in HW sand (DS25)*	E14D-2	-86
<b>Elmendorf (pure smectite CSF)</b>		
Fault A dense sZDB (DS01) in FW sand (NMT03)	EA-1	-119
Fault A dense sZDB (DS01) in HW sand (NMT12)	EA-2	-125
Fault B diffuse sZDB (DL04) in HW sand (NMT03)	EB	-95

FW = foot wall; HW = hanging wall; sZDB = small-displacement zone of deformation bands; lZDB = large-displacement ZDB; CSF = clay size fraction.

\* No HW samples for site E14D were completely analyzed, so we use a HW sand sample for site E14 instead, even though fault E14D does not crosscut this particular sand. Sample DS25 is very similar in properties to the two other HW samples, DS24 and DS03 (Figure 4.3).

#### 4.5.1 Modeling results

**4.5.1.1 Gravity-driven flow and transport.** Fault-enhanced infiltration is only significant if it is appreciably larger than the liquid-phase flow of water through an unfaulted bed, and if it exceeds the fluxes of competing processes, e.g., vapor-phase water flux. We define net water flux,  $q_{net}$ , as the difference between downward liquid-phase,  $q_l$ , and upward geothermal-driven vapor-phase,  $q_v$ , flux densities (Appendix 4.A):

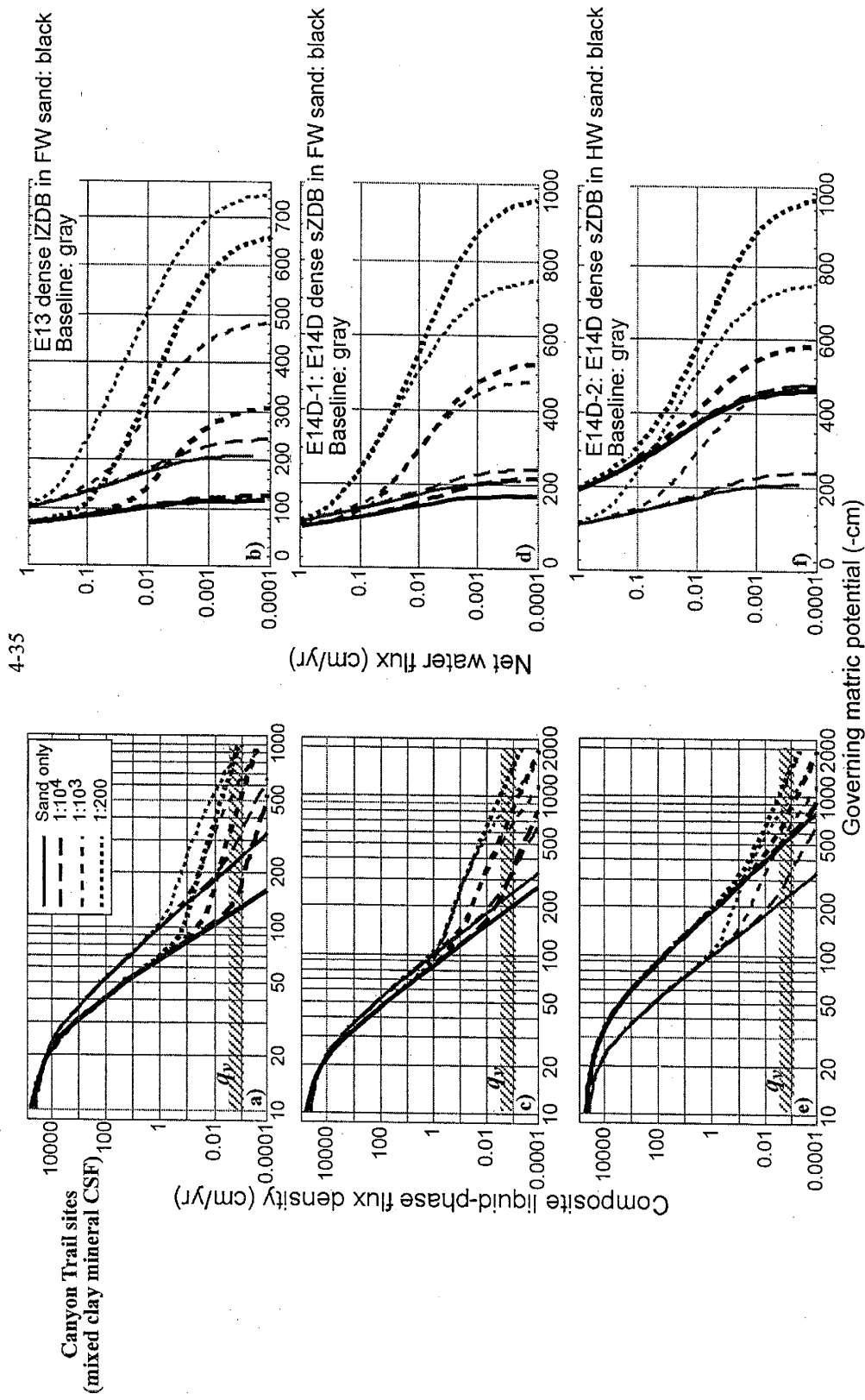
$$q_{net} = q_l - q_v \quad (4.3).$$

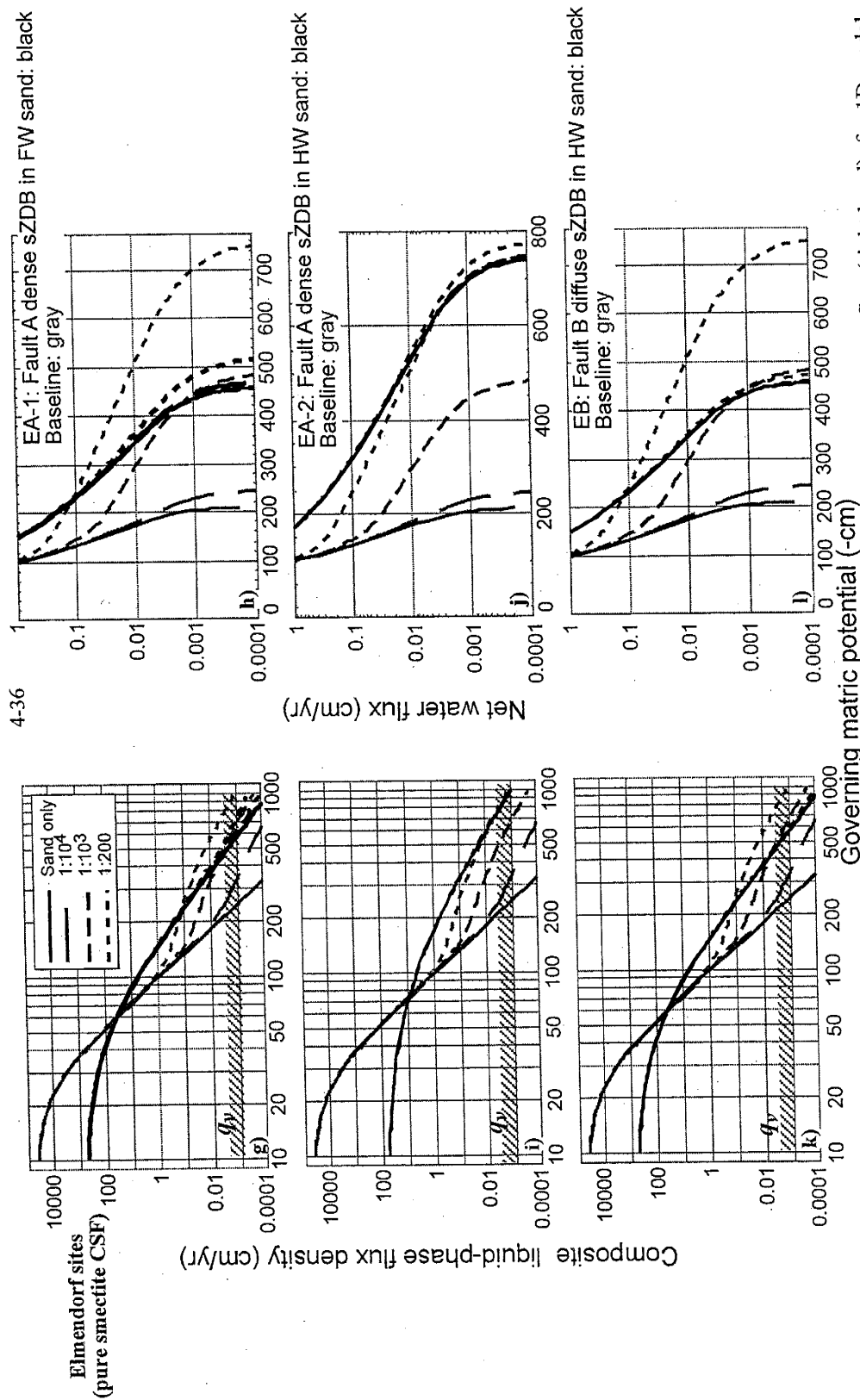
In this analysis,  $q_l$  also represents the composite flux density,  $q_c$ , for a sand bed with or without faults (Figure 4.3). The maximum vapor-phase flux density from the geothermal gradients observed in the vadose zone of the Rio Grande rift's Albuquerque Basin is estimated to range between  $9 \times 10^{-4}$  to  $3 \times 10^{-3}$  cm/year [Chapter 3], and is depicted as a

hatched area on the plots in Figure 4.3. To calculate net water flux (4.3), we arbitrarily selected the upper end of this range,  $q_v = 3 \times 10^{-3}$  cm/year [Chapter 3].

For protolith, infiltration varies widely in magnitude and net water flux varies in magnitude and direction, depending on matric potential and protolith CSF composition (solid curves in Figure 4.4). Under relatively wet conditions ( $\psi > \psi_x$ ), infiltration is substantial and net flux is downward, but as the system becomes drier ( $\psi \rightarrow \psi_x$ ), net water flux switches from downward to upward (Figure 4.4). This occurs at larger (wetter)  $\psi$  values for protolith with mixed clay mineral CSF than protolith with pure smectite CSF (Figure 4.4). The variability in dominance thresholds, which are transition points from dominance by one process to dominance by a competing process [Chapter 3], for protolith samples with mixed clay mineral CSF (Figure 4.4) suggest that at a given matric potential, some unfaulted beds will be dominated by liquid-phase infiltration whereas others will be dominated by upward vapor-phase water movement.

Infiltration through faulted sand beds can be greatly enhanced, relative to unfaulted beds, but enhancement depends on matric potential, fault density, and the composition of the clay size fraction (Figure 4.4). Fault spatial densities of  $1:10^4$ ,  $1:10^3$ , and  $1:200$  (Figure 4.A.1 in Appendix 4.A) can extend downward net water flux into much drier conditions than is possible with sand-only columns, but the minimum fault spatial density and associated matric potential vary from site to site (Figure 4.4). Under wet conditions, the matric potential is high enough (close to zero) that none of the fault spatial densities considered has any significant effect on increasing infiltration because all of the flow is focused within the protolith. Yet at sites with mixed clay mineral CSF under drier





conditions ( $\psi \leq -100$  cm), fault densities of at least  $1:10^3$  (one 1 cm wide fault every 10 m of sand) enhance infiltration by as much as one to two orders of magnitude, thereby extending downward net water flux into drier conditions (Figure 4.4a-f). Fault densities of  $1:10^4$  show slight or no infiltration enhancement. The amount of infiltration enhancement and the matric potential range over which enhancement occurs vary significantly between sites with mixed clay mineral CSF. At a fault density of  $1:10^3$ , for example, infiltration enhancement occurs roughly within the range  $-90 \geq \psi \geq -300$  cm for site E13,  $-130 \geq \psi \geq -500$  cm for the baseline (E10) site, and for the E14D site the range is  $-100 \geq \psi \geq -550$  cm for the E14D-1 pair of samples and  $-300 \geq \psi \geq -600$  cm for the E14D-2 pair of samples (Figure 4-6a-f). In contrast, for sites with pure smectite CSF, Fault A's dense zone of deformation bands enhances infiltration and extends downward net flux into drier conditions at fault densities of  $1:200$  and greater, but Fault B's diffuse zone of bands has no impact at the densities studied (Figure 4.4g-j).

Under the gravity-driven flow scenario, solute transport through faults is far faster than transport through protolith given dry vadose-zone conditions. Whereas solute residence times,  $t_r$  (A.7), for protolith are shorter than those for faults under relatively wet ( $\psi$  near 0) vadose-zone conditions, under drier conditions protolith  $t_r$  is as much as four orders of magnitude longer than fault  $t_r$ , whether transport is dominated by advection or diffusion (Figure 4.5a-b). Indicated by the sharp change in slope for each  $t_r(\psi)$  curve, the transition from dominance by advection to dominance by diffusion (dominance threshold for diffusion [Chapter 3]) occurs in relatively wet conditions for protolith and in much drier conditions for faults (Figure 4.5a-b). The differences in protolith and fault residence

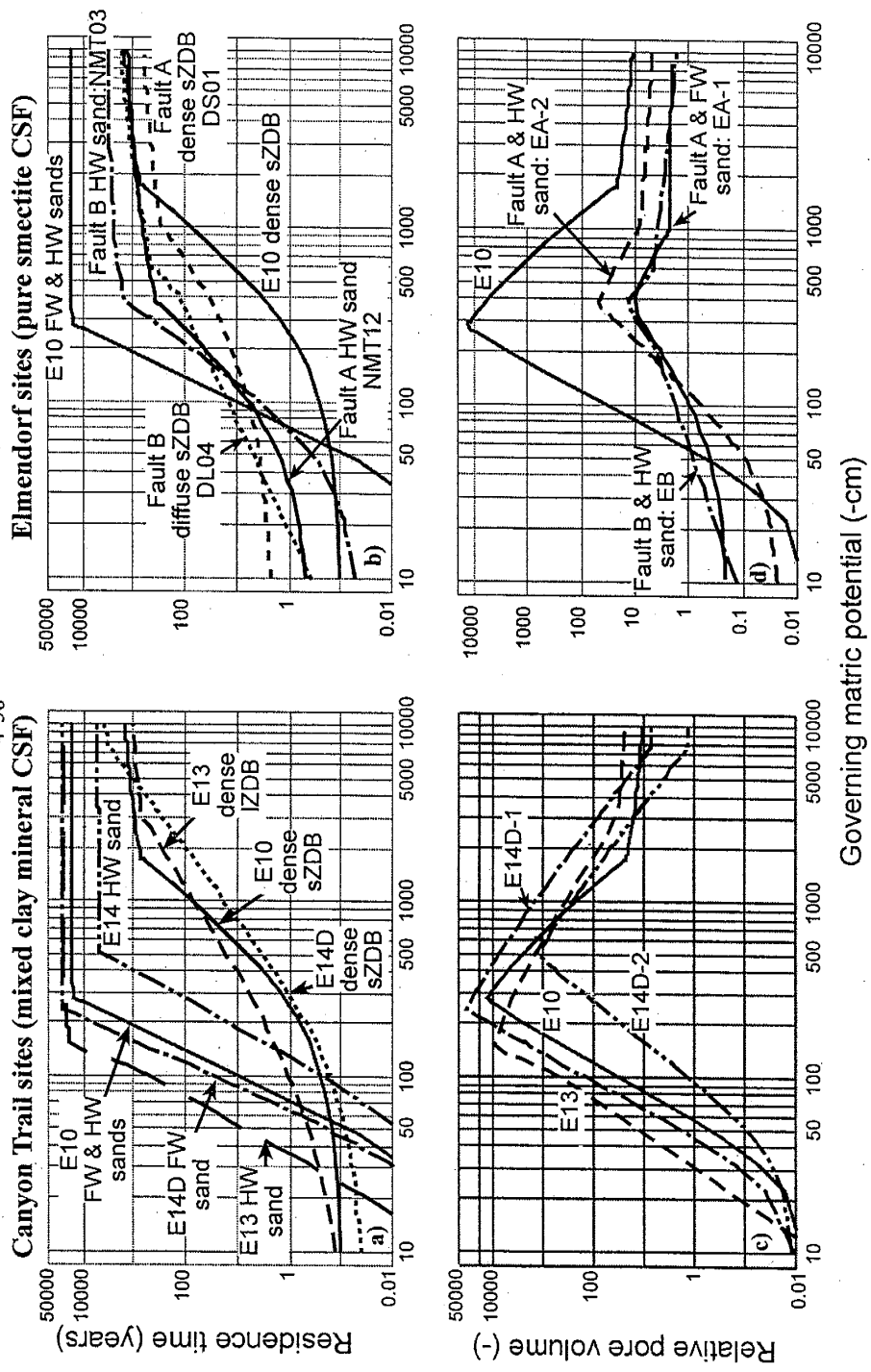


**Figure 4.5:** Transport in gravity-driven flow. Residence time,  $t_r$ , (top row), and relative pore volumes,  $P_r$ , (bottom row) versus governing matrix potential. Canyon Trail results are plotted in a) and c); Elmendorf results are plotted in b) and d). Residence time is the larger of advection and diffusion residence times. FW = footwall; HW = hanging wall; szDB = small-displacement zone of deformation bands; LZDB = large-displacement ZDB.

times are largest for sites with mixed clay mineral CSF (Figure 4.5a), whereas the differences are smaller, though significant, for sites with pure smectite CSF (Figure 4.5b).

The much shorter solute residence times predicted for faults, relative to protolith, imply faults are much more likely to undergo a more rapid rate of diagenesis than protolith under drier vadose-zone conditions. Our estimates of relative pore volume,  $P_r$  (A.8), predict that, given drier ( $\psi < -100$  cm) conditions, 1,000 to ~40,000 pore volumes will pass through a 1 m column of fault in the time it takes to pass a single pore volume through a 1 m column of protolith at sites with mixed clay mineral CSF (Figure 4.5c). For sites with pure smectite CSF, relative pore volumes range from less than 1 to less than 100 given the same conditions (Figure 4.5d).

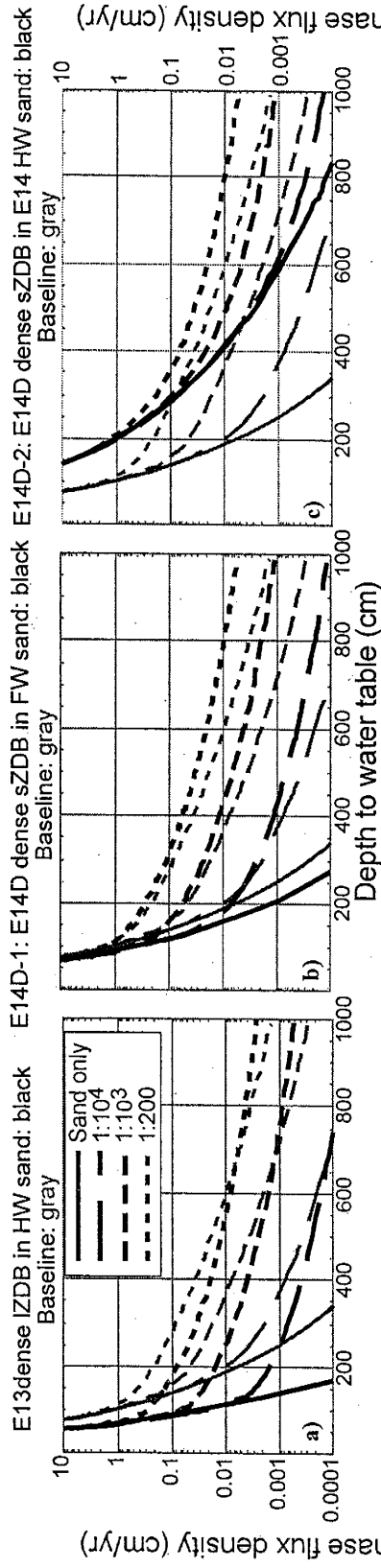
**4.5.1.2 Evaporation-driven flow and transport.** Exfiltration, which is liquid-phase flow up and out of the vadose zone, through a faulted sand bed only becomes hydrologically significant if it is appreciably larger than exfiltration through an unfaulted bed, and if it exceeds competing flow processes. The controlling variable for liquid-phase exfiltration is depth to the shallow water table,  $H$  (Appendix 4.A). Thermally driven vapor-phase flux, which is a potential competing flow process, is controlled by time-varying surface boundary conditions such as those investigated by Scanlon and Milly [1994] in their model of the Hueco Bolson of the Rio Grande valley near El Paso, TX. They estimated a maximum downward vapor-phase flux density of  $\sim 10^{-3}$  cm/yr and a maximum upward value of  $5 \times 10^{-3}$  cm/yr for the summer and winter, respectively. Flux maxima were predicted to occur at roughly 2 m depth (Figure 12 in Scanlon and Milly [1994]). Although these seasonal fluxes are not directly comparable to our steady

state fluxes, we use the largest downward value,  $10^{-3}$  cm/yr as a threshold for the competing process. If the liquid-phase flux from exfiltration falls below this value, vapor-phase flow is possibly more important than exfiltration in this scenario.

Exfiltration fluxes through protolith vary significantly with depth to the water table and CSF mineralogy (Figure 4.6 solid curves). Exfiltration flux rates decrease with increasing depth to the water table, but fluxes through all protolith samples with mixed clay mineral CSF except those from the E14 HW decrease most steeply, whereas those from the E14 HW and those with pure smectite CSF decrease less steeply (Figure 4.6). This allows the E14 HW and Elmendorf sands to transmit exfiltration fluxes which are orders of magnitude larger than those transmitted by the protolith from E13, E14 FW, and E10 sites, which reach the threshold for competing thermal vapor-phase flow at fairly wet conditions ( $> -300$  cm). The E14 HW and Elmendorf protolith samples do not reach the threshold until conditions are far drier (Figure 4.6).

Exfiltration is significantly enhanced in faulted sands and is controlled by fault spatial density, density of deformation bands, and CSF mineralogy (dashed curves in Figure 4.6). Exfiltration enhancement can reach two orders of magnitude for faulted sands with mixed clay mineral CSF, even at the  $10^4$  spatial density (Figure 4.6a-c), whereas enhancement is negligible for all faulted sands with pure smectite CSF, except pair EA-1, fault A in its footwall protolith (Figure 4.6d-f). Enhancement is possible at fault spatial densities of  $1:10^3$  and greater for water table depths between roughly 100 and 1000 cm for the sites with mixed clay mineral CSF (Figure 4.6a-c), but is limited to a range of only 400 to 1000 cm at a density of 1:200 or greater for sample pair EA-1 (Figure 4.6d-f).

### Canyon Trail sites (mixed clay mineral CSF)



### Elmendorf sites (pure smectite CSF)

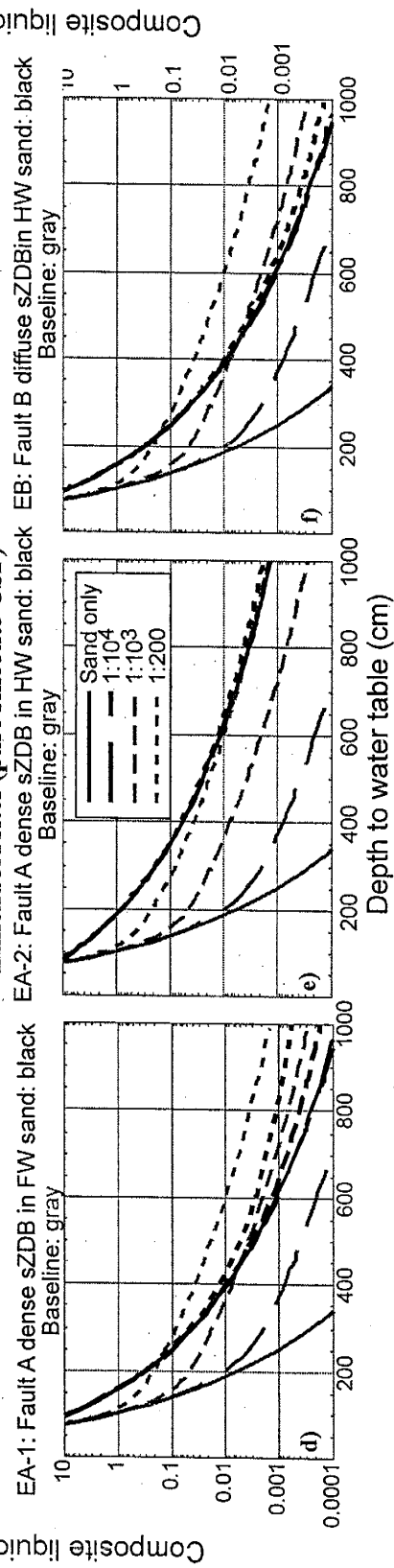


**Figure 4.6:** Evaporation-driven flow. Curves show upward liquid-phase composite flux density,  $q_e$ , from evaporation as a function of water table depth and fault density. Baseline (E10) shown in gray. Solid curves show flux density from unfaulted sand columns. a) Canyon Trail E13; b) and c) are from Canyon Trail E14 site; d) - f) are from Elmendorf area.

Evaporation-driven solute transport is also greatly enhanced for faults versus protolith. Controlled by water table depth, CSF mineralogy, hydraulic properties, and deformation band density, solute residence time,  $t_r$ , for the evaporation-driven scenario (A.7, A.11, A.12) can be as much as four orders of magnitude longer for protolith than faults at sites with mixed clay mineral CSF (Figure 4.7a and c). For sites with pure smectite CSF, the difference in fault and sand residence times is less than three orders of magnitude (Figure 4.7b and d). Only protolith samples show a switch from transport dominance by advection to diffusion; in contrast, solute transport through faults is dominated by advection over the entire range of depths to the water table studied.

Estimates of relative pore volume,  $P_r$  (A.8), indicate that faults should be preferentially altered given dry conditions for the evaporation-driven scenario. Sites with mixed clay mineral CSF can transmit more than 10,000 pore volumes in the time needed for a single sand pore volume for water table depths greater than 100 cm (Figure 4.7c). Maximum relative pore volume for sites with pure smectite CSF is much less, between only 1 and 200, for water table depths  $> 100$  cm (Figure 4.7d).

#### 4.5.2 Discussion of modeling

Our modeling results predict that deformation band faults can significantly affect flow and transport through vadose zone sand beds by increasing infiltration, exfiltration, and diagenesis as well as greatly reducing solute residence times. Our results, which corroborate predictions made for the baseline fault [Chapter 3], provide an affirmative answer to the question, “Are differences in fault and sand hydraulic properties

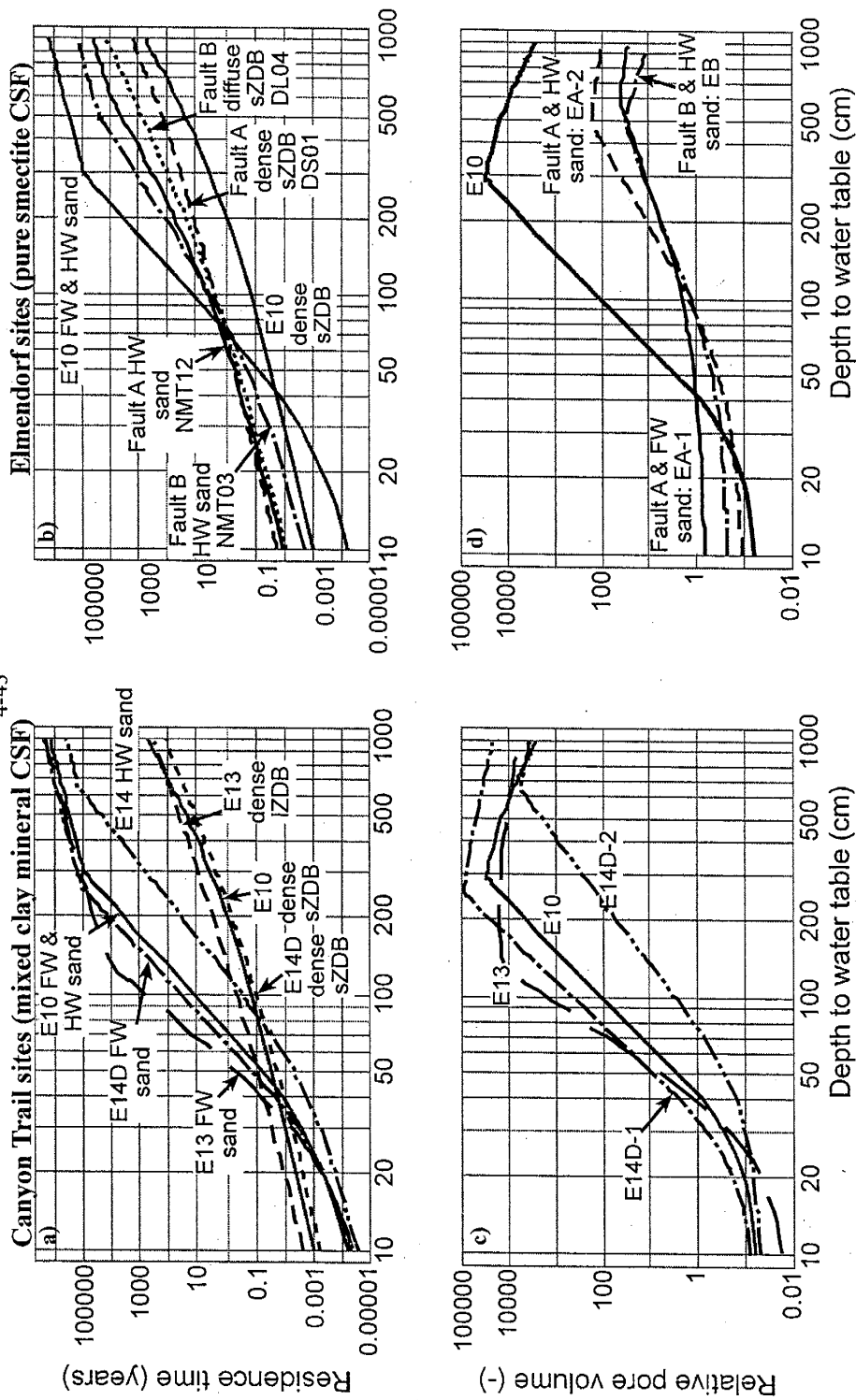


**Figure 4.7:** Evaporation-driven transport. Residence time,  $t_r$ , (top row), and relative pore volumes,  $P_r$ , (bottom row) as a function of depth to water table. Results for Canyon Trail data are plotted in a) and c); Elmdorf data are plotted in b) and d). CSF = clay size fraction; FW = footwall; HW = hanging wall; SZDB = small-displacement zone of deformation bands; IZDB = large-displacement ZDB.

hydrologically significant?”. The modeling results also offer an initial answer to the question, “Do protolith and fault characteristics cause significant variability in preferential flow and solute transport through faulted vadose-zone sand beds?” Predicted hydrologic impacts depend on the mineralogy of the clay size fraction and on the spacing between deformation bands, but are not significantly affected by the range of fault displacements studied here.

Infiltration and exfiltration through faulted sand beds can be as much as two orders of magnitude greater than fluxes in unfaulted beds only or fluxes from competing processes, given fault spatial densities previously observed in the Rio Grande rift. Flow enhancement is far greater at sites with mixed clay mineral CSF than sites with pure smectite CSF. Flow enhancement is also greater at faults with dense distributions of deformation bands than faults with diffusely distributed bands. Predicted flow enhancement is negligible for the one fault with a diffuse distribution of deformation bands, Elmendorf fault B, which crosscuts protolith with pure smectite CSF (pair EB in Table 4.6). Infiltration enhancement by faults extends dominance by liquid-phase flow over geothermal-driven vapor-phase flow into much drier conditions, thereby allowing downward net water flux to occur at matric potential values as low as approximately -900 cm for a fault spatial density of 1:200 or greater at sites with mixed clay mineral CSF (Canyon Trail area). Similarly, these same faults can extend transport of water from a shallow water table to the atmosphere into systems with much greater depths to the water table given fault densities of 1:10<sup>4</sup> and greater.

There is appreciable variability in flow behavior between the four new sites, with some sites causing greater impacts and others causing smaller impacts than those predicted for the baseline site [Sigda and Wilson, 2003 and Chapter 3]. The observed variability in behavior for faults and for protolith indicates that the vadose-zone flow processes studied here should vary widely in space. Enhanced infiltration begins and ends at different matric potentials for each site, and, similarly, enhanced exfiltration begins and ends at different water table depths for each site. To achieve enhanced flow, higher fault densities are needed for infiltration than exfiltration. Likewise, higher fault densities are required for enhanced flow at sites with pure smectite CSF than sites with mixed clay mineral CSF. This suggests that for any given steady flow system in relatively dry vadose-zone conditions, preferential liquid-phase fluxes could vary widely within the same faulted sand beds. Observed fault widths vary from the model's assumed width of 1 cm, so a fault 6 - 15 cm wide, such as E13, can enhance infiltration through a much wider sand bed than a 1 cm wide fault with the same properties. The 1D analysis ignores any effects from variations in dip and cross-cutting relationships.

All the faults studied here can significantly accelerate solute transport through sand beds under the range of conditions encountered in arid and semi-arid vadose zones. Solute residence times are roughly one to nearly five orders of magnitude longer in protolith than faults, whether flow is driven by gravity or evaporation. The differences in solute residence times, and therefore relative pore volumes, between fault and protolith is much greater at sites with mixed clay mineral CSF than sites with pure smectite CSF. The location of the dominance threshold for diffusion, the point at which the advective flux rate decreases to the magnitude of diffusive flux rate, also appears to vary with

protolith CSF as the threshold occurs under wetter conditions (larger  $\psi$  or smaller  $H$ ) for mixed clay mineral CSF than pure smectite CSF. Thus, advective solute flux exceeds diffusive flux in protolith with mixed clay mineral CSF for a narrower range of matric potential ( $\psi$ ) or water table depth ( $H$ ) than in protolith with pure smectite CSF, making diffusion the dominant solute transport process in protolith across most of the  $\psi$  and  $H$  ranges studied here. Differences in  $t_r$  for protolith and fault are larger for faults with dense distributions of deformation bands than faults with diffusely distributed bands. Whereas advection yields to diffusion in protolith as conditions become drier (decreasing  $\psi$  in the gravity scenario or increasing  $H$  in the evaporation scenario), advection dominates transport through faults across much of the  $\psi$  and  $H$  ranges.

Preferential diagenesis, such as cementation, in faults rather than protolith can thus be explained by the large differences in calculated relative pore volumes. As many as four orders of magnitude more pore volumes pass through faults in the time needed to pass through a single pore volume through the same amount of protolith. Relative pore volumes are larger under evaporation-driven flow than gravity-driven flow, which suggests the preferentially cemented fault fins observed at the northern Elmendorf area [Chapter 3, Figure 4.1a] were more likely caused by exfiltration than infiltration.

The presence authigenic smectite within the clay size fraction appears to have a very significant impact on the hydraulic properties of protolith and, to a lesser extent, on faults. Although it is possible that another, as yet undetermined, cause is responsible for the differences between Canyon Trail and Elmendorf areas in protolith properties and hydraulic behavior, the similarities in the point count data (Table 4.2) and physical

proximity (3 km) of the two study areas suggest otherwise. Sites containing smectite and a mixture of other clay minerals in the clay size fraction demonstrate much larger differences in the hydraulic behavior of faults and protolith than sites with pure smectite CSF. Smectites constitute approximately 2.4% by volume of the Canyon TrailE10 footwall protolith, compared to 6% of the Elmendorf hanging wall protolith for fault A (Tables 4.1 and 4.3), but is the cause this difference in the amount of smectite or some other characteristic, such as the orientation of the smectite plates discussed previously? As smectite is a common alteration product of volcanic detritus (glass, lithic fragments), it is likely distributed across a significant portion of the Rio Grande rift and similar areas, and should be tested for in hydrologic characterization studies.

#### **4.6. Conclusions**

Our measurements and modeling reveal that there are very significant differences in hydraulic properties and hydrologic behavior between deformation band fault and poorly lithified parent sand for the four new fault sites studied here. These differences indicate that faults can act as preferential pathways for flow and transport through vadose-zone sand beds under arid or semi-arid conditions. Fault saturated hydraulic conductivity ( $K$ ) is one to three orders of magnitude less than protolith saturated  $K$ , and depends on the composition of the clay size fraction (CSF). Fault porosity and air entry matric potentials are appreciably smaller and larger, respectively, than those for the protolith. One study area has a CSF with pure and presumably authigenic smectite, whereas the other study area has a CSF with a mixture of smectite, other clay minerals, and other minerals.

Protolith hydraulic properties differ greatly between the two areas, as saturated  $K$  is more than two orders of magnitude lower for protolith with pure smectite CSF than for protolith with mixed clay mineral CSF, even though point count analyses show no significant differences between the protolith samples. CSF mineralogy appears to have a smaller impact on fault hydraulic properties than it does on protolith properties.

Given an adequate fault spatial density, the large differences in hydraulic properties can induce greater infiltration or exfiltration from a shallow water table, effectively extending liquid-phase fluxes into drier conditions where competing vapor-phase flow processes would otherwise dominate water movement. Gravity-driven infiltration as well as evaporation-driven exfiltration flux rates in faulted sands, given a sufficient fault density, can be increased up to two orders of magnitude above the flux rates predicted for either unfaulted sand or the competing vapor-phase flow process. The fault densities necessary to enhance flow are higher for infiltration than for exfiltration and higher for sites with pure smectite CSF than sites with mixed clay mineral CSF. We have observed fault densities that are more than sufficient to increase infiltration and exfiltration under the relatively dry vadose-zone conditions of the Rio Grande rift and similar areas.

Solute residence times are roughly one to nearly five orders of magnitude longer in protolith than faults, whether flow is driven by gravity or evaporation. Advection yields to diffusion as the dominant transport process in protolith for drier conditions, i.e., decreasing matric potential  $\psi$  for the gravity scenario or increasing depth to water table  $H$  for the evaporation scenario. In contrast, advection dominates transport through faults across much of the ranges for both  $\psi$  and  $H$ . As many as four orders of magnitude more

pore volumes pass through faults in the time needed to pass through a single pore volume through the same amount of protolith. Consequently, faults are far more likely to undergo preferential cementation or other diagenetic changes.

Clay size fraction mineralogy and density of the distribution of deformation bands within the fault help control enhancement of flow and transport processes. However, differences between fault and protolith in properties and behavior remain consistent regardless of CSF composition for the materials studied here. Enhancement is greater for sites having a clay size fraction (CSF) that contains mixed clay minerals than for sites that have a pure (authigenic) smectite CSF. Enhancement is also greater for faults with closely spaced (dense) deformation bands than faults with more widely spaced (diffuse) deformation bands. For the range of displacement studied here, fault displacement appears to have no significant impact on hydraulic property differences or enhancement of flow and solute transport processes. The location of the dominance threshold for diffusion, the point at which the advective flux rate decreases to the magnitude of diffusive flux rate, also appears to vary with protolith CSF because the threshold occurs under wetter conditions (larger  $\psi$  or smaller  $H$ ) for mixed clay mineral CSF than pure smectite CSF. Thus, advective solute flux exceeds diffusive flux in protolith with mixed clay mineral CSF for a narrower range of matric potential ( $\psi$ ) or water table depth ( $H$ ) than in protolith with pure smectite CSF, making diffusion the dominant solute transport process in protolith across most of the  $\psi$  and  $H$  ranges studied here. Differences in solute residence times between protolith and fault are larger for faults with dense distributions of deformation bands than faults with diffusely distributed bands.

**Acknowledgements.** This National Science Foundation's Hydrologic Sciences Program funded this study, grant number EAR-9614385. We thank the staff of the Bosque del Apache National Wildlife Refuge and the Burlington Northern Santa Fe Railroad for access to the study site; our fellow members of New Mexico Tech's Faults and Fluid Flow group, especially Bill Haneberg, Matt Herrin, and Geoff Rawling for many hours of helpful discussion; Judith Wright and Paula Heller of UFA Ventures for access to multiple UFA systems and assistance in conducting the UFA experiments; Bob Glass of Sandia National Laboratories for use of his Flow and Transport Laboratory; and George Austin of the New Mexico Bureau of Geology and Mineral Resources for the XRD analyses.

#### **Appendix 4.A: Flow and transport models**

**Gravity-driven advection and diagenesis.** Under the assumptions of one-dimensional, steady flow, uniform ambient matric potential, and uniform hydraulic properties, the liquid-phase flux density, which is given by Darcy's law,

$$q_l(\psi) = -K(\psi) \frac{d}{dz}(\psi + z) = -K(\psi) \left( \frac{d\psi}{dz} + 1 \right) = -K(\psi) \quad (\text{A.1})$$

which depends only on the constant ambient matric potential, where  $q_l$  is liquid-phase flux density ( $\text{LT}^{-1}$ ),  $\psi$  is matric potential (L),  $K(\psi)$  is the hydraulic conductivity ( $\text{LT}^{-1}$ ) function,  $z$  is the vertical axis (L) oriented positive upwards,. This flow regime can be used to describe the steady movement of water through the middle portion of a thick vadose zone, well below the root zone and well above the capillary fringe.

We gauged the effect of the number of deformation band faults per unit area on moisture movement by calculating the relative increase in exfiltration or infiltration through an idealized vadose zone column, composed of a fault and surrounding sand, as a function of fault spatial density (Figure 4.A.1). The composite flux density for any column is determined by weighting the flow through fault and through sand according to their contributions to the composite column's total width ( $W_T$ ). Sand and fault properties are each considered uniform. Faults are assumed to have a constant width of 1 cm (e.g., fault E10), 90° dip, and spatial densities ranging between one fault per 2 m and one fault per 100 m. As fault width is always much less than the column width occupied by sand (thus  $W_T \approx W_s$ ), the expression for the flux density of the composite column can be simplified:

$$q_c = \frac{q_s W_s + q_f W_f}{W_s + W_f} \approx \frac{q_s W_s + q_f W_f}{W_s} = q_s + \frac{W_f}{W_s} q_f \approx q_s + d_f q_f \quad (\text{A.2})$$

where  $q_c$  is liquid-phase flux density for the composite column (L/T);  $W_s$ ,  $W_f$ ,  $q_s$ , and  $q_f$  are the widths (L) and flux densities (L/T) for the sand and fault portions, respectively; and  $d_f$  is the fault spatial density (-). The composite flux density was calculated as a function of fault spatial density and either ambient matric potential (gravity-driven scenario) or depth to water table (evaporation-driven scenario – see below).

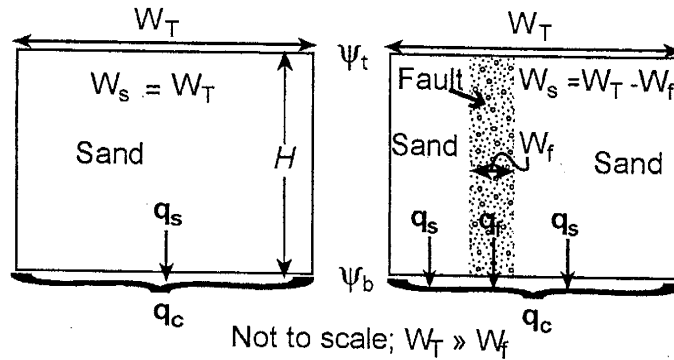


**Figure 4.A.1:** Idealized columns for determining impact of fault spatial density. Fault width ( $W_f = 1$  cm) is much smaller than total column width ( $W_T = 100, 10$ , or  $2$  m). Composite flux density for column is  $q_c$ . Sand and fault flux densities,  $q_s$  and  $q_f$ , are shown for the gravity-driven scenario in which the matric potential is uniform throughout column ( $\psi_t = \psi_b$ ). For the evaporation-driven scenario,  $H$  is the water table depth, the bottom boundary is at the water table ( $\psi_b = 0$  cm) and the top boundary at ground level ( $\psi_t = -10,000$  cm). Taken from [Chapter 3].

The time,  $t_a$ , to advectively pass one pore volume of a conservative solute moving with no dispersion through a uniform, vertical column of length  $L$  is then

$$t_a(\psi) = L/v_s(\psi) = L\theta(\psi)/q_l(\psi) \quad (\text{A.3})$$

where  $v_s$  is the seepage velocity ( $\text{LT}^{-1}$ ) and  $\theta$  is the volumetric moisture content ( $\text{L}^3\text{L}^{-3}$ ).

It too only depends on the domain's ambient matrix potential.

The time to diffusively pass one pore volume of the same solute through the same column can be calculated by solving Fick's second law for an appropriate set of initial and boundary conditions. We assumed a semi-infinite domain with a constant concentration ( $C_0$ ) boundary at  $L = 0$  and a zero initial concentration throughout the domain. A constant source concentration is appropriate for the relatively short travel distance considered (10 m column length out of a 100 – 300 m thick vadose zone) and a semi-infinite domain is reasonable given the length and time scales considered. There are other reasonable choices of initial, boundary, and breakthrough conditions, but they do not change the relative differences observed in fault and sand behavior. The solution of Fick's law for this set of initial and boundary conditions is [Crank, 1975, pp. 20-21]:

$$C(L,t)/C_0 = 1 - \text{erf}(L/2\sqrt{Dt}) \quad (\text{A.4})$$

where  $L$  (L) is the distance from the constant source,  $\text{erf}$  is the error function, and  $D$  is the diffusion coefficient ( $\text{L}^2/\text{T}$ ). The time needed for the solute concentration at a distance  $L$  (cm) from the boundary to reach the arbitrary value  $0.5C_0$  can be calculated by recalling the error function value essentially equals its argument value if it is near 0.5:

$$t_d(\psi) \cong L^2 / D(\theta(\psi)) \quad (\text{A.5}).$$

Here  $t_d$  is the time to diffusively pass one pore volume (T) and  $D(\theta)$  is the effective diffusion coefficient ( $L^2/T$ ) for a porous medium with volumetric moisture content  $\theta$ . Substituting  $D(\theta)$  for  $D$  in (A.5) is valid for a gravity-driven flow regime because matric potential and moisture content are constant throughout the domain length. The  $D(\theta)$  coefficient is estimated using the Millington and Quirk [1961] model, which equates  $D(\theta)$  to the product of the free water diffusion coefficient,  $D_0$ , and a tortuosity factor,  $\tau$ , dependent on  $\theta$  and the saturated moisture content (porosity),  $\theta_s$ .

$$D(\theta) = D_0 \tau(\theta) = D_0 \theta^{\frac{10}{3}} \theta_s^{-2} \quad (\text{A.6})$$

The effective diffusion coefficient (A.6) and diffusion residence time (A.5) can all be restated as functions of the ambient matric potential using the fitted  $K$ - $\psi$  curves.

We define solute residence time,  $t_r$ , as the greater of advective or diffusive residence times (Equations A.4 and A.6) for a given matric potential:

$$t_r(\psi) = \begin{cases} t_a(\psi) & \text{if } t_a \geq t_d \\ t_d(\psi) & \text{if } t_a < t_d \end{cases} \quad (\text{A.7}).$$

This approach ignores any additive interaction between advection and diffusion when they are of similar magnitude, yielding unrealistically sharp changes in the slope of  $t_r(\psi)$ . Solute residence time is defined in the same way for evaporation-driven flow and transport, but water table depth  $H$  replaces  $\psi$  as the governing variable (see below).

Our proxy measure for diagenesis is the relative number of pore volumes,  $P_r$ , defined as the number of fault pore volumes which are displaced in the time needed to displace a single sand pore volume. This is simply the ratio of sand to fault residence times:

$$P_r(\psi) = \frac{\text{sand } t_r(\psi)}{\text{fault } t_r(\psi)}. \quad (\text{A.8})$$

**Evaporation-driven advection and diagenesis.** Gravity, pulling downwards, and the matric potential gradient, pulling upwards, determine the advective flux density for steady upward liquid-phase flow from a shallow water table to the ground surface, where evaporation removes water from the domain. Matric potential, moisture content, and thus  $K$  vary within the domain. Flux density is a nonlinear function of the domain length, material properties, and the boundary  $\psi$  values. Under conditions of one dimensional, steady flow, Darcy's law can be written in integral form as [Irmay, 1968]

$$z_T - z_B = - \int_{\psi_B=0}^{\psi_T} \left[ \frac{q_l}{K(\psi)} + 1 \right]^{-1} d\psi \quad (\text{A.9})$$

where  $z$  is the vertical axis (positive upwards),  $z_T$  and  $z_B$  are the elevations [L] of the top and bottom boundaries,  $\psi_T$  and  $\psi_B$  are the matric potential values at those boundaries,  $q_l$  is the liquid-phase flux density through the column (positive for upward flow), and  $K(\psi)$  is the hydraulic conductivity. The bottom boundary condition is  $\psi = 0$  cm for a water table boundary. We take  $z_T = 0$  and  $z_B = -H$ , where  $H$  (L) is the depth to the water table. By assuming  $K(\psi)$  is an exponential function of the form

$$K(\psi) = K_s \exp(-\alpha|\psi|), \quad (\text{A.10})$$

Gardner [1958] solved (A.9) analytically and then determined the maximum flux density,  $q_l$ , by setting  $\psi_T = -\infty$ . As (A.10) poorly matched the UFA results, we constructed a series of piecewise continuous Gardner exponential functions (A.8) to mimic the sand and fault MvG  $K(\psi)$  functions. Equation (A.9) can then be rewritten as a system of nonlinear equations dependent on the constant flux density and the water table depth,  $H$ . A new system of equations was generated for each  $H$  value, which varied between 10 and 1000 cm, and solved for  $q_l$  using *Mathematica*. The upper boundary potential,  $\psi_T$ , was arbitrarily set to -10,000 cm, because the flux density  $q_l(H)$  varies negligibly with  $\psi_T$  once it drops below -1000 cm [Gardner, 1958; Selker et al., 1999, p. 127].

Calculation of the time to advectively pass one pore volume through a given column length under the evaporation-driven flow scenario can be calculated using

$$t_a(H) = q_l(H)^{-1} \int_{z=H}^{z=0} \theta(z) dz \quad (\text{A.11}).$$

Solving the system of nonlinear equations for a given water table depth also yields information about the distribution of matric potential along column length, which can be used to calculate  $\theta(z)$  and so solve (A.10). The right-hand side integral in (A.11) is evaluated numerically. Diffusion-driven residence time for a pore volume (A.12) is calculated numerically for each value of  $H$  in a manner similar to that for (A.11):

$$t_d(H) \cong L \int_{z=H}^{z=0} D(\theta(z))^{-1} dz \quad (\text{A.12}).$$

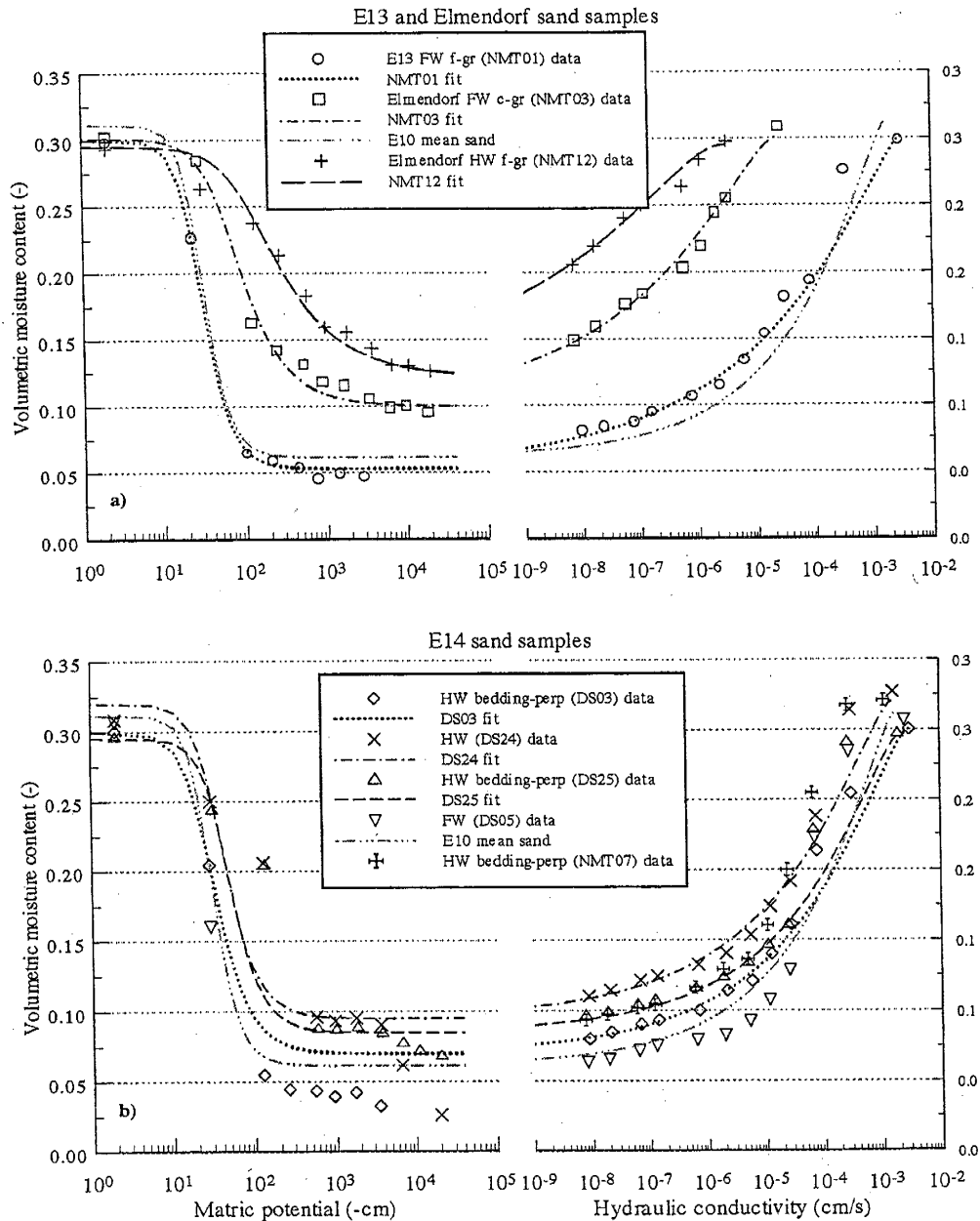
where  $D(\theta(z))$  is estimated from the Millington-Quirk model (A.6).

## Appendix 4.B: Sample MvG model fits

This appendix presents experimental observations, and data and Mualem-van Genuchten model fits (Figure 4.B.1) for all samples from the four new sites.

$\theta$ - $\psi$  experiments for two E14 samples, DS24 and DS25, may not have achieved equilibrium conditions because of a lapse in experimental procedure. All but the first two  $\theta$ - $\psi$  data points for site E14's sample DS03 are questionable because they force the  $\theta_r$  estimate to be far lower than can be supported by its  $K$ - $\theta$  data. The  $K$ - $\theta$  experiments yielded only a few  $K$ - $\theta$  data points for the two Elmendorf samples (DS01 and NMT19) from narrow zones of deformation bands. As noted by Sigda and Wilson [2003], the MvG model curves could not be made to closely match the  $K$ - $\theta$  data points just below saturation and still maintain a reasonably good fit at mid and lower saturation for the sand samples. Residual moisture content ( $\theta_r$ ) appeared to be typically higher in the  $K$ - $\theta$  curves than the  $\theta$ - $\psi$  curves.

$K_s$  is unexpectedly larger for bedding<sub>⊥</sub> DS25 than bedding<sub>∥</sub> DS24 at site E14. Also unexpected is the greater hydraulic conductivity of the bedding<sub>⊥</sub> samples relative to their paired bedding<sub>∥</sub> samples for any given moisture content (Figures B-). Perhaps this is indicative of experimental error. Yet we note the close agreement in  $K$ - $\theta$  data for the three bedding<sub>⊥</sub> samples from site E14: DS03, NMT07, and DS25.



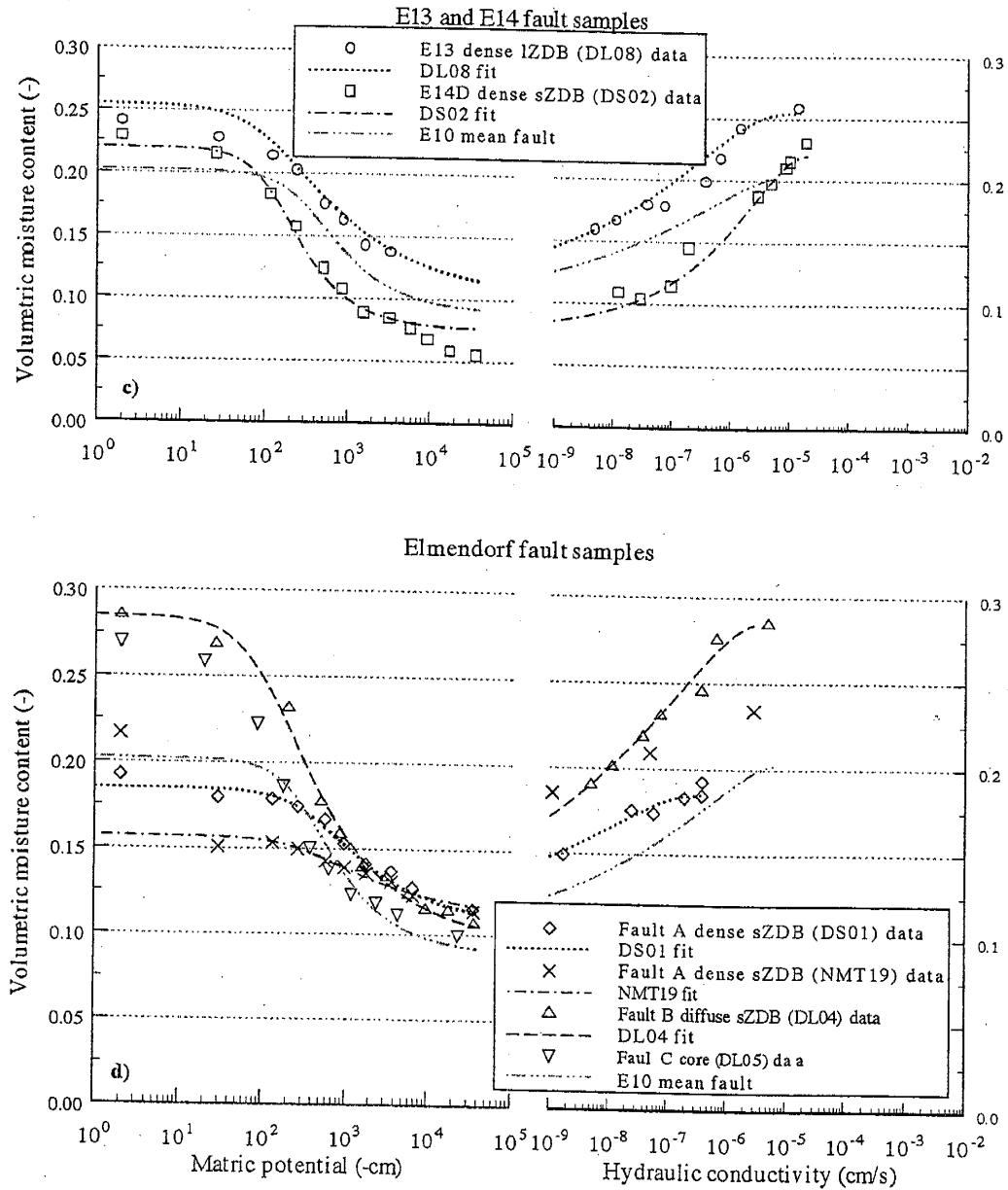


**Figure 4.B-1:** Mualem-van Genuchten model fits. Data and fitted curves for all samples.  
a) E13 and E14 protolith. b) Elmendorf protolith c) E14 and E14D faults  
d) Elmendorf faults

## 4.7 References

- Antonellini, M. and A. Aydin, Effect of faulting on fluid flow in porous sandstones: petrophysical properties, *AAPG Bulletin*, 78, 355-377, 1994.
- Antonellini, M., A. Aydin, and D. Pollard, Microstructure of deformation bands in porous sandstones at Arches National Park, Utah, *J. Struct. Geol.*, 16, 941-959, 1994.
- Aydin, A., Small faults formed as deformation bands in sandstone, *Pure and Applied Geophysics*, 116, 913-930, 1978.
- Aydin, A. and Myers, R., The permeability structure of fault zones formed from shearing of pre-existing joint zones, *Geological Society of America Abstracts with Programs*, 29, 416, 1997.
- Cashman, S. and K. Cashman, Cataclasis and deformation-band formation in unconsolidated marine terrace sand, Humboldt County, California, *Geology*, 28, 111-114, 2000.
- Conca, J. L. and J. V. Wright, Flow and diffusion in unsaturated gravel, soil and whole rock, *Applied Hydrogeology*, 1, 5-24, 1992.
- Conca, J., D. G. Levitt, P. R. Heller, T. J. Mockler, and M. J. Sully, Direct UFA measurements of unsaturated hydraulic conductivity, comparisons to van Genuchten/Mualem estimations, and applications to recharge mapping in *Arid Regions, in Characterization and Measurement of the Hydraulic Properties of Unsaturated*

- Porous Media*, M. Th. van Genuchten, F. J. Leij and L. Wu (eds.), Univ. Calif., Riverside, CA, vol. 2, 1173-1197, 1999.
- Crank, J., *The Mathematics of Diffusion*, 2nd edition, Oxford University Press, Oxford, UK, 414 pages, 1975.
- Davis, J. M., R. C. Lohmann, F.M. Phillips, J.L. Wilson, and D. W. Love, Architecture of the Sierra Ladrones Formation, central New Mexico: depositional controls on the permeability correlation structure, *Geological Society of America Bulletin*, 105, 998-1007, 1993.
- Forbes, P. L., Simple and accurate methods for converting centrifuge data into drainage and imbibition capillary pressure curves, *Log Analyst*, 35, 31-53, 1994.
- Gardner, W. R., Some steady state solutions of the unsaturated moisture flow equation with application to evaporation from a water table, *Soil Science*, 85, 228-232, 1958.
- Hassler, G. L., and E. Brunner, Measurement of capillary pressures in small core samples, *Transactions, AIME*, 160, 114-123, 1945.
- Hawley, J. W., compiler, Guidebook to Rio Grande Rift in New Mexico and Colorado, New Mexico Bureau of Mines and Mineral Resources, Socorro, New Mexico, 1978.
- Hawley, J.W. and Kernodle, J.M., Overview of the hydrogeology and geohydrology of the northern Rio Grande basin—Colorado, New Mexico, and Texas, in Ortega-Klett, C.T., ed., *Proceedings of the 44th Annual New Mexico Water Conference*: New

Mexico Water Resources Research Institute Report 312, 79-102, 2000.

<http://wrrri.nmsu.edu/publish/watcon/proc/proc44/contents.html>

Hawley, J. W., Haase, C. S., and Lozinsky, R. P., An underground view of the Albuquerque Basin, New Mexico, in Ortega-Klett, C. T., ed., Proceedings of the 39th Annual New Mexico Water Conference, New Mexico Water Resource Research Institute Report 290, 37-55, 1995.

Hawley, J.W., Kennedy, J.F., Creel, B.J., The Mesilla Basin aquifer system of New Mexico, West Texas and Chihuahua—an overview of its hydrogeologic framework and related aspects of groundwater flow and chemistry, in Angle, E.S., and Mace, R.E., Aquifers of West Texas: Texas Water Development Board Special Conference Proceedings Volume, 76-99, 2001.

Herrin, J. M., Characteristics of deformation bands in poorly lithified sand: Rio Grande rift, New Mexico, M.S. (Geology), New Mexico Institute of Mining and Technology, Socorro, New Mexico, 2001.

Heynekamp, M. R., L.B. Goodwin, P.S. Mozley, and W.C. Haneberg, Controls on fault-zone architecture in poorly lithified sediments, Rio Grande Rift, New Mexico; implications for fault-zone permeability and fluid flow, in *Faults and subsurface fluid flow in the shallow crust*, W. C. Haneberg, P.S. Mozley, J.C. Moore, and L.B. Goodwin, eds., *American Geophysical Union Monograph* 113, Washington, DC, US, 27-49, 1999.

- Hong, Sung-ho, Anisotropic hydraulic conductivity of faulted poorly consolidated eolian sands: Bosque, New Mexico, M.S. (Geology), New Mexico Institute of Mining and Technology, Socorro, New Mexico, 1999.
- Irmay, S., Solutions of the non-linear diffusion equation with a gravity term in hydrology, H. W. Rijtema and P. E. Wassink, editors, In Symposium on Water in the Unsaturated Zone, International Association of Scientific Hydrology-UNESCO, 1966, Wageningen, Netherlands, 1968.
- Khaleel, R., J. F. Relyea, and J. L. Conca, Estimation of van Genuchten-Mualem relationships to estimate unsaturated hydraulic conductivity at low water contents, *Water Resour. Res.*, 31, 2659-2668, 1995.
- Millington, R.J. and J.P. Quirk, Permeability of porous solids, *Trans. Faraday Soc.*, 57, 1200-1207, 1961.
- Mollema, P.N. and Antonellini, M.A., Compaction bands: a structural analog for anti-mode I cracks in aeolian sandstone, *Tectonophysics*, 267, 209-228, 1996.
- Mozley, P., J. Beckner, and T. M. Whitworth, Spatial distribution of calcite cement in the Santa Fe Group, Albuquerque Basin, NM; implications for ground-water resources, *New Mexico Geology*, 17, 88-93, 1995.
- Mualem, Y., A new model for predicting the hydraulic conductivity of unsaturated porous media, *Water Resour. Res.*, 12, 513-522, 1976.

- Ogilvie, S. R., J.M. Orribo, and P.W. Glover, The influence of deformation bands upon fluid flow using profile permeametry and positron emission tomography, *Geophysical Research Letters*, 28, 61-64, 2001.
- Rawling, G. C., Goodwin, Laurel B., Wilson, John L, Internal architecture, permeability structure, and hydrologic significance of contrasting fault-zone types, *Geology*, 29, 43-46, 2001.
- Ross, B., A conceptual model of deep unsaturated zones with negligible recharge, *Water Resour. Res.*, 28, 1627-1629, 1984.
- Scanlon, B. R. and P. C. Milly, Water and heat fluxes in desert soils, 2, Numerical simulations, *Water Resour. Res.*, 30, 721-734, 1994.
- Scanlon, B. R., S.W. Tyler, and P.J. Wierenga, Hydrologic issues in arid, unsaturated systems and implications for contaminant transport, *Rev. Geophy.*, 35, 461-490, 1997.
- Selker, J. S., C. K. Keller, and J. T. McCord, *Vadose Zone Processes*, CRC Press LLC, Boca Raton, Florida, 339 pages, 1999.
- Sigda, J.M., Effects of small-displacement faults on the permeability distribution of poorly consolidated Santa Fe Group sands, Rio Grande rift, New Mexico, MS thesis, New Mexico Institute of Mining and Technology, Socorro, New Mexico, 1997.
- Sigda, J.M., Preferential flow and transport through deformation band faults in the semi-arid vadose zone of the Rio Grande rift, New Mexico, USA, Ph.D. dissertation, New Mexico Institute of Mining and Technology, Socorro, New Mexico, 2004.

- Sigda, J.M. and J.L. Wilson. Are faults preferential flow paths through semi-arid and arid vadose zones?, *Water Resour. Res.*, 39, 1225, doi:10.1029/2002WR001406, 2003.
- Sigda, J. M., L. B. Goodwin, P. S. Mozley, and J. L. Wilson, Permeability alteration in small-displacement faults in poorly lithified sediments; Rio Grande Rift, central New Mexico, in *Faults and subsurface fluid flow in the shallow crust*, W. C. Haneberg, P.S. Mozley, J.C. Moore, and L.B. Goodwin, eds., *American Geophysical Union Monograph* 113, Washington, DC, US, 51-68, 1999.
- Taylor, W.L. and Pollard, D.D., Estimation of in situ permeability of deformation bands in porous sandstone, Valley of Fire, Nevada, *Water Resour. Res.*, 36, 2595-2606, 2000.
- van Genuchten, M. T., A closed-form equation for predicting the hydraulic conductivity of unsaturated soils, *Soil Science Society of America Journal*, 44, 892-898, 1980.
- Wilson, M.D. and E.D. Pittman, Authigenic clays in sandstones: Recognition and influence on reservoir properties and paleoenvironmental analysis, *J. Sed. Petrology*, 47, 3-31, 1977.
- Wilson, M.D. and P.T. Stanton, Diagenetic mechanisms of porosity and permeability reduction and enhancement, in *Reservoir Quality Assessment and Prediction in Clastic Rocks*, M.D. Wilson, ed., SEPM Short Course 30, Society for Sedimentary Geology, Tulsa, OK, USA, 59-118, 1994.
- Winograd, I.J., Radioactive waste disposal in thick unsaturated zones, *Science*, 212, 1457-1464, 1981.

## **CHAPTER 5: FROM CATCHMENTS TO CONDUITS: VADOSE-ZONE FAULTS AND CLIMATE**

### **5.0 Abstract**

Recent property measurements and one-dimensional modeling suggest that, in climates drier than a specific point called a crossover point, vertical deformation band faults can significantly enhance infiltration, exfiltration, solute transport, and diagenesis within sandy vadose zones. For a given fault and its sand protolith, this crossover point is the system state, such as climate, for which fluxes through the fault and protolith are equivalent. In a climate-driven system with a climate-controlled crossover point, water and solute fluxes through the protolith will dominate fault fluxes for climates wetter than the crossover point, whereas fault fluxes will dominate sand fluxes for climates drier than the crossover point. We extended the modeling of different climates to investigate fault dip and water exchange between fault and protolith, two-dimensional aspects not captured in the previous 1D models. Using previously reported hydraulic properties for fault and sand protolith, we numerically simulated steady, gravity-driven, liquid-phase, variably saturated flow (infiltration) with climatically controlled boundary conditions through two-dimensional faulted and unfaulted sand beds in which normal faults have either 90° or 65° dips. Wet to dry climates were represented by specified matric potentials at the boundaries. Simulated 2D matric potential, flux density (specific discharge), and seepage velocity distributions reveal that faults with dips less than

possessing markedly different hydraulic properties than the parent material [Aydin, 1978; Antonellini and Aydin, 1994; Sigda et al; 1999; Hong, 1999; Sigda and Wilson, 2003]. Non-cataclastic deformation bands and deformation band faults in well-lithified porous sandstones are not considered here. Distinct from macropore flow, gravity fingering, and funnel flow, this recently identified type of preferential flow and solute transport, a type of “capillary wicking”, is caused by the fault’s network of much smaller pores, relative to protolith pore sizes [Sigda and Wilson, 2003; Chapter 3]. Under relatively dry conditions capillary forces maintain a much higher moisture content in the fault than the parent sand (protolith). Driven by gravity and/or matric potential gradients, liquid-phase movement of water and solutes through the fault can be orders of magnitude larger than movement through the sand beds (Figure 5.1) [Sigda and Wilson, 2003; Chapter 3]. The onset of capillary wicking is defined by the conditions or system state for which sand and fault fluxes are equivalent. We call this equivalence point a climate crossover point because water and solute fluxes through the sand dominate the system for climatic conditions wetter than the crossover point, whereas fault fluxes dominate for climatic conditions drier than the crossover point. A simple example of a crossover point is provided by a one-dimensional model of steady, gravity-driven infiltration in which matric potential, uniform throughout the system, is the governing variable (Figure 5.1) [Chapter 3].

The propensity for capillary wicking in vadose-zone faults has been identified through property measurements and simple one-dimensional modeling, as well as observations of zones of preferential diagenesis [Sigda and Wilson, 2003; Chapters 3 and 4]. The necessary conditions for significant capillary wicking include low matric potentials, associated with semi-arid and arid climates, as well as sufficiently high fault

vertical induce preferential flow and transport for both wet and dry climates (boundary matric potentials above and below the climate crossover point, respectively), but by different mechanisms. Under dry climatic conditions, faults, whether vertical or not, act as conduits (capillary wicks) by localizing preferential flow and transport, consistent with the previously reported 1D models of faults when corrected for fault dip. Under wet conditions, non-vertical faults act as catchments by intercepting and channeling liquid-phase water, creating a zone of enhanced water content located just above the fault-hanging wall contact, the ‘catchment’ in the title. Previous 1D analyses completely missed this phenomenon. The enhanced moisture content, matric potential, and amount of preferential flow depend on the climate-controlled boundary matric potential, fault length, fault dip, and sand hydraulic properties. Under wet climatic conditions, fault catchment behavior could increase infiltration and reduce solute residence time within vadose-zone sand beds. Catchment behavior should also occur for large-displacement faults containing clay cores, extensive cementation, or numerous zones of deformation bands, and for other geometrically similar geologic features like clastic dikes.

## 5.1 Introduction

In dry climates, like those found in arid or semi-arid vadose zones, beds of poorly lithified sand that are crosscut by deformation band faults can convey substantially greater liquid-phase water and solute fluxes than unfaulted sands [Sigda and Wilson, 2003; Chapters 3 and 4]. In this study, deformation band faults refer to deformation bands and zones of bands created by faulting-induced shearing (cataclasis) of poorly lithified sands that forms narrow, tabular zones of reduced pore and grain sizes

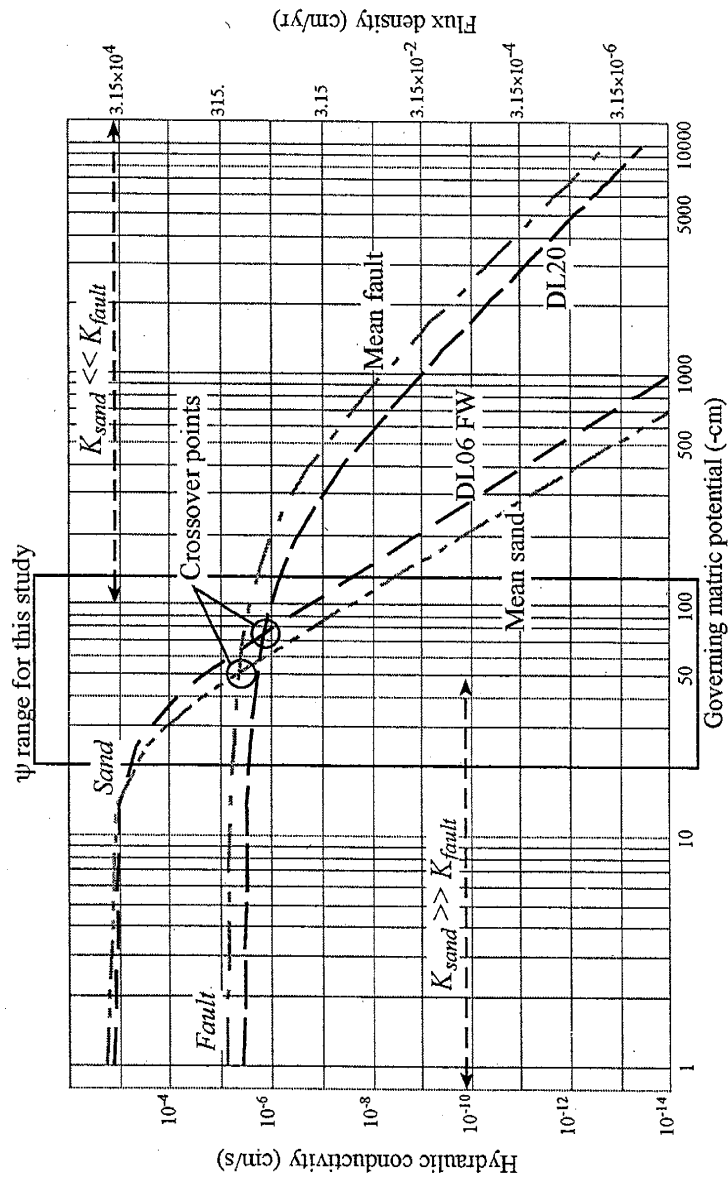


**Figure 5.1:**  $K$ - $\psi$  relationships and gravity-driven flux density for Canyon Trail site E10 showing crossover points. Shown is the mean relationship for all samples from site E10 and the relationship for the fault-protolith pair with the smallest property contrast. Adapted from Sigda and Wilson [2003].

spatial densities such as found in the Rio Grande rift of central New Mexico. The 1D models have been used to predict infiltration (downward flow) enhancement for a steady gravity-driven flow scenario, exfiltration (upward flow) enhancement for a scenario with steady evaporation-driven flow from a shallow water table, and, under both scenarios, reduced solute residence times as well as accelerated diagenesis for faults compared to protolith [Sigda and Wilson, 2003; Chapters 3 and 4]. Significant flow enhancement occurred for conditions drier than the infiltration and exfiltration crossover points and for fault spatial densities greater than one 1 cm wide fault for every 100 m of sand, while travel time and diagenesis were enhanced regardless of the spatial density [Chapters 3 and 4].

Several assumptions employed in the previous one-dimensional models conflict with our field observations of fault architecture. The 1D conceptual models assumed that faults have uniform width, vertical ( $90^\circ$ ) dip, and that there is no exchange of water or solutes between fault and protolith [Chapter 3]. Deformation band faults in the basins of the central Rio Grande rift, even those with displacements less than a meter, display a remarkable variability in width, dip, strike, and architecture. Fault widths can vary from roughly 1 cm to more than 50 cm and change considerably along strike and dip. Dips range from roughly vertical to very low (near horizontal) angles, but most fall between  $50^\circ$  and  $90^\circ$ . Strike and dip can vary within individual faults and between nearby faults. Architectural complexity, which can increase the amount of contact between fault and protolith and thereby the amount of water and solute exchange, is also demonstrated by the number and orientation of deformation bands and zones of deformation band within each fault zone [Sigda et al, 1999; Hong, 1999; Herrin 2001; Chapters 2 and 4].

In this paper we investigate the influence of fault dip and protolith-fault water exchange on fault-induced preferential flow and transport by modeling two-dimensional variably saturated flow in a faulted sandy vadose zone. We assume a steady, gravity-driven flow scenario. Climatic conditions vary from well above the crossover matric potential (wet) to well below the crossover point (dry). Specifically, we address two research questions. How do different but uniform fault dips influence capillary wicking and other vadose-zone processes for steady gravity-driven flow? Under what conditions do the assumptions of the 1D conceptual model no longer adequately describe flow?

To answer these questions, we numerically simulated steady gravity-driven, liquid-phase flow and advective solute transport through two-dimensional vadose-zone sand beds, with either a vertical or a non-vertical fault, across a range of wet to dry climatic conditions. Our proxy for climate is the governing matric potential, which we varied from values near zero, representing wet climates, to very negative values that represent dry climates. The matric potential range was roughly centered on the crossover matric potential value ( $\psi_x$ ) for the sand and fault hydraulic properties. Two faulted beds were considered: one with a vertical ( $90^\circ$ ) dip, which was expected to give results closely resembling those for the 1D model [Chapters 3 and 4], and one with a non-vertical ( $65^\circ$ ) dip, which was expected to have cross-flow between fault and protolith. Protolith and fault unsaturated hydraulic properties were taken from those measured for a sand and fault pair from the previously studied Canyon Trail E10 site in central New Mexico [Chapter 2]. We tested for hydrologically significant preferential flow and solute transport by comparing spatial distributions of matric potential ( $\psi$ ), volumetric moisture

content ( $\theta$ ), flux density ( $q$ ), and seepage velocity ( $v$ ) for faulted and unfaulted sand beds. Unlike the 1D model, local gradients in  $\psi$  created by interactions between fault and sand become possible in 2D, potentially forming zones of enhanced water and solute flux. We examined changes in the spatial distributions of  $\psi$ ,  $\theta$ ,  $q$ , and  $v$  as the simulated climates varied from wet to dry to identify and characterize preferential flow and transport.

## 5.2 Methods

The conceptual model adopted for this study shares many characteristics and several important differences with the simple 1D conceptual model for semi-arid and arid vadose zones used in Chapters 3 and 4. The two-dimensional fault dip, either  $90^\circ$  (vertical) or  $65^\circ$  (non-vertical), is uniform along fault length. The fault has a uniform width of 1 cm. Modeled protolith and fault, based on the Canyon Trail fault E10 site [Chapter 2], have uniform hydraulic properties represented by the commonly used Mualem-van Genuchten model [Mualem, 1976; van Genuchten, 1980]. Steady, gravity-driven liquid-phase flow is assumed, such as is expected to occur in the middle portions of relatively thick vadose zones located between the root and capillary zones. We focus on a relatively narrow range of matric potential values for the boundary conditions, -20 to -120 cm, which bracket the climate crossover value,  $\psi_x$ , for the selected sand and fault pair. This  $\psi$  range, specifically chosen to study interactions between the sand and fault as the boundary  $\psi$  varies above and below a  $\psi_x$ , lies above the matric potential ( $\psi \sim -200$  cm) below which the competing process of geothermal-driven upward vapor-phase flow begins to dominate liquid-phase flow in the protolith [Chapter 3].

The simulations of variably saturated flow were conducted with the commercially available finite element code HYDRUS-2D [Simunek et al, 1999]. The 10m x 10m domain is bounded on the top and bottom with time independent Dirichlet boundaries and on the sides by no flow boundaries (Figure 5.2). Separate triangular element meshes for the 90° and 65° dip domains have very finely spaced discretization in and adjacent to the 1 cm-wide fault, so that six elements composed of fault-only nodes are fully contained within the deformation band fault. Unlike most FEM codes, HYDRUS-2D assigns hydraulic properties to nodes rather than elements [Simunek et al, 1999]. The transition element separating fault-only and sand-only nodes had a maximum width of 2 mm to minimize the effects of property interpolation (a version of the code with element properties failed to converge). Three simulations were performed for each fault dip: first, an unfaulted domain was simulated, then a fault fully penetrating the sand bed was simulated, and last we simulated a partially faulted domain with the fault tipping out ~50 cm from the top and bottom boundaries. A separate mesh was generated for each fault dip and used to simulate fully faulted, partially faulted, and unfaulted domains.

We used sand and fault hydraulic properties (Table 5.1) determined for the sample pair of DL06 hanging wall sand and DL20 fault from the Canyon Trail site E10 [Chapter 2]. This pair has the smallest difference in hydraulic properties for all E10 samples (site E10 mean values are given in Table 5.1 for comparison). The climate crossover value,  $\psi_x$ , for this sample pair is -76.08 cm. We disabled HYDRUS-2D's default nodal estimate of hydraulic conductivity ( $K$ ), and instead directed the code to calculate  $K$  explicitly from the Mualem-van Genuchten model using the most recent matric potential estimate.

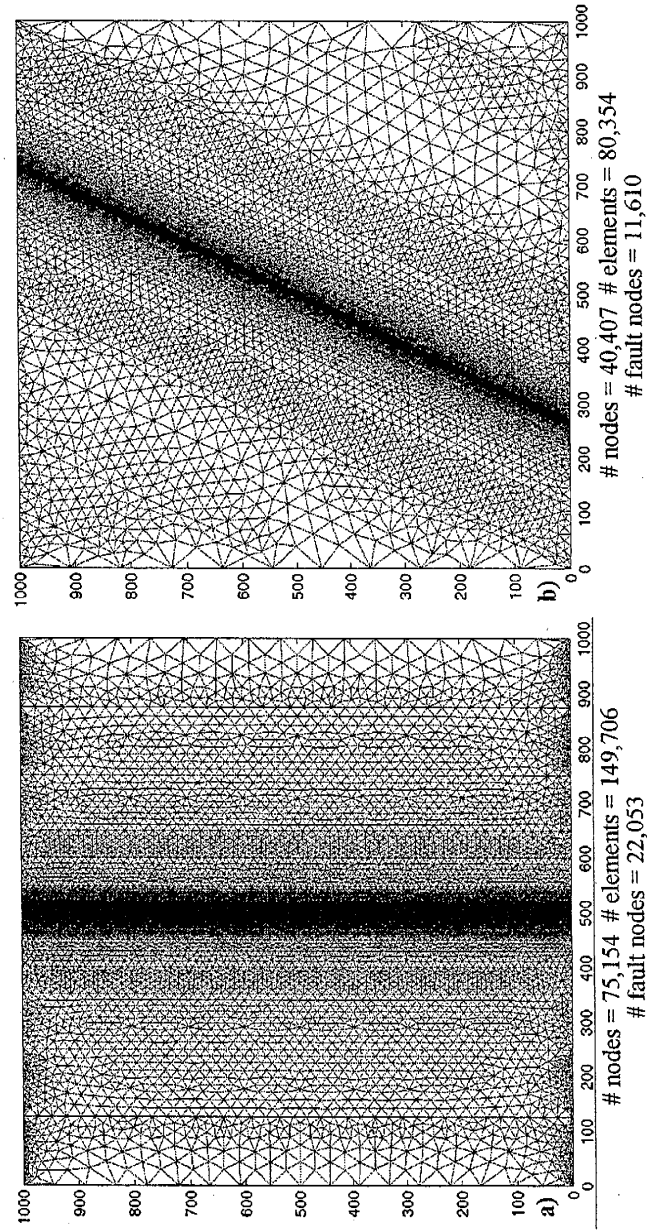


**Figure 5.2:** Domain meshes for vertical plane model. **a)** 90° dip fault. Unfaulted domains use same meshes with all nodes set to sand properties. Units are cm. Left and right sides are no-flow boundaries. Top and bottom sides are set as specified matric potential (Dirichlet) boundary conditions.

**Table 5.1:** Parameter values for Mualem-van Genuchten model

Sample ID	$\theta_s$ ( $\text{cm}^3 \text{cm}^{-3}$ )	$\theta_r$ ( $\text{cm}^3 \text{cm}^{-3}$ )	$\alpha$ ( $1/\text{cm}$ )	$n$ (-)	$\beta$ (-)	$K_s$ ( $\text{cm/s}$ )
Footwall sand						
DL06	0.315	0.058	0.030	3.40	0.20	$1.20 \times 10^{-3}$
Mean sand	0.318	0.062	0.038	3.34	0.42	$1.72 \times 10^{-3}$
Fault DL20	0.198	0.105	0.004	1.80	1.20	$3.50 \times 10^{-6}$
Mean fault	0.202	0.089	0.003	1.74	1.56	$7.36 \times 10^{-6}$

Notes: DL06 and DL20 were used in the simulations, the mean values are for comparison. Mean  $K_s$  values are the geometric means of the saturated hydraulic conductivity values. All other means are arithmetic means of estimated parameter values. Data from Sigda and Wilson [2003].

Steady-state flow regimes were determined for seven governing matric potential values representing different climates:  $\psi_{ss} \in \{-20, -30, -40, -60, -80, -100, -120 \text{ cm}\}$ . After beginning with an arbitrary wet initial condition of -10 cm everywhere for the wettest case,  $\psi_{ss} = -20$ , initial guess for each subsequently drier case was the final steady state matric potential distribution from the previous wetter case, e.g., the solution for  $\psi_{ss} = -20$  cm became the initial guess for  $\psi_{ss} = -30$  cm. To hasten convergence to steady state, each model began with the top boundary =  $\psi_{ss}$  and a “free drainage” (unit gradient [Simunek et al, 1999]) bottom boundary condition. This permitted the column to drain much more rapidly than if the bottom boundary had been initially set equal to  $\psi_{ss}$ . The bottom boundary was later switched to a Dirichlet boundary condition, equal to  $\psi_{ss}$ , as the system began to approach steady state. We ran each model under these conditions until there was no significant change in matric potential contours (-1 cm contours for  $\psi_{ss}$  above  $\psi_x$ , -0.1 cm contours below).

Model outputs of matric potential,  $\psi$ , volumetric moisture content,  $\theta$ , flux density,  $\mathbf{q}$ , and seepage velocity,  $\mathbf{v} = \mathbf{q}/\theta$ , were then plotted and analyzed. We used plots of faulted and unfaulted steady-state values for  $\psi$  and  $\theta$  and differences in  $\mathbf{q}$  and  $\mathbf{v}$  at each node to quantify the changes induced by the presence of the fault for each node  $i$ :

$$\Delta \mathbf{q}_i = \mathbf{q}_i^{\text{faulted}} - \mathbf{q}_i^{\text{unfaulted}} \quad (5.1a)$$

$$\Delta \mathbf{v}_i = \mathbf{v}_i^{\text{faulted}} - \mathbf{v}_i^{\text{unfaulted}} \quad (5.1b)$$

Nodal flux density and seepage velocity are two-dimensional vector quantities. Differences in nodal flux density,  $\Delta \mathbf{q}_i$ , and seepage velocity,  $\Delta \mathbf{v}_i$ , were examined as vector field (arrow) plots to show differences in flow and advective solute transport directions and magnitudes. We also calculated a relative flux density

$$m_i = |\mathbf{q}_i^{\text{faulted}}| / |\mathbf{q}_i^{\text{unfaulted}}| \quad (5.2a)$$

and a relative seepage velocity

$$n_i = |\mathbf{v}_i^{\text{faulted}}| / |\mathbf{v}_i^{\text{unfaulted}}| \quad (5.2b)$$

at each node to better identify areas of changes in flux magnitude using contour plots.

We calculated a composite flux density across the bottom boundary of the 2D domain using HYDRUS-2D outputs to ensure total flux between the 1D and 2D models did not differ significantly. The composite flux density,  $q_c$ , for a vertical fault in the 1D model can be estimated by [Chapter 3]

$$q_c = (1 - d_f)q_s + d_f q_f \equiv q_s + d_f q_f \quad (5.3)$$

where  $q_c$  is the composite liquid-phase flux density for the entire domain (L/T);  $q_s$  and  $i$

are the flux densities (L/T) for the sand and fault components, respectively; and  $d_f$  is the fault spatial density (-). The latter parameter was set equal to  $10^{-3}$  (one 1 cm wide fault in a 1000 cm wide sand column) to match the simulated domain. Equation (5.3) can be amended to predict composite flux density for a non-vertically fault with dip angle  $\alpha$ :

$$q_c = q_s + \sin(\alpha) d_f q_f \quad (5.4).$$

### 5.3 Results

Simulations of the unfaulted sand beds, for both grids, predict uniform matric potential and moisture content distributions throughout the domains for all  $\psi_{ss}$  values, as they should for these conditions. Nodal flux density and matric potential values are in excellent agreement with those predicted by the 1D model, as is the total flux over the width of the domain; both deviate by  $\ll 1\%$  from the predicted 1D values (Tables 5.2 and 5.3). We focus our description of results for the faulted domains on two comparisons: how do the variables of interest differ from the numerical simulations of unfaulted 2D domains, and how do they differ from those for the previously published 1D analytical solutions of faulted domains?

Simulation time required to reach steady state from the initial guess varied greatly with the domain and climate ( $\psi_{ss}$ ). Unfaulted domains generally required only one-third to three quarters of the time it took faulted domains to converge. Convergence was often very sensitive to the prescribed maximum time step size, and was monitored for each run.

Table 5.2: Minima and maxima matrix potential  $\psi$  (cm) for 2D numerical models

Table 5.2: Minima and maxima matrix potential  $\psi$  (cm) for 2D numerical models

$\psi_{ss}$ (cm)	Vertical fault mesh				65° dip fault mesh					
	Unfaulted		Fully faulted		Unfaulted		Fully faulted			
	min	max	min	max	min	max	min	max		
-20	-20.00	-20.00	-20.06	-19.91	-20.00	-20.00	-29.35	29.09	-28.85	27.75
-30					-30.00	-30.00	-36.17	-5.15	-35.98	-5.81
-40	-40.00	-40.00	-40.06	-39.92	-40.00	-40.00	-43.01	-28.49	-42.74	-28.60
-60	-60.00	-60.00	-60.03	-59.97	-60.00	-60.00	-60.51	-58.75	-60.27	-58.75
-80	-80.00	-80.00	-80.01	-79.99	-80.00	-80.00	-80.12	-79.90	-80.25	-79.82
-100	-100.00	-100.00	-100.05	-99.97	-100.00	-100.00	-100.42	-99.76	-102.47	-97.98
-120	-120.00	-120.00	-120.00	-119.98	-120.00	-120.00	-120.51	-119.70	-127.29	-114.36

Table 5.3: Flux density comparison for 1D analytical and 2D numerical models

$\psi_{ss}$ (cm)	90° dip						65° dip						
	1D analytical*			$\Delta q_c^{***}$ (%)	2D numerical**			Fully faulted			Partially faulted		
	Flux density (cm/s)		1D $\Delta\%$		$\Delta q_c$ (%)	1D $\Delta\%$	Faulted	Unfaulted	1D $\Delta\%$	Faulted	1D $\Delta\%$	Faulted	
	Unfaulted	Faulted											
-20	6.393E-04	6.393E-04	0.0	0.0	-0.1	-0.1	0.0	-0.7	0.0	-0.7	0.0	0.0	0.0
-30	2.416E-04	2.416E-04	0.0					-0.4	0.0	-0.4	0.0	0.0	0.0
-40	7.104E-05	7.105E-05	0.0	0.0	-0.1	-0.1	0.0	-0.3	0.0	-0.3	0.0	0.0	0.0
-60	6.546E-06	6.548E-06	0.0	0.0	-0.1	-0.1	0.0	-0.1	0.0	-0.1	0.0	0.0	0.0
-80	9.307E-07	9.318E-07	0.1	0.0	-0.1	0.0	0.0	-0.1	0.0	-0.1	0.1	0.0	0.0
-100	1.924E-07	1.934E-07	0.5	0.0	-0.1	0.4	0.0	0.0	0.0	0.0	0.4	0.0	0.0
-120	5.206E-08	5.286E-08	1.5	0.0	0.1	1.4	0.0	0.0	0.0	0.0	1.3	1.3	0.0

\* The 1D faulted system represents a composite of 1D fault and sand analytical solutions, which are weighted to describe a 1 cm wide fault in a 1000 cm wide sand column [Chapter 3].

\*\* Composite flux density,  $q_c$ , for 2D numerical models is computed along the bottom boundary from HYDRUS-2D output. 1D  $\Delta\%$  column shows the % difference between 2D numerical and 1D analytical flux estimates.

\*\*\*\*  $\Delta q_c$  gives the % difference in composite flux density between the simulated faulted and unfaulted domains relative to the unfaulted domain, or  $\Delta q_c = 100[q_c^{faulted}/q_c^{unfaulted} - 1]$ .  $\Delta q_c = 0$  by definition for unfaulted domains.

### 5.3.1 Fully penetrating vertical fault

Matric potential is uniform throughout the domain with a fully penetrating vertical fault for all climates (prescribed  $\psi_{ss}$  values). There is little or no evidence for significant local gradients, and no reason there should be other than the effects of numerical approximations. Differences in predicted  $\psi$  in faulted and unfaulted domains at each node are negligibly small (Table 5.2), showing no significant exchange of liquid water between protolith and the vertical fault. Moisture content is uniform within the protolith, and different but uniform within the fault, consistent with Figure 5.1 and the uniform matric potential. Our metric for total flux, composite flux density, shows the 2D numerical simulations differ by no more than 0.1% from those predicted by the analytical 1D model, and that the differences in total flux between simulated faulted and unfaulted domains are correctly preserved (Table 5.3). The 2D simulations corroborate the 1D results and, in turn, are corroborated by them, indicating the 1D approach suffices for modeling a vertical fault in a sand bed across wet to dry climate conditions.

### 5.3.2 Fully penetrating non-vertical fault

For wetter climates and the domain with a fully penetrating 65° dip fault, flow differs sharply from that observed in the vertically faulted domain under the same conditions. When  $\psi_{ss} > \psi_x$  (wetter climate), the inclined fault creates significant local gradients in matric potential, volumetric water content, and flux density, which are not present in the vertical fault model (Table 5.2 and Figures 5.3, 5.4, and 5.5). These gradients diminish as the climate becomes drier, i.e., as  $\psi_{ss}$  decreases. The 65° dip fault also creates a zone of enhanced  $\psi$ ,  $\theta$ , and  $q$  values in the hanging wall just above the fault and a shadow with

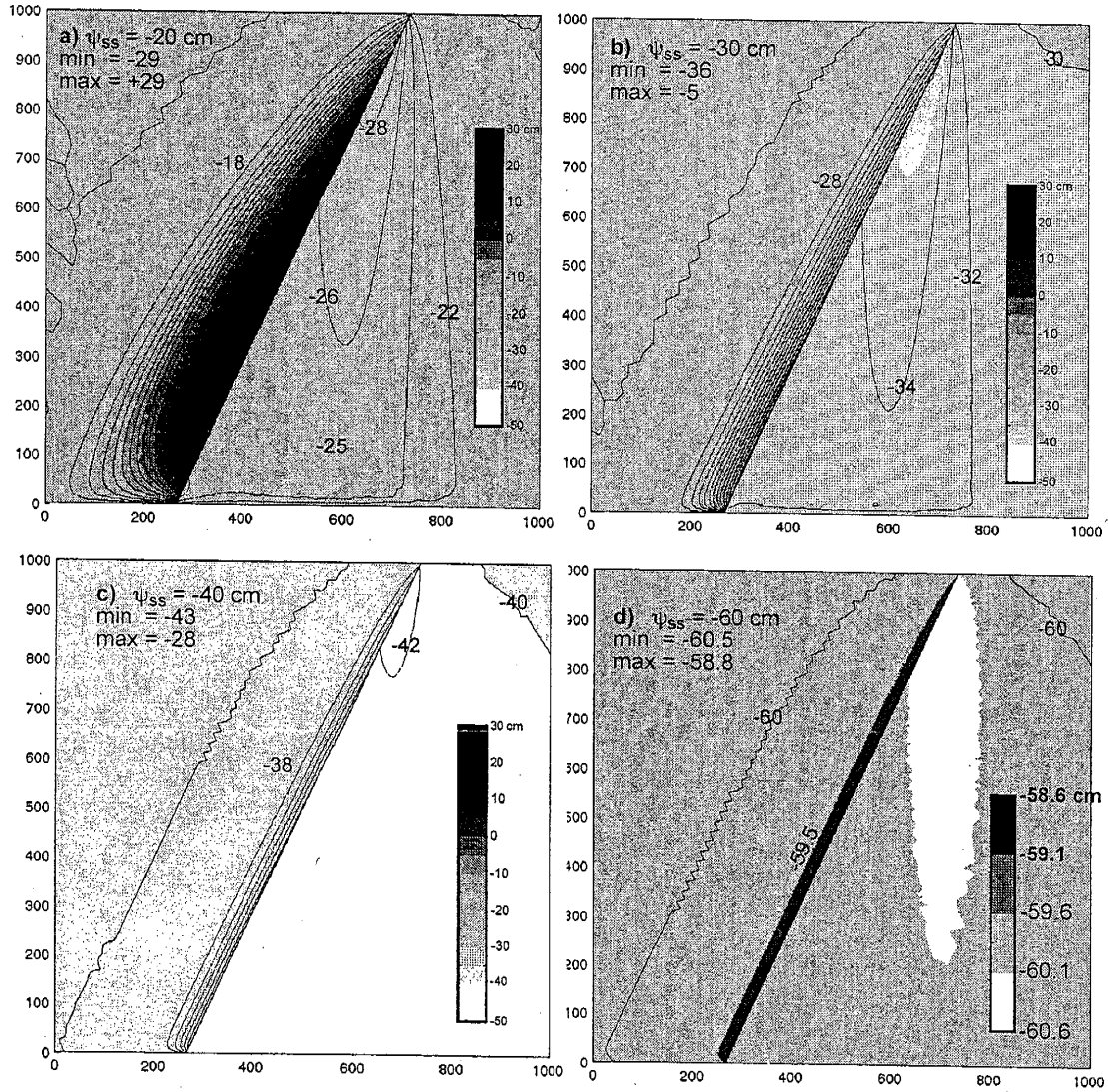


**Figure 5.3:** Matric potential distributions for domains with a fault dipping 65°. Contour interval = 2 cm unless otherwise specified. Note the colorbar scales vary for **d - g**. Water accumulates above fault in hanging wall and the footwall is much drier for wet climates with  $\psi_{ss} > \psi_x$  (**a - d**). A perched water table forms for  $\psi_{ss} \geq -20$  cm. For drier climates with  $\psi_{ss} < \psi_x$  (**e - g**), local matric potential gradients are negligible as the fault becomes an increasingly significant conduit for flow.

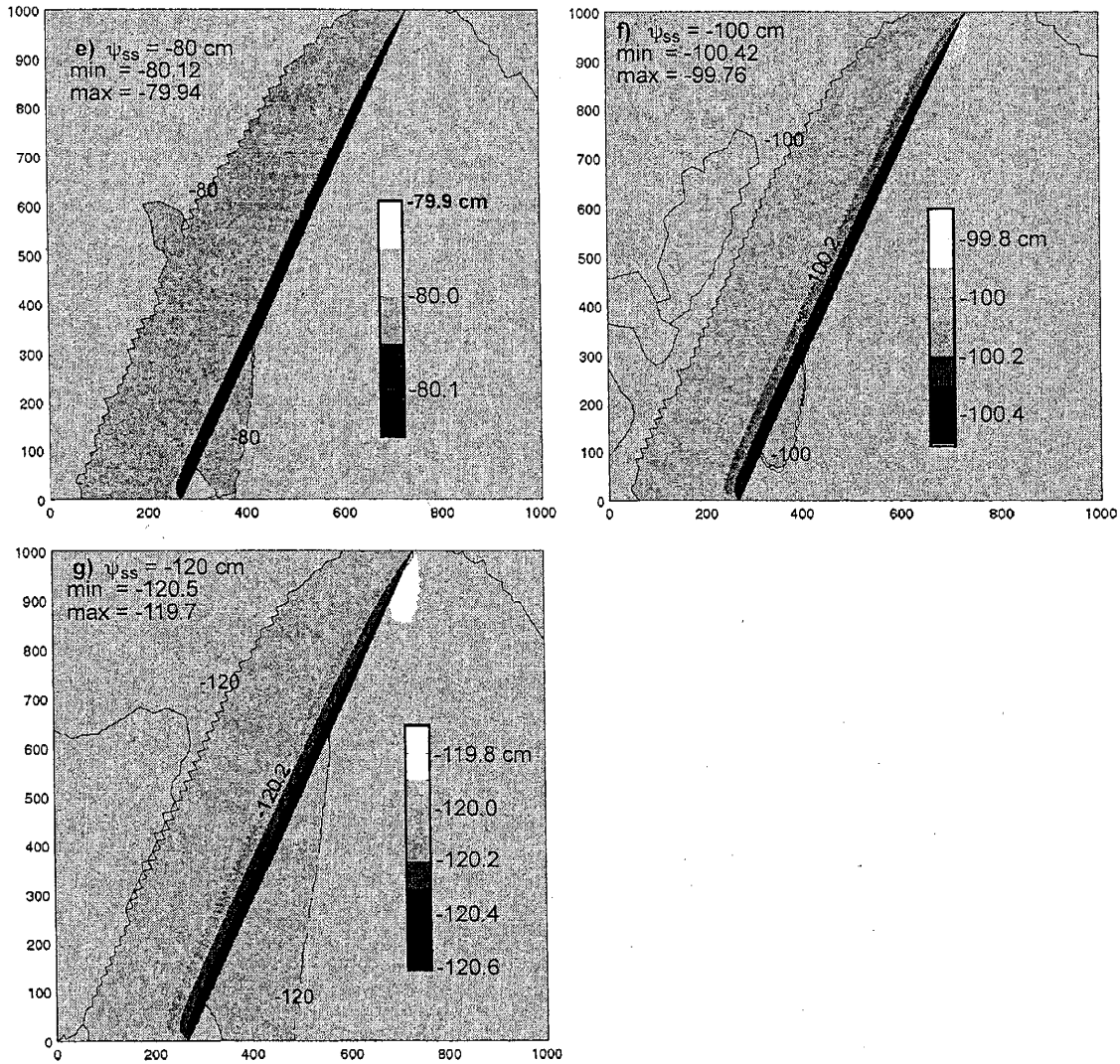


**Figure 5.3:** Matric potential distributions for domains with a fault dipping 65°. Contour interval = 2 cm unless otherwise specified. Note the colorbar scales vary for **d - g**. Water accumulates above fault in hanging wall and the footwall is much drier for wetter climates with  $\psi_{ss} > \psi_x$  (**a - d**). A perched water table forms for  $\psi_{ss} \geq -20$  cm. For drier climates with  $\psi_{ss} < \psi_x$  (**e - g**), local matric potential gradients are negligible as the fault becomes an increasingly significant conduit for flow.

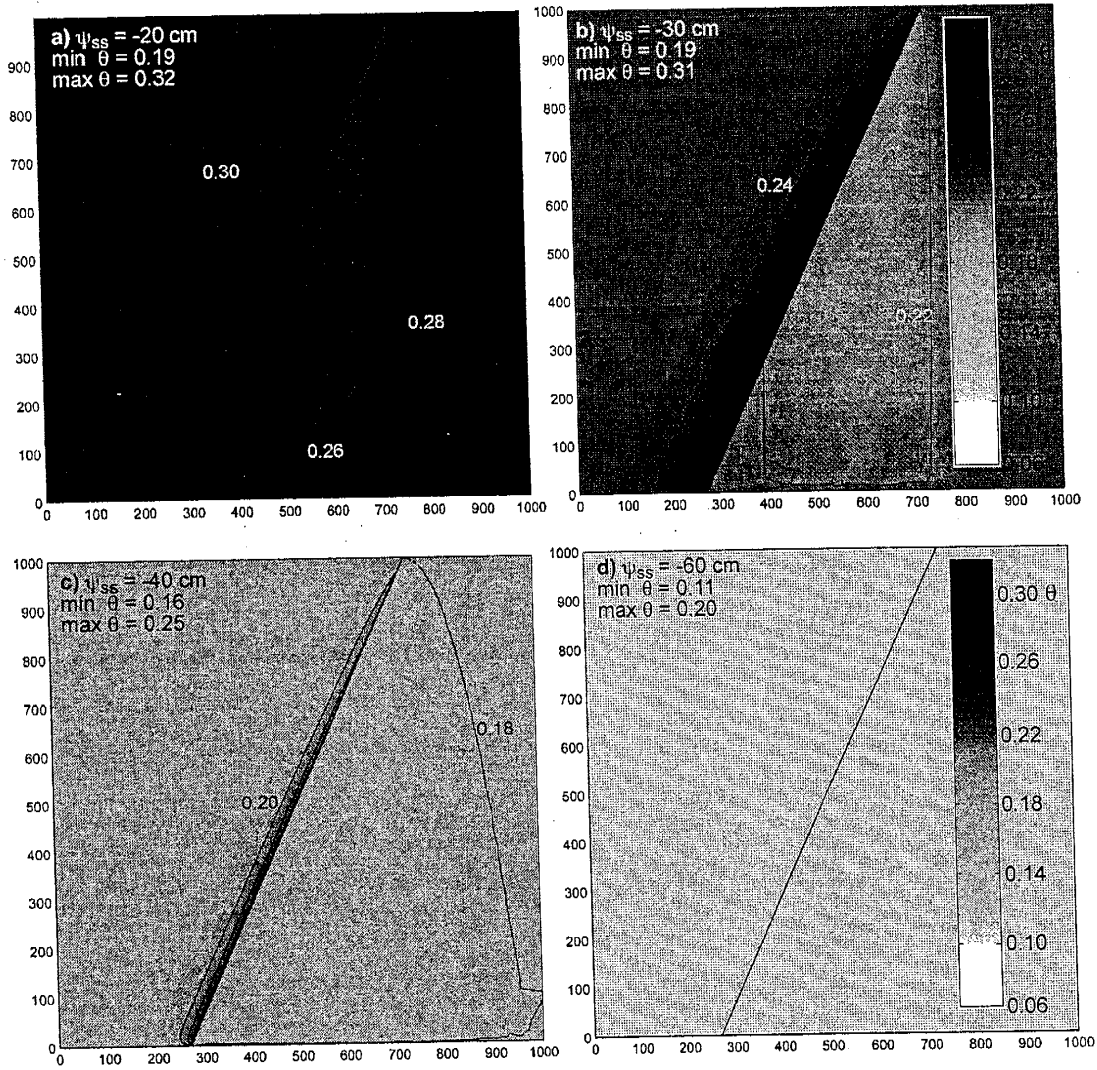


**Figure 5.4:** Volumetric moisture content ( $\theta$ ) distributions for domains with a fault dipping  $65^\circ$ . Contour interval = 0.02. Water accumulates above fault in hanging wall and the footwall is much drier for  $\psi_{ss} \gg \psi_x$  (a - c). For  $\psi_{ss}$  near  $\psi_x$  (d), fault moisture content remains high whereas sand  $\theta$  quickly drops to residual moisture content (only  $\psi_{ss} = -60$  cm shown).

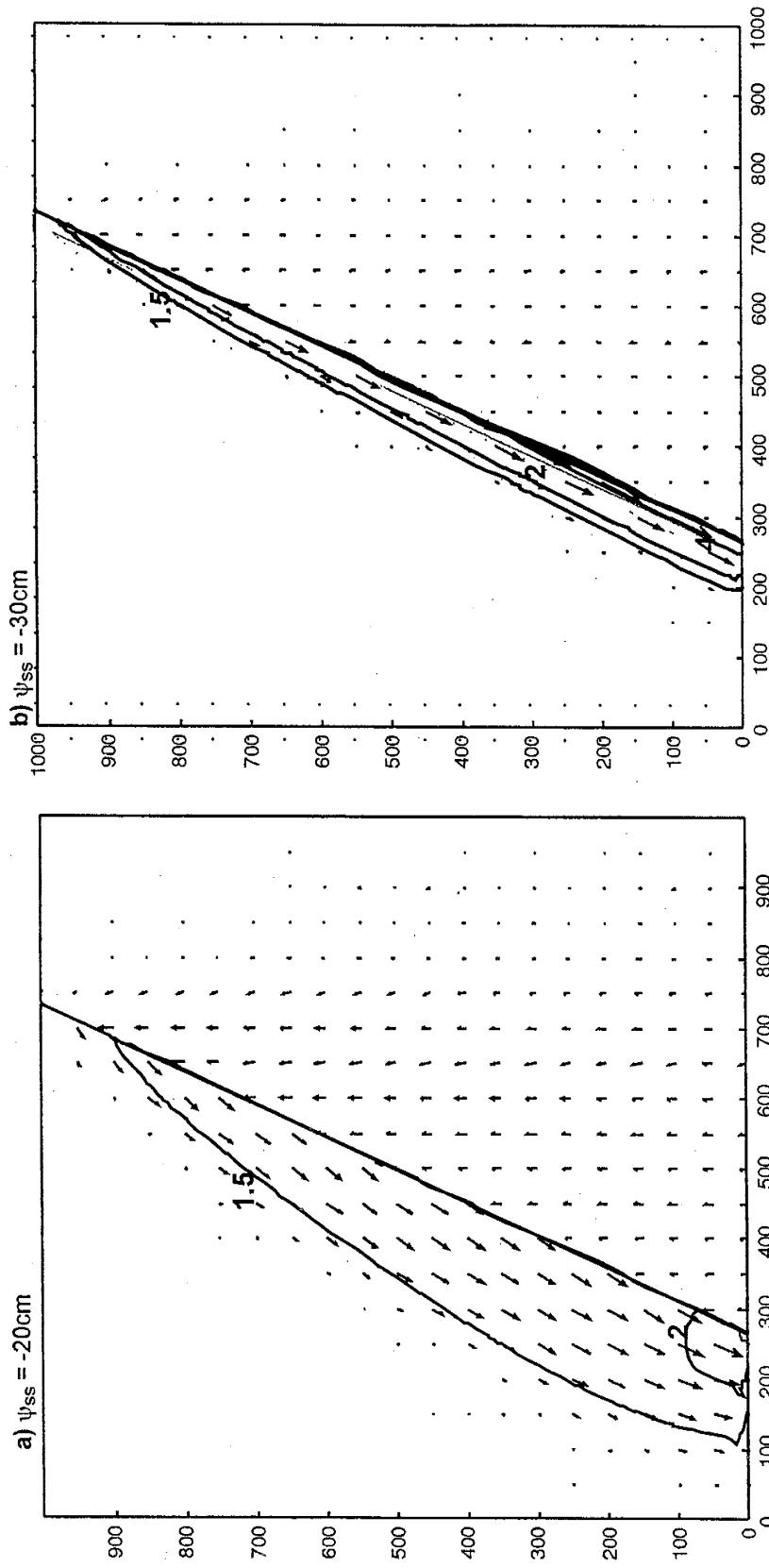


**Figure 5.5:** Differences between unfaulted and faulted flux density distributions for 65° dip domain. Vector field plots show the  $\Delta q_i$  (5.1a) resultants from subtracting unfaulted  $q$  from faulted  $q$  at each node  $i$ . Contours show the ratio of faulted to unfaulted flux density magnitudes:  $m_i$  (5.2a). Enhanced flow occurs within a zone of enhancement located along the hanging wall contact with the fault for wet climates (high  $\psi_{ss}$  values) (a-d). For drier climates (low  $\psi_{ss}$  values) (e-g), enhanced flow occurs only within the 1 cm wide fault.

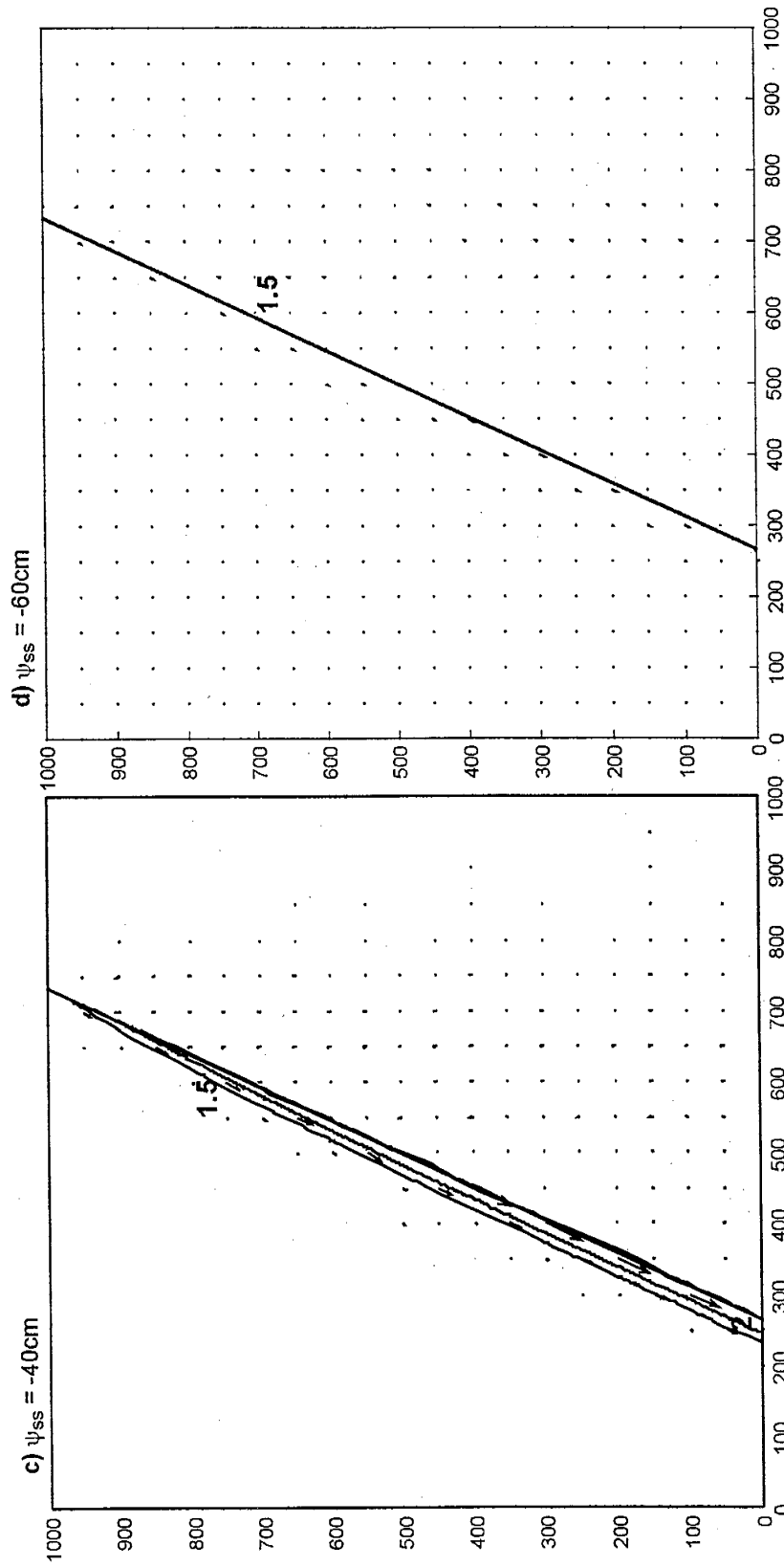


**Figure 5.5:** Differences between unfaulted and faulted flux density distributions for 65° dip domain. Vector field plots show the  $\Delta q_i$  (5.1a) resultants from subtracting unfaulted  $q$  from faulted  $q$  at each node  $i$ . Contours show the ratio of faulted to unfaulted flux density magnitudes:  $m_i$  (5.2a). Enhanced flow occurs within a zone of enhancement located along the hanging wall contact with the fault for wet climates (high  $\psi_{ss}$  values) (e-g). For drier climates (low  $\psi_{ss}$  values) (a-d), enhanced flow occurs only within the 1 cm wide fault.

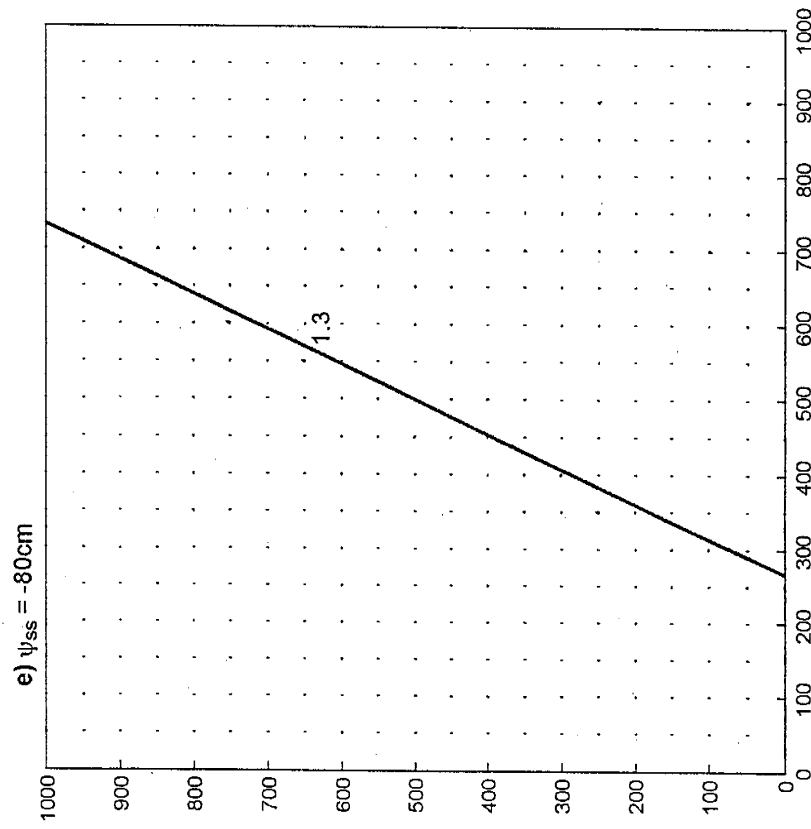


**Figure 5.5:** Differences between unfaulted and faulted flux density distributions for  $65^\circ$  dip domain. Vector field plots show the  $\Delta q_i$  (5.1a) resultants from subtracting unfaulted  $q$  from faulted  $q$  at each node  $i$ . Contours show the ratio of faulted to unfaulted flux density magnitudes:  $m_i$  (5.2a). Enhanced flow occurs within a zone of enhancement located along the hanging wall contact with the fault for wet climates (high  $\psi_{ss}$  values) (a-d). For drier climates (low  $\psi_{ss}$  values) (e-g), enhanced flow occurs only within the 1 cm wide fault.

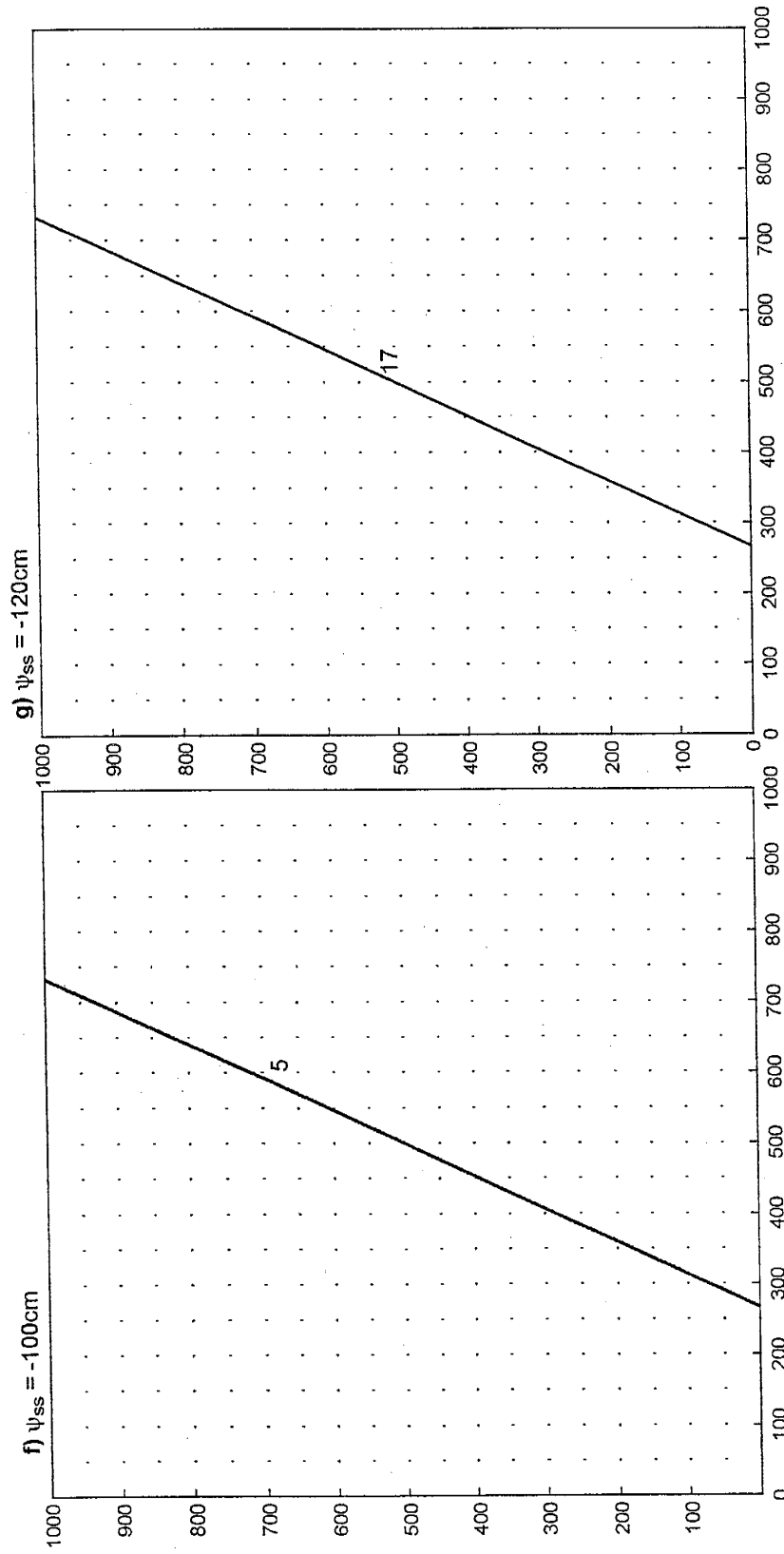


**Figure 5.5:** Differences between unfaulted and faulted flux density distributions for 65° dip domain. Vector field plots show the  $\Delta qi$  (5.1a) resultants from subtracting unfaulted  $q$  from faulted  $q$  at each node  $i$ . Contours show the ratio of faulted to unfaulted flux density magnitudes:  $m_i$  (5.2a). Enhanced flow occurs within a zone of enhancement located along the hanging wall contact with the fault for wet climates (high  $\psi_{ss}$  values) (a-d). For drier climates (low  $\psi_{ss}$  values) (e-g), enhanced flow occurs only within the 1 cm wide fault.

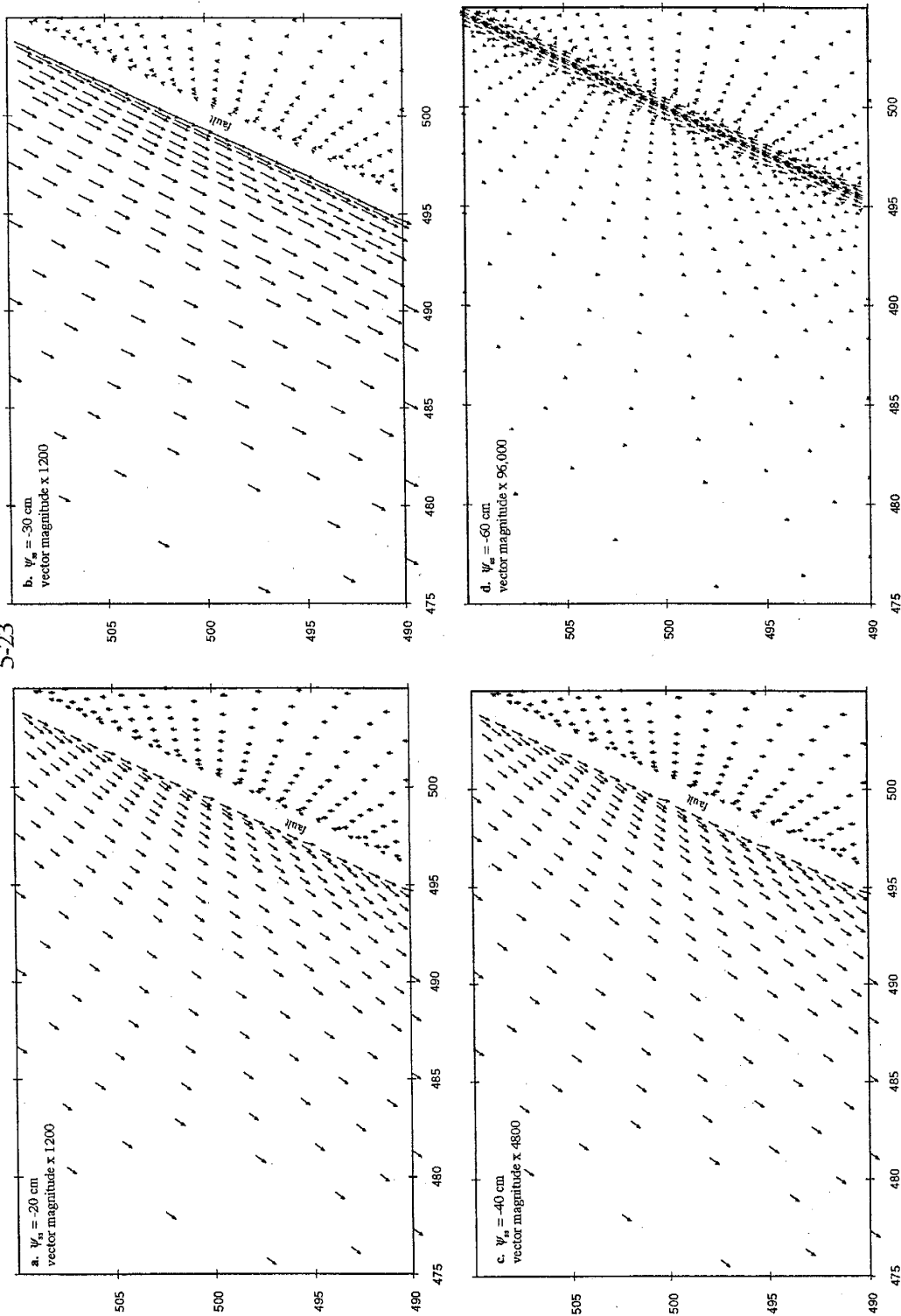


**Figure 5.6:** Close-up of differences in flux density between faulted and unfaulted domains with 65° dip. Vectors within fault are omitted in plots a - c for clarity.

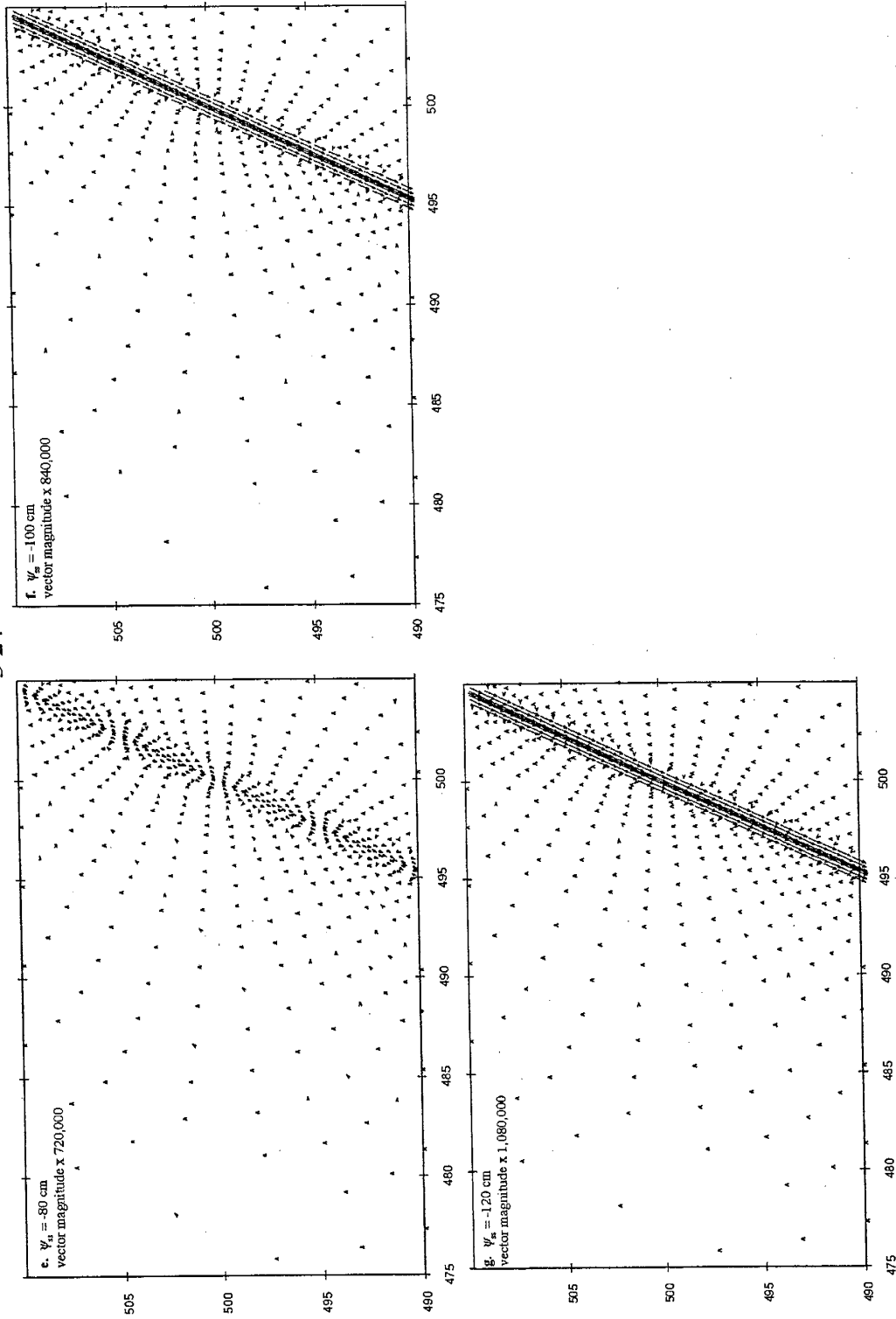
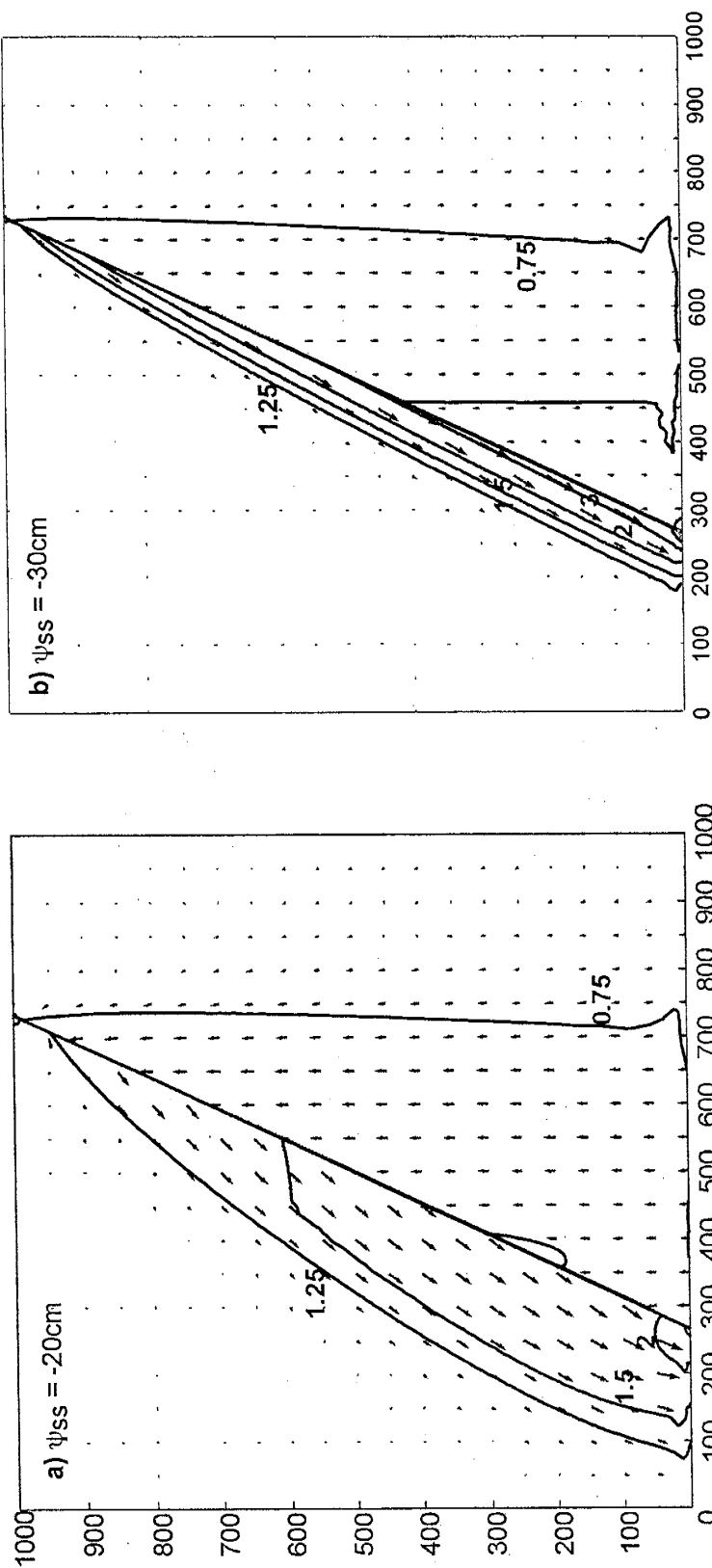


Figure 5.6: Close-up of differences in flux density between faulted and unfaulted domains with 65° dip. Vectors within fault are omitted in plots a - c for clarity.

decreased  $\psi$ ,  $\theta$ , and  $q$  values in the footwall below the fault (Figures 5.3, 5.4, 5.5, and 5.6). Downward flowing water is intercepted by the fault's lower hydraulic conductivity and channeled along the fault-hanging wall contact. The zone of enhancement widens down-dip. Perched conditions exist in the zone for the wettest climate,  $\psi_{ss} = -20$  cm, with a large portion of the hanging wall saturated with as much as 30 cm of positive pressure head (Figures 5.3a and 5.4a). The hanging wall zone of enhancement and the footwall moisture shadow persist as  $\psi_{ss}$  approaches the crossover matric potential, but their width and cross-fault gradients decrease rapidly (Figures 5.3, 5.4, 5.5. and 5.6).

Seepage velocity values, which indicate the rate of non-dispersive advective solute transport, follow the same pattern as flux density. The maximum magnitudes of relative seepage velocities,  $n_i$  (5.2b), at any node indicate that preferential solute transport by advection can occur for both wet and dry climates in a non-vertically dipping fault (Figure 5.7). In dry climates, the preferential flow is through the fault, whereas in wet climates it occurs in the hanging wall zone of enhancement.

Values of composite flux density,  $q_c$ , across the bottom boundary of the simulated 2D domain closely agree with the flux density values predicted for the 1D analytical solutions for dry climates (Table 5.3). In wet climates the 2D numerical simulations for faulted domains underestimate  $q_c$  by a small amount ( $< 1\%$  of the 1D analytical value for this case of one 1cm fault every 10m), whereas the dry climate simulations and analytical results are essentially the same (Table 5.3). The 1D  $q_c$  values for the  $65^\circ$  dip fault domain under dry conditions are slightly smaller than those for the vertical fault because fault-only flux is decreased slightly by the sine of the dip (4), hence flux enhancement is



**Figure 5.7:** Differences between unfaulted and faulted seepage velocity distributions for 65° dip domain. Vector field plots show the  $\Delta v_i$  (5.1b) resultants from subtracting unfaulted  $v$  from faulted  $v$  at each node  $i$ . Contours show the ratio of faulted to unfaulted seepage velocity magnitudes,  $v_i$  (5.2b). Enhanced advective solute transport occurs within a zone of enhancement located along the hanging wall contact with the fault for wet climates (high  $\psi_{ss}$  values) (a-d). For drier climates (low  $\psi_{ss}$  values) enhanced solute flux occurs only within the 1 cm wide fault itself (not shown).

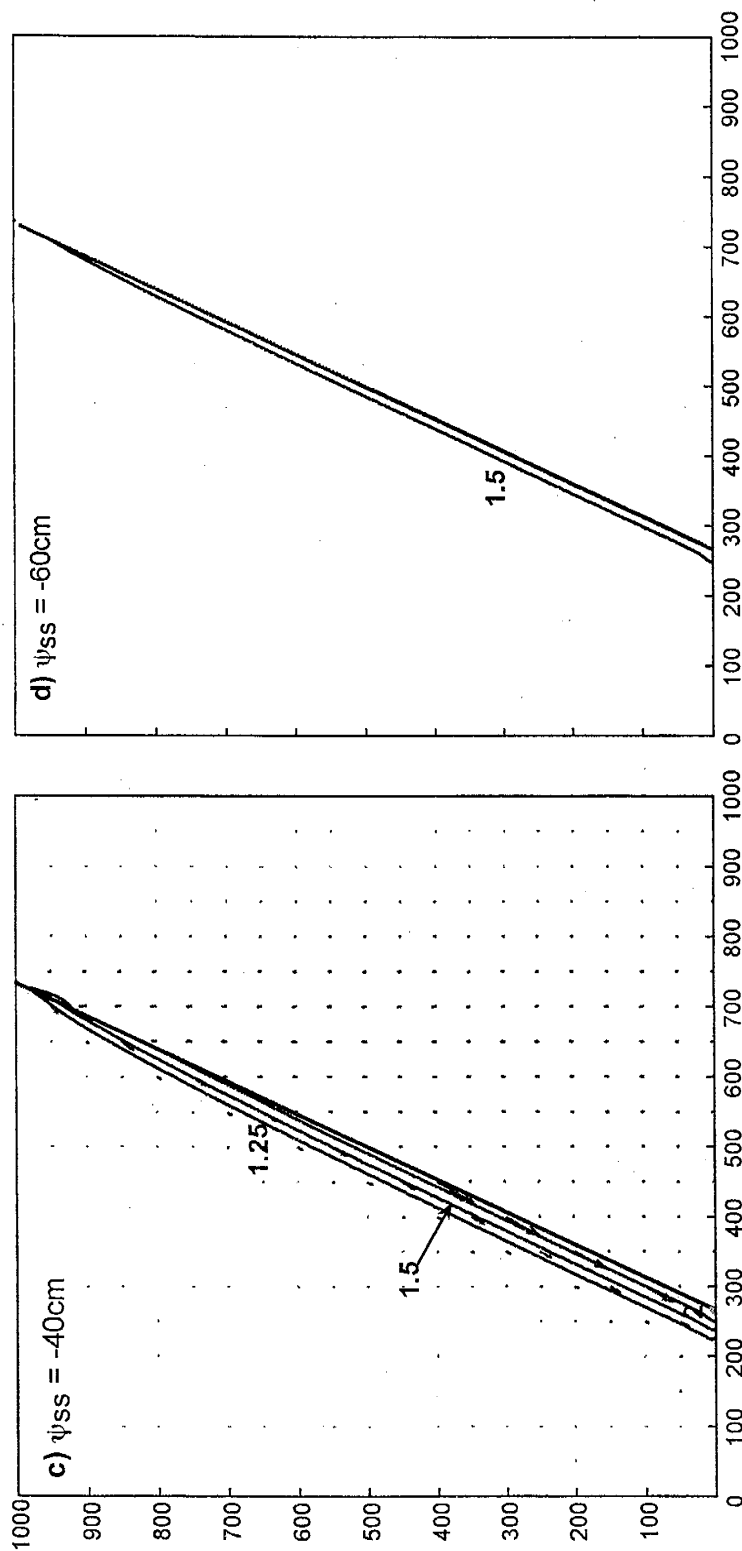


**Figure 5.7:** Differences between unfaulted and faulted seepage velocity distributions for 65° dip domain. Vector field plots show the  $\Delta v_i$  (5.1b) resultants from subtracting unfaulted  $v$  from faulted  $v$  at each node  $i$ . Contours show the ratio of faulted to unfaulted seepage velocity magnitudes,  $n_i$  (5.2b). Enhanced advective solute transport occurs within a zone of enhancement located along the hanging wall contact with the fault for wet climates (high  $\psi_{ss}$  values) (a-d). For drier climates (low  $\psi_{ss}$  values) enhanced solute flux occurs only within the 1 cm wide fault itself (not shown).

slightly smaller (Table 5.3). The dip-induced difference is very small for the climate conditions considered here. At  $\psi_{ss} = -120$  cm, vertical fault flux enhancement is 1.5% (5.3) whereas enhancement is only 1.3% when accounting for the sine of the dip (5.4). The disparity increases with drier climates (decreasing  $\psi_{ss}$ ).

### 5.3.3 Partially faulted domain

Decreasing fault length so that the fault tips out 50 cm below the top and above the bottom boundaries has only a modest effect on preferential flow and advective transport, relative to the fully penetrating case. Matric potential distributions are relatively unchanged from those for the fully penetrating fault domain under wet climate conditions. The partially penetrating fault intercepts and channels infiltrating water along the fault-hanging wall for wet climates just like the fully penetrating fault. The fault's lower tip becomes a discharge point with elevated matric potential and moisture contents whereas the upper tip is a locus for lower matric potentials (Figure 5.8). The significantly lower  $\psi$  values near the upper fault tip extend far into the footwall, creating a "plume" (Figure 5.8l-n) of lower matric potential and flux that is not as apparent in the domain with a fully faulted sand bed for  $\psi_{ss} < \psi_x$  (Figures 5.3-8).

For dry climate conditions the local matric potential gradients are larger in the partially faulted domain than in the fully faulted domain. This suggests fault tips might more quickly capture transient infiltration pulses by their larger local  $\psi$  gradients than would be expected from a fully faulted domain. Composite flux density,  $q_c$ , across the bottom boundary of the simulated domain is essentially the same as for the unfaulted domain ( $\Delta q_c = 0$ ) because the fault does not reach the bottom boundary (Table 5.3).

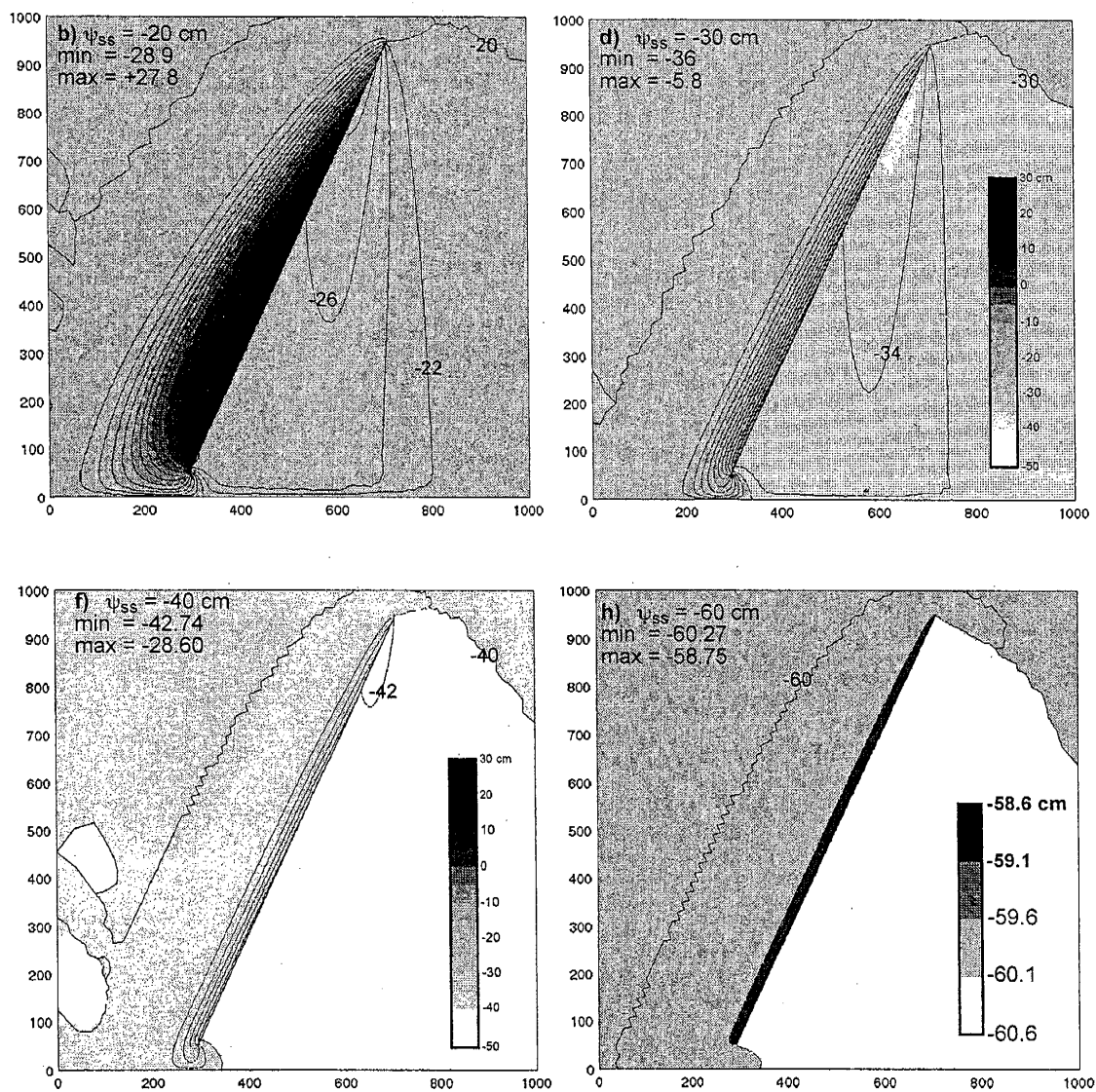


**Figure 5.8:** Matric potential distributions for partially faulted domains with a 65° dip fault. Contour interval = 2 cm unless otherwise specified. Note the colorbar scales vary for **d - g**. Water accumulates above fault in hanging wall and the footwall is much drier for  $\psi_{ss} > \psi_x$  (**a - d**). A perched water table forms for  $\psi_{ss} \geq -20$  cm. For  $\psi_{ss} < \psi_x$  (**e - g**), local matric potential gradients can be significant even as the fault becomes an increasingly significant conduit for flow.

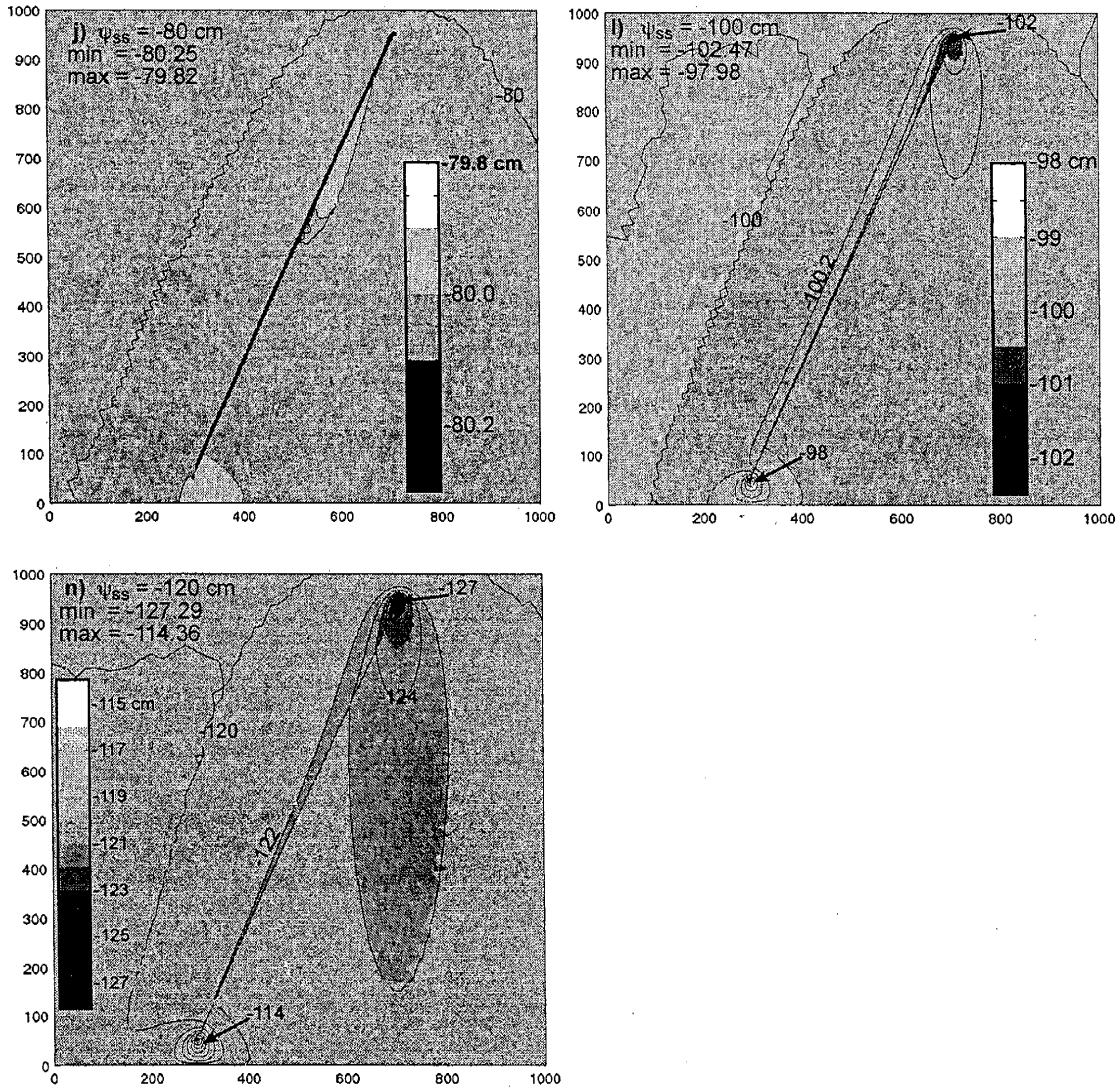


**Figure 5.8:** Matrix potential distributions for partially faulted domains with a 65° dip fault. Contour interval = 2 cm unless otherwise specified. Note the colorbar scales vary for d - g. Water accumulates above fault in hanging wall and the footwall is much drier for  $\psi_{ss} > \psi_x$  (a - d). A perched water table forms for  $\psi_{ss} \geq -20$  cm. For  $\psi_{ss} < \psi_x$  (e - g), local matrix potential gradients can be significant even as the fault becomes an increasingly significant conduit for flow.

## 5.4 Discussion

If dip is non-vertical, deformation band faults can induce preferential flow and transport through poorly lithified vadose-zone sand beds in wet as well as dry climates. Corroborating the 1D analysis for dry climate conditions [Chapter 4], capillary forces preferentially wick water into the fault, which then becomes a preferred flow path or conduit with the flux rate slightly attenuated by the non-vertical dip's lower gravitational gradient. For wet climates, a new mode of preferential flow and transport is predicted for non-vertically dipping faults, here illustrated by a 65° dip fault. This new mode does not occur in vertical faults. By intercepting and channeling infiltrating water, the non-vertical fault acts as a catchment and creates a wetter, more conductive zone within the hanging wall sand adjacent to the fault. In intermediate climates (governing matrix potential  $\psi_{ss}$  near the crossover potential  $\psi_x$ ), faults do not significantly influence liquid-phase water flow and advective solute transport. In answer to our research questions, preferential flow and transport is affected by fault dip, and wet climates require a 2D model whereas a simple 1D conduit model, corrected for dip, can suffice for dry climates.

Fault conduit behavior caused by capillary wicking can be effectively captured by the 1D analytical model for the dry-climate flow scenario studied here. The 1D fault flux can be easily corrected for the dip angle (5.4), and such corrections may be significant for other scenarios, such as for infiltration in areas with very high fault spatial densities or where other metrics, like solute residence time, are used. A 2D dry-climate analysis is likely to be necessary for single faults with wide variations in width and dip or for densely faulted areas with numerous fault intersections. A 2D dry-climate analysis could

also be warranted for a partially-faulted sand bed because the fault's upper tip can induce significant local matric potential gradients (Figure 5.8e-g).

The new mode of fault-induced preferential flow and transport, which we call catchment behavior, is predicted to occur under relatively wet climate conditions (governing matric potential  $\psi_{ss} >$  crossover potential  $\psi_x$ ) for faults with non-vertical dip. The fault's inclined angle and hydraulic conductivity contrast with the protolith enable it to catch and collect infiltrating water, creating a zone of increased matric potential and moisture content. Located along the hanging wall contact with the fault, this zone encompasses an area with sufficiently greater hydraulic conductivity, flux density, and seepage velocity to enhance flow and transport relative to the remainder of the domain. The zone of enhancement decreases in width and in enhancement of matric potential, moisture content, flux density, and seepage velocity with increasingly drier climates until it disappears altogether for climates near the crossover matric potential. Differences in sand and fault hydraulic properties, especially air entry matric potential can also affect the climate-dependant dimensions of the enhanced zone. The largest relative flux density encountered in the simulations (5.2a), with a value near 4, is observed not for the wettest climate ( $\psi_{ss} = -20$  cm) but at  $\psi_{ss} = -30$  cm, which is just above the air entry value for the sand (-33 cm). Maximum relative flux density then decreased to 2 for the next driest climate represented by  $\psi_{ss} = -40$  cm (Figure 5.5c). We observed the same drop-off in maximum relative flux density for climates drier than the air entry matric potential in a separate set of model runs which used a different value for sand air entry value.

Flow and transport enhancement by fault catchment is modest compared to conduit enhancement in drier climates. Conduits can enhance flux density by orders of magnitude (Figure 5.1). The maximum catchment enhancement is less than one order of magnitude (Figure 5.5). If we consider only the range of simulated  $\psi$  values and climates studied here, fluxes are roughly comparable whether measured by the maximum relative flux density (5.2a),  $m_i$ , or relative seepage velocity (2b),  $n_i$ . Maximum  $m_i$  reaches 13 within the fault catchment (at  $\psi_{ss} = -30$  cm) and 17 in the fault conduit (at  $\psi_{ss} = -120$  cm). Maximum relative seepage velocity is slightly less. This measure does not include any information about the proportion of the domain undergoing enhanced flow and transport, but conduit flow is confined to the 1 cm wide fault whereas catchment width can reach 200 cm. Better measures for predicting transport enhancement, including estimating travel time by particle tracking or numerically simulating advection-dispersion transport, were not attempted.

The horizontal area intercepted by a fault catchment is a function of fault dip and the thickness of the faulted sand bed. We define the dimensionless catchment ratio,  $R_c$ , as the ratio of horizontal distance over which the fault collects infiltrating water,  $W$  (L), to the faulted sand bed thickness,  $H$  (L). That is,  $R_c = W/H = \tan(90^\circ - \alpha)$ , where  $\alpha$  ( $^\circ$ ) is the uniform dip of the fault. The catchment ratio is effectively 0 for a vertical fault, which means it does not intercept a significant amount of infiltrating water,, whereas the ratio equals 0.47 for a fault with a  $65^\circ$  dip, indicating the fault intercepts infiltrating water over a horizontal distance roughly half of the total faulted bed thickness. Normal faults, which are common throughout the Rio Grande rift, typically dip between  $50^\circ$  and  $90^\circ$ ,

yielding  $R_c$  values between 0.84 and 0. Major fault strands at the Canyon Trail site in the Bosque del Apache National Wildlife Refuge display dips between  $54^\circ$  and  $87^\circ$  with a mean of  $68^\circ$  [Chapter 2; Herrin, 2001], yielding  $R_c$  values that range from 0.73 to 0.05. A splay from one of these faults dips even less, between  $40^\circ$  -  $60^\circ$ , and thus has a catchment ratio between 1.19 and 0.58. The splay is the only fault structure with such a low dip and it is also the only structure, out of the roughly 31 faults found at the site, to have any significant cementation.

Catchment behavior also depends on the number and orientation of nearby faults. Fault densities at the Canyon Trail site are roughly one fault every 4 m, and those at the Elmendorf site [Sigda et al., 1999], 3 km further south, are even higher at roughly one fault every 2 m [Chapters 3 and 4]. These observed fault spatial densities are sufficiently high to create interactions between adjacent faults analogous to destructive or constructive interference in optics. A north-dipping fault will be “shaded” by a north-dipping northern neighbor, thereby decreasing its effective catchment width, whereas a south-dipping northern neighbor could reinforce the catchment behavior of both faults down to the point where the “fault funnel” is closed by fault crosscutting.

Properties of the infiltrating liquid may also significantly affect catchment behavior. We have seen that climates with sufficient recharge to bring  $\psi_{ss}$  near to  $\psi_x$  are unlikely to demonstrate aqueous preferential flow or transport because there is little difference in fault and sand hydraulic conductivity values. Another liquid, such as a non-aqueous phase liquid (NAPL), with completely different wetting and capillarity, could produce significantly more enhanced flow or transport than the infiltrating water because it would

respond differently to the disparity in pore sizes. For non-wetting liquids, fault catchment behavior would extend into much drier climate conditions.

Climate, represented by the governing matric potential in this study of gravity-driven flow, can also be represented by a steady-state infiltration rate. Rates of infiltration or recharge for other areas can be used to estimate whether faults in those locales will act, on average, as conduits or catchments or have no significant effect. Annual infiltration is estimated at 66 cm for the area near Otis Air Force Base, now the Massachusetts Military Reservation on western Cape Cod, MA [Masterson et al, 2002]. Matching a governing matric potential of -71 cm for the sand studied here (Figure 5.1), this infiltration rate suggests any glacio-tectonically faulted sands in western Cape Cod will experience little or no fault-induced infiltration enhancement by either catchment or conduit behavior. A wetter climate should lead to more evident catchment behavior. Maximum infiltration rate can reach 102 cm/yr for the northern part of Hawaii island [Oki, 2002], which matches a governing matric potential of -67 cm for this study's sand properties (Figure 5.1) and again suggests minimal fault-induced flow enhancement. This simple steady-state approach suggests fault catchment behavior is on average not likely for these climate conditions and sand properties. However, temporal variability in the infiltration flux and reported spatial variability in sand properties [Chapter 4] could very well permit infiltration enhancement. For example, infiltration flux rate can vary enough about its mean that the fault switches from catchment behavior during wetter seasons to conduit behavior during drier seasons. Catchment behavior can be expected to occur beneath surface water bodies or other areas with high infiltration rates, e.g., topographically-driven collection of runoff within drainages, regardless of climate conditions.

Our modeling results suggest that faulted sand beds with only slight zones of enhancement would induce significant preferential flow and solute transport from intermittent solute or water pulses. The advancing wetting front will increase  $K$ ,  $q$ , and  $v$  in the enhanced zone far more rapidly than in the surrounding sand column, further accelerating transport through the faulted sand bed. This behavior suggests that deformation band faults that crosscut semi-arid arroyo drainages can significantly increase local infiltration and perhaps even enhance recharge to the underlying aquifer. We speculate that any abrupt changes in cementation of faults along strike, with cements concentrated in the hanging wall, may be an indicator that paleo-drainages had previously flowed above and preferentially infiltrated along the fault at that location. A key question for future work is how quickly does the enhanced zone's increased moisture content dissipate relative to the frequency of episodic infiltration events.

Large displacement faults in poorly lithified sediments could also act as catchments because they can comprise numerous deformation band faults, a continuous clay core, or extensive cementation [Goodwin and Mozley, 1995; Heynekamp et al, 1999; Rawling et al, 2001]. Only the deformation band fault components and perhaps the clay core would function as conduits for dry climate conditions.

Based on our results and discussion, we propose an expanded conceptual model to describe fault networks within sedimentary basins where climate ranges from very wet to very dry ( $0 > \psi_{ss} > -2000 \text{ cm} = \sim 2 \text{ bar}$ ). Deformation band faults in sandy beds will act as catchments, with preferential flow and transport occurring within a zone of enhanced matric potential and water content along the hanging wall, if dip angles are less than

roughly  $80^\circ$  (catchment width  $> 15\%$  depth) and if the climate is relatively wet ( $\psi_{ss} > \psi_x$ ).

Catchment behavior could also occur episodically if the fault underlies an ephemeral surface water body or a site of focused infiltration. The width and water content of the hanging wall enhanced zone will vary with fault dip and length, geometry of nearby faults, and sand hydraulic properties. Furthermore, it is likely that large-displacement faults can act as catchments because of large disparities in hydraulic conductivity between the sand bed and the dipping structure. If, on the other hand, the climate is semi-arid or arid ( $\psi_x > \psi_{ss} > 2 \text{ bar}$ ), the fault will act as a conduit because preferential liquid-phase flow and transport will move through the fault via capillary wicking [Chapter 3].

## 5.5 Conclusions

Deformation band faults can act as loci for preferential flow and transport through vadose-zone sand beds under both wet and dry climates. In wet climate conditions ( $\psi_{ss} > \psi_x$ ), a non-vertically dipping fault can act as a catchment by intercepting and channeling water along its contact with the hanging wall. Increased water content in this zone of enhancement leads to higher flux densities and seepage velocities, which can accelerate water and solute movement through the faulted domain, relative to the surrounding protolith. In a dry climate ( $\psi_{ss} < \psi_x$ ), due to capillarity, the fault instead acts like a conduit by conveying water and solutes far more rapidly than the surrounding protolith.

Wet climate models of faults require, at a minimum, a 2D model domain, whereas a simple 1D model can suffice for dry climates given a uniform and simple fault geometry.

Flow enhancement for a non-vertical fault can be accurately calculated using the 1D model for dry climates and a correction to the flux for the dip angle can be easily applied.

Governing matric potentials near the sand's air entry matric potential create the largest zone of enhancement in the hanging wall of a normal fault for wet climates. Increases in flux density and seepage velocity can be several times greater than those expected in an unfaulted domain under the same boundary conditions. Flux enhancement by conduit behavior in dry climates can exceed that from catchment behavior in wet climates by many orders of magnitude.

Episodic catchment behavior may occur under transient conditions, such as those from ephemeral surface waterways or sites of focused infiltration. More work is required to determine the amount of time required to dissipate the zone of enhanced moisture.

Large displacement faults in poorly lithified sediments may also exhibit catchment behavior because some component structures, e.g., clay core and deformation band faults, have much lower saturated hydraulic conductivity values than the protolith. There are other geological features, such as clastic dikes, that may have similar behavior, acting as either a capillary wicking conduit in dry climates or a catchment in wet climates.

## 5.6 References

Antonellini, M. and A. Aydin, Effect of faulting on fluid flow in porous sandstones: petrophysical properties, *AAPG Bull.*, 78, 355-377, 1994.

- Aydin, A., Small faults formed as deformation bands in sandstone, *Pure Applied Geophys.*, 116, 913-930, 1978.
- Aydin, A. and Myers, R., The permeability structure of fault zones formed from shearing of pre-existing joint zones, *Geol. Soc. Amer. Abstracts with Programs*, 29, 416, 1997.
- Herrin, J. M., Characteristics of deformation bands in poorly lithified sand: Rio Grande rift, New Mexico, M.S. (Geology), New Mexico Institute of Mining and Technology, Socorro, New Mexico, 2001.
- Heynekamp, M.R., L.B. Goodwin, P.S. Mozley, and W.C. Haneberg, Controls on fault-zone architecture in poorly lithified sediments, Rio Grande Rift, New Mexico; implications for fault-zone permeability and fluid flow, in *Faults and subsurface fluid flow in the shallow crust*, W.C. Haneberg, P.S. Mozley, J.C. Moore, and L.B. Goodwin, eds., American Geophysical Union Monograph 113, Washington, DC, US, 27-49, 1999.
- Hong, Sung-ho, Anisotropic hydraulic conductivity of faulted poorly consolidated eolian sands: Bosque, New Mexico, M.S. (Geology), New Mexico Institute of Mining and Technology, Socorro, New Mexico, 1999.
- Masterson, J.P., K.M. Hess, D.A. Walter, and D.R. LeBlanc. Simulated Changes in the Sources of Ground Water for Public-Supply Wells, Ponds, Streams, and Coastal Areas on Western Cape Cod, Massachusetts, U.S. Geological Survey Water-Resources Investigations Report 02-4143, 2002.

- Mollema, P.N. and Antonellini, M.A., Compaction bands: a structural analog for anti-mode I cracks in aeolian sandstone, *Tectonophysics*, 267, 209-228, 1996.
- Mozley, P. S., and L. B. Goodwin, Patterns of cementation along a Cenozoic normal fault: A record of paleoflow orientations, *Geology*, 23, 539-542, 1995.
- Oki, D.S., Reassessment of Ground-Water Recharge and Simulated Ground-Water Availability for the Hawi Area of North Kohala, Hawaii, U.S. Geological Survey Water-Resources Investigations Report 02-4006. 2002.
- Rawling, G., L. Goodwin, and J. Wilson, Internal architecture, permeability structure, and hydrologic significance of contrasting fault-zone types, *Geology*, 29, 43-46, 2001.
- Sigda, J.M. and J.L. Wilson. Are faults preferential flow paths through semi-arid and arid vadose zones?, *Water Resour. Res.*, 39, 1225, doi:10.1029/2002WR001406, 2003.
- Sigda, J.M., L.B. Goodwin, P.S. Mozley, and J.L. Wilson, Permeability alteration in small-displacement faults in poorly lithified sediments; Rio Grande Rift, central New Mexico, in *Faults and subsurface fluid flow in the shallow crust*, W. C. Haneberg, P.S. Mozley, J.C. Moore, and L.B. Goodwin, eds., American Geophysical Union Monograph 113, Washington, DC, US, pages 51-68, 1999.
- Simunek, J., M. Sejna, and T. van Genuchten, The HYDRUS-2D software package for simulating the two-dimensional movement of water, heat, and multiple solutes in variably saturated media, Version 2.0, U.S. Salinity Lab, Agricultural research Service, U.S. Dept. of Agriculture, Riverside, CA, USA, April, 1999.

## CHAPTER 6: CONCLUSIONS AND RECOMMENDATIONS FOR FUTURE WORK

### 6.0 Conclusions

Deformation band faults possess strikingly different saturated and unsaturated hydraulic properties than their poorly lithified parent sands. Based on studies of five faults and associated protolith, the differences in hydraulic properties persist between fault and protolith despite variations in fault displacement, mineral composition of the clay size fraction (CSF), and spatial distribution of the deformation bands within the fault. Fault saturated hydraulic conductivity ( $K$ ) is one to three orders of magnitude less than protolith saturated  $K$  and the difference depends on the CSF composition of both fault and protolith. Fault porosity and air entry matric potentials are appreciably smaller and larger, respectively, than those for the protolith. Under unsaturated conditions, fault  $K$  equals sand  $K$  at some matric potential value that we call the crossover point. Each pair of fault and sand samples has its own crossover point, all of which fall between -35 to -120 cm for the samples studied. As matric potential  $\psi$  decreases, correlating to drier climates, fault  $K$  declines much less steeply than protolith  $K$ . For  $\psi < -100$  cm, typical for semi-arid and arid zones, fault  $K$  exceeds protolith  $K$  by one to six orders of magnitude.

One study area, the Elmendorf area, has a clay size fraction (CSF) with pure and presumably authigenic smectite, whereas the other study area, at Canyon Trail, has a clay size fraction with a mixture of smectite, other clay minerals, and other minerals.

Differences in CSF composition are associated with significant differences in protolith hydraulic properties. Despite point count analyses that show no significant difference between the protolith samples, saturated  $K$  is more than two orders of magnitude lower for protolith with pure smectite CSF than saturated  $K$  for protolith with mixed clay mineral CSF. CSF mineralogy appears to have a smaller impact on fault hydraulic properties.

Simple, one dimensional flow and transport models which incorporate the measured hydraulic properties for five faults and associated protolith predict that faults can act as preferential pathways, or conduits, for flow and transport through vadose-zone sand beds under arid or semi-arid conditions. Areas within the Rio Grande rift possess the conditions necessary for allowing preferential flow and transport. Conduit behavior is predicted for both a steady, gravity-driven infiltration scenario, in which the matric potential is constant throughout the domain, and for a steady, evaporation-driven exfiltration scenario, in which a matric potential gradient drives water upward from a shallow water table to the atmosphere.

Given an adequate fault spatial density, faulted sand beds can induce greater infiltration or exfiltration than unfaulted sand beds, effectively extending liquid-phase fluxes into drier conditions where competing vapor-phase flow processes would otherwise dominate water movement. Depending on fault spatial density, infiltration and

exfiltration flux rates through faulted sands can be enhanced by up to two orders of magnitude above the flux rates predicted for either unfaulted sand or the competing vapor-phase flow process. Fault densities necessary to enhance flow are much higher for sites with pure smectite CSF than sites with mixed clay mineral CSF, at least in cases like those documented here, where the CSF composition is similar in both protolith and fault. We have observed fault densities that are more than sufficient to increase infiltration and exfiltration under the relatively dry vadose-zone conditions expected for the Rio Grande rift and similar arid and semi-arid areas.

Solute residence times are roughly one to nearly five orders of magnitude longer in protolith than faults, whether flow is driven by gravity or evaporation. Advection yields to diffusion as the dominant transport process in protolith for drier conditions, i.e., decreasing  $\psi$  for the gravity scenario or increasing depth to water table  $H$  for the evaporation scenario. In contrast, advection dominates solute transport through faults across much of the ranges for both  $\psi$  and  $H$ . Many more pore volumes, as many as four orders of magnitude more, can pass through a fault in the time needed to pass a single pore volume through the same amount of protolith. The large difference in pore volumes indicates faults are far more likely to undergo preferential cementation or other diagenetic changes. Relative pore volumes are larger under evaporation-driven flow than gravity-driven flow.

Of the three geological characteristics investigated here, only the mineralogy of the clay size fraction and the spacing between deformation bands within the fault were associated with significant effects on hydraulic properties or flow and solute transport

behavior. Fault displacement appears to have a negligible impact on either hydraulic property differences or enhancement of flow and solute transport for the displacement range studied here.

Clay size fraction mineralogy strongly influences the amount of preferential flow and solute transport. However, differences between fault and protolith in properties and behavior remain consistent regardless of CSF composition for the materials studied here. Enhancement of flow and solute transport is greater for sites with mixed clay mineral CSF than for sites with a pure, and likely authigenic, smectite CSF. The location of the dominance threshold for diffusion, the point at which the advective flux rate decreases to the magnitude of diffusive flux rate, also appears to vary with protolith CSF because the threshold occurs under wetter conditions (larger  $\psi$  or smaller  $H$ ) for mixed clay mineral CSF than pure smectite CSF. Thus, advective solute flux exceeds diffusive flux in protolith with mixed clay mineral CSF for a narrower range of  $\psi$  or  $H$  than in protolith with pure smectite CSF, making diffusion the dominant solute transport process in protolith across most of the  $\psi$  and  $H$  ranges studied here.

The spacing between deformation bands within the fault also influences the amount of preferential flow and solute transport. Flow and transport enhancement is greater for faults with closely spaced (dense) deformation bands than faults with more widely spaced (diffuse) deformation bands. Differences in solute residence times between protolith and fault are larger for faults with dense distributions of deformation bands than faults with diffusely distributed deformation bands.

I propose the term “capillary wicking” to describe the preferential flow and transport behavior predicted for crosscutting deformation band faults in poorly lithified sands given dry climate conditions. Capillary wicking, and thus conduit flow within the fault, occur under governing conditions drier than the crossover point for the fault and sand.

Deformation band faults can also act as loci for preferential flow and transport through vadose-zone sand beds under wet climates if fault dip is less than vertical. In a wet climate ( $\psi_{ss} > \psi_x$ ), a fault with dip less than  $90^\circ$  can act as a catchment by intercepting and channeling water along its contact with the hanging wall. The intercepted water increases water content along the contact between the fault and the hanging wall. The enhanced moisture content leads to a greater hydraulic conductivity, hence higher flux densities and seepage velocities. This zone of enhanced moisture content accelerates the movement of liquid-phase water and solutes relative to the footwall, fault, or other parts of the hanging wall. However, enhancement of flow and transport by conduit behavior in semi-arid or arid climate conditions is far greater than catchment enhancement in wetter climates.

Evaluation of catchment behavior in a wet climate for a non-vertically dipping fault requires a 2D model, whereas a simple 1D model suffices for all faults, regardless of dip, in dry climates, given a uniform and simple fault geometry. Flow enhancement for a non-vertical fault as measured by the composite flux density can be accurately calculated using the 1D model for dry climates after adjusting fault flux for the dip angle.

## 6.1 Recommendations for future work

My recommendations for future work fall into two general categories. The first focuses on additional hypothesis tests and the second focuses on application of our approach to other locations, lithologies, vadose-zone processes, etc.

Additional tests of the hypotheses considered in this study should include field-based observation of preferential flow through faults. However, observing fault conduit behavior during infiltration experiments is likely to be very difficult because the crossover points for most fault and protolith pairs occur in conditions sufficiently dry to only allow very small fluxes through either fault and protolith. Long-term tracer tests using non-reactive tracers and/or tracer dyes could be used in both infiltration and exfiltration experiments. Geophysical detection of differences in the wetting fronts is not likely to succeed, given the relatively small thicknesses common to most faults and the finest resolution possible with the geophysical instruments, although a high frequency ground penetrating radar (GPR) instrument might have some limited success.

Another possible hypothesis test is to compare stable isotope tracers collected from deformation band faults and adjacent protolith. Assuming samples can be recovered from depth, preferential infiltration from steady gravity-driven flow might be successfully measured, especially if tracers specific for liquid-phase water are used. Mapping calcite cementation textures, compositions, and distributions within and adjacent to faults could also potentially reflect the expected disparities in flux rates.

Further work is needed to investigate the mineralogy of the fault's clay size fraction and other intergranular material. How does this material vary within and between faults and between different protolith beds? Do these variations affect the differences between sand and fault hydraulic properties and behavior? How does smectite differ between the Canyon Trail and Elmendorf clay size fractions?

Fault solute transport properties, especially dispersion and adsorption, should be investigated further to confirm whether fault conduit behavior accelerates solute transport. Some classes of solutes may be highly retarded by the fault's pseudomatrix whereas others may not be affected. Retardation of solutes may also be strongly affected by the clay mineralogy of the pseudomatrix.

There are numerous possible applications of our approach to identify preferential flow and solute transport by capillary wicks or catchments. These include application to other geologic materials, other time and space scales, and inclusion of other vadose zone processes.

Comparison of hydraulic properties for coarser grained protolith and associated deformation band faults should be made. We speculate that the differences in hydraulic properties will be even greater between faults and coarser-grain sandy protolith, than for the faults and finer-grained sandy sediments we studied here. This assumes that the deformation-induced changes in pore networks are independent of grain size. Such an assumption may be warranted in litharenites and similarly heterolithic sands rich in volcanoclastics and other relatively weak lithics. Deformation band faults may prove to be fast paths through unwelded ignimbrites [Wilson et al., 2003], because faulting may

greatly increase the number of interconnections between pores, relative to those found in the parent rock.

Larger scales should also be investigated, especially with regard to heterolithic basin fill. A single fault can crosscut many lithologies in the Santa Fe Group of the Rio Grande rift, not just sands, but can we expect either conduit or catchment behavior along the segments of that fault without any deformation bands or zones of deformation bands? Could the action of the other lithologies and other fault architectures enhance recharge or solute transport? If the conduit and catchment behavior described here are only found in sandy sediments, how do the other lithologies and segments with different fault architectures affect the infiltrating water and solutes?

The effect of time-varying surface boundary conditions (matric potential and fluxes) should be investigated for catchment and conduit behaviors. Can enhancement of infiltration by catchment behavior be expected if the top matric potential or flux rate change with time? An example is ephemeral waterways like arroyos or streams in semi-arid and arid areas.

The effects of other fluid phases, such as water vapor or non-aqueous phase liquids (NAPLs) should be investigated. Could faults accelerate the transport of light or dense NAPLs through the vadose zone? What are the differences in vapor-phase movement through fault and protolith in extremely dry vadose zones?

The relative differences in multi-phase water flow and heat transport between fault and protolith should be evaluated. Could deformation band faults act as heat pipes?

Characterizing the cementation in faults and nearby protolith and mapping the spatial distribution of the cements over larger scales could indicate the relative proportions of conduit and catchment behavior. For example, comparing the incidence of fault cementation to hanging wall cementation between faults or along strike for a single fault could provide some measure of whether conduit or catchment behavior is areally more significant.

Faults of various displacements could be reliable indicators of paleo-recharge via catchment behavior, but this needs to be confirmed. Stratigraphic columns of sediments overlying well-cemented zones of enhanced moisture content could show signs of ponded water or long-term saturation. Perhaps the isotopic signatures of the cements could determine whether the cements originated from gravity-driven infiltration of atmospheric water.

## CHAPTER 7: REFERENCES

- Affek, H. P., D. Ronen, and D. Yakir, Production of CO<sub>2</sub> in the capillary fringe of a deep phreatic aquifer, *Water Resour. Res.*, 34, 989-996, 1998.
- Antonellini, M. and A. Aydin, Effect of faulting on fluid flow in porous sandstones: petrophysical properties, *AAPG Bull.*, 78, 355-377, 1994.
- Antonellini, M., A. Aydin, and D. Pollard, Microstructure of deformation bands in porous sandstones at Arches National Park, Utah, *J. Struct. Geol.*, 16, 941-959, 1994.
- Aydin, A. and Myers, R., The permeability structure of fault zones formed from shearing of pre-existing joint zones, *Geological Society of America Abstracts with Programs*, 29, 416, 1997.
- Aydin, A., Small faults formed as deformation bands in sandstone, *Pure Applied Geophys.*, 116, 913-930, 1978.
- Basha, H. A., and N. I. Mina, Estimation of the unsaturated hydraulic conductivity from the pressure distribution in a centrifugal field, *Water Resour. Res.*, 35, 469-477, 1999.
- Bear, J., M. Y. Corapcioglu, and J. Balakrishna, Modeling of centrifugal filtration in unsaturated deformable porous-media. *Advan. in Water Resour.*, 7, 150-167, 1984.
- Boggs, S., *Principles of Sedimentology and Stratigraphy*, Macmillan Publishing Co., New York, NY, 784 pages, 1987.
- Brainard, J. R., Glass, R. J., Alumbaugh D. L., Paprocki, L., Labrecque, D. J., Yang, X., Yeh, T.-C. J., Baker, K. E., and Rautman, C. A., *The Sandia-Tech Vadose Zone*

- Facility experimental design and data report of a constant flux infiltration experiment, Sandia Rep. SAND02-2168, Sandia Natl. Laboratories, Albuquerque, N. M., 2002.
- Brainard, J. R., Vadose zone flow processes in heterogeneous alluvial fan deposits: experimental design, data evaluation, and error analysis, M.S. (Geology), University of New Mexico, Albuquerque, New Mexico, 1997.
- Brooks, R. H. and A. T. Corey, Hydraulic properties of porous media, Hydrology Paper No. 3, Colorado State University, Fort Collins, CO, 1964.
- Caine, J.S., J.P. Evans, and C.B. Forster, Fault zone architecture and permeability structure, *Geology*, 24, 1025-1028, 1996.
- Carter K.E. and C.L. Winter, Fractal nature and scaling of normal faults in the Espanola Basin, Rio Grande rift, New Mexico: Implications for fault growth and brittle strain, *J. Struct. Geol.*, 17, 863-873, 1995.
- Cashman, S. and K. Cashman, Cataclasis and deformation-band formation in unconsolidated marine terrace sand, Humboldt County, California, *Geology*, 28, 111-114, 2000.
- Conca, J. L. and J. V. Wright, Diffusion coefficients in gravel under unsaturated conditions, *Water Resour. Res.*, 26, 1055-1066, 1990.
- Conca, J. L. and J. V. Wright, Flow and diffusion in unsaturated gravel, soil and whole rock, *Applied Hydrogeology*, 1, 5-24, 1992.
- Conca, J. L. and J. V. Wright, The UFA method for rapid, direct measurements of unsaturated transport properties in soil, sediment, and rock, *Australian J. Soil Res.*, 36, 291-315, 1998.

- Conca, J., D. G. Levitt, P. R. Heller, T. J. Mockler, and M. J. Sully, Direct UFA measurements of unsaturated hydraulic conductivity, comparisons to van Genuchten/Mualem estimations, and applications to recharge mapping in Arid Regions, in *Characterization and Measurement of the Hydraulic Properties of Unsaturated Porous Media*, M. Th. van Genuchten, F. J. Leij and L. Wu (eds.), Univ. Calif., Riverside, CA, vol. 2, 1173-1197, 1999.
- Conca, J., D. Levitt, P. Heller, T. Mockler, and M. Sully, Direct UFA measurements of unsaturated hydraulic conductivity, comparisons to van Genuchten/Mualem estimations, and applications to recharge mapping in arid regions, in *Characterization and Measurement of the Hydraulic Properties of Unsaturated Porous Media*, M. Th. van Genuchten, F. J. Leij, and L. Wu (eds.), Univ. Calif., Riverside, CA, 2, 1173-1197, 1999.
- Connell, S.D., Koning, D.J., and Cather, S.M., Revisions to the stratigraphic nomenclature of the Santa Fe Group, northwestern Albuquerque Basin, New Mexico: *New Mexico Geological Society Guidebook, 50th Field Conference*, p. 337-353, 1999.
- Crank, J., *The Mathematics of Diffusion*, 2nd edition, Oxford University Press, Oxford, UK, 414 pages, 1975.
- Davis, G. H., Fault-fin landscape, *Geological Magazine*, 135, 283-286, 1998.
- Davis, J. M., R. C. Lohmann, F.M. Phillips, J.L. Wilson, and D. W. Love, Architecture of the Sierra Ladrones Formation, central New Mexico: depositional controls on the permeability correlation structure, *Geological Society of America Bulletin*, 105, 998-1007, 1993.

- Edwards, H. E., A.D. Becker, and J.A. Howell, Compartmentalization of an eolian sandstone by structural heterogeneities: Permo-Triassic Hopeman Sandstone, Moray Firth, Scotland, in *Characterization of Fluvial and Aeolian Reservoirs*, edited by C. P. North and D. J. Prosser, Geologic Society (UK), London, 339-365, 1993.
- Fischer, U., B. Kulli, and H. Fuhler, Constitutive relationships and pore structure of undisturbed fracture zone samples with cohesionless fault gouge layers, *Water Resour. Res.*, 34, 1695-1702, 1998.
- Flint, L.E., D. B. Hudson, and A.L. Flint, Unsaturated hydraulic parameters determined from direct and indirect methods, in *Characterization and Measurement of the Hydraulic Properties of Unsaturated Porous Media*, M. Th. van Genuchten, F. J. Leij and L. Wu (eds.), Univ. Calif., Riverside, CA, 293-302, 1999.
- Forbes, P. L., Simple and accurate methods for converting centrifuge data into drainage and imbibition capillary pressure curves, *Log Analyst*, 35, 31-53, 1994.
- Forbes, P.L., Centrifuge data analysis techniques: An SCA survey on the calculation of drainage capillary pressure curves from centrifuge measurements, Society of Core Analysts report, 184 pages, 1997.
- Fowles, J. and S. Burley, Textural and permeability characteristics of faulted, high porosity sandstones, *Mar. Petrol. Geol.*, 11, 608-623, 1994.
- Gardner, W. R., Some steady state solutions of the unsaturated moisture flow equation with application to evaporation from a water table, *Soil Science*, 85, 228-232, 1958.
- Goldstein, H., *Classical Mechanics*, Addison-Wesley Publishing, Reading, MA USA. 399 pgs, 1959.

- Goodwin, L.B. and B. Tikoff, Competency contrast, kinematics, and the development of foliations and lineations in the crust, *J. Struct. Geol.*, 24, 1065-1085, 2002.
- Grauch, V. J., High-resolution aeromagnetic data, a new tool for mapping intrabasinal faults: Example from the Albuquerque basin, New Mexico, *Geology*, 29, 367-370, 2001.
- Hagoort, J., Oil recovery by gravity drainage, *Soc. Petrol. Eng. J.*, SPE 1424, 20, 139-150, 1980.
- Hall, J. S., P.S. Mozley, J.M. Davis, and N. Delude-Roy, Environments of formation and controls on spatial distribution of calcite cementation in Plio-Pleistocene fluvial deposits, New Mexico, USA, *Jour. Sedimentary Res.* 74, in press, 2004.
- Hassler, G. L., and E. Brunner, Measurement of capillary pressures in small core samples, *Transactions, AIME*, 160, 114-123, 1945.
- Hawley, J. W., compiler, *Guidebook to Rio Grande Rift in New Mexico and Colorado*, New Mexico Bureau of Mines and Mineral Resources, Socorro, New Mexico, 1978.
- Hawley, J. W., Haase, C. S., and Lozinsky, R. P., An underground view of the Albuquerque Basin, New Mexico, in Ortega-Klett, C. T., ed., *Proceedings of the 39th Annual New Mexico Water Conference*, New Mexico Water Resource Research Institute Report 290, 37-55, 1995.
- Hawley, J.W. and Kernodle, J.M., Overview of the hydrogeology and geohydrology of the northern Rio Grande basin—Colorado, New Mexico, and Texas, in Ortega-Klett, C.T., ed., *Proceedings of the 44th Annual New Mexico Water Conference*: New Mexico Water Resources Research Institute Report 312, 79-102, 2000.
- <http://wrri.nmsu.edu/publish/watcon/proc/proc44/contents.html>

- Hawley, J.W., Kennedy, J.F., Creel, B.J., The Mesilla Basin aquifer system of New Mexico, West Texas and Chihuahua—an overview of its hydrogeologic framework and related aspects of groundwater flow and chemistry, in Angle, E.S., and Mace, R.E., Aquifers of West Texas: Texas Water Development Board Special Conference Proceedings Volume, 76-99, 2001.
- <http://www.twdb.state.tx.us/publications/reports/GroundWaterReports/GWReports/Individual%20Report%20htm%20files/Report%20356.htm>
- Herrin, J. M., Characteristics of deformation bands in poorly lithified sand: Rio Grande rift, New Mexico, M.S. (Geology), New Mexico Institute of Mining and Technology, Socorro, New Mexico, 2001.
- Heynekamp, M. R., L.B. Goodwin, P.S. Mozley, and W.C. Haneberg, Controls on fault-zone architecture in poorly lithified sediments, Rio Grande Rift, New Mexico; implications for fault-zone permeability and fluid flow, in Faults and Subsurface Fluid Flow in the Shallow Crust, W. C. Haneberg, P.S. Mozley, J.C. Moore, and L.B. Goodwin, eds., American Geophysical Union Monograph 113, Washington, DC, US, 27-49, 1999.
- Hillel, D., Environmental Soil Physics, Academic Press, San Diego, CA, 771 p., 1998.
- Hong, S., Anisotropic hydraulic conductivity of faulted poorly consolidated eolian sands: Bosque, New Mexico, M.S. (Geology), New Mexico Institute of Mining and Technology, Socorro, New Mexico, 1999.
- Irmay, S., Solutions of the non-linear diffusion equation with a gravity term in hydrology, H. W. Rijtema and P. E. Wessink, editors, In Symposium on Water in the

- Unsaturated Zone, International Association of Scientific Hydrology-UNESCO, 1966, Wageningen, Netherlands, 1968.
- Kelley, V.C., Geology of Albuquerque Basin, New Mexico, Memoir 33, New Mexico Bureau of Mines and Mineral Resources, Socorro, NM, 60 pages, 1977.
- Khaleel, R., J. F. Relyea, and J. L. Conca, Estimation of van Genuchten-Mualem relationships to estimate unsaturated hydraulic conductivity at low water contents, Water Resour. Res., 31, 2659-2668, 1995.
- Kundu, P.K. and I.M. Cohen, Fluid Mechanics, 2nd ed., Academic Press, New York, 730 pgs, 2002.
- Kung, K-J.S., Laboratory observation of funnel flow mechanism and its influence on solute transport, J. Environmental Quality, 22, 91-102, 1993.
- Kung, K-J.S., Preferential flow in a sandy vadose zone. 1. Field observation, Geoderma, 46, 51-58, 1990.
- Kung, K-J.S., Preferential flow in a sandy vadose zone. 2. Mechanism and implications, Geoderma, 46, 59-71, 1990.
- Masterson, J.P., K.M. Hess, D.A. Walter, and D.R. LeBlanc. Simulated Changes in the Sources of Ground Water for Public-Supply Wells, Ponds, Streams, and Coastal Areas on Western Cape Cod, Massachusetts, U.S. Geological Survey Water-Resources Investigations Report 02-4143, 2002.
- Mattson, E.D., Field simulation of waste impoundment seepage in the vadose zone: Experiment design in two dimensional modeling, M.S. (Hydrology) thesis, New Mexico Institute of Mining and Technology, Socorro, New Mexico, , 1989.

- McCord, J. T. and D. B. Stephens, Lateral moisture flow beneath a sandy hillslope without an apparent impeding layer, *Hydrological Processes*, 1, 225-238, 1987.
- McCord, J. T., D. B. Stephens, and J. L. Wilson, Hysteresis and state-dependent anisotropy in modeling unsaturated hillslope hydrologic processes. *Water Resour. Res.* 27:1501-1518, 1991.
- McCord, J. T., D. B. Stephens, and John L. Wilson. 1991. Hysteresis and state-dependent anisotropy in modeling unsaturated hillslope hydrologic processes. *Water Resour. Res.* 27:1501-1518.
- Millington, R.J. and J.P. Quirk, Permeability of porous solids, *Trans. Faraday Soc.*, 57, 1200-1207, 1961.
- Mollema, P.N. and Antonellini, M.A., Compaction bands: a structural analog for anti-mode I cracks in aeolian sandstone, *Tectonophysics*, 267, 209-228, 1996.
- Mozley, P. S., and L. B. Goodwin, Patterns of cementation along a Cenozoic normal fault: A record of paleoflow orientations, *Geology*, 23, 539-542, 1995.
- Mozley, P., J. Beckner, and T. M. Whitworth, Spatial distribution of calcite cement in the Santa Fe Group, Albuquerque Basin, NM; implications for ground-water resources, *New Mexico Geology*, 17, 88-93, 1995.
- Mualem, Y, A new model for predicting the hydraulic conductivity of unsaturated porous media, *Water Resour. Res.*, 12, 513-522, 1976.
- Nimmo, J. R. Adaptation of the steady-state centrifuge method to extend the range of hydraulic conductivity measurement, *Ground Water*, 26, 785-786, 1988.
- Nimmo, J. R., and K. A. Mello, Centrifugal techniques for measuring saturated hydraulic conductivity. *Water Resour. Res.*, 27, 1263-1269, 1991.

- Nimmo, J. R., Experimental testing of transient unsaturated flow theory at low water-content in a centrifugal field, *Water Resour. Res.*, 26, 1951-1960, 1990.
- Nimmo, J. R., J. Rubin, and D. P. Hammermeister, Unsaturated flow in a centrifugal field: measurement of hydraulic conductivity and testing of Darcy's law, *Water Resour. Res.*, 23, 124-134, 1987.
- O'Meara, D. J., Jr. and Crump, J. G., Measuring capillary pressure and relative permeability in a single centrifuge experiment, presented at the SPE 60th Annual Technical Conference and Exhibition, Las Vegas, Nevada, Sept. 22-25, paper SPE 14419, *Soc. Petrol. Eng. J.*, 1985.
- Ogilvie, S. R., J.M. Orribo, and P.W. Glover, The influence of deformation bands upon fluid flow using profile permeametry and positron emission tomography, *Geophys. Res. Lett.*, 28, 61-64, 2001.
- Oki, D.S., Reassessment of Ground-Water Recharge and Simulated Ground-Water Availability for the Hawi Area of North Kohala, Hawaii, U.S. Geological Survey Water-Resources Investigations Report 02-4006. 2002.
- Olesen, T., P. Moldrup, K. Henriksen, and L. W. Petersen, Modeling diffusion and reaction in soils: IV. New models for predicting ion diffusivity, *Soil Science*, 161, 633-645, 1996.
- Philip, J.R. and D.A. DeVries, Moisture movement in porous materials under temperature gradients, *Trans. Am. Geophysical Union*, 38, 222-228, 1957.
- Phillips, F. M., J.L. Mattick, and T.A. Duval, Chlorine 36 and tritium from nuclear weapons fallout as tracers for long-term liquid and vapor movement in desert soils, *Water Resour. Res.*, 24, 1877-1891, 1988.

Pittman, E.D., Effect of fault-related granulation on porosity and permeability of quartz sandstones, Simpson Group (Ordovician), Oklahoma, AAPG Bull., 65, 2381-2387, 1981.

Rawling, G. C., Goodwin, L. B., Wilson, J. L, Internal architecture, permeability structure, and hydrologic significance of contrasting fault-zone types, *Geology*, 29, 43-46, 2001.

Rawling, G. C., L. B. Goodwin, and J. L. Wilson, Internal architecture, permeability structure, and hydrologic significance of contrasting fault-zone types, *Geology*, 29, 43-46, 2001.

Reiter, M., Hydrothermal studies on the southern part of Sandia National Laboratories/Kirtland Air Force Base; data regarding ground-water flow across the boundary of an intermontane basin, in *Faults and subsurface fluid flow in the shallow crust*, W. C. Haneberg, P.S. Mozley, J.C. Moore, and L.B. Goodwin, eds., American Geophysical Union Monograph 113, Washington, DC, US, pages 207-222, 1999.

Rockhold, ML, CS Simmons, and MJ Fayer, An analytical solution technique for one-dimensional, steady vertical water flow in layered soils, *Water Res. Resour.*, 33, 897-902, 1997.

Ross, B., A conceptual model of deep unsaturated zones with negligible recharge, *Water Resour. Res.*, 28, 1627-1629, 1984.

Ross, B., The diversion capacity of capillary barriers, *Water Resour. Res.*, 26, 2625-2629, 1990.

Ruth, D. W., and S. Wong, Centrifuge capillary pressure curves, *J. Canadian Petrol. Tech.*, 29(3), 67-72, 1990.

Ruth, D. W., and S. Wong, Calculation of capillary pressure curves from data obtained by the centrifuge method, *Log Analyst*, 32, 575-581, 1991.

Scanlon, B. R. and P. C. Milly, Water and heat fluxes in desert soils, 2, Numerical simulations, *Water Resour. Res.*, 30, 721-734, 1994.

Scanlon, B. R., Evaluation of liquid and vapor water flow in desert soils based on chlorine 36 and tritium tracers and nonisothermal flow simulations, *Water Resour. Res.*, 28, 285-297, 1992.

Scanlon, B. R., S.W. Tyler, and P.J. Wierenga, Hydrologic issues in arid, unsaturated systems and implications for contaminant transport, *Reviews of Geophysics*, 35, 461-490, 1997.

Scanlon, B. R., Water and heat fluxes in desert soils, 1, Field studies, *Water Resour. Res.*, 30, 709-720, 1994.

Selker, J. S., C. K. Keller, and J. T. McCord, *Vadose Zone Processes*, CRC Press LLC, Boca Raton, Florida, 339 pages, 1999.

Sigda, J.M., Effects of small-displacement faults on the permeability distribution of poorly consolidated Santa Fe Group sands, Rio Grande rift, New Mexico, MS. (Hydrology) thesis, New Mexico Institute of Mining and Technology, Socorro, New Mexico, 1997.

Sigda, J.M., Preferential flow and transport through deformation band faults in the semi-arid vadose zone of the Rio Grande rift, New Mexico, USA, Ph.D. (Hydrology) dissertation, New Mexico Institute of Mining and Technology, Socorro, New Mexico, 2004.

- Sigda, J. M., L. B. Goodwin, P. S. Mozley, and J. L. Wilson, Permeability alteration in small-displacement faults in poorly lithified sediments; Rio Grande Rift, central New Mexico, in *Faults and subsurface fluid flow in the shallow crust*, W. C. Haneberg, P.S. Mozley, J.C. Moore, and L.B. Goodwin, eds., American Geophysical Union Monograph 113, Washington, DC, US, pages 51-68, 1999.
- Sigda, J.M. and J.L. Wilson. Are faults preferential flow paths through semi-arid and arid vadose zones?, *Water Resour. Res.*, 39, 1225, doi:10.1029/2002WR001406, 2003.
- Simunek, J., K. Huang, and M. Th. van Genuchten, The HYDRUS code for simulating the one-dimensional movement of water, heat, and multiple solutes in variably-saturated media. Version 6.0, Research Report No. 144, U.S. Salinity Laboratory, USDA, ARS, Riverside, California, 164pp., 1998.
- Simunek, J., M. Sejna, and T. van Genuchten, The HYDRUS-2D software package for simulating the two-dimensional movement of water, heat, and multiple solutes in variably saturated media, Version 2.0, U.S. Salinity Lab, Agricultural research Service, U.S. Dept. of Agriculture, Riverside, CA, USA, April, 1999.
- Smith, L., Forster, C., and Evans, J., Interaction of fault zones, fluid flow, and heat transfer at the basin scale, in Neuman, S.P. and Neretnieks, I., eds., *Hydrogeology of Low Permeability Environments*, Verlag Heinz Heise, Hannover, Germany, 41-67, 1989.
- Stephens, D. B. and R. Knowlton Jr., Soil water movement and recharge through sand at a semiarid site in New Mexico, *Water Resour. Res.*, 22. 881-889, 1986.

- Taylor, W.L. and Pollard, D.D., Estimation of in situ permeability of deformation bands in porous sandstone, Valley of Fire, Nevada, *Water Resour. Res.*, 36, 2595-2606, 2000.
- van Genuchten, M. T., A closed-form equation for predicting the hydraulic conductivity of unsaturated soils, *Soil Sci. Soc. Am. J.*, 44, 892-898, 1980.
- van Genuchten, M. T., F. J. Leij, and S.R. Yates, The RETC code for quantifying the hydraulic functions of unsaturated soils, EPA/600/2-91/065, U. S. Environ. Protection Agency, Cent. Environ. Res. Inf., Cincinnati, OH, United States, 1991.
- Walvoord M., M.A. Plummer, F.M. Phillips F. M., and A.V. Wolfsberg, Deep arid system hydrodynamics, Part 1: Equilibrium states and response times in thick desert vadose zones, *Water Resour. Res.*, 38 (12), 1308, doi:10.1029/2001WR000824, 2002.
- Wilson, J. E., L. B. Goodwin, and C. J. Lewis, Deformation bands in nonwelded ignimbrites: Petrophysical controls on fault-zone deformation and evidence of preferential fluid flow, *Geology* 31, 837-840, 2003.
- Winograd, I.J., Radioactive waste disposal in thick unsaturated zones, *Science*, 212, 1457-1464, 1981.
- Wood, B. D., C. K. Keller, and D. L. Johnstone, In situ measurement of microbial activity and controls on microbial CO<sub>2</sub> production in the unsaturated zone, *Water Resour. Res.*, 29, 647-660, 1993.
- Wright, J. V., J. L. Conca, and X. Chen.. Hydrostratigraphy and recharge distributions from direct measurements of hydraulic conductivity using the UFA™ method, Technical Report PNL-9424, Pacific Northwest Laboratory, Richland, Washington, 1994.

## APPENDIX 8.A: CENTRIFUGE METHODS

### 8.A.1 FORCES IN A CENTRIFUGAL FIELD

Rigorous description of a centrifugal field requires an appropriate frame of reference. A fixed point  $P$ , located by radial vector  $\mathbf{r}(t)$  (L) within a non-deforming body rotated at constant angular velocity  $\omega$  ( $T^{-1}$ ) in a centrifuge, experiences a tangential velocity  $\mathbf{v}_I$  ( $LT^{-1}$ ) when observed from an inertial reference frame (Figure 8.A.1a). Inertial reference frames are distinguished by coordinate axes  $x_I, y_I$  which remain constant in space and time (subscript  $I$  indicates a quantity observed from an inertial reference frame). Point  $P$  is accelerating even though its speed remains constant because the direction of velocity  $\mathbf{v}_I$  continually changes. This radial center-directed acceleration, created by the mechanical force of the rotor arm, is the centripetal (center-seeking) acceleration and is given by

$$\begin{aligned}\mathbf{a}_I &= \frac{d\mathbf{v}_I}{dt} = \frac{d}{dt}(\omega \times \mathbf{r}(t)) = \left(\omega \times \frac{d\mathbf{r}(t)}{dt}\right) + \left(\frac{d\omega}{dt} \times \mathbf{r}(t)\right) \\ &= (\omega \times \mathbf{v}_I) + 0 = \omega \times (\omega \times \mathbf{r}(t))\end{aligned}\tag{8.A.1}$$

simplified for constant  $\omega$ . Note that  $\mathbf{a}_I$  is directed radially inwards to the axis of rotation according to the right hand rule for vector cross-products.

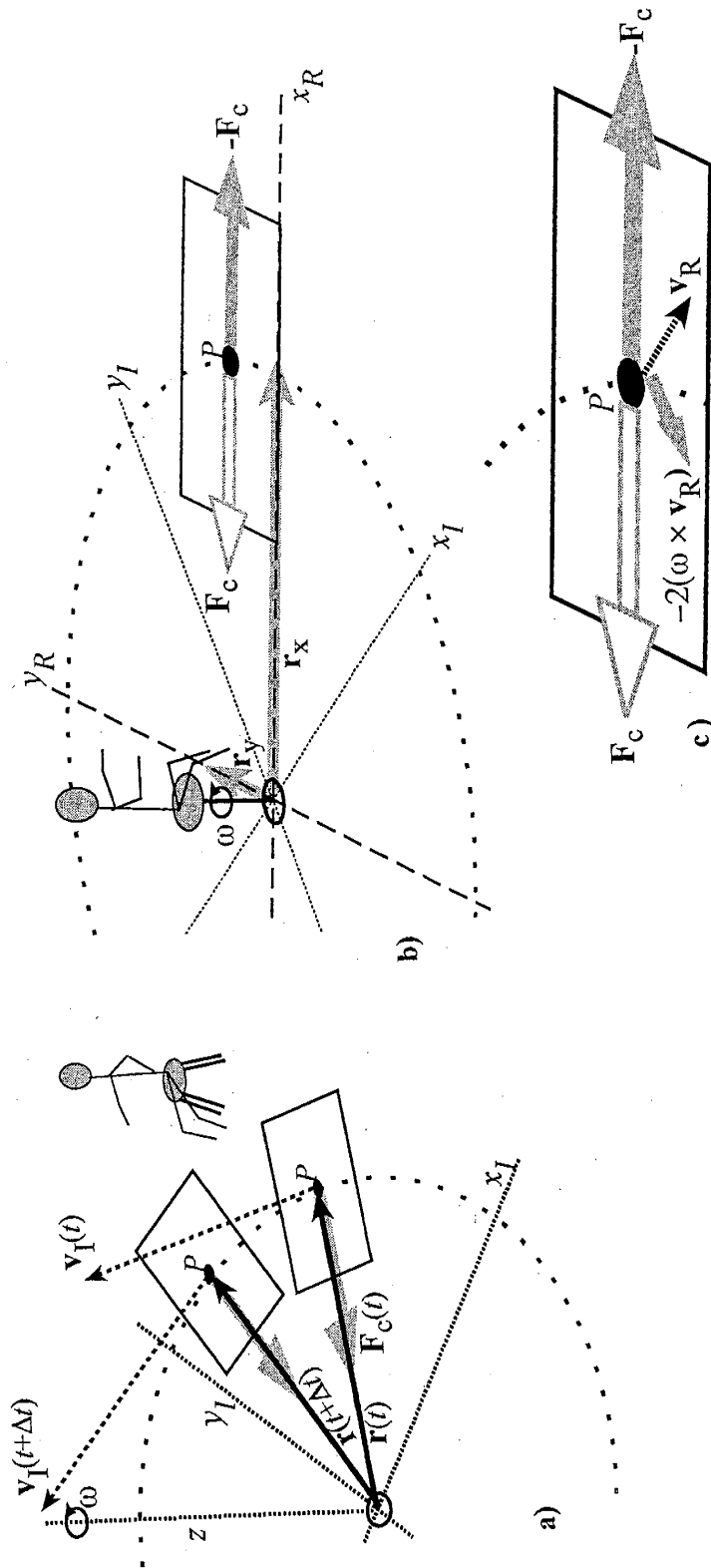


**Figure 8.A.1:** Inertial and rotating reference frames. **a)** An observer monitors the motion of fixed point  $P$  within a centrifuge sample moving at angular velocity  $\omega$  with regard to an inertial reference frame described by axes  $x_I, y_I$ . At time  $t$ ,  $P$ 's position and tangential velocity are given by  $r(t)$  and  $v_I(t)$ . The centrifugal force  $F_c$  causes the time-varying direction in  $v_I(t)$ . **b)** The observer moves at speed  $|\omega|$  together with the centrifuge sample,  $P$ 's position is given by the resultant of position vectors  $r_x$  and  $r_y$  which are defined within the rotating reference frame denoted by axes  $x_R, y_R$ . Neither velocity  $v_I(t)$  nor  $F_c$  are apparent to the observer within this reference frame. The inward force is counterbalanced by another pseudo-force  $-F_c$  (centrifugal force), otherwise  $P$  would accelerate. **c)** If  $P$  is not fixed, but moves with velocity  $v_R$  as observed within the rotating reference frame, then it experiences apparent acceleration from the centripetal ( $F_c$ ), centrifugal ( $-F_c$ ), and Coriolis ( $-2(\omega \times v_R)$ ) forces.

If point  $P$  is observed by someone moving with the sample, i.e., from the rotating reference frame given by axes  $x_R, y_R$  that share the same origin as the inertial axes but rotate with constant angular velocity  $\omega$ ,  $P$  will appear to be stationary (Figure 8.A.1b). The observer will not notice the changing direction of the tangential (inertial) velocity  $\mathbf{v}_I$ . Though not perceived by the rotating observer, the centripetal force still operates within the rotating reference frame by exerting a pull on  $P$  towards the axis of rotation through the action of the rotor arm. To the rotating observer, the centripetal force must therefore be balanced by another force, otherwise  $P$  would accelerate towards the center. This pseudo-balancing force is defined as the centrifugal (center-fleeing) force,  $\mathbf{F}_{cf}$ , and has the same magnitude but opposite direction of the centripetal force,  $\mathbf{F}_{cp}$ , yielding a zero force balance on  $P$ . Moreover, the centrifugal force is only apparent in the rotating reference frame, not in the inertial frame.

The force balance changes if  $P$  is no longer fixed (Figure 8.A.1c) and instead represents a packet of fluid molecules with mass  $m$  moving with constant fluid velocity  $\mathbf{v}_R$  (as measured by the observer in the rotating reference frame) through a non-deforming porous medium. Determining the force balance on  $P$  requires a vector transform operator  $[d()/dt]_I = \{[d()/dt]_R + \omega \times ()\}$  which describes the time rate of change in both frames of reference [Goldstein, 1959]. The inertial and rotating reference frame velocities are determined by applying the transform operator to the vector  $\mathbf{r}(t)$  describing  $P$ 's time-varying position:

$$\mathbf{v}_I = \left( \frac{d}{dt} \right)_I \mathbf{r}(t) = \left( \left( \frac{d}{dt} \right)_R + \omega \times \right) \mathbf{r}(t) = \mathbf{v}_R + \omega \times \mathbf{r}(t) \quad (8.A.2)$$

Applying the same transform again to (8.A.2),

$$\mathbf{a}_I = \left( \left( \frac{d}{dt} \right)_R + \boldsymbol{\omega} \times \right) (\mathbf{v}_R + \boldsymbol{\omega} \times \mathbf{r}(t)) = \mathbf{a}_R + 2(\boldsymbol{\omega} \times \mathbf{v}_R) + \boldsymbol{\omega} \times (\boldsymbol{\omega} \times \mathbf{r}(t)), \quad (8.A.3a)$$

relates  $\mathbf{a}_I$  to  $\mathbf{a}_R$ , the net acceleration for the inertial and rotational frames, respectively.

Solving for acceleration in the rotational frame,  $\mathbf{a}_R$ ,

$$\mathbf{a}_R = \mathbf{a}_I - 2(\boldsymbol{\omega} \times \mathbf{v}_R) - \boldsymbol{\omega} \times (\boldsymbol{\omega} \times \mathbf{r}(t)), \quad (8.A.3b)$$

and multiplying by the fluid packet mass,  $m$  (M), leads to the net force in the rotating frame,  $\mathbf{F}_R$ , written in terms of the net force in the inertial frame,  $\mathbf{F}_I$ , or

$$\mathbf{F}_R = \mathbf{F}_I - 2m(\boldsymbol{\omega} \times \mathbf{v}_R) - m[\boldsymbol{\omega} \times (\boldsymbol{\omega} \times \mathbf{r}(t))] \quad (8.A.3c)$$

The second term on the right-hand side,  $-2m(\boldsymbol{\omega} \times \mathbf{r}(t))$ , is another pseudo-force that affects the moving fluid packet, the Coriolis force, and the last term is the centrifugal force,  $-m[\boldsymbol{\omega} \times (\boldsymbol{\omega} \times \mathbf{r}(t))]$ , also acting on the fluid parcel. The Coriolis force points away from the direction of rotation (Figure 8.A.1c), scales linearly with the rotation speed,  $|\boldsymbol{\omega}|$ , and with the fluid packet's velocity  $\mathbf{v}_R$  (as measured in the rotating reference frame), whereas the centrifugal force points outward from the axis of rotation along  $\mathbf{r}(t)$ , and is proportional to  $\mathbf{r}(t)$  as well as to the square of the rotation speed,  $|\boldsymbol{\omega}|^2$ . For example, on the earth's surface, the Coriolis force caused by the earth's rotation imparts a rightwards deflection to traveling fluid packets in the earth's Northern Hemisphere, but a leftwards deflection to those in the Southern Hemisphere [p. 103, Kundu and Cohen, 2002]. Note that the centrifugal force acting on the fluid packet depends on the packet's position

within the rotating frame of reference  $\mathbf{r}(t)$ , whereas the Coriolis force depends on the packet's fluid velocity  $\mathbf{v}_r$ .

For a fluid packet, the force  $\mathbf{F}_I$  represents the inertial frame forces governing fluid movement. In the case of variably saturated flow through the porous medium these forces include gravity, capillary, and viscous forces. In the rotating reference frame, these forces are joined by the centrifugal and Coriolis (pseudo) forces. Each of these forces must be considered in determining the fluid's dynamic behavior.

Understanding the interplay of gravity, inertial, and pseudo forces operating on flowing fluids is critical to appropriate application of centrifuge methods for measuring unsaturated hydraulic properties of porous materials. Centrifuge methods have long been popular in various fields because the centrifugal body force gradient is easily manipulated and can greatly reduce the time needed to complete measurements near the dry end of the saturation range. The following sections review centrifuge methods, noting the underlying physics, for measuring two important unsaturated relationships: hydraulic conductivity as a function of moisture content,  $K-\theta$ , and moisture content as a function of matric potential,  $\theta-\psi$ .

### 8.A.2 MEASURING $\theta-\psi$ RELATIONSHIPS IN A CENTRIFUGE

Hassler and Brunner [1945] developed the centrifuge method still used today for measuring  $\theta-\psi$  drainage relationships (pressure-saturation or moisture retention curves) in centrifuges. A mainstay of petroleum core analysis laboratories since its introduction, this method subjects a sample, initially saturated with one fluid but in contact with a

second fluid, to a stepwise-increasing series of angular velocities followed by accurate monitoring of changes in fluid saturation. If the initial fluid is wetting and the introduced phase non-wetting, the experiment provides a drainage curve; the converse arrangement provides an imbibition curve. For vadose-zone drainage experiments, the sample is initially saturated with liquid water. Air, the non-wetting fluid, is allowed to freely enter and leave from both ends of the sample during the test. Water drains from the outer end of the rotating sample and is retained in an effluent collection chamber. At each step, centrifuge angular velocity is held constant until the capillary and centrifugal forces equilibrate, and the water flux goes to zero. Then a final average water saturation (% of pore volume occupied by water) or volumetric water content (% of total sample volume occupied by water) is determined. The procedure is repeated after increasing the angular velocity to the next level (see Table 2.1). Centrifugation is continuous during a typical Hassler-Brunner petroleum engineering experiment because highly accurate volumetric effluent chambers are used to collect and measure the expelled liquid. Centrifugation is, however, repeatedly interrupted during an Unsaturated Flow Apparatus (UFA) [Conca et al, 1999; Flint et al, 1999]  $\theta$ - $\psi$  drainage experiment in order to allow the sample weighing necessary to determine average moisture content. At equilibrium for each experimental step, the matric potential and the moisture content distributions within the sample are functions of radial distance  $r$ , the angular velocity  $\omega$ , the sample's (presumed homogeneous) hydraulic properties, and the boundary conditions. The average moisture content – rpm data produced by each experiment must then be inverted to local  $\theta$ - $\psi$  values using one of the many methods developed by Hassler and Brunner [1945] or numerous subsequent researchers (see below).

Hassler and Brunner [1945] derived a pressure – saturation relation for a centrifugally driven flow experiment in which only one-dimensional flow is considered. They treated capillary pressure,  $p$ , as the independent variable solely determining the wetting phase saturation,  $S$ , within a core sample. Given a uniform sample at constant acceleration but in equilibrium, negligible influence by gravity, and an outflow face saturated with the wetting phase, they defined capillary pressure ( $M L^{-1} T^{-2}$ ) for centrifuge drainage experiments as

$$p(\omega, r) = \frac{\Delta\rho\omega^2}{2}(r_o^2 - r^2) = p_i \frac{(r_o^2 - r^2)}{(r_o^2 - r_i^2)} \quad (8.A.4)$$

where  $\Delta\rho$  equals the difference in the wetting and non-wetting phase fluid densities ( $M L^{-3}$ ),  $r$  is the radial distance ( $L$ ) to any point within the sample,  $r_o$  and  $r_i$  are the radial distances ( $L$ ) to the outflow and inner faces, respectively, and  $p_i$  is the capillary pressure at the inlet face ( $M L^{-1} T^{-2}$ ). Wetting phase saturation at the outflow face causes the boundary pressure there,  $p_o$ , to equal zero. At equilibrium in one dimension, the two opposing forces acting on the wetting phase fluid, the capillary pressure and centrifugal body force gradients, are in balance. Note that capillary pressure and saturation should vary along the sample's length, even at equilibrium, and that  $p(r)$  is proportional to the pressure at the inner face.

The Navier-Stokes equations for incompressible fluid momentum conservation in a rotating field, properly augmented to include the centrifugal and Coriolis body forces is:

$$\frac{D\mathbf{u}}{Dt} = -\frac{\nabla p}{\rho} + \nu \nabla^2 \mathbf{u} + \mathbf{g} + \omega^2 \mathbf{r} - 2(\boldsymbol{\omega} \times \mathbf{u}). \quad (8.A.5)$$

where  $\mathbf{u}$  is the fluid velocity,  $D( )/Dt$  the material derivative,  $p$  the fluid pressure,  $\rho$  the fluid density,  $\nu$  the kinematic viscosity,  $\mathbf{g}$  the gravitational acceleration,  $\mathbf{r}$  the location vector, and  $\boldsymbol{\omega}$  the angular velocity [Kundu and Cohen, 2002]. It can be simplified to provide an analog to the equilibrium capillary pressure equation for porous media (8.A.4). Assuming one-dimensional steady flow with negligible influence from gravity and let the fluid velocity  $\mathbf{u}$  go to zero, along with the viscous force and Coriolis pseudo-force terms, so that (8.A.5) simplifies to

$$\frac{dp}{dr} = \rho \omega^2 r \Rightarrow \int_{p_i}^{p_o} dp = \int_{r_i}^{r_o} \rho \omega^2 r dr. \quad (8.A.6)$$

Note that  $p_i$  and  $p_o$  are the boundary pressures at the inflow ( $r_i$ ) and outflow ( $r_o$ ) faces respectively. Flipping the limits and then integrating yields

$$p_i = p_o + \frac{\rho \omega^2}{2} (r_i^2 - r_o^2) \quad (8.A.7)$$

Assuming a zero pressure condition at  $r_o$  ( $r_o > r_i$ ) forces (8.A.7) to give negative pressure values – just as expected. This equation is readily transformed into an analog of (8.A.4) by replacing the water density,  $\rho$ , with the density difference between water and air,  $\Delta\rho$ , and the pressure  $p$  with capillary pressure  $p$ , accounting for the sign change.

The local saturation for the sample at a given angular acceleration,  $S(r, \omega)$ , can be integrated over the sample's length to arrive at the experimentally determined average saturation for the core:

$$\underline{S}(\omega) = \frac{1}{r_o - r_i} \int_{r_i}^{r_o} S(r, \omega) dr \quad (8.A.8)$$

where  $\underline{S}$  is the average wetting phase saturation (dimensionless),  $\omega$  is the angular velocity (radians  $T^{-1}$ ), and  $p$ ,  $r$ ,  $r_i$ , and  $r_o$  are defined as above. By solving (8.A.4) for  $r$  and substituting the result into (8.A.8), Hassler and Brunner arrived at an integral relation between the average saturation and the local saturation as a function of capillary pressure and angular velocity:

$$\underline{S}(\omega) = \frac{r_i + r_o}{2\sqrt{p_i}} \int_0^{p_i} \frac{S(p)}{\sqrt{r_o^2 p_i - (r_o^2 - r_i^2)p}} dp = \frac{A}{p_i} \int_0^{p_i} \frac{S(p)}{\sqrt{1 - B \frac{p}{p_i}}} dp. \quad (8.A.9)$$

Here  $S(p)$  is the local saturation-capillary pressure relation which we want to know,  $p$  is the capillary pressure and is a function of  $r$ , and  $A$  and  $B$  are geometric factors, relating centrifuge rotor length to sample length and given by  $A = (r_i + r_o) / 2 r_o$  and  $B = 1 - (r_i / r_o)^2$ . Solving the centrifuge pressure-saturation equation (8.A.9) has produced a petroleum engineering literature rich in inversion techniques over the last five decades. The geometric factors can be used to find approximate solutions to (8.A.9). For example, Hassler and Brunner's first approximation to (8.A.9) for saturation and pressure at the inflow face ( $r = r_i$ ) assumed ( $r_o \sim r_i$ )  $A = 1$  and  $B = 0$  [Ruth and Wong, 1991], yielding:

$$S(p) = \frac{d(\underline{S}p_i)}{dp}. \quad (8.A.10)$$

Pairs of  $\underline{S}$  and  $\omega$  data could then be numerically manipulated to estimate the derivative in (8.A.10) and yield  $S(r_i)$ ,  $p(r_i)$  pairs for plotting and fitting parameters to the pressure-

saturation relationship. The geometric factor, B, can vary from ~0.35 to as high as 0.73 in UFA systems, and so the first Hassler and Brunner approximation is not appropriate.

I restate the problem with variables more commonly used in vadose zone hydrology. At equilibrium in one dimension and assuming that gravity has a negligible effect, the matric potential and centrifugal body force gradients are equal in magnitude but opposite in sign so that the matric potential at any point  $r$  within the sample can be derived by transforming the capillary pressure equation (8.A.4):

$$\psi(r, \omega) = \psi_o(\omega) + \frac{\omega^2}{2g}(r^2 - r_o^2) = \psi_o(\omega) + \frac{r_i^2 - r_o^2}{r_i^2 - r_o^2} [\psi_i(\omega) - \psi_o(\omega)], \quad (8.A.11)$$

because the capillary pressure difference across the sample length, written in terms of  $\psi$ , is given by

$$-[\psi_i(\omega) - \psi_o(\omega)] = -\frac{\omega^2}{2g}(r_i^2 - r_o^2) \text{ therefore } \frac{\psi_i(\omega) - \psi_o(\omega)}{r_i^2 - r_o^2} = \frac{\omega^2}{2g}$$

Solving for the independent variable  $r$  in terms of  $\psi$  gives

$$r = \left[ r_o^2 + \frac{2g}{\omega^2} (\psi(r, \omega) - \psi_o(\omega)) \right]^{\frac{1}{2}} = \left[ r_o^2 + \frac{\psi(r, \omega) - \psi_o(\omega)}{\psi_i(\omega) - \psi_o(\omega)} (r_i^2 - r_o^2) \right]^{\frac{1}{2}} \quad (8.A.12)$$

whereas the differentials for  $\psi$  and  $r$  are related by

$$d\psi = 2 \frac{\psi_i(\omega) - \psi_o(\omega)}{r_i^2 - r_o^2} r dr \quad dr = \frac{1}{2r} \frac{r_i^2 - r_o^2}{\psi_i(\omega) - \psi_o(\omega)} d\psi \quad (8.A.13)$$

For every constant  $\omega$ , there is average volumetric moisture content,  $\theta$ , which is

$$\underline{\theta}(\omega) = \frac{1}{r_o - r_i} \int_{r_i}^{r_o} \theta(r, \omega) dr. \quad (8.A.14)$$

After a change of variable from  $r$  to  $\psi$ , this becomes

$$\underline{\theta}(\omega) = \frac{1}{r_o - r_i} \int_{\psi_i}^{\psi_o} \frac{r_i^2 - r_o^2}{2r} \frac{\theta(\psi, \omega)}{\psi_i - \psi_o} d\psi = \frac{-1}{2} \int_{\psi_i}^{\psi_o} \frac{r_i + r_o}{r} \frac{\theta(\psi, \omega)}{\psi_i - \psi_o} d\psi \quad (8.A.15)$$

Here  $\psi_i$  and  $\psi_o$  are understood to be functions of  $\omega$ , which is kept constant for each measurement of  $\underline{\theta}(\omega)$ . Now replace  $r$  with (8.A.12) above and switch the limits:

$$\underline{\theta}(\omega) = \frac{r_i + r_o}{2\sqrt{\psi_i - \psi_o}} \int_{\psi_o}^{\psi_i} \frac{\theta(\psi, \omega)}{\left[ r_o^2(\psi_i - \psi_o) + (r_i^2 - r_o^2)(\psi(r) - \psi_o) \right]^{\frac{1}{2}}} d\psi \quad (8.A.16)$$

Noting that  $\psi$  is a linear function of the matrix potentials at the inlet and outlet faces (8.A.11), replace  $\psi$  with  $[x(\psi_i - \psi_o) + \psi_o]$ , where  $x$  is a dummy variable, to get

$$\underline{\theta}(\omega) = \frac{r_i + r_o}{2\sqrt{\psi_i - \psi_o}} \int_0^1 \frac{\theta(x(\psi_i - \psi_o) + \psi_o)(\psi_i - \psi_o)}{\left[ r_o^2(\psi_i - \psi_o) + (r_i^2 - r_o^2)(x(\psi_i - \psi_o) + \psi_o - \psi_o) \right]^{\frac{1}{2}}} dx. \quad (8.A.17)$$

If, as is typical, the outlet face matrix potential is assumed to be zero, then the transform reduces to  $x\psi_i$ . The unreduced transform yields

$$\underline{\theta}(\omega) = \frac{r_i + r_o}{2r_o} \int_0^1 \frac{\theta(x(\psi_i - \psi_o) + \psi_o)}{\left[ 1 - x \left( 1 - \frac{r_i^2}{r_o^2} \right) \right]^{\frac{1}{2}}} dx. \quad (8.A.18)$$

Recall the definition for the geometric factor  $B$  and substitute it into (8.A.18) to get the centrifuge  $\theta$ - $\psi$  equation:

$$\underline{\theta}(\omega) = \frac{1 + \sqrt{1-B}}{2} \int_0^1 \frac{\theta(x(\psi_i - \psi_o) + \psi_o)}{\sqrt{1-Bx}} dx \quad (8.A.19)$$

To solve this integral equation for  $\theta(r_i)$ , the local volumetric moisture content at the inlet face, I adopted the approximate inversion approach described by Forbes [1994], replacing the volumetric moisture content by the function  $\theta_\alpha$ .

$$\underline{\theta}(\omega) = (1 + \alpha) \int_0^1 x^\alpha \theta_\alpha(x\psi_i) dx, \text{ where } \alpha = \frac{1 - \sqrt{1-B}}{1 + 2\sqrt{1-B}}. \quad (8.A.20)$$

Forbes [1994] showed that the error added by the approximation is very small for values of  $0 \leq B \leq 0.7$ , which works for many sample sizes possible with the UFA system. This approximation integral is inverted by replacing  $x$  with  $x/\psi_i$  and multiplying both sides by  $\psi_i^{1+\alpha}$ .

$$\underline{\theta}(\omega) = \frac{1 + \alpha}{\psi_i^{1+\alpha}} \int_0^{\psi_i} x^\alpha \theta(x) dx \text{ becomes } \psi_i^{1+\alpha} \underline{\theta}(\omega) = (1 + \alpha) \int_0^{\psi_i} x^\alpha \theta(x) dx \quad (8.A.21)$$

Now differentiating with respect to  $\psi_i$  and applying Leibniz's rule yields:

$$\frac{d[\psi_i^{1+\alpha} \underline{\theta}(\omega)]}{d\psi_i} = (1 + \alpha) \psi_i^\alpha \theta(\psi_i) \quad \text{or} \quad \theta(\psi_i) = \underline{\theta}(\omega) + \frac{\psi_i(\omega)}{1 + \alpha} \frac{d\underline{\theta}(\omega)}{d\psi_i(\omega)} \quad (8.A.22)$$

The set of discrete data pairs  $(\omega_j, \underline{\theta}_j)$  resulting from  $j = 1$  to  $n$  stepwise desaturations are transformed to corrected  $[\psi(r_j), \theta(r_j)]$  pairs with differencing schemes such as those proposed by Ruth and Wong [1990] or Forbes [1994]. The latter's algorithm is given by

$$\theta_{\alpha j-1/2} = \frac{\underline{\theta}_j - \left( \frac{\psi_{j-1}}{\psi_j} \right)^{1+\alpha} \underline{\theta}_{j-1}}{1 - \left( \frac{\psi_{j-1}}{\psi_j} \right)^{1+\alpha}} \quad (8.A.23)$$

where  $j-1/2$  represents the midway point between two successive pairs of data  $j$  and  $j-1$  and  $\alpha$  is given in (8.A.20).

For sample and centrifuge geometries which have  $0.7 < B \leq 1.0$ , another solution is needed because the  $\theta_\alpha$  inversion can give a poor approximation [Forbes, 1994]. As an alternative, Forbes [1994] derived another estimate more appropriate for this range of  $B$  values, which he called  $\theta_\beta(\psi)$  with  $\beta = 2/\alpha$ , which is defined using Hassler and Brunner's [1945] solution ( $\theta_{HB}$ ):

$$\theta_\beta(\psi) = (1 + \beta) \int_0^1 x^\beta \theta_{HB}(x\psi) dx \quad (8.A.24)$$

The algorithm for applying the  $\theta_\beta$  inversion to (8.A.24) to discrete pairs of experimental data is given by [Forbes, 1994]

$$\theta_{\beta j} = \left( \frac{\psi_{j-1}}{\psi_j} \right)^{1+\beta} \theta_{\beta j-1} + \frac{1 - \left( \frac{\psi_{j-1}}{\psi_j} \right)^{1+\beta}}{1 - \left( \frac{\psi_{j-1}}{\psi_j} \right)} \left[ \underline{\theta}_j - \left( \frac{\psi_{j-1}}{\psi_j} \right) \underline{\theta}_{j-1} \right] \quad (8.A.25)$$

A general solution can be defined for the entire range of  $B$  values ( $0 < B \leq 1.0$ ) by combining the  $\theta_\alpha$  and  $\theta_\beta$  solutions [Forbes, 1994]:

$$\theta(\psi_i) \approx \theta_{\alpha\beta} = \frac{B}{2}\theta_\beta + \left(1 - \frac{B}{2}\right)\theta_\alpha \quad (8.A.26).$$

Corrections for effects from the centrifugal field's two-dimensional heterogeneity and from gravity can also be incorporated into this scheme [Forbes, 1997] to yield more accurate estimates of the  $\theta$ - $\psi$  relation. A similar pair of equations can be derived for an imbibition experiment [Forbes, 1994, 1997].

One potential source for error in determining the  $\theta$ - $\psi$  relation with the UFA is stopping the centrifuge several times during each experimental step. To avoid confusion, a "leg" refers to the amount of time a sample is spun at a given rate between stoppages, whereas a "step" refers to the next step (higher spin rate) in the centrifuge  $\theta$ - $\psi$  experiment. Stopping the UFA to weigh the sample in order to determine the average volumetric moisture content allows water to redistribute within the sample as well as imbibe water held in the bottom assembly. These changes in local water content will cause local deviations from the primary drainage curve. It is unlikely that these deviations will affect the  $(\omega_i, \bar{\theta}_i)$  data if the subsequent leg or step lasts for a sufficient amount of time to return the sample to the primary drainage curve. Near saturation,  $K$  values near the outflow face are relatively high, so re-equilibration occurs relatively rapidly during the next leg or step. Conversely,  $K$  values are very low across much of the sample towards the end of the experiment, so only minimal redistribution of water will occur during a brief stoppage. (I typically required 5-10 minutes to remove, weigh, and spin up the re-attached samples.) This issue should be investigated with numerical models and, if possible, with experiments.

Evaporative loss of water is another potential source of error in the UFA method for  $\theta$ - $\psi$  relations. At high spin rates ( $\geq 3000$  rpm), a significant amount of air can be forced through the sample, and if the air is relatively dry, it can remove water from the sample during long experimental run times. The air was relatively dry at the UFFA Ventures lab when the samples were analyzed, and the data show a downward trend in residual moisture content for numerous sand and fault samples [Chapters 2 and 4]. Humidifying the air during UFA  $\theta$ - $\psi$  runs should help reduce evaporative loss, but should be investigated.

The inversion method can also introduce errors the estimate of the  $\theta$ - $\psi$  relation. Poor estimates from equations (8.A.23 and 8.A.25) can result from having too few data pairs, as well as wide or irregual intervals between data pairs. Such errors can be prevented or minimized by collecting many data pairs, spaced regularly with regard to the angular speed.

### **8.A.3 MEASURING $K$ - $\theta$ RELATIONSHIPS IN A CENTRIFUGE**

Hagoort [1980] proposed the first use of a centrifuge to measure relative permeability. Widely used in the petroleum industry, Hagoort's [1980] method determines relative permeability from measurements of the time rate of change in saturation from a sample subjected to a constant centrifugal acceleration, assuming centrifugal force dominates capillary forces (no capillary end effects), the relative permeability functional form is known, the ratio of relative permeability to viscosity (mobility) of the non-wetting invading phase is infinite, and that the centrifugal force is uniform throughout the sample. These experiments require a centrifuge specially

equipped with highly accurate volumetric effluent chambers to collect and measure the expelled liquid, typically using automated image acquisition and processing [e.g., O'Meara and Crump, 1985], as the sample drains from fully saturated to some equilibrium saturation. Subsequent papers detailing improvements or variations on the method are too numerous to permit adequate discussion here.

Nimmo et al.[1987] proposed the first steady-state centrifuge method for measuring relative permeability curves, or as used in soil science, unsaturated hydraulic conductivity,  $K-\theta$ , curves. Their measurements were made with a novel centrifuge design that established specified matric potential boundary conditions at the sample's inlet and outlet faces via porous plates. They argued that it is relatively easy to establish steady unsaturated flow through a sample with only the centrifugal gradient as the primary driving force ( $\text{grad } \psi \approx 0$ ), based on experimental measurements and modeling results [Nimmo et al, 1987]. Another novel centrifuge system – the Unsaturated Flow Apparatus (UFA) [Conca and Wright, 1992; Khaleel et al, 1994; Conca et al, 1999; ASTM, 2001], permits flow to be transmitted through the spinning rotor onto the samples. The UFA method subjects an initially saturated sample to a stepwise-increasing series of angular velocities while applying a constant flux to the inlet face of the sample. The liquid flux rate and angular velocity are held constant until the sample reaches steady state, and then the final average fluid content is gravimetrically determined. The procedure is repeated after increasing the angular velocity,  $\omega$ , to the next higher level and either maintaining or reducing the liquid flux rate ( see Table 2.1). Unlike Nimmo's

method, the UFA  $K$ - $\theta$  method does not control the matric potential boundary value at the outflow face.

I applied Darcy's law for a rotating frame [Bear et al, 1984] to determine unsaturated hydraulic conductivity from a steady flow experiment on a homogeneous, isotropic porous medium in a centrifugal field. Bear et al.[1984] state, but do not derive, their form of Darcy's law (their equation 24) for a liquid-gas experiment, which we will take as water and air:

$$\mathbf{q} = -\frac{k_0 k_{rel}(S_w)}{\mu} \left( \nabla p - \nabla \frac{\rho_w |\boldsymbol{\omega}|^2 |\mathbf{r}|^2}{2} \right) \quad (8.A.27)$$

where  $\mathbf{q}$  is the water-phase flux density vector ( $\text{LT}^{-1}$ );  $k_0$  is the intrinsic or saturated permeability ( $\text{L}^2$ );  $k_{rel}(S_w)$  is the water-phase relative permeability (-) given as a function of water-phase saturation,  $S_w$  (-);  $\mu$  is the dynamic viscosity of water ( $\text{ML}^{-1}\text{T}^{-1}$ );  $p$  is the matric pressure ( $\text{ML}^{-1}\text{T}^{-2}$ );  $\rho_w$  is water density ( $\text{ML}^{-3}$ );  $\boldsymbol{\omega}$  is the angular velocity ( $\text{T}^{-1}$ ) vector, and  $\mathbf{r}$  is the radial distance (L) vector from the centrifuge's axis of rotation. Gravity is assumed to be negligible relative to the pressure and centrifugal force gradients.

Nimmo et al. [1987] present another form of Darcy's law for 1D flow in a centrifugal field with negligible gravity (their Equation 2):

$$q = -K(\psi) \left( \frac{d}{dr} \psi - \rho_w \omega^2 r \right). \quad (8.A.28)$$

where the terms are defined as above. Although the units do not appear to balance in (8.A.28), it has been used in numerous other papers, including Conca and Wright [1992],

Nimmo et al.[1994], Conca and Wright [1994], Conca et al.[1999], and Flint et al.[1999]. Compared to (8.A.27), the Darcy's law form employed by Nimmo and coworkers and Conca and coworkers (8.A.28) underestimates the matric potential gradient and overestimates the centrifugal head gradient along the sample length by a factor equal to gravitational acceleration. As discussed later in this section, using (8.A.28) instead of (8.A.27), which does have balanced units, can have very significant impacts on  $K$ - $\theta$  measurements.

Simplifying (8.A.27) to 1D and restating in terms of matric potential yields:

$$q = \frac{-k}{\mu} \left( \frac{d}{dr} p - \rho \omega^2 r \right) = -K \left( \frac{d}{dr} \psi - \frac{\omega^2 r}{g} \right). \quad (8.A.29)$$

Measuring the  $K$ - $\theta$  relationship by centrifuge requires several important assumptions in addition to those made for Darcy flow. The matric potential gradient must be very small and much smaller than the centrifugal body force gradient. The resulting essentially uniform matric potential produces an essentially uniform volumetric moisture content distribution within the sample, thus flow is driven only by the difference in centrifugal body force between the sample's inlet and outlet faces. The sample is assumed to be homogeneous and non-deforming. The constant flux boundary condition must be distributed equally across the inlet face.

Hydraulic conductivity is calculated by rearranging the 1D form of Darcy's law for a one-dimensional rotating frame of reference (8.A.27) to solve for  $K$ :

$$\frac{q}{K} = -\frac{d}{dr}\psi + \frac{\omega^2 r}{g} \Rightarrow \frac{q}{K} dr = -d\psi + \frac{\omega^2 r}{g} dr. \quad (8.A.30)$$

Treating  $K$  as a function of  $r$  and integrating from the inlet to the outlet face gives

$$\int_{r_i}^{r_o} \frac{q}{K(r)} dr = -\int_{\psi_i}^{\psi_o} d\psi + \int_{r_i}^{r_o} \frac{\omega^2 r}{g} dr \quad (8.A.31a)$$

$$\int_{r_i}^{r_o} \frac{q}{K(r)} dr = (\psi_i - \psi_o) + \frac{\omega^2}{2g} (r_o^2 - r_i^2) = (\psi_i - \psi_o) + \frac{\omega^2}{g} (r_o - r_i) \left( \frac{r_o + r_i}{2} \right) \quad (8.A.31b)$$

$$\frac{q}{r_o - r_i} \int_{r_i}^{r_o} \frac{dr}{K(r)} = \frac{\psi_i - \psi_o}{r_o - r_i} + \frac{\omega^2}{g} \left( \frac{r_o + r_i}{2} \right) \quad (8.A.31c)$$

Dividing through by the flux density  $q$  leaves the inverse of the harmonic average of  $K(r)$  on the left hand side of (8.A.31c). I denote this quantity as  $\underline{K}_H(\underline{\theta})$ , because each harmonic average is associated with the average volumetric moisture content (determined gravimetrically) for that combination of angular velocity and applied flux rate. If, for the applied combination of angular velocity and water flux rate, the matric potential gradient is indeed negligible across the entire sample length, then the local  $K$  values and harmonic average of  $K$  are essentially the same:

$$K(\underline{\theta}) = \underline{K}_H(\underline{\theta}) = \frac{2gq}{\omega^2(r_o + r_i)} \quad (8.A.32)$$

This contrasts with the equation presented by Nimmo et al.[1987] and Conca and Wright [1992]:

$$K(\theta) = \frac{q}{\rho_w \omega^2 r}.$$

(8.A.33)

This equation states that  $K$  varies with  $r$ , despite the foregoing argument that  $K$  should not vary significantly if the experimental conditions are appropriate, and it forces  $K$  to have units of ( $L^3 M^{-1} T$ ). Accordingly, I used (8.A.30) in this study rather than (8.A.31).

This method assumes steady flow and so is vulnerable to deviations in the applied flow rates. The AVI pumps used in the UFA system are rated by the manufacturer to  $\pm 2\%$  of the nominal flow rate. However, my validation measurements show that flow rates can far exceed the 2% rating for some pumps for some flow rates (Table 8.A.1)

**Table 8.A.1:** Measured flow rates for selected AVI pumps

Nominal Q (ml/hr)	% deviation for selected pumps (10)					% deviation for rejected pumps (4)				
	mean	stdev	n	min	max	mean	stdev	n	min	max
0.1	4.0	1.7	3	2.2	5.5	1.4	0.9	2	0.7	2.0
1	1.3	2.3	14	-2.0	5.0	3.8	8.8	12	-9.0	17.0
2	4.5	1.9	2	3.2	5.9	4.4	3.1	4	1.5	7.7
15	-0.2	2.6	4	-3.0	2.8	-0.1	1.5	2	-1.2	1.0
50	-1.6	1.3	7	-3.0	1.0	-1.7	0.6	3	-2.0	-1.0
99.9	-1.5	1.2	14	-3.1	0.9	-1.5	0.7	6	-2.1	-0.6

On average the two sets of pumps show very similar behavior, but the rejected pumps had much more extreme values, and standard deviations, than the selected pumps. If possible, only tested pumps were used, but time or other constraints may have caused pumps with more variable flow rates to be used. Assuming the worst case and using the highest observed deviations (Table 8.A.1),  $K$  estimates could deviate from their true values by as much as 12%, because measured  $K$  is directly proportional to the flow rate,  $Q$  (8.A.30). Variability in flow rate with time could also provide another source of error, but I had too little time with the UFA instruments to examine this. For example, if  $Q$  for

a pump varied sinusoidally with time, the sample may never reach steady state conditions, thereby violating one of the method's major assumptions. This should be investigated both numerically and experimentally. However, these errors may not be significant because the measured  $K$  represents a harmonic average of the possible local variations of  $K$  within the sample due to variations in moisture content.

Errors in saturated  $K$  measurements could also be caused by desaturation during the constant head experiment with the UFA. My measurements of moisture content immediately following the saturated  $K$  experiments showed only small declines, roughly 2-4%, in the bulk volumetric moisture content for protolith samples and smaller declines for fault samples. It may be possible to avoid these uncertainties in the saturated  $K$  values by using a lab permeameter, constant or falling head as appropriate, to provide an independent estimate of saturated  $K$ .

Another source of error is the choice of Darcy's law, such as (8.A.28), (8.A.29), or another form. As mentioned previously, using the unbalanced form (8.A.28) overestimates the influence of the centrifugal body force gradient relative to the matric potential gradient. Out of the set of combinations of flow and spin rates possible for a  $K$ - $\theta$  experiment, some of them will not be feasible. One possible set of infeasible conditions is the set that employs high flows and low spin rates, which could create roughly commensurate gradients in both  $\psi$  and the centrifugal body force. (Low flow and low spin rates are not usually typically considered because the sample would quickly desaturate, causing the experiment to miss much of the  $K$ - $\theta$  relation near the wet end.) I suggest that the original set of experimental conditions set up by Conca and Wright

[1992] (see Table 2.1) have such high initial flow rates (50 ml/hr) and such low spin rates (300 rpm) that the matric potential and centrifugal body force gradients are both significant for fine sands. This overestimates the measured  $K$  values near saturation, because two gradients are driving flow – not just one. I suggest this is the reason for the great difficulty in fitting Mualem-van Genuchten functions through the estimated  $K$  values near saturation for all sands with mixed clay mineral CSF [Chapters 2 and 4]. Modeling and experimentation should be used to investigate this further.

#### 8.A.4 REFERENCES

- Basha, H. A., and N. I. Mina, Estimation of the unsaturated hydraulic conductivity from the pressure distribution in a centrifugal field, *Water Resour. Res.*, 35, 469-477, 1999.
- Bear, J., M. Y. Corapcioglu, and J. Balakrishna, Modeling of centrifugal filtration in unsaturated deformable porous-media. *Advan. in Water Resour.*, 7, 150-167, 1984.
- Conca, J. L. and J. V. Wright, Diffusion coefficients in gravel under unsaturated conditions, *Water Resour. Res.*, 26, 1055-1066, 1990.
- Conca, J. L. and J. V. Wright, Flow and diffusion in unsaturated gravel, soil and whole rock, *Applied Hydrogeology*, 1, 5-24, 1992.
- Conca, J. L. and J. V. Wright, The UFA method for rapid, direct measurements of unsaturated transport properties in soil, sediment, and rock, *Australian J. Soil Res.*, 36, 291-315, 1998.
- Conca, J., D. Levitt, P. Heller, T. Mockler, and M. Sully, Direct UFA measurements of unsaturated hydraulic conductivity, comparisons to van Genuchten/Mualem estimations, and applications to recharge mapping in arid regions, in *Characterization*

- and Measurement of the Hydraulic Properties of Unsaturated Porous Media*, M. Th. van Genuchten, F. J. Leij, and L. Wu (eds.), Univ. Calif., Riverside, CA, 2, 1173-1197, 1999.
- Flint, L.E., D. B. Hudson, and A.L. Flint, Unsaturated hydraulic parameters determined from direct and indirect methods, in *Characterization and Measurement of the Hydraulic Properties of Unsaturated Porous Media*, M. Th. van Genuchten, F. J. Leij and L. Wu (eds.), Univ. Calif., Riverside, CA, 293-302, 1999.
- Forbes, P. L., Simple and accurate methods for converting centrifuge data into drainage and imbibition capillary pressure curves, *Log Analyst*, 35, 31-53, 1994.
- Forbes, P.L., Centrifuge data analysis techniques: An SCA survey on the calculation of drainage capillary pressure curves from centrifuge measurements, Society of Core Analysts report, 184 pages, 1997.
- Goldstein, H., *Classical Mechanics*, Addison-Wesley Publishing, Reading, MA USA. 399 pgs, 1959.
- Hagoort, J., Oil recovery by gravity drainage, *Soc. Petrol. Eng. J.*, SPE 1424, 20, 139-150, 1980.
- Hassler, G. L., and E. Brunner, Measurement of capillary pressures in small core samples, *Transactions, AIME*, 160, 114-123, 1945.
- Khaleel, R., J. F. Relyea, and J. L. Conca, Estimation of van Genuchten-Mualem relationships to estimate unsaturated hydraulic conductivity at low water contents, *Water Resour. Res.*, 31, 2659-2668, 1995.
- Kundu, P.K. and I.M. Cohen, *Fluid Mechanics*, 2<sup>nd</sup> ed., Academic Press, New York, 730 pgs, 2002.

- Nimmo, J. R., J. Rubin, and D. P. Hammermeister, Unsaturated flow in a centrifugal field: measurement of hydraulic conductivity and testing of Darcy's law, *Water Resour. Res.*, 23, 124-134, 1987.
- Nimmo, J. R. Adaptation of the steady-state centrifuge method to extend the range of hydraulic conductivity measurement, *Ground Water*, 26, 785-786, 1988.
- Nimmo, J. R., Experimental testing of transient unsaturated flow theory at low water-content in a centrifugal field, *Water Resour. Res.*, 26, 1951-1960, 1990.
- Nimmo, J. R., and K. A. Mello, Centrifugal techniques for measuring saturated hydraulic conductivity. *Water Resour. Res.*, 27, 1263-1269, 1991.
- O'Meara, D. J., Jr. and Crump, J. G., Measuring capillary pressure and relative permeability in a single centrifuge experiment, presented at the SPE 60th Annual Technical Conference and Exhibition, Las Vegas, Nevada, Sept. 22-25, paper SPE 14419, *Soc. Petrol. Eng. J.*, 1985.
- Ruth, D. W., and S. Wong, Centrifuge capillary pressure curves, *J. Canadian Petrol. Tech.*, 29(3), 67-72, 1990.
- Ruth, D. W., and S. Wong, Calculation of capillary pressure curves from data obtained by the centrifuge method, *Log Analyst*, 32, 575-581, 1991.

## APPENDIX 8.B: BROOKS AND COREY MODEL FITS TO UFA DATA

Data from the UFA hydraulic conductivity – volumetric moisture content ( $K$ - $\theta$ ) and volumetric moisture content – matric potential ( $\theta$ - $\psi$ ) experiments for fault and sand samples from Canyon Trail site E10 were fit to the Brooks and Corey [1964] (BC) forms for these relations (8.B.1 and 8.B.2) to estimate parameters for a hydraulic conductivity – matric potential ( $K$ - $\psi$ ) model.

$$\theta(\psi) = \theta_r + (\theta_s - \theta_r) |\alpha\psi|^{-n} \text{ if } |\alpha\psi| > 1, \text{ otherwise } \theta(\psi) = \theta_s \quad (8.B.1)$$

$$K(\theta) = K_s \left( \frac{\theta - \theta_r}{\theta_s - \theta_r} \right)^{\beta+2+\frac{2}{n}} \text{ if } \theta < \theta_s, \text{ otherwise } K(\theta) = K_s \quad (8.B.2)$$

where  $K_s$  is the saturated hydraulic conductivity ( $LT^{-1}$ ),  $\alpha$  is the inverse of the air entry matric potential ( $L^{-1}$ ),  $\theta_s$  is saturated volumetric moisture content ( $L^3L^{-3}$ ) and equals the connected porosity for vacuum saturation,  $\theta_r$  is the residual volumetric moisture content ( $L^3L^{-3}$ ), and  $n$  and  $\beta$  are dimensionless fitting parameters. The latter two parameters,  $n$  and  $\beta$ , differ for the Mualem-van Genuchten (MvG) and BC models. The fitting process is described in section 2.3.

Plots used for fitting and the resulting BC parameter values (Table 8.B.1) follow.

## UFA Results with Brooks and Corey Fits

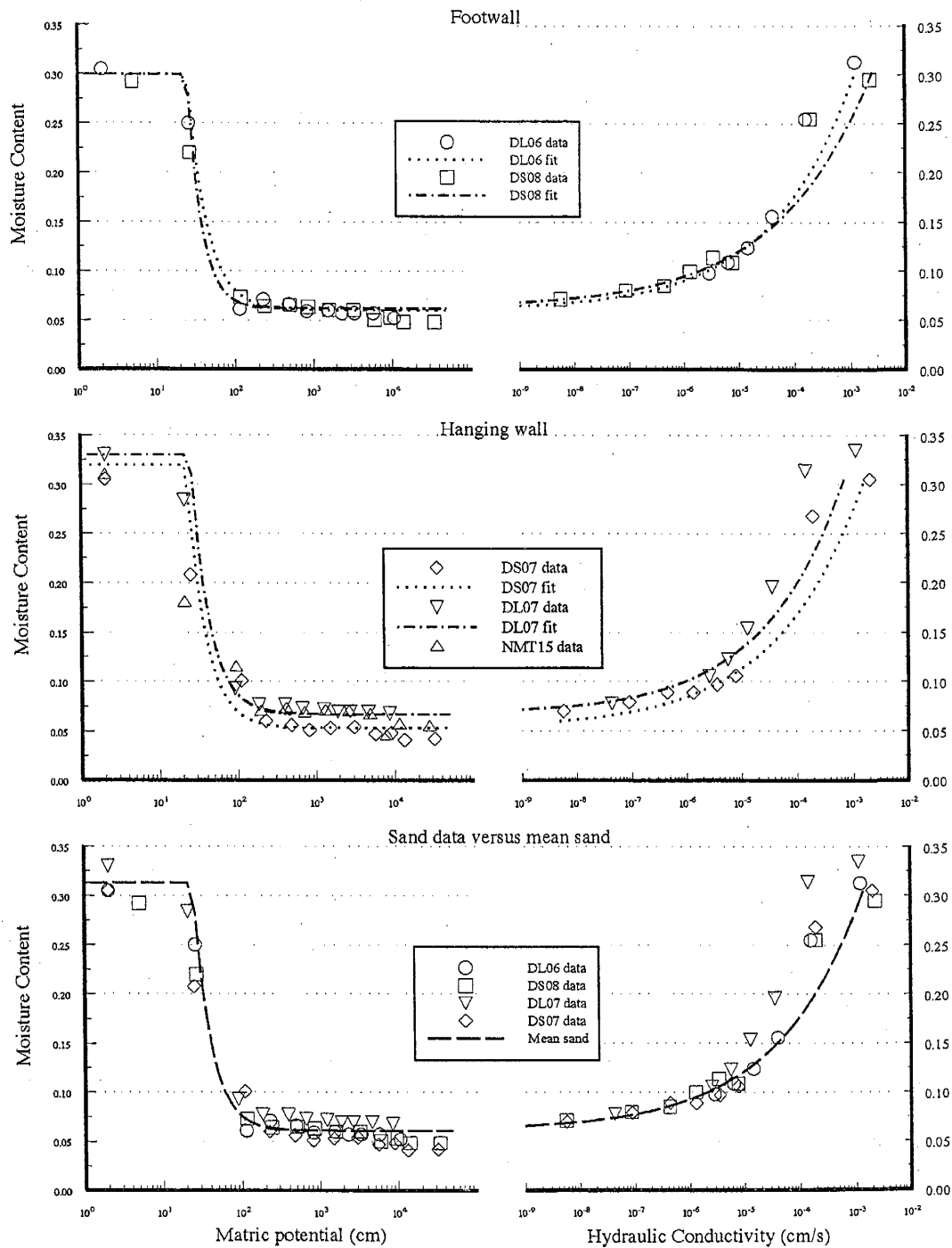


Figure 8.B.1: Brooks and Corey fits to UFA experimental results.

## UFA Results with Brooks and Corey Fits

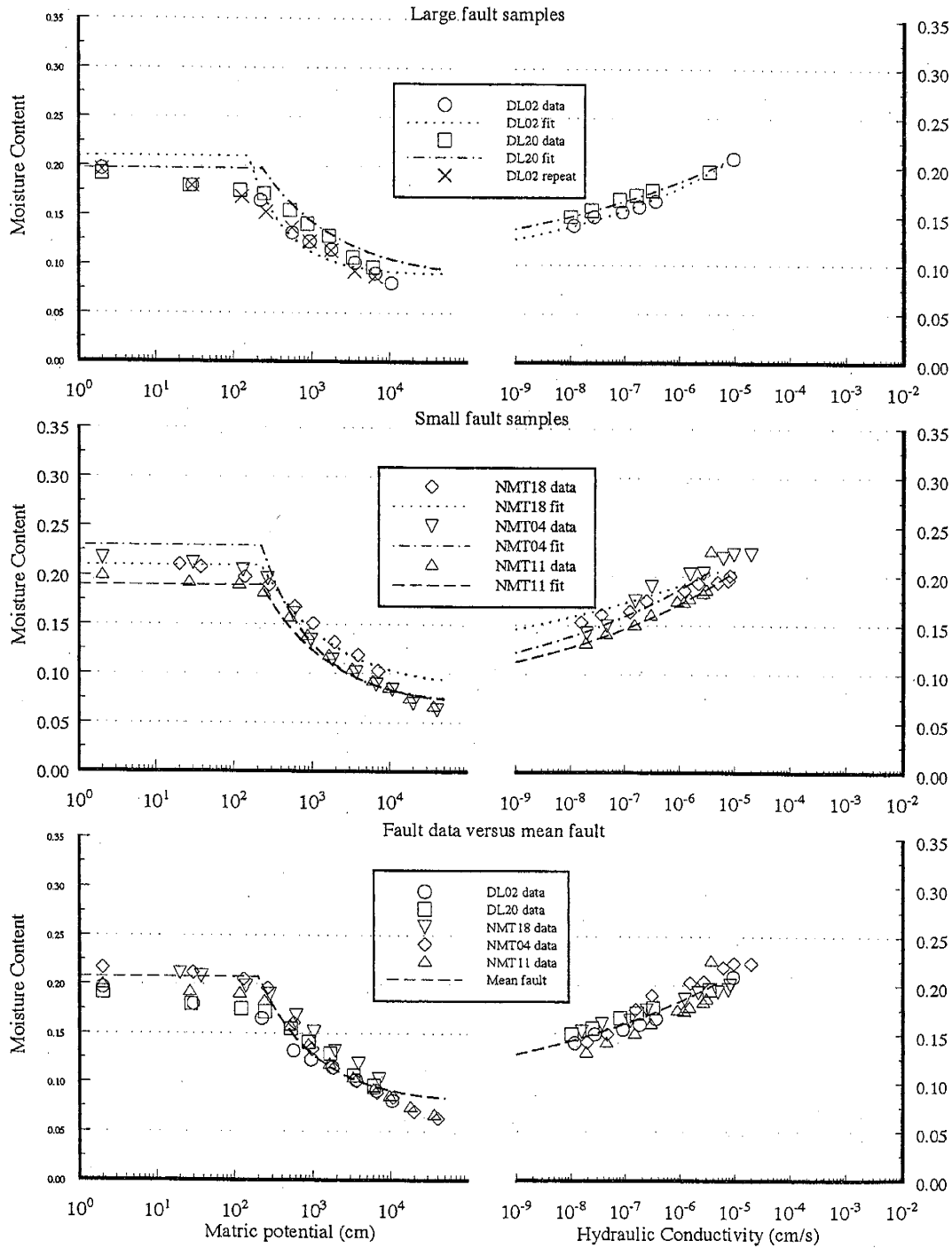


Figure 8.B.1: Brooks and Corey fits to UFA experimental results.

## APPENDIX 8.C: USING PIECEWISE CONTINUOUS GARDNER $K(\psi)$ MODELS TO SOLVE STEADY EVAPORATIVE FLOW PROBLEMS

### 8.C.1 INTRODUCTION

The analytically unwieldy functional forms of unsaturated hydraulic relationships which appear to better fit experimental observations generally require numerical modeling even of relatively simple one dimensional, variably saturated, steady flow problems. The large matric potential gradients and domain lengths that are customary to many arid and semi-arid vadose zones often necessitate long model run times before the numerical technique converges to a solution. Various analytical solutions of steady state and transient flow problems have been developed for analytically tractable functional forms of the hydraulic conductivity – matric potential ( $K$ - $\psi$ ) relationship, such as Gardner's model [Rockhold et al., 1997],

$$K(\psi) = K_s \exp(\alpha\psi) \quad (8.C.1)$$

where  $K_s$  is the saturated hydraulic conductivity ( $LT^{-1}$ ),  $\alpha$  ( $L^{-1}$ ) is a parameter describing the influence of capillarity relative to gravity in driving infiltration, and  $\psi$  is the matric potential (L) ( $-\infty < \psi \leq 0$ ). The Gardner model's log-linear  $K$ - $\psi$  relationship enables analytical solutions to be obtained for many variably-saturated flow problems. Few such solutions exist for those functional forms, e.g., the Mualem-van Genuchten model, which

typically provide a better match to experimental measurements of  $K-\psi$  or  $K-\theta$  relationships than the Gardner and other similarly tractable models.

Rockhold et al. [1997] described an analytical method which represents arbitrary  $K-\psi$  relationships as a set of piecewise continuous Gardner exponential models to solve steady-state Richards equation problems with a known flux (Neumann) boundary through segment-by-segment integration. Their approach easily handles infiltration into homogeneous single and multi-layered media by segmenting each given  $K-\psi$  curve into tens to hundreds of piecewise continuous Gardner models. It is not applicable to flow problems with Dirichlet boundary conditions (flux is unknown) such as capillarity-driven upward flux from a shallow water table.

We describe a more general approach that combines piecewise-continuous representation of the  $K-\psi$  relationship with an exact piecewise analytical solution and is based on an approach first mooted by Robert Holt in the mid-1990's. The set of simultaneous equations, built from the piecewise-continuous  $K-\psi$  relationship can be quickly solved using readily available software tools such as *Mathematica*. Our semi-analytical approach is simple to implement, accommodates steady flow 1D problems with either only Dirichlet or mixed Dirichlet and Neumann boundary conditions.

### 8.C.2 APPROACH

A vertical column of variably saturated media has an applied matric potential at one boundary and either an applied matric potential or an applied flux at the other boundary. Under conditions of one dimensional, steady flow, the twice-integrated Richards equation

reveals that the vertical elevation difference between the top and bottom boundaries is related to the hydraulic conductivity, and distribution of matric potential values within the column. [Irmay, 1968]:

$$z_T - z_B = \Delta z = - \int_{\psi_B}^{\psi_T} \frac{d\psi}{\frac{q}{K(\psi)} + 1} \quad (8.C.2)$$

Here  $z$  is the vertical axis (positive upwards),  $z_T$  and  $z_B$  are the elevations (L) of the top and bottom boundaries,  $\psi_T$  and  $\psi_B$  are the matric potential values (L) at those boundaries,  $q$  is the flux density ( $LT^{-1}$ ) through the column, and  $K(\psi)$  is the hydraulic conductivity ( $LT^{-1}$ ). This geometry causes  $q$  to be positive for upward flow and negative for infiltration.

Using only the Gardner exponential model to describe the  $K$ - $\psi$  relationship, the analytical solution to (8.C.2) is

$$z_T - z_B = \frac{-1}{\alpha} \ln \left( \frac{q + Ks \exp(\alpha\psi_T)}{q + Ks \exp(\alpha\psi_B)} \right) \quad (8.C.3)$$

Gardner [1958] used (8.C.3) to estimate the maximum evaporative flux density flow from a water table at some depth  $z_T - z_B$  to the surface where evaporation forces the boundary matric potential to have a value of  $-\infty$ . This infinite boundary value simplifies (8.C.3) so that liquid-phase flux density  $q$  can be determined from an algebraic function of domain length, material properties, and the boundary matric potentials ( $\psi = 0$  cm water table bottom boundary). We take  $z_T = 0$  and  $z_B = -H$ , where  $H$  (L) is the depth of the water table.

The Gardner model (8.C.1) often provides such a poor match to the Mualem-van Genuchten (MvG)  $K(\psi)$  functions used in this research [Chapter 3], that (8.C.3) is seldom adopted to model evaporative flow from a shallow water table. Instead, we approximate each  $K_{MvG}(\psi)$  function with a series of piecewise continuous Gardner exponential functions  $K_{pw}(\psi)$ :

$$K_{MvG}(\psi) \cong K_{pw}(\psi) = Ks_i \exp(\alpha_i \psi), \quad (8.C.4a)$$

$$\text{where } \psi_{i-1} \leq \psi \leq \psi_i, \quad (8.C.4b)$$

$$Ks_{i-1} \exp(\alpha_{i-1} \psi_{i-1}) = Ks_i \exp(\alpha_i \psi_{i-1}), \text{ and} \quad (8.C.4c)$$

$$Ks_{i+1} \exp(\alpha_{i+1} \psi_i) = Ks_i \exp(\alpha_i \psi_i). \quad (8.C.4d)$$

Here each MvG  $K$ - $\psi$  function becomes a set of  $n$  piecewise continuous linear segments which span matric potential values from saturation ( $\psi_B = 0$ ) to the smallest (most negative)  $\psi$  value required by the problem. Each of the  $n$   $\psi$  segments bounded by  $[\psi_{i-1}, \psi_i]$  yields a pair of  $Ks_i$  and  $\alpha_i$  values for all  $i = 1, \dots, n$ . The  $n+1$   $\psi_i$  values span the entire  $\psi$  range ( $\psi_0 \leq \psi \leq \psi_n$ ) and form the breakpoints for the  $i$  segments. By definition,  $\psi_0 = 0$  and  $Ks_0 = K(\psi_0)$ . Each pair of parameters is calculated from

$$\alpha_i = \frac{\ln[K(\psi_{i-1})] - \ln[K(\psi_i)]}{|\psi_{i-1} - \psi_i|} \quad (8.C.5a)$$

$$Ks_i = \exp[(\psi_0 - \psi_i) \alpha_i + \ln(K(\psi_{i-1}))] \quad (8.C.5b)$$

$$\text{such that } 0 \leq \alpha \text{ and } 0 \leq Ks \text{ for all } i \quad (8.C.5c)$$

As noted by Rockhold et al. [1997], the number and placement of  $\psi$  breakpoints controls the deviation between the piecewise linear  $K$  function and the  $K$  function to be matched, e.g., Mualem-van Genuchten.

The next step is to replace the integral in (8.C.2) with a sum of integrals partitioned according to the  $\psi$  breakpoints:

$$\sum_{i=2}^n z_i - z_{i-1} = - \sum_{i=2}^n \int_{\psi_{i-1}}^{\psi_i} \frac{d\psi'}{\frac{q}{Ks_i \exp(\alpha_i \psi')} + 1} \quad (8.C.6)$$

where  $\psi'$  refers to the value of  $\psi$  within the interval  $[\psi_{i-1}, \psi_i]$ . This produces a set of  $n$  equations which can be solved for the remaining unknowns after stipulating the boundary conditions. If the domain has two Dirichlet boundaries then (8.C.6) can be solved for the flux density  $q$  and the  $n-1$  unknown  $z_i$  values (as  $z_T$  and  $z_B$  are given) corresponding to the  $\psi_i$  values. If, on the other hand, mixed Dirichlet and Neumann boundaries are given, (8.C.6) can then be solved to get the  $\psi$  value at the flux boundary and the  $n-1$  unknown  $z_i$  values.

We applied Equations (8.C.5) and (8.C.6) to solve the evaporation-driven flow from the shallow water table problem described in Chapters 3 and 4. We partitioned the MvG  $K(\psi)$  functions for each material into roughly 40 piecewise continuous segments across a matric potential range of 0 (water table at bottom boundary) to  $-10,000$  cm (top boundary), a value we judged representative of long-term surface matric potential for many semi-arid and arid vadose zones. The Gardner piecewise hydraulic conductivity function  $K_{pw}(\psi)$  deviated from the true Mualem-van Genuchten hydraulic conductivity

function  $K_{MvG}(\psi)$  at any point by less than 5% for sands and by less than 3% for faults (Figure 8.C.1).

We then assembled a system of nonlinear equations specific to a single depth to the water table,  $H$  (L) and solved the system for the upward liquid-phase flux density,  $q_l$ . Each equation has a range of matric potential values over which it is valid. For this problem, matric potential corresponds in one-to-one fashion to elevation, so the minimum and maximum bounding matric potentials uniquely correspond to maximum and minimum elevations. Thus, each equation describes water flow through a particular physical segment of the soil column as well as water flow through a particular range of matric potential values. The system of equations is then solved with a suitably sensitive nonlinear search algorithm. We initially tried the solver contained in *MathCad* (by MathSoft), but numerical limitations precluded consistent success because flux density and hydraulic conductivity values can become very small. *Mathematica*'s arbitrary precision and its robust solver the system of equations, FindRoot, consistently returned values for  $q_l$  and the matric potential – elevation relationship for each value of  $H$ . Comparison of Mathematica's estimates for  $q_l$  and  $\psi(z)$  relations with those from a numerical Richards equation finite element code, HYDRUS-1D [Simunek et al., 1998] showed no significant differences (< 1%). Annotated *Mathematica* code is presented in Section 8.3.4.

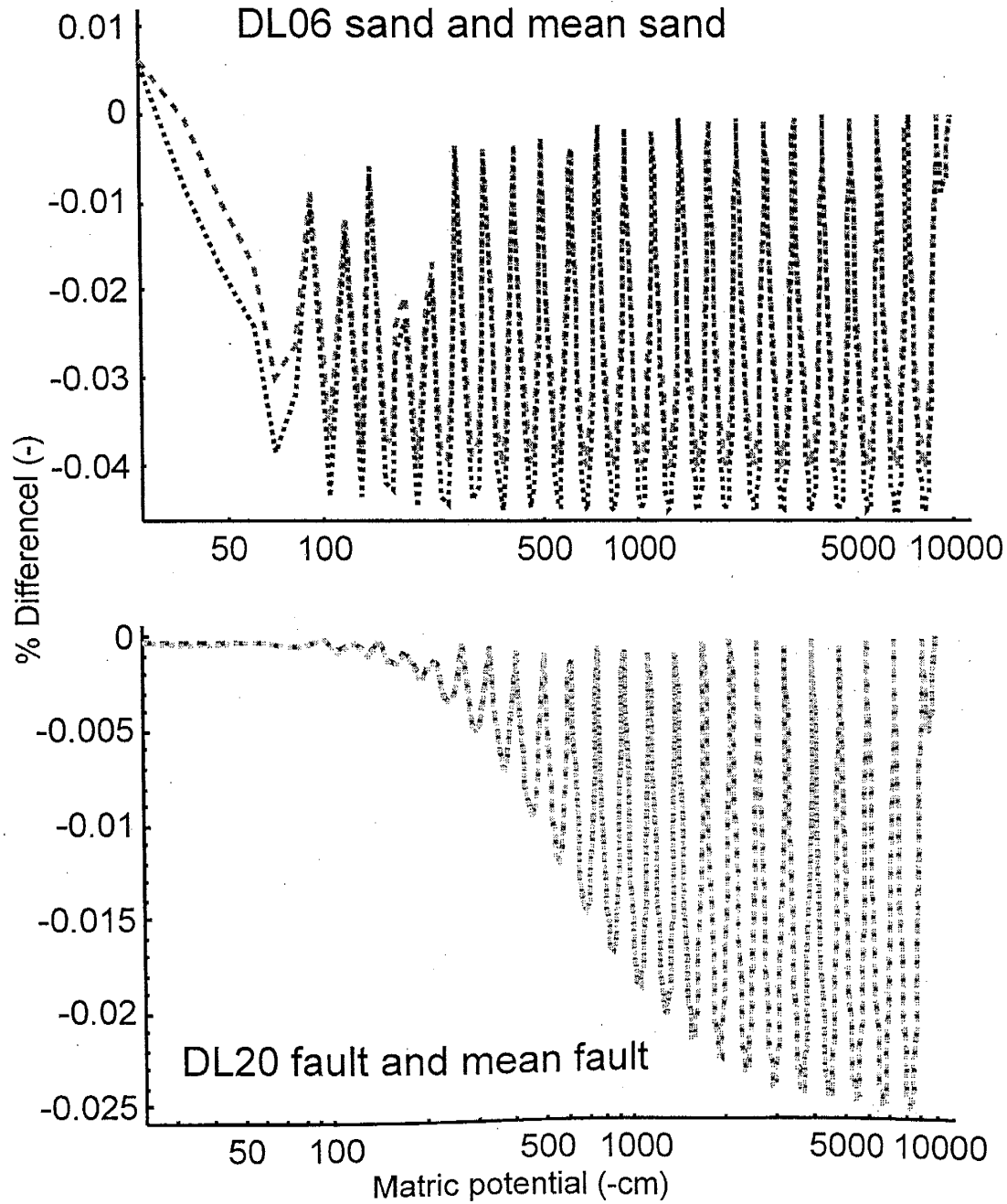


Figure 8.C.1: Piecewise continuous Gardner models of MvG  $K(\psi)$ . Plots show the percent difference between the PC Gardner approximation and the Mualem-van Genuchten hydraulic conductivity functions relative to the magnitude of the MvG value.

### 8.C.3 REFERENCES

- Gardner, W. R., Some steady state solutions of the unsaturated moisture flow equation with application to evaporation from a water table, *Soil Science*, 85, 228-232, 1958.
- Irmay, S., Solutions of the non-linear diffusion equation with a gravity term in hydrology, H. W. Rijtema and P. E. Wassink, editors, In Symposium on Water in the Unsaturated Zone, International Association of Scientific Hydrology-UNESCO, 1966, Wageningen, Netherlands, 1968.
- Rockhold, ML, CS Simmons, and MJ Fayer, An analytical solution technique for one-dimensional, steady vertical water flow in layered soils, *Water Res. Resour.*, 33, 897-902, 1997.
- Simunek, J., K. Huang, and M. Th. van Genuchten, The HYDRUS code for simulating the one-dimensional movement of water, heat, and multiple solutes in variably-saturated media. Version 6.0, Research Report No. 144, U.S. Salinity Laboratory, USDA, ARS, Riverside, California, 164pp., 1998.

#### 8.C.4 MATHEMATICA CODE

evapQpcw\_dissApp8C.nb

file:///Users/johnsigda/rsrch/03/03papers/diss/evapPWCdiss\_mo

### Calculating 1D evaporative flux using piecewise-continuous Gardner $K$ - $\psi$ models

#### •Parameter declarations

Mualem-van Genuchten (MvG) parameter values for sand sample DL06, fault sample DL20, and the mean sand  $s_{mean}$  and mean fault  $f_{mean}$ :

Undeformed sands:

In[46]:=

```
DL06 = {0.058, 0.315, 0.03, 3.4, 0.2, 3600*1.2*10^(-3.0)};  
(*MvG parameters:  $\alpha$ ,  $\theta_s$ ,  $s$ ,  $n$ ,  $\beta$ , and  $K_{sat}$  in cm/hr *)
```

In[47]:=

```
smean = {0.062, 0.318, 0.038, 3.34, 0.42, 3600*1.72*10^(-3.0)};
```

Deformation band faults:

In[48]:=

```
DL20 = {0.105, 0.198, 0.004, 1.8, 1.2, 3600*3.5*10^(-6.0)};  
(*MvG parameters:  $\alpha$ ,  $\theta_s$ ,  $s$ ,  $n$ ,  $\beta$ , and  $K_{sat}$  in cm/hr *)
```

In[49]:=

```
fmean = {0.089, 0.202, 0.003, 1.74, 1.56, 3600*7.36*10^(-6.0)};
```

In[50]:=

```
hrcnyr = 24*365;
```

In[51]:=

```
<< Graphics`
```

In[52]:=

```
<< Graphics`MultipleListPlot`
```

#### • $K$ - $\psi$ model definitions

Mualem-van Genuchten hydraulic conductivity:

In[53]:=

```
KMvG[ $\psi$ _,  $\alpha$ _,  $n$ _,  $\beta$ _,  $Ks$ _] :=  
Module[{ $m$ ,  $\bar{\psi}$ },  
   $m = (n - 1.0) / n$ ;  
   $\bar{\psi} = (1.0 + ((\alpha \psi)^n))^(-1/m)$ ;  
   $Ks ((\bar{\psi}^(-m))^n) ((1.0 - ((1.0 - ((\bar{\psi}^(-m))^n)^(1.0/m)))^2)$ 
```

In[54]:=

```
XL06mvg[ $\psi$ _] = KMvG[ $\psi$ , DL06[[3]], DL06[[4]], DL06[[5]], DL06[[6]]];
```

In[55]:=

```
XL20mvg[ $\psi$ _] = KMvG[ $\psi$ , DL20[[3]], DL20[[4]], DL20[[5]], DL20[[6]]];
```

```
In[56]:=
Ksmvvg[ψ_] = KMvG[ψ, smean[[3]], smean[[4]], smean[[5]], smean[[6]]];
```

```
In[57]:=
Kfmvvg[ψ_] = KMvG[ψ, fmean[[3]], fmean[[4]], fmean[[5]], fmean[[6]]];
```

Mualem-van Genuchten moisture retention:

```
In[58]:=
thMvG[ψ_, a_, n_, ths_, thr_] :=
Module[{m, s},
  m = (n - 1.0) / n;
  s = (1.0 + (a Abs[ψ])^n);
  thr + ((ths - thr) ((s)^(-m)))
```

```
In[59]:=
thL06mvg[ψ_] = thMvG[ψ, DL06[[3]], DL06[[4]], DL06[[2]], DL06[[1]]];
```

```
In[60]:=
thL20mvg[ψ_] = thMvG[ψ, DL20[[3]], DL20[[4]], DL20[[2]], DL20[[1]]];
```

```
In[61]:=
thsmvvg[ψ_] = thMvG[ψ, smean[[3]], smean[[4]], smean[[2]], smean[[1]]];
```

```
In[62]:=
thfmvvg[ψ_] = thMvG[ψ, fmean[[3]], fmean[[4]], fmean[[2]], fmean[[1]]];
```

Gardner hydraulic conductivity:

```
In[63]:=
KG[ψ_, a_, Ks_] := If[ψ < 0, Ks Exp[a ψ], Ks]
```

#### •Replace MvG K-ψ with set of piecewise continuous Gardner models

Set bottom and top  $\psi$ , then the step value  $\Delta \log \psi$  used to segment the  $\log \psi$  range ( $\text{Log}[\psi_{\text{top}}] - \text{Log}[\psi_{\text{bot}}]$ ). This yields the number of segments (partitions) of the  $K(\psi)$  curve and thus the number of equations, neqn.

```
In[64]:=
ψbot = 0; ψtop = -10000;

In[65]:=
Alogψ = 0.09; n1 = Round[Log[10, Abs[ψtop - ψbot]] / Alogψ]; y = Table[-10^(i + Alogψ), {i, 0, n1}];
y[[1]] = 0;
If[Abs[y[[n1 + 1]]] < Abs[ψtop], y = Append[y, ψtop], y[[n1 + 1]] = ψtop];
neqn = Length[y] - 1
```

```
Out[67]:=
45
```

```
In[68]:=
K[y];
```

evapQpcw\_dissApp8C.nb

file:///Users/johnsigda/rsrch/03/03papers/diss/evapPWCdiss\_moz.html

Reduce the number of  $\psi$  points < -10 cm

In[69]:=

```
y2 = Flatten[List[y[[1]], y[[5]], y[[8]], y[[11]], y[[Range[12, neqn + 1]]]]; y = y2;
neqn = Length[y] - 1
```

Out[69]=

38

In[70]:=

```
Length[y]
```

Out[70]=

39

In[71]:=

```
neqn
```

Out[71]=

38

Calculate slope and intercepts for set of piecewise continuous Gardner models:

Sand sample DL06:

In[72]:=

```
(KL06 = Table[DL06[[6]], {i, 1, neqn}];
aL06 = Table[(Log[DL06[[6]]] - Log[KL06avg[-y[[2]]]]) / (-y[[2]]), {i, 1, neqn}];
Do[
  (aL06[[j]] = (Log[KG[y[[j]]], aL06[[j - 1]], KL06[[j - 1]]] - Log[KL06avg[-y[[j + 1]]]]) /
  Abs[(y[[j]] - y[[j + 1]]);
  KL06[[j]] = Exp[aL06[[j]] (0 - y[[j]]) + Log[KG[y[[j]]], aL06[[j - 1]], KL06[[j - 1]]];),
  {j, 2, neqn}]; aL06
```

Out[72]=

```
{0.00142082, 0.00572652, 0.0139203, 0.0236763, 0.0320814, 0.0434625, 0.0585131, 0.0772768,
0.0979313, 0.115798, 0.125001, 0.122913, 0.112037, 0.0970447, 0.0815657, 0.0574424,
0.0552924, 0.0451363, 0.0367662, 0.0299162, 0.0243295, 0.0197809, 0.0160805, 0.0130716,
0.0106253, 0.0086367, 0.00702023, 0.00570628, 0.00463825, 0.00377011, 0.00306446,
0.00249089, 0.00202467, 0.00164571, 0.00133769, 0.00108731, 0.000883801, 0.00076204}
```

Mean sand:

In[73]:=

```
(Ksm = Table[smean[[6]], {i, 1, neqn}];
asm = Table[(Log[smean[[6]]] - Log[Ksmavg[-y[[2]]]]) / (-y[[2]]), {i, 1, neqn}];
Do[
  (asm[[j]] = (Log[KG[y[[j]]], asm[[j - 1]], Ksm[[j - 1]]] - Log[Ksmavg[-y[[j + 1]]]]) /
  Abs[(y[[j]] - y[[j + 1]]);
  Ksm[[j]] = Exp[asm[[j]] (0 - y[[j]]) + Log[KG[y[[j]]], asm[[j - 1]], Ksm[[j - 1]]];),
  {j, 2, neqn}];
```

Fault sample DL20:

evapQpcw\_dissApp8C.nb

file:///Users/johnsigda/rsrch/03/03papers/diss/evapPWCdiss\_moz.html

In[74]:=

```

(KL20 = Table[DL20[[6]], {i, 1, neqn}];
aL20 = Table[(Log[DL20[[6]]] - Log[KL20avg[-y[[2]]]]) / (-y[[2]]), {i, 1, neqn}];
Do[
  (aL20[[j]] = (Log[KG[y[[j]], aL20[[j-1]], KL20[[j-1]]] - Log[KL20avg[-y[[j+1]]]) /
    Abs[(y[[j]] - y[[j+1]])]);
  KL20[[j]] = Exp[aL20[[j]] (0 - y[[j]]) + Log[KG[y[[j]], aL20[[j-1]], KL20[[j-1]]]];
  {j, 2, neqn});

```

Mean fault:

In[75]:=

```

(Kfm = Table[fmean[[6]], {i, 1, neqn}];
afm = Table[(Log[fmean[[6]]] - Log[Kfmavg[-y[[2]]]]) / (-y[[2]]), {i, 1, neqn}];
Do[
  (afm[[j]] = (Log[KG[y[[j]], afm[[j-1]], Kfm[[j-1]]] - Log[Kfmavg[-y[[j+1]]]) /
    Abs[(y[[j]] - y[[j+1]])]);
  Kfm[[j]] = Exp[afm[[j]] (0 - y[[j]]) + Log[KG[y[[j]], afm[[j-1]], Kfm[[j-1]]]];
  {j, 2, neqn});

```

Declare piecewise continuous Gardner functions for each material:

In[76]:=

```

pcwKL06[ψ_, n_] := If[ψ > 0, KG[0, aL06[[1]], KL06[[1]]],
  Do[If[ψ > y[[i]], Return[KG[ψ, aL06[[i-1]], KL06[[i-1]]], Continue[]], {i, 2, n+1}]]

```

In[77]:=

```

pcwKsm[ψ_, n_] := If[ψ > 0, KG[0, asm[[1]], Ksm[[1]]],
  Do[If[ψ > y[[i]], Return[KG[ψ, asm[[i-1]], Ksm[[i-1]]], Continue[]], {i, 2, n+1}]]

```

In[78]:=

```

pcwKL20[ψ_, n_] := If[ψ > 0, KG[0, aL20[[1]], KL20[[1]]],
  Do[If[ψ > y[[i]], Return[KG[ψ, aL20[[i-1]], KL20[[i-1]]], Continue[]], {i, 2, n+1}]]

```

In[79]:=

```

pcwKfm[ψ_, n_] := If[ψ > 0, KG[0, afm[[1]], Kfm[[1]]],
  Do[If[ψ > y[[i]], Return[KG[ψ, afm[[i-1]], Kfm[[i-1]]], Continue[]], {i, 2, n+1}]]

```

•Build and solve sets of piecewise continuous Gardner models for given  $\psi$  range and varying depth to water table

Define function to build set of neqn-1 equations for each z breakpoint:

In[80]:=

```

zNeqn[nz_, α_, Ks_, ψ_] :=
  {
    Kb = KG[ψ[[1]], α[[1]], Ks[[1]]];
    Table[
      -1
      α[[j]] (Log[q + KG[ψ[[j+1]], α[[j]], Ks[[j]]] - Log[q + Kb] -
        Sum[
          Evaluate["z" <> ToString[i]] (α[[i+1]] - α[[i]])
        ], {i, 1, j-1})
    ], {j, 2, neqn}} == Symbol["z" <> ToString[j]].

```

evapQpcw\_dissApp8C.nb

file:///Users/johnsigda/rsrch/03/03papers/diss/evapPWCdiss\_moz.html

$$\{j, 1, nn\}]$$

Define function to build last equation:

In[81]:=

```
zlast[nn_, a_, Kb_, &, Zs_] :=
  {
    Kb = KG[&][[1]], a[[1]], Kb[[1]]];
    {
      -1
      a[[nn]]
      {
        Log[q + KG[&][[nn + 1]], a[[nn]], Kb[[nn]]] - Log[q + Kb] -
        {
          Sum[
            (Symbol["z" <> ToString[i]] (a[[i + 1]] - a[[i]]))
          ]
        }
      }
    }
  }
```

Define function to build and solve set of equations for the flux, q, and the pairs of (z, ψ) at the breakpoints:

In[82]:=

```
qNeqn[nn_, a_, Kb_, &, ZZ_] := {
  Kb = KG[&][[1]], a[[1]], Kb[[1]]];
  allb1 =
  Table[
    -1
    a[[j]]
    {
      Log[q + KG[&][[j + 1]], a[[j]], Kb[[j]]] - Log[q + Kb] -
      {
        Sum[
          (Symbol["z" <> ToString[i]] (a[[i + 1]] - a[[i]]))
        ]
      }
    }
    == Symbol["z" <> ToString[j]],
    {j, 1, nn - 1}];
  lastz =
  -1
  a[[nn]]
  {
    Log[q + KG[&][[nn + 1]], a[[nn]], Kb[[nn]]] - Log[q + Kb] -
    {
      Sum[
        (Symbol["z" <> ToString[i]] (a[[i + 1]] - a[[i]]))
      ]
    }
  }
  == ZZ;
  alleqn = Append[allb1, lastz];
  qinit = Which[ZZ < 50, 10^(-1), ZZ < 100, 10^(-2), ZZ < 200, 10^(-6), ZZ < 400,
    10^(-8), ZZ < 500, 10^(-10), ZZ < 800, 10^(-12), ZZ < 1000, 10^(-15), ZZ < 10000,
    10^(-18)];
  x = Table[{Symbol["z" <> ToString[i]], (ZZ * (i / nn))}, {i, 1, nn - 1}];
  allinit = Append[x, {Symbol["q"], qinit}];
  ToExpression[
    (tstr = ""; Do[tstr = tstr <> ToString[allinit[[j]], StandardForm] <> " ", {j, 1, nn}];
    "FindRoot[alleqn, {tstr <> " MaxIterations->100}"])]
```

Set minimum and maximum values over which to vary depth to water table, ZZ:

In[83]:=

```
imin = 1; imax = 1000; istep = 50;
idel = (Log[10, imax] - Log[10, imin]) / (istep - 1);
```

Define functions for each material to determine q (ZZ)

In[84]:=

```
QL06[ZZ_] := qNeqn[neqn, aL06, KL06, γ, ZZ]
```

evapQpcw\_dissApp8C.nb

file:///Users/johnsigda/rsrch/03/03papers/diss/evapPWCdiss\_moz.html

Depth to water table is 10 cm:

In[85]:=

 $x_{10} = Q_{L06}[10];$ 

In[86]:=

 $q_{10L06} = \text{hrsnyr } q /. x$ 

Out[86]=

57233.2

This is the flux density in cm/yr.

Depth to water table is 100 cm:

In[87]:=

 $x_{100} = Q_{L06}[100];$ 

In[88]:=

 $q_{100L06} = \text{hrsnyr } q /. x$ 

Out[88]=

7.69002

This is the flux density in cm/yr.

Depth to water table is 1000 cm:

In[89]:=

 $x_{1000} = Q_{L06}[1000];$ 

In[90]:=

 $q_{1000L06} = \text{hrsnyr } q /. x$ 

Out[90]=

 $4.28604 \times 10^{-2}$ Converted by Mathematica (June 29, 2003)

## APPENDIX 8.D: UFA EXPERIMENTAL DATA

Data from the UFA hydraulic conductivity – volumetric moisture content ( $K$ - $\theta$ ) and volumetric moisture content – matric potential ( $\theta$ - $\psi$ ) experiments for fault and sand samples from all Canyon Trail and Elmendorf sites follow below. The first list describes all the samples collected from each location and the UFA analyses performed on them. The next list shows the raw data from each  $\theta$ - $\psi$  experiment for each sample. The last table provides the raw data for each  $K$ - $\theta$  experiment.

## SAMPLE LIST

Location	Tare ID	Sleeve ID	L/S	K-θ	ψ - θ
<b>E10 fault &amp; fault zone</b>					
E10 FL	T7	nmt11	S	Y	Y
E10 FL002 5-6-99 lower wet	T20	dl20	L	Y	Y
E10 FZ a lower	T27	nmt18	S	Y	Y
E10FL001 5-2-99	VII - 15	dl02	L	Y	Y
E10 upper fault	T26	nmt04	S	Y	Y
E10 FZ @ contact	Q2				
<b>E10 footwall</b>					
E10 FW 02a		DL06	L	Y	Y
E10 FW 02b grey	IV - 12	DS08	S	Y	Y
E10 FW upper c gr A	U07	DS30	S		
E10 FW02 B grey c gr 5-2-99	IV - 12	ds04	S		Y
E10 upper FW c gr A	L	DS33	S		
E10 FW c gr B    bedding	U03	DS22	S	Y	Y
E10 FW c gr B perp bedding	Q1	DS23	S	Y	Y
E10 FW03a f gr	III - N		S		
E10 FW 02a repacked		DS26	S		
E10 FW f gr D	U09				
<b>E10 hanging wall</b>					
E10 HW 01 mixed		DL07	L	Y	Y
E10 HW upper f gr	U11	DS31	S		
E10 upper HW		DL21	L		
E10 upper HW C	T24	nmt13-XXX	S		
E10 upper HW D	T32	dl09	L		
E10 HW H f gr	16	nmt15	S		Y
E10 HW03 buff & grey	V - 13	ds06	S		
E10 HW04 a grey c gr	VI - 14	ds07	S	Y	Y
E10 HW c gr A	U10				
E10 HW f gr A	U06				
E10 HW l c gr	15				
<b>E13 fault zone</b>					
E13 FZ A	T20	dl08	L	Y	Y
E13 FZ B	T34	nmt05	S		
E13 FZ A 6/9/99	Q5				
<b>E13 footwall</b>					
E13 FW f gr B	E	DS32	S		
E13 FW B	T23	nmt01	S	Y	Y
<b>E13 hanging wall</b>					
E13 HW c gr A	T6				
E13 HW f gr A	T1				
E13 HW A buff + grey	T2				

Location	Tare ID	Sleeve ID	L/S	K-θ	ψ - θ
<b>E14 fault zone</b>					
E14A FZ	T33	nmt20	S		
E14DFL001 6-2-98	VIII -16	ds02	S	Y	y
E14D FL001	T28	not epoxied			
<b>E14 footwall</b>					
E14FW    bedding	13	ds05	S		
E14FW perp to bedding	T20	nmt14-XXX	S		
<b>E14 hanging wall</b>					
E14HW    to bedding	T21	ds03	S	Y	Y
E14HW perp to bedding	T22	nmt07	S	Y	Y
E14 HW A perp bedding	Q4	DS25	S	Y	Y
E14 HW A    bedding	Q3	DS24	S	Y	Y
E14 HW A repacked		DS25	S		
<b>Elmendorf fault zone</b>					
EI A 01 6/98		DS01		Y	
EI A FZ lower	T30	dl05			Y
EI C FZ lower	T31	dl03			
EI FZ A		NMT19		Y	Y
EI ZDB	T29	dl04		Y	Y
EI A 01 6/16/98	T6				
<b>Elmendorf footwall</b>					
EL A-B	12	nmt03		Y	Y
EI A-B c gr		DL01			
EI A-B c gr	T25				
EI A-B c gr	Q6				
<b>Elmendorf hanging wall</b>					
EI A HW c gr	T24	dl05			
EL A HW f gr	T25	nmt10 - XXX			
EL A HW f gr		NMT12		Y	Y

L = large sample; S = small sample; Y = yes; N = no; gr = grained; perp = perpendicular; FW = foot wall; HW = hanging wall.

XXX indicates sample was destroyed.

Data from  $\psi$ - $\theta$  UFA experiments

Sample ID	Rotation speed (rpm)	Sample wet weight (g)	Water weight (g)	Vol. Moisture content (cm <sup>3</sup> /cm <sup>3</sup> )	Matric potential (cm)
DL02	0	82.33	7.75	0.208	0
	300	81.16	7.42	0.196	30
	800	80.49	6.88	0.180	223
	1200	79.60	6.07	0.147	563
	1500	79.18	5.72	0.138	942
	2100	78.62	5.28	0.130	1765
	3000	78.02	4.79	0.117	3578
	4000	77.53	4.40	0.105	6522
	5000	77.13	4.07	0.095	10461
	7000	76.74	3.79	0.094	19617
	10000	76.39	3.47	0.085	39752
DL02 repeat	0	82.33	8.16	0.208	0
	300	80.57	6.83	0.180	30
	600	80.11	6.46	0.168	131
	800	79.74	6.13	0.153	261
	1200	79.06	5.53	0.136	563
	1500	78.61	5.15	0.122	942
	2100	78.03	4.69	0.113	1765
	3000	77.23	4.00	0.092	3578
	4000	76.78	3.65	0.087	6522
DL06	0	146.82	22.73	0.312	0
	300	199.67	18.79	0.253	26
	600	187.83	7.04	0.055	113
	800	186.71	5.96	0.065	226
	1200	185.70	5.03	0.060	487
	1500	185.16	4.56	0.053	816
	2100	184.74	4.26	0.054	1527
	2500	184.52	4.09	0.051	2317
	3000	184.35	3.98	0.051	3324
	4000	184.13	3.86	0.051	5646
	5500	183.75	3.58	0.045	10547
	7000	183.35	3.26	0.038	17626
	10000	183.15	3.09	0.040	34378

Sample ID	Rotation speed (rpm)	Sample wet weight (g)	Water weight (g)	Vol. Moisture content (cm <sup>3</sup> /cm <sup>3</sup> )	Matric potential (cm)
DL07	0	122.61	20.79	0.336	0
	300	168.76	17.61	0.282	21
	600	158.86	7.80	0.083	90
	800	157.08	6.06	0.067	182
	1200	155.85	4.91	0.067	390
	1500	155.37	4.50	0.063	660
	2100	154.88	4.13	0.061	1229
	2500	154.67	3.97	0.059	1879
	3000	154.51	3.87	0.059	2695
	4000	154.33	3.79	0.060	4552
	5500	154.09	3.65	0.057	8491
	7000	153.91	3.55	0.055	14244
	10000	153.63	3.30	0.050	27630
DL20	0	76.15	6.95	0.198	0
	300	75.46	6.52	0.179	28
	600	75.21	6.38	0.175	123
	800	75.08	6.29	0.171	245
	1200	74.63	5.87	0.155	528
	1500	74.31	5.56	0.141	883
	2100	73.80	5.06	0.128	1654
	3000	73.11	4.38	0.106	3352
	4000	72.66	3.94	0.096	6114
DS02	0	43.78	4.75	0.229	0
	300	43.00	4.58	0.215	27
	600	42.40	4.04	0.183	118
	800	42.04	3.70	0.157	241
	1200	41.38	3.06	0.123	516
	1500	41.07	2.75	0.107	874
	2100	40.60	2.29	0.088	1624
	3000	40.32	2.02	0.084	3287
	4000	40.13	1.83	0.076	6022
	5000	39.97	1.67	0.067	9707
	7000	39.73	1.44	0.058	18050
	10000	39.58	1.30	0.055	36526

Sample ID	Rotation speed (rpm)	Sample wet weight (g)	Water weight (g)	Vol. Moisture content (cm <sup>3</sup> /cm <sup>3</sup> )	Matric potential (cm)
DS04	0	88.76	6.56	0.258	
	300	87.75	4.61	0.160	2
	600	85.92	2.83	0.083	10
	800	85.29	2.22	0.055	21
	1200	84.90	1.88	0.058	46
	1500	84.73	1.75	0.055	78
	2100	84.53	1.61	0.053	145
	3000	84.42	1.57	0.055	294
	4000	84.36	1.56	0.055	540
	5000	84.29	1.53	0.053	871
	6000	84.24	1.52	0.053	1283
	10000	84.07	1.39	0.047	3085
					6
DS07	0	55.825	8.23	0.322	0
	300	53.57	6.19	0.207	25
	600	50.99	3.66	0.101	109
	800	50.07	2.76	0.060	223
	1200	49.36	2.10	0.056	476
	1500	49.08	1.86	0.051	809
	2100	48.86	1.70	0.053	1501
	3000	48.72	1.63	0.054	3037
	4000	48.54	1.50	0.047	5568
	5000	48.46	1.46	0.048	8984
	6000	48.34	1.38	0.041	13223
	10000	48.20	1.28	0.042	31844
					4
S08	0	69.10	10.18	0.294	0
	300	66.63	7.93	0.225	26
	600	62.36	3.71	0.073	116
	800	61.64	3.01	0.064	236
	1200	61.15	2.57	0.065	506
	1500	60.97	2.43	0.063	857
	2100	60.74	2.26	0.060	1593
	3000	60.58	2.17	0.060	3223
	4000	60.33	1.97	0.050	5905
	5000	60.24	1.92	0.053	9519
	6000	60.12	1.84	0.048	14003
	10000	59.97	1.73	0.048	33842
					2

Sample ID	Rotation speed (rpm)	Sample wet weight (g)	Water weight (g)	Vol. Moisture content (cm <sup>3</sup> /cm <sup>3</sup> )	Matric potential (cm)
DS22	0	48.86	6.72	0.310	0
	300	46.96	4.97	0.197	28
	600	46.72	4.76	0.191	126
	800	46.12	4.18	0.143	256
	1200	45.87	3.95	0.154	548
	1500	45.65	3.74	0.138	928
	2100	44.12	2.23	0.035	1725
	3000	44.02	2.15	0.084	3492
	4000	43.90	2.03	0.077	6395
	5000	43.82	1.95	0.074	10306
	7000	43.74	1.87	0.073	19172
	10000	43.65	1.78	0.069	38799
DS23	0	50.44	7.45	0.286	0
	300	46.69	3.88	0.147	32
	600	44.92	2.14	0.066	140
	800	44.64	1.88	0.062	281
	1200	44.41	1.67	0.060	606
	1500	44.33	1.60	0.058	1018
	2100	44.27	1.56	0.059	1902
	3000	44.19	1.50	0.057	3852
NMT04	0	33.05	3.64	0.242	0
	300	32.40	3.18	0.211	30
	600	32.25	3.09	0.205	132
	800	32.15	3.01	0.196	267
	1200	31.77	2.65	0.161	573
	1500	31.51	2.39	0.134	966
	2100	31.14	2.03	0.114	1802
	3000	30.85	1.75	0.101	3648
	4000	30.65	1.55	0.089	6672
	5000	30.53	1.43	0.084	10737
	7000	30.32	1.23	0.070	20019
	10000	30.16	1.08	0.063	40530

Sample ID	Rotation speed (rpm)	Sample wet weight (g)	Water weight (g)	Vol. Moisture content (cm <sup>3</sup> /cm <sup>3</sup> )	Matric potential (cm)
NMT11	0	27.52	2.68	0.198	0
	300	27.16	2.47	0.190	27
	600	27.08	2.45	0.189	118
	800	27.00	2.39	0.180	241
	1200	26.76	2.17	0.156	516
	1500	26.60	2.01	0.137	874
	2100	26.33	1.75	0.117	1624
	3000	26.09	1.52	0.102	3287
	4000	25.92	1.35	0.090	6022
	5000	25.81	1.24	0.083	9707
	7000	25.64	1.08	0.072	18050
	10000	25.50	0.95	0.064	36526
NMT15	0	48.49	7.32	0.309	0
	300	45.35	4.40	0.180	21
	600	43.97	3.07	0.114	93
	800	43.28	2.40	0.069	192
	1200	42.82	1.99	0.072	409
	1500	42.63	1.84	0.068	699
	2100	42.47	1.74	0.070	1293
	3000	42.35	1.69	0.069	2614
	4000	42.24	1.63	0.066	4802
	5000	41.98	1.41	0.045	7762
	6000	41.92	1.39	0.056	11440
	10000	41.80	1.31	0.054	27299
NMT18	0	45.57	4.15	0.207	0
	300	45.00	4.19	0.209	32
	600	44.76	4.01	0.198	140
	800	44.64	3.91	0.190	283
	1200	44.30	3.59	0.168	608
	1500	44.07	3.36	0.151	1025
	2100	43.68	2.98	0.132	1911
	3000	43.34	2.65	0.119	3870
	4000	43.06	2.37	0.103	7076
	5000	42.86	2.17	0.094	11384
	7000	41.49	0.81	-0.020	21236
	10000	41.40	0.73	0.033	42997

Sample wet weight is the sample weight at the end of the centrifugation step. Water weight is the weight of water remaining in the sample. Volumetric moisture content and matric potential are values inverted from raw data using Forbes [1994].

Data from K- $\theta$  UFA experiments

Sample ID	Rotation speed (rpm)	Flux rate (ml/hr)	Sample wet weight (g)	Water weight (g)	Vol. Moisture content (cm <sup>3</sup> /cm <sup>3</sup> )	Hydraulic conductivity (cm/s)
DL02	1000	12.9	81.19	7.89	0.209	9.88E-06
	1000	10.0	80.86	8.01	0.212	7.30E-06
	1200	10.0	80.62	7.76	0.205	5.07E-06
	1500	10.0	80.47	7.62	0.202	3.25E-06
	2000	10.0	80.19	7.35	0.194	1.83E-06
	2000	2.0	79.12	6.28	0.166	3.65E-07
	2000	1.0	78.89	6.05	0.160	1.83E-07
	2000	0.5	78.71	5.87	0.155	9.13E-08
	2300	0.2	78.51	5.67	0.150	2.76E-08
	2485	0.1	78.17	5.33	0.141	1.18E-08
DL06	300	386.2	205.29	23.46	0.318	1.20E-03
	300	50.0	200.92	19.09	0.259	1.56E-04
	600	50.0	193.44	11.70	0.159	3.89E-05
	1000	50.0	191.01	9.33	0.127	1.40E-05
	1500	50.0	189.73	8.18	0.111	6.22E-06
	2000	40.0	188.82	7.37	0.100	2.80E-06
	2000	5.0	187.83	6.38	0.086	3.50E-07
	2455	1.0	186.84	5.46	0.074	4.65E-08
DL07	300	397.9	172.19	20.77	0.335	1.14E-03
	300	50.0	170.04	19.46	0.314	1.44E-04
	600	50.0	162.62	12.13	0.196	3.60E-05
	1000	50.0	159.95	9.52	0.154	1.29E-05
	1500	50.0	157.95	7.65	0.123	5.75E-06
	2000	40.0	156.74	6.54	0.106	2.59E-06
	2455	1.0	154.97	4.84	0.078	4.29E-08
DL20	1000	5.4	76.11	7.36	0.198	3.50E-06
	1000	5.0	75.95	7.20	0.199	3.26E-06
	1200	5.0	75.90	7.14	0.197	2.26E-06
	1500	5.0	75.75	7.00	0.193	1.45E-06
	2000	5.0	75.56	6.82	0.188	8.14E-07
	2000	2.0	75.14	6.40	0.177	3.26E-07
	2000	1.0	74.96	6.22	0.172	1.63E-07
	2000	0.5	74.80	6.06	0.167	8.14E-08
	2300	0.2	74.40	5.66	0.156	2.46E-08
	2485	0.1	74.17	5.43	0.150	1.05E-08

Sample ID	Rotation speed (rpm)	Flux rate (ml/hr)	Sample wet weight (g)	Water weight (g)	Vol. Moisture content (cm <sup>3</sup> /cm <sup>3</sup> )	Hydraulic conductivity (cm/s)
DS02	1400	35.9	43.80	4.89	0.230	1.93E-05
	1400	25.0	43.49	4.58	0.215	1.02E-05
	1500	25.0	43.36	4.46	0.210	8.91E-06
	2000	25.0	43.03	4.18	0.197	5.01E-06
	2000	15.0	42.82	3.97	0.187	3.01E-06
	2000	5.0	42.26	3.41	0.000	1.00E-06
	2000	1.0	41.92	3.07	0.145	2.00E-07
	2000	0.5	41.27	2.42	0.114	1.00E-07
	2300	0.2	41.02	2.20	0.104	3.03E-08
	2500	0.1	41.12	2.31	0.109	1.28E-08
	3000	0.0	40.64	1.87	0.088	6.24E-10
DS07	300	514.3	87.79	9.40	0.322	2.03E-03
	300	50.0	86.21	7.82	0.268	1.97E-04
	1500	50.0	81.32	3.09	0.106	7.90E-06
	2000	40.0	81.02	2.84	0.097	3.55E-06
	2000	15.0	80.79	2.61	0.089	1.33E-06
	2000	5.0	80.78	2.60	0.089	4.44E-07
	2500	0.1	80.18	2.04	0.070	5.68E-09
	3000	0.0	79.90	1.80	0.062	2.76E-10

Sample ID	Rotation speed (rpm)	Flux rate (ml/hr)	Sample wet weight (g)	Water weight (g)	Vol. Moisture content (cm <sup>3</sup> /cm <sup>3</sup> )	Hydraulic conductivity (cm/s)
DS08	300	578.8	99.80	10.29	0.295	2.22E-03
	300	50.0	98.40	8.89	0.255	1.92E-04
	1500	50.0	93.15	3.80	0.109	7.68E-06
	2000	40.0	93.28	3.98	0.114	3.46E-06
	2000	15.0	92.79	3.49	0.100	1.30E-06
	2000	5.0	92.27	2.97	0.085	4.32E-07
	2500	0.1	91.72	2.46	0.071	5.53E-09
	3000	0.0	91.30	2.08	0.060	2.69E-10
DS22	300	411.2	93.04	7.91	0.320	2.27E-03
	300	50.0	92.43	7.30	0.296	2.76E-04
	600	50.0	89.59	4.46	0.181	6.91E-05
	1000	50.0	88.97	3.85	0.156	2.49E-05
	1500	50.0	88.84	3.72	0.151	1.11E-05
	2000	40.0	88.45	3.33	0.135	4.97E-06
	2000	5.0	88.13	3.12	0.127	6.22E-07
	2000	1.0	87.96	2.95	0.120	1.24E-07
	2000	0.5	87.91	2.90	0.118	6.22E-08
	2300	0.2	87.80	2.80	0.114	1.88E-08
	2500	0.1	87.71	2.72	0.110	7.96E-09
	3000	0.01	87.48	2.50	0.101	3.87E-10
DS23	300	357.1	92.17	7.33	0.287	2.16E-03
	300	50.0	92.11	7.27	0.284	3.02E-04
	600	50.0	89.39	4.55	0.178	7.55E-05
	1500	15.0	87.49	2.77	0.108	3.63E-06
	1500	15.0	87.49	2.77	0.108	3.63E-06
	2000	15.0	87.29	2.58	0.101	2.04E-06
	2000	5.0	87.33	2.62	0.103	6.80E-07
	2000	1.0	86.89	2.18	0.085	1.36E-07
	2000	0.5	86.80	2.09	0.082	6.80E-08
	2300	0.2	86.62	1.92	0.075	2.06E-08
	2500	0.1	86.56	1.87	0.073	8.70E-09
	3000	0.01	86.28	1.60	0.062	4.23E-10

Sample ID	Rotation speed (rpm)	Flux rate (ml/hr)	Sample wet weight (g)	Water weight (g)	Vol. Moisture content (cm <sup>3</sup> /cm <sup>3</sup> )	Hydraulic conductivity (cm/s)
NMT04	800	19.0	33.09	3.63	0.242	2.12E-05
	800	5.0	32.80	3.34	0.223	9.71E-06
	1000	5.0	32.73	3.28	0.219	6.21E-06
	1500	5.0	32.43	3.06	0.204	2.76E-06
	2000	5.0	32.41	3.04	0.203	1.55E-06
	2000	1.0	32.16	2.84	0.190	3.11E-07
	2000	0.5	31.94	2.62	0.175	1.55E-07
	2300	0.2	31.54	2.25	0.150	4.70E-08
	2500	0.1	31.41	2.13	0.142	1.99E-08
	3000	0.01	31.07	1.83	0.122	9.66E-10
NMT11	1400	6.1	27.21	2.43	0.187	3.74E-06
	1400	5.0	27.19	2.41	0.186	3.06E-06
	1500	5.0	27.13	2.36	0.182	2.67E-06
	2000	5.0	27.01	2.29	0.177	1.50E-06
	2000	4.0	26.96	2.24	0.173	1.20E-06
	2000	3.0	26.97	2.25	0.174	9.01E-07
	2000	1.0	26.79	2.07	0.160	3.00E-07
	2000	0.5	26.66	1.94	0.150	1.50E-07
	2300	0.2	26.52	1.83	0.141	4.54E-08
	2500	0.10	26.37	1.69	0.131	1.92E-08
	3000	0.01	26.08	1.44	0.111	9.34E-10
NMT18	1100	10.1	45.05	4.03	0.201	8.30E-06
	800	5.0	44.97	3.92	0.196	7.74E-06
	1000	5.0	44.93	3.89	0.194	4.95E-06
	1500	5.0	44.82	3.86	0.193	2.20E-06
	2000	5.0	44.63	3.72	0.186	1.24E-06
	2000	1.0	44.42	3.51	0.175	2.48E-07
	2000	0.5	44.19	3.28	0.164	1.24E-07
	2300	0.2	44.11	3.23	0.161	3.75E-08
	2500	0.1	43.93	3.06	0.153	1.59E-08
	3000	0.01	43.60	2.77	0.138	7.71E-10

Sample wet weight is the sample weight at the end of the centrifugation step. Water weight is the weight of water remaining in the sample. Volumetric moisture content is the average moisture content for the sample. Hydraulic conductivity is calculated using (8.A.31).